Stellar Feedback, AGN Feedback and Fluid Microphysics in Galaxy Evolution

Thesis by
Kung-Yi Su

In Partial Fulfillment of the Requirements for the
Degree of
Doctor of Philosophy

CALIFORNIA INSTITUTE OF TECHNOLOGY
Pasadena, California

2019
Defended May 23, 2019

Kung-Yi Su
ORCID: 0000-0003-1598-0083

ACKNOWLEDGEMENTS

First, I would like to thank my advisor, Philip Hopkins, who literally picked me up at the lowest point of my life. When I switched fields in the fourth year of my Ph.D. study, Phil took me into the group, and bear with my ignorance. He not only provided academic, research, and career advice, but is also more than generous in sharing the credit, promoting my work, and supporting my trips. I feel lucky for having such an advisor and mentor whom I would not hesitate going to whenever I need advice. Phil set an exceptionally great example and high standards, with his broad knowledge in each sub-field of galaxy formation, sharp physical intuition, and extremely high efficiency. I will always look up to these attributes.

I also thank Chris Hayward, with whom I collaborated for all my thesis work. Chris helped me tremendously not only in developing and defining the projects, but also in numerous other aspects, especially during the first year after I switched fields. As I will become Chris's colleague at the CCA, Flatiron Institute, I look forward to our continued collaboration.

Moreover, I appreciate all the fellow graduate students in Phil's group, especially Xiangcheng Ma and Matt Orr. Xiangcheng, being the first student of Phil, was frequently bothered by me with all sorts of questions I had, and always provided me with timely help. Matt Orr, being also my officemate, proof-read almost everything I wrote, and is probably the person I chatted/discussed with the most frequently.

I feel very blessed to be in the Feedback in Realistic Environments (FIRE) collaboration, in which I can do cutting-edge physics research with state-of-the-art simulations, building on the great achievements and developments of Phil and the others. I feel fortunate to discuss and work with the greatest scientists, including Chris Hayward, Eliot Quataert, Dušan Kereš, Claude-André Faucher-Giguère, Daniel Anglés-Alcázar, Michael Boylan-Kolchin, Shea Garrison-Kimmel, Coral Wheeler, Cameron Hummels, Paul Torrey, Andrew Wetzel, Suoqing Ji, Victor Robles, TK Chan, and all the others. I especially thank Chris, Dušan, Shea, Claude, and Eliot for all their help and support during my job application.

I also thank the other faculty members at Caltech and elsewhere whom I have interacted with, especially my thesis committee members, Chuck Steidel, Evan Kirby, and Chris Martin.

Being a physics graduate student at Caltech, I genuinely benefited from the forgiving

legislation and the funding flexibility, which made it possible for me to switch fields even in the fourth year of my graduate study. I also thank the administrative staff, especially JoAnn in TAPIR and Daniel and Laura in ISP for all the prompt help.

Throughout the eight years of my graduate study in Caltech, I was fortunate to have lots of friends around to enjoy life outside of work. I owe my special thanks to Shun-Jia and Min-Feng for being with me thick and thin during my graduate study. I also thank Yun-Ting, Ying-Hsuan, Yu-Li, Hsiao-Yi, Linhan, Nien-En, Sunny, Chia-Hsien, Han-Hsin, Felix, Ying-Yu, Yen-Yung, Vincent, Mike, Jenny, Jill, and the Wu family for enduring friendships. I would especially like to single out Shu-Heng Shao, my lifetime best friend and 6th cousin according to 23andMe, for all the encouragement and support during my hardest time.

Finally, I also want to thank my undergraduate advisor, Pisin Chen, for first bringing me into physics research, and staying as a great mentor and friend after I left Taiwan for my graduate study. Most importantly, I owe my greatest thanks to my parents for their understanding and unconditional support throughout my life.

Dedicated to my father 蘇再興,
and to my mother 余芳美.

ABSTRACT

Understanding how the baryonic physics affects the formation and evolution of galaxies is one of the most critical questions in modern astronomy. Significant progress in understanding stellar feedback and modeling them explicitly in simulations have made it possible to reproduce a wide range of observed galaxy properties. However, there are still various pieces of missing physics and uncertainties in galaxies of different mass range.

In this thesis, I will explore these missing pieces in baryonic physics on top of the Feedback in Realistic Environments (FIRE) stellar feedback in the cosmological hydrodynamic zoom-in simulations (FIRE-2 suite) and isolated galaxy simulations. These high-resolution simulations with FIRE physics capture multi-phase realistic interstellar medium (ISM) with gas cooling down to 10K, and star formations in dense clumps in giant molecular clouds. They are, therefore, an ideal tool for investigating the missing pieces in baryonic physics.

In the first part of the thesis, Chapter 2, I will focus on the discrete effects of stellar feedback like individual supernovae, hypernovae, and initial mass function (IMF) sampling in dwarfs (10^9 – $10^{10} M_\odot$). These discrete processes of stellar feedback can have maximum effects on the small galaxies without being averaged out. I will show that the discretization of supernovae (SNe) is absolutely necessary, while the effects from IMF sampling and hypernovae (HNe) is not apparent, due to the strong clustering nature of star formation.

In the second part of the thesis, Chapter 3 - 4, I will focus on fluid microphysics, exploring their effects on galaxy properties and their interplay with stellar feedback in sub-L* galaxies. I will demonstrate that, once the stellar feedback is explicitly implemented as FIRE stellar feedback model, fluid microphysics such as magnetic fields, conduction, and viscosity only have minor effects on the galaxy properties like star formation rate (SFR), phase structure, or outflows. Stellar feedback also strongly alters the amplifications and morphology of the magnetic fields, resulting in much more randomly-oriented field lines. However, despite the stellar feedback, the amplification of magnetic fields in ISM gas is primarily dominated by flux-freezing compression.

In the final part of my thesis, I focus on the massive cluster ellipticals of 10^{12} – $10^{14} M_\odot$, where the physical mechanisms that regulate the observation-inferred cool-

ing flows are highly uncertain — the classic "cooling flow problem". I showed that solutions in the literature not associated with an active galactic nucleus (AGN), including stellar feedback, the cosmic ray from stellar feedback, magnetic fields, conduction, and morphological quenching, cannot possibly quench the galaxies, mostly because of the insufficient energy and the limited size of the affected region. After ruling out the non-AGN feedback solutions to the cooling flow problem, I will go into the most accessible, and perhaps promising solution: "AGN feedback", exploring the generic classes of AGN feedback models proposed in the literature. I am going to show that enhancing turbulence and injecting cosmic ray are probably the most important aspects of AGN feedback in galaxy quenching. Since they provide non-thermal pressure support that stably suppresses the core density, they can stably reduce the cooling flows without overheating the galactic cores.

PUBLISHED CONTENT AND CONTRIBUTIONS

K.-Y. Su, P. F. Hopkins, C. C. Hayward, C.-A. Faucher-Giguère, D. Kereš, X. Ma, and V. H. Robles. Feedback first: the surprisingly weak effects of magnetic fields, viscosity, conduction and metal diffusion on sub-L∗galaxy formation. *MNRAS*, 471:144–166, October 2017. doi: 10.1093/mnras/stx1463.

K.-Y. Su, C. C. Hayward, P. F. Hopkins, E. Quataert, C.-A. Faucher-Giguère, and D. Kereš. Stellar feedback strongly alters the amplification and morphology of galactic magnetic fields. *MNRAS*, 473:L111–L115, January 2018a. doi: 10.1093/mnrasl/slx172.

K.-Y. Su, P. F. Hopkins, C. C. Hayward, X. Ma, C.-A. Faucher-Giguère, D. Kereš, M. E. Orr, and V. H. Robles. The failure of stellar feedback, magnetic fields, conduction, and morphological quenching in maintaining red galaxies. *MNRAS, in press, arXiv:1809.09120*, September 2018b.

Kung-Yi Su, Philip F. Hopkins, Christopher C. Hayward, Claude-André Faucher-Giguère, Dušan Kereš, Xiangcheng Ma, Matthew E. Orr, T. K. Chan, and Victor H. Robles. Cosmic Rays or Turbulence can Suppress Cooling Flows (Where Thermal Heating or Momentum Injection Fail). *arXiv e-prints*, art. arXiv:1812.03997, December 2018c.

Kung-Yi Su, Philip F. Hopkins, Christopher C. Hayward, Xiangcheng Ma, Michael Boylan-Kolchin, Daniel Kasen, Dušan Kereš, Claude-André Faucher-Giguère, Matthew E. Orr, and Coral Wheeler. Discrete effects in stellar feedback: Individual Supernovae, Hypernovae, and IMF Sampling in Dwarf Galaxies. *MNRAS*, 480(2):1666–1675, October 2018d. doi: 10.1093/mnras/sty1928.

In all of the papers above, Kung-Yi Su was involved in developing the idea, ran the simulations, did the analysis, and wrote the manuscript.

TABLE OF CONTENTS

LIST OF ILLUSTRATIONS

LIST OF TABLES

Chapter 1

INTRODUCTION

Baryons, only contributing to $\sim 16-17\%$ (Jarosik et al., 2011) of the matter in the universe, is the key to understand the evolution of galaxies. Traditional dark matter only simulations, which only include gravity and assume that the baryonic mass follows the dark matter mass simply fail the galaxy mass function and the stellar mass–halo mass relations. As shown in Fig. 1.1, too many stars are formed, and the total stellar mass is significantly over-predicted especially in the most massive galaxies and the dwarfs. Simulations without strong stellar feedback also face similar challenges (Bournaud et al., 2010, Dobbs et al., 2011, Harper-Clark & Murray, 2011, Hopkins et al., 2011, Krumholz et al., 2011, Tasker, 2011).

Moreover, dark-matter-only simulations (cold dark matter) also predict other results contradicting to the observations, e.g., too many satellites (e.g., Kauffmann et al., 1993, Klypin et al., 1999, Moore et al., 1999), much denser galactic cores with cuspy profiles (Amorisco et al. 2014, Flores & Primack 1994, Kuzio de Naray et al. 2008, Ogiya & Burkert 2015, Oh et al. 2008, Salucci et al. 2012, Walker & Peñarrubia 2011, de Blok et al. 2008, but see Strigari et al. 2014), etc.

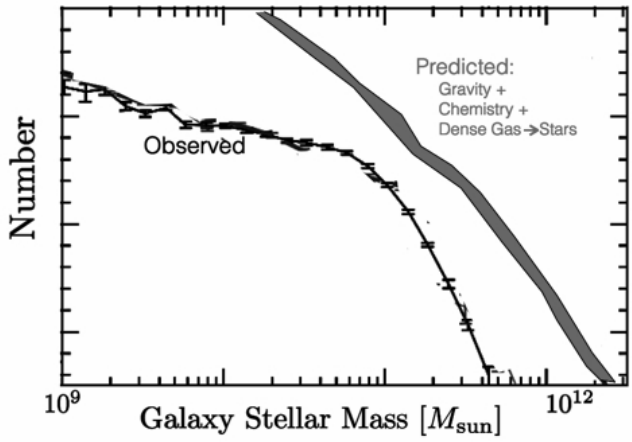

Figure 1.1: Simulations include only gravity and assume that the baryonic mass follows the dark matter mass over-predicts the total stellar mass. The plot is taken from the slide from Philip Hopkins used in "Mapping the Pathways of Galaxy Transformation Across Time and Space" conference (2016).

1.1 Important baryonic physics in galaxy evolution

Rapid progress has been made in the last decade in modeling baryonic physics, especially stellar feedback, in galaxy simulations (see e.g., Agertz & Kravtsov, 2016, Ceverino & Klypin, 2009, Governato et al., 2007, Hopkins et al., 2011, 2012a,b, Uhlig et al., 2012). Explicitly modeling stellar feedback in simulations (Hopkins et al., 2011, 2012a, Hu et al., 2016, 2017, Richings & Schaye, 2016) can result in a self-regulated multi-phase ISM, with giant molecular clouds (GMCs) turning only a few percent of their mass into stars in a dynamical time, and SFRs in agreement with observations (Hopkins et al., 2012b, 2013a,d). Cosmological zoom-in simulations in the FIRE[1] (Feedback In Realistic Environments) suite (Hopkins et al., 2014), especially, have been shown to be able to reproduce a wide range of observations, including star formation histories (Hopkins et al., 2014), the Kennicutt-Schmidt relation (Orr et al., 2018), the star-forming "main sequence" and time-variability of star formation (Sparre et al., 2017), galactic winds (e.g., Anglés-Alcázar et al., 2017b, Muratov et al., 2015, 2017), the dense HI content of galaxy haloes (Faucher-Giguère et al., 2015, 2016, Hafen et al., 2017), the implied photon escape fractions of high-redshift galaxies (Ma et al., 2016b), and galaxy metallicities (Ma et al., 2015a). I will briefly discuss the essential pieces of baryonic physics in the following.

1.1.1 Gas heating and cooling

As gas accretes onto the galaxies, accretion shocks can heat the gas up to the viral temperature. Other heating sources include Compton heating, photoionization and photoelectric heating from stars, black hole, and ionizing background. The reionization is the primary cause of the quenching of the ultra-faint dwarfs (Bullock et al., 2000). Finally, there is also cosmic rays and shock heating from supernovae and AGN feedback.

On the other hand, various cooling mechanisms have to cool down the gas before they can fall into the galactic core and form stars. Important terms include bremsstrahlung for hot gas ($> 10^6$ K), metal-line cooling and atomic cooling for warm gas ($10^4 - 10^6$ K), and fine-structure lines, molecular, and dust cooling for cold gas ($< 10^4$ K).

1.1.2 Star formation

As the gas cools down, gravitational instabilities result in the gas fragmentation and the formation of the supersonically turbulent self-gravitating GMCs in the ISM. The fragmentation continues until the scale of proto-star. The initial stellar mass follows

[1] Project web site: http://fire.northwestern.edu

initial mass function.

In FIRE, self-gravitating molecular gas denser than 1000cm^{-3} is allowed to form stars in a free-fall time. Although stars form in a free-fall time, stellar feedback quickly disrupts the GMC allowing only $\sim$ 1% of the gas to form stars. The star particles in the simulations are treated as single stellar populations following Kroupa (2002) IMF.

1.1.3 Stellar feedback

Through the life of a star, its feedback injects energy and momentum to the surrounding gas through the following mechanism: (1) Photo-heating: The photons from stars ionize and heat up the surrounding gas through photoionization and photoelectric heating. (2) Radiation pressure: The photons absorbed by dust grains also deposit photon momentum to the gas. (3) Supernovae: SN Types II or Ia generates a Sedov-Talor blast waves depositing 10^{51} erg to the surrounding gas. (4) Stellar winds: Stellar mass losses with continuously injected mass, metals, energy, and momentum from OB and AGB winds. Stellar feedback can effectively regulate the star formation for any galaxy $\lesssim 10^{12}$M$_\odot$, and results in a realistic multi-phase ISM.

1.2 Uncertainties from other baryonic physics

Explicitly modeling the aforementioned gas cooling/heating, star formation and stellar feedback in cosmological zoom-in simulations (FIRE) has reached great success in reproducing a wild range of galactic properties and scaling relations. However, there are still various uncertainties and open questions in baryonic physics and how they affect galaxy evolution. In the following, I will address the points that will be the main focus of this theses.

1.2.1 How the discrete effect of stellar feedback affects dwarfs

Despite the success of stellar feedback, certain discrete stellar feedback processes still have uncertain effects on dwarfs, where the potential well is shallow, and the total number of stars is low. The following are the two major points that will be discussed in Chapter 2.

The star to star variation in stellar feedback

It is common in galaxy-scale simulations to treat continuous quantities (e.g., stellar mass-loss and radiative heating rates) as IMF-averaged. In reality, these rates are highly variable star-to-star, with most of the feedback from OB-winds, ionizing

photons, and radiation pressure coming from massive O stars. When galaxies are sufficiently massive, these effects should average out, but in dwarfs, in particular, failure to account for these fluctuations could lead to biased predictions for galaxy properties. This is certainly the case for measurements of e.g., the ionizing flux and spectral shapes of such systems (see Krumholz et al., 2015, da Silva et al., 2012). IMF sampling gets more important when the mass resolution increases, and the baryonic particle mass fall below $\sim 10^4 M_\odot$ (Hensler et al., 2016, Hu et al., 2017). In such cases, the IMF is poorly sampled in a single star particle.

Super-energetic stellar feedback event: Hypernovae

HNe are core-collapse SNe that have energies that exceed the typical SN energy ($\sim 10^{51}$ erg) by a factor of 10 or more ($E > 10^{52}$ erg; Nomoto et al. 2004, Podsiadlowski et al. 2004). Such extreme events could potentially blow out all the gas in a dwarf galaxy, consequently completely quenching star formation if the dark matter halo is too low-mass to accrete further gas post-reionization. Whether or not an HNe quenches star formation determines whether its yield products can be incorporated into next-generation stars, which in turn determines whether or not the yield products of HNe should be observable.

1.2.2 The role of fluid microphysics in galaxies

Fluid microphysics such as magnetic fields, conduction and viscosity are not always included in galaxy simulations but can potentially affect various galactic properties. In Chapter 3, I will discuss their effects in a wide range of sub-L* galaxies. In Chapter 5, I will explore whether fluid microphysics especially magnetic fields and conduction can help suppress the cooling flows (§ 1.2.3).

Magnetic fields

The tiny magnetic field seeded in the early universe is amplified by cosmic structure formation and by magnetic dynamos in the ISM or circum-galactic medium (CGM). However, there are uncertainties on what the dominant field amplification mechanism is in the galaxies and whether stellar feedback affects the whole picture. These will be explored in Chapter 4.

Given that the magnetic pressure can reach equipartition with the thermal and turbulent pressures (Beck, 2009, Beck et al., 1996) in certain regions of galaxies, magnetic fields have long been suspected to play a role in galaxy evolution. The magnetic

pressure can provide extra support, thus slowing down in-falling or collapsing of gas at various scale and suppressing the star formation. Magnetic fields can also be relevant because of their effects on fluid mixing instabilities, including the Rayleigh-Taylor (RT) and Kelvin-Helmholtz (KH) instabilities (Armillotta et al., 2017, Jun et al., 1995, McCourt et al., 2015). These instabilities can potentially affect galaxy evolution through processes including the evolution of supernovae (SN) remnants (Jun & Jones, 1999, Jun & Norman, 1996a,b, Kim & Ostriker, 2015b, Thompson, 2000) and AGN bubbles.

Conduction

Thermal conduction, which in the presence of magnetic fields is highly anisotropic, affects the stability of plasmas at both galactic and cluster scales (Armillotta et al., 2017, Choi & Stone, 2012, Parrish et al., 2012b, Sharma et al., 2009, 2010) and the survival and mixing of multi-phase fluids. Combined with the effect of magnetic fields, conduction may be critical to determine the survival of cool clouds in galactic winds.

Due to the strong temperature dependence of the conductivity, conduction is expected to have maximum effect in the hot halo of the massive galaxies and clusters. It can transport heat to the inner cool core and potentially suppress the inflow of the gas.

Viscosity

Viscosity has been more extensively studied in simulations of galaxy clusters. It has been suggested that viscosity can affect the turbulent motion of the intracluster medium (ICM) or CGM and affect the KH stability of various structures in the ICM (Markevitch & Vikhlinin, 2007). It has been shown in particular that viscosity may be important for the dynamics of bubbles in the ICM inflated by AGN feedback or bursts of SNe activity (Reynolds et al., 2005, Sijacki & Springel, 2006).

1.2.3 Cooling flow problem in massive galaxies

As we go up in galactic mass, one of the most significant missing pieces in understanding the galaxy evolution reveals. Massive galaxies and clusters are typically quenched, which is in contrast to the naive prediction from the classical "cooling flow" picture. The observed high X-ray luminosities in massive galaxies/clusters suggest that a large amount of cold gas should be accreting onto those galactic cores

and presumably forming stars. This discrepancy is known as the "cooling flow problem". How to suppress the cooling flows and SFRs are the essential missing pieces in the evolution of massive galaxies. I will present the solutions not associated with an AGN in Chapter 5, and those related to AGN feedback in Chapter 6.

Non-AGN feedback solutions

Given that stellar feedback kicks and heats up the surrounding gas, conduction transports heat from the outer hot halo to the inner cool-core, and that magnetic fields provide extra pressure support, they can all possible suppress the cooling flows.

Martig et al. (2009) and Dekel et al. (2009) described another scenario they referred to as "morphological quenching," whereby quenching could be accomplished (SF suppressed) simply by altering a galaxy's morphology. Specifically, they argued that turning a stellar disk into a more gravitationally stable spheroid would raise the Toomre-Q and stabilize the gas against fragmentation/star formation.

Cosmic rays

Cosmic rays (CRs) are the results of shocks, which accelerate protons to $>$ GeV. Structure formation, supernovae, and AGN feedback can all generate cosmic rays. Roughly 10% of the supernovae energy can go into the cosmic ray.

Cosmic rays can provide additional pressure support to gas, drive galactic outflows, and heat the CGM/ICM directly via hadronic, Coulomb and streaming losses (Enßlin et al., 2011, Fujita & Ohira, 2011, Fujita et al., 2013, Guo & Oh, 2008, Jacob & Pfrommer, 2017a,b, Jacob et al., 2018, Pfrommer, 2013, Pfrommer et al., 2017a, Ruszkowski et al., 2017a,b, Sharma et al., 2010, Wiener et al., 2013). Therefore, the cooling flows and star formations can also possibly be suppressed.

Black hole and AGN feedback

A supermassive black hole ($\gtrsim 10^6 M_\odot$)is expected to present most of the galaxies. The accretion of matter by a supermassive black hole resulting in an active galactic nucleus, which provides feedback (AGN feedback) with energy orders of magnitudes higher than stellar feedback. Consequently, AGN feedback seem to be the most promising possible solution to the cooling flow problem, and there has been a tremendous amount of theoretical work on the topic (for recent studies see Eisenreich

et al. 2017, Gaspari & Sądowski 2017, Jacob & Pfrommer 2017a,b, Li et al. 2017, 2018, Martizzi et al. 2018, Pellegrini et al. 2018, Weinberger et al. 2018, Yoon et al. 2018; and see e.g., Choi et al. 2012, Ciotti & Ostriker 2001, Ciotti et al. 2009, Croton et al. 2006, Fabian 1999, Guo & Oh 2008, Hopkins et al. 2005, 2006a, McNamara & Nulsen 2007, Ostriker et al. 2010, Pfrommer 2013, Silk & Rees 1998, Wiener et al. 2013 for earlier works).

AGN can expel gas from galaxies, inject thermal energy via shocks or sound waves or photoionization and Compton heating, generate CRs via shocks, "stir" the CGM and ICM, and create "bubbles" of hot plasma with non-negligible relativistic components (see e.g., Hickox & Alexander, 2018, for a detailed review). Commonly, AGN feedback is classified as 'quasar mode' and 'radio mode'. The former happens when the accretion rate is high and can quickly shut down the gas inflow. The latter one happens at lower accretion rate and is believed to be what responsible for the quench maintenance.

Despite its plausibility, unlike the stellar evolution and feedback, the growth and feedback from supermassive black holes are poorly constraint and much less understood. As a result, many studies choose a specific sub-grid AGN model with parameters marginalized over certain statistical halo properties. As an attempt to more physically understand AGN feedback, in Chapter 6, I explore how each aspect of AGN feedback (heating, expelling and stirring up gas, and injecting CRs) can affect the galaxy properties and cooling flows.

Chapter 2

DISCRETE EFFECTS IN STELLAR FEEDBACK: INDIVIDUAL SUPERNOVAE, HYPERNOVAE, AND IMF SAMPLING IN DWARF GALAXIES

Kung-Yi Su, Philip F. Hopkins, Christopher C. Hayward, Xiangcheng Ma, Michael Boylan-Kolchin, Daniel Kasen, Dušan Kereš, Claude-André Faucher-Giguère, Matthew E. Orr, and Coral Wheeler. Discrete effects in stellar feedback: Individual Supernovae, Hypernovae, and IMF Sampling in Dwarf Galaxies. *MNRAS*, 480(2):1666–1675, October 2018. doi: 10.1093/mnras/sty1928.

Using high-resolution simulations from the FIRE-2 (Feedback In Realistic Environments) project, we study the effects of discreteness in stellar feedback processes on the evolution of galaxies and the properties of the ISM. We specifically consider the discretization of supernovae (SNe), including hypernovae (HNe), and sampling the initial mass function (IMF). We study these processes in cosmological simulations of dwarf galaxies with $z = 0$ stellar masses $M_* \sim 10^4 - 3 \times 10^6\,\mathrm{M}_\odot$ (halo masses $\sim 10^9 - 10^{10}\,\mathrm{M}_\odot$). We show that the discrete nature of individual SNe (as opposed to a model in which their energy/momentum deposition is continuous over time, similar to stellar winds) is crucial in generating a reasonable ISM structure and galactic winds and in regulating dwarf stellar masses. However, once SNe are discretized, accounting for the effects of IMF sampling on continuous mechanisms such as radiative feedback and stellar mass-loss (as opposed to adopting IMF-averaged rates) has weak effects on galaxy-scale properties. We also consider the effects of rare HNe events with energies $\sim 10^{53}$ erg. The effects of HNe are similar to the effects of clustered explosions of SNe – which are already captured in our default simulation setup – and do not quench star formation (provided that the HNe do not dominate the total SNe energy budget), which suggests that HNe yield products should be observable in ultra-faint dwarfs today.

2.1 Introduction

Stellar feedback is crucial in galaxy evolution. In cosmological simulations without feedback, gas cools rapidly onto galaxies, leading to runaway collapse and star formation, and stellar masses orders of magnitude larger than observed (Cole et al.

2000, Katz et al. 1996, Kereš et al. 2009, Somerville & Primack 1999, Springel & Hernquist 2003 and references therein).

Rapid progress has been made in the last decade in modeling stellar feedback in galaxy simulations (see e.g., Agertz & Kravtsov, 2016, Ceverino & Klypin, 2009, Governato et al., 2007, Hopkins et al., 2011, 2012a,b, Uhlig et al., 2012). In Hopkins et al. (2011, 2012a), for example, a detailed feedback model including radiation pressure, stellar winds, supernovae, and photo-heating was developed and applied to idealized isolated galaxy simulations. It was shown that this stellar feedback model was able to maintain a self-regulated multi-phase ISM, with giant molecular clouds (GMCs) turning only a few percent of their mass into stars in a dynamical time, and SFRs in agreement with observations (Hopkins et al., 2012b, 2013a,d). Other groups that implement stellar feedback and explicitly follow molecular hydrogen also see a similar regulation of star formation efficiencies (Hu et al., 2016, 2017, Richings & Schaye, 2016). With numerical improvements and additional cooling physics, similar models were applied to cosmological zoom-in simulations in the FIRE[1] (Feedback In Realistic Environments) project (Hopkins et al., 2014). Subsequent work showed these feedback models could reproduce a wide range of observations, including star formation histories (Hopkins et al., 2014), the Kennicutt-Schmidt relation (Orr et al., 2018), the star forming "main sequence" and time-variability of star formation (Sparre et al., 2017), galactic winds (e.g., Anglés-Alcázar et al., 2017b, Muratov et al., 2015, 2017), the dense HI content of galaxy haloes (Faucher-Giguère et al., 2015, 2016, Hafen et al., 2017), the implied photon escape fractions of high-redshift galaxies (Ma et al., 2016b), and galaxy metallicities (Ma et al., 2015a).

However, there are several properties of discrete feedback processes that without proper modeling could potentially yield very different or even unreasonable ISM phase structures and galaxy morphologies. Supernovae (SNe) are very effective at regulating the SFR (e.g., Kim & Ostriker 2017, Kim et al. 2013, 2014), and they are naturally discrete events and tend to be clustered in time and space. Idealized studies of the ISM have shown that if the same total amount of energy is injected continuously into the ISM rather than in discrete SNe (or at too low resolution), the energy could be effectively smeared throughout the whole galaxy and be radiated away too efficiently (Kim & Ostriker, 2015a, Martizzi et al., 2015, 2016b), thus making SNe feedback much less effective than when the spatiotemporal clustering

[1]Project web site: http://fire.northwestern.edu

of SNe is properly modeled (e.g., Fielding et al., 2017, Girichidis et al., 2016a). In many simulations (including those referenced above), SNe are indeed correctly treated as individual discrete events, but this is not always the case in the literature. The effects of the discreteness and clustering of SNe are explicitly studied in high-resolution simulations of ISM gas with various densities in Kim et al. (2017). It is shown that how clustered SNe are can affect the evolution of the resulting supperbubbles and the effective radial momentum per SN event. It is therefore interesting to see how this would affect galaxy-scale simulations.

Moreover, it is common in galaxy-scale simulations to treat continuous quantities (e.g., stellar mass-loss and radiative heating rates) as IMF-averaged. In reality, these rates are highly variable star-to-star, with most of the feedback from OB-winds, ionizing photons, and radiation pressure coming from massive O stars. When galaxies are sufficiently massive, these effects should average out, but in dwarfs, in particular, failure to account for these fluctuations could lead to biased predictions for galaxy properties. This is certainly the case for measurements of e.g., the ionizing flux and spectral shapes of such systems (see Krumholz et al., 2015, da Silva et al., 2012). IMF sampling gets more important when the mass resolution increases, and the baryonic particle mass fall below $\sim 10^4 M_\odot$ (Hensler et al., 2016, Hu et al., 2017). In such case, the IMF is poorly sampled in a single star particle.

In addition to the aforementioned effects, hypernovae (HNe) may be yet another important discrete feedback channel. HNe are core-collapse SNe that have energies that exceed the typical SN energy ($\sim 10^{51}$ erg) by a factor of 10 or more ($E > 10^{52}$ erg; Nomoto et al. 2004, Podsiadlowski et al. 2004). Such extreme events could potentially blow out all the gas in a dwarf galaxy, consequently completely quenching star formation if the galaxy's dark matter halo is too low-mass to accrete further gas post-reionisation. Whether or not an HNe quenches star formation determines whether its yield products can be incorporated into next-generation stars, which in turn determines whether or not the yield products of HNe should be observable.

In this paper, we investigate the effects of the discretization of SNe, IMF sampling and the inclusion of HNe on the formation of dwarf galaxies. In § 2.2, we describe the simulations. Then, we analyze the effects on the star formation histories, morphologies, phase structures, outflows and ionizing photon escape fractions of our simulated galaxies in § 2.3. In § 2.4, we discuss our results, and our conclusions are presented in § 2.5.

Table 2.1: Galaxy simulations

Simulation Name	$M_{\rm halo}^{\rm vir}$ [$M_\odot$]	$R_{\rm vir}$ [kpc]	M_g [$M_\odot$]	M_* [$M_\odot$]	$m_{i,1000}$ [$1000 M_\odot$]	$\epsilon_{\rm gas}^{\rm min}$ [pc]	Description
m10q	8.0e9	52.4	8.4e6	1.8e6	0.25	0.52	isolated dwarf, early-forming halo
m10v	8.3e9	53.1	2.1e7	1.0e5	0.25	0.73	isolated dwarf, late-forming halo
m09	2.4e9	35.6	1.2e5	9.4e3	0.25	1.1	early-forming, ultra-faint field dwarf

Parameters of the galaxy models studied here:
(1) Simulation name: Consistent with Hopkins et al. (2018b).
(2) $M_{\rm halo}^{\rm vir}$: Virial mass (Bryan & Norman, 1998) of the main halo at $z = 0$.
(3) $R_{\rm vir}$: Viral radius of the main halo at $z = 0$.
(4) M_g: Total gas mass within $\sim 0.1 R_{vir}$ at $z = 0$ ($z = 2$ for m09).
(5) M_* : Total stellar mass within $\sim 0.1 R_{vir}$ at $z = 0$.
(6) $m_{i,1000}$: Baryonic (star and gas) mass resolution in units of 1000 $M_\odot$. Dark matter particles are always ~ 5 times heavier.
(7) $\epsilon_{\rm gas}^{\rm min}$: Minimum gravitational force softening reached by the gas in the simulation (force softenings are adaptive following the inter-particle separation). Force from a particle is exactly Keplerian at $> 1.95\epsilon_{\rm gas}$; the "Plummer-equivalent" softening is $\approx 0.7\epsilon_{\rm gas}$.

2.2 Methodology

The simulations use GIZMO (Hopkins, 2015)[2], a mesh-free, Lagrangian finite-volume Godunov-type code designed to capture both the advantages of grid-based and smoothed-particle hydrodynamics (SPH) methods, in its meshless finite mass (MFM) mode. The numerical details and tests of the method are discussed in Hopkins (2015). The default simulations use the FIRE-2 version of the code, which is described in detail in Hopkins et al. (2018b). Cooling is followed from $10-10^{10}$ K, including free-free, inverse Compton, atomic, and molecular cooling, accounting for photoionization and photoelectric heating by a UV background (Faucher-Giguère et al., 2009) and local sources.[3] Star formation occurs only in molecular, self-shielding, and self-gravitating (Hopkins et al., 2013b) gas above a minimum density $n > 1000 {\rm cm}^{-3}$.

[2] A public version of this code is available at *http://www.tapir.caltech.edu/~phopkins/Site/GIZMO.html*.

[3] Since this paper was submitted, we identified an error in the treatment of heating by cosmic-ray backgrounds (usually only important in very dense, star forming gas) which artificially enhances the intergalactic medium (IGM) temperature at very high redshifts $z \sim 100$ (it has no effect after re-ionization begins). This leads to some artificial suppression of star formation in our smallest galaxies (m09 and m10v) at $z \gg 10$. However, since it affects all runs in the same way, and we do not include any "first stars" model in the first place to properly capture the behavior at these redshifts, our conclusions in this paper should be un-affected.

We focus on low-mass dwarf galaxies, where the effects we explore should be more significant than in more massive galaxies. Three fully cosmological zoom-in simulations from the FIRE-2 suite (Hopkins et al., 2018b) are included in this study: m10q (an early-forming $10^{10} M_\odot$ halo), m10v (a late-forming $10^{10} M_\odot$ halo) and m09 (a $10^9 M_\odot$ halo). Note that the tabulated halo masses are from $z = 0$.

The initial conditions of the runs are listed in Table 2.1. Most of the simulations have been re-run at different resolutions, with the initial gas particle masses differing by a factor of ~ 100. We find all of the conclusions of this paper are insensitive to mass resolution. A resolution test can be found in Appendix A.1. For all runs, a flat ΛCDM cosmology with $h = 0.702$, $\Omega_M = 1 - \Omega_\Lambda = 0.27$, and $\Omega_b = 0.046$ is adopted.

For each galaxy, we consider four variations of the stellar feedback implementation in the simulations:

1. **Default FIRE-2 Feedback Physics ("Default"):** This is our standard FIRE-2 implementation (Hopkins et al., 2018b). To summarize: once formed, a star particle is treated as a single-age stellar population with metallicity inherited from its parent gas particle and age appropriate for its formation time. All corresponding stellar feedback inputs (SNe and mass-loss rates, spectra, etc.) are determined by using STARBURST99 (Leitherer et al., 1999) to compute the IMF-averaged rate for a Kroupa (2002) IMF. The stellar feedback model includes the following: (1) radiative feedback in the form of photoionization and photoelectric heating, in addition to single and multiple-scattering radiation pressure with five bands (ionizing, FUV, NUV, optical-NIR, IR) tracked; (2) stellar mass loss with continuously injected mass, metals, energy, and momentum from OB and AGB winds; (3) SNe Types II and Ia using tabulated SNe rates as a function of stellar age the IMF to determine the probability of an SN originating in the star particle during each timestep[4] and then determine stochastically whether an SN occurs by drawing from a binomial distribution. If an event occurs, the appropriate gas mass, metal mass, momentum, and energy are injected – in other words, SNe are discrete events. We assume that each SNe has an initial ejecta energy of 10^{51} erg (see Hopkins et al. 2017, 2018b for details regarding how this is coupled). To separate the effects of IMF sampling and HNe from purely simulation

[4]For particle masses $\approx 250\,M_\odot$ and typical timesteps in dense star-forming gas of ~ 100 yr, the probability of a SN in a young ($\sim 3 - 10$ Myr old) star particle in one timestep is $dp \sim 10^{-5}$.

stochastic effects (which vary from simulation to simulation, for the same physics), two m10q simulations are evolved with the same default physics but different random number seeds. They are labeled "Default" and "Default 2," respectively.

2. **Continuous SNe Energy Injection ("Continuous"):** Here we take our "Default" model but modify it by treating SN feedback as a continuous rather than discrete process. Specifically, for each star particle, we take the expectation value for the probability of an SN occurring in a given timestep in a star particle and simply inject that *fraction* of a single SN's feedback-related quantities (e.g., gas mass, metal mass, energy, and momentum).[5] Thus, the energy in this case is "smeared" in both time and space, as if SN feedback were continuous (as stellar winds and radiation are). The Continuous feedback simulations are not evolved all the way to $z = 0$, as they become very expensive as gas catastrophically collapses into dense structures.

3. **(Approximate) IMF-Sampling Effects ("IMF-SMP"):** In this case, we take our "Default" model and implement a very simple approximation for the effects of discreteness resulting from IMF sampling, particularly for the radiative feedback and stellar mass-loss channels. Since the simulations are still far too low-resolution to actually resolve the IMF and the feedback channels of interest are completely dominated by massive stars, we implement an intentionally simplified "toy model" for IMF sampling. Specifically, each time a star particle forms, we determine the number of massive "O stars", $N_{\rm O}$, from a Poisson distribution with expectation value $\langle N_{\rm O} \rangle \approx m_{\rm particle}/100\,{\rm M}_{\odot}$. All feedback rates that depend on massive stars (photoionization and photoelectric heating, radiation pressure in the UV, OB winds, and core-collapse SNe rates) are then scaled by the "O-star number," i.e. their IMF-averaged rates are multiplied by $N_O/\langle N_O \rangle$ (so, by definition, the IMF-averaged rates are recovered). In the SNe case, whether SN event happen is then determine stochastically by drawing from a binomial distribution according to the updated SNe rate. Each time a core-collapse SN occurs, we delete one "O star."

4. **Hypernovae ("IMF-SMP+HNe"):** Observationally, HNe are rare. One category of events that is referred to as HNe is energetic SNe associated with gamma-ray bursts (broad-lined Type Ic SN). They occur at a rate that is only

[5] This can be as little as $\sim 10^{46}$ erg per time step in dense, star-forming gas.

$\sim$ 5% of the Type Ib/Ic rate, with more energetic events ($E_{\rm HNe} \gtrsim 10^{52}$ erg) representing roughly $\sim$ 1% of the total core-collapse SNe rate (Guetta & Della Valle, 2007, Podsiadlowski et al., 2004, Soderberg et al., 2006). Another class of HNe have been theorized to come from the pair-instability SN from massive stars with 10^{53}erg but $< 10^{-4}$ of the SN rate (Gal-Yam, 2012).

Here, we are interested in the most extreme events (which would have the most dramatic effects on their host galaxies), so based on the event rate distribution in Hansen (1999), we assume an HN energy of $E_{\rm HNe} = 10^{53}$ erg (i.e. 100$\times$ a typical SN) and event rate that is 10^{-3} times the normal core-collapse SN rate. [6] In our m10q simulation, we simply assign each core-collapse event a random probability of being an HN equal to 0.1%, and, if the event is defined a HNe, we increase the energy of the ejecta by a factor of 100, but the ejecta mass is kept the same. In our m09 and m10v simulations, the stellar mass is sufficiently low that the expectation value of the number of HNe is $\lesssim 1$, so we take our "IMF-SMP" runs, re-start them just after one of the peak star formation events (at $z = 0.31$ for m10v and $z = 4.0$ for m09), and manually insert a single HN explosion at that time. Note that these choices ensure that the *total* energy contributed by HNe is only $\sim$ 10% of the SNe budget, so we are not changing the IMF-averaged properties significantly.

2.3 Results

2.3.1 Star formation rates

The first two rows of Fig. 2.1 show the cumulative stellar mass and SFR averaged in a 100-Myr interval for each galaxy. In all cases, the "Continuous" runs have an order-of-magnitude greater final stellar mass, indicating that the SN feedback is effectively weaker than in the "Default" model. Although the same amount of SNe energy is deposited into the surrounding gas particles in an integral sense, it is radiated away before doing significant work on the surrounding dense ISM significantly because the feedback is temporally diluted (a manifestation of the well-known overcooling problem in galaxy formation simulations).

On the other hand, IMF sampling does not appear to have a significant systematic effect on stellar masses, i.e. the effects of IMF sampling appear smaller than purely stochastic simulation variations. The m10q "Default" and "Default 2" runs differ significantly in star formation histories, with final stellar masses differing by a factor

[6] This may be close to an upper limit unless the IMF is more top-heavy.

of ~ 2, even though these two runs use exactly the same physics. Two more m10q "IMF-SMP" runs evolved to $z \sim 0.6$ show a similar range of stochastic differences. We thus find that the purely stochastic run-to-run variation with the same physics but with different random number seeds (resulting in variations in the detailed ages and relative positions of star particles, and therefore, the feedback injection sites) is larger than the variation when IMF sampling is included. The difference in SFRs among m10q runs is connected to the variations in gas phase structure and outflows, which will be discussed in § 2.3.2 and § 2.3.3.

In the m10q "IMF-SMP" run, an extreme but apparently stochastic overlap of many SNe at the same time (at $z \sim 0.2$) expels a large fraction of the galaxy's gas supply, causing a decrease in the SFR for an extended period of time. A similar event can be observed in the m10q "IMF-SMP+HNe" run at $z \sim 0.09$, although it is not as dramatic. These events are also a result of stochastic variations instead of differences in the feedback implementations. Of course, the very fact that stochastic effects can be this dramatic in such small dwarfs owes to the fact that just a relatively small number of highly-clustered SNe can significantly perturb the galaxy.

After manually exploding HNe in m10v and m09, star formation ceases for only a few million years. HNe do not indefinitely quench star formation even in our smallest halo in this study (m09), nor do they affect the star formation histories in a qualitatively different manner from overlapping SNe events that occur after, e.g., the formation of a modest-size star cluster in a massive GMC. Note that m09 is quenched after reionisation, although it takes until $z \sim 3$ for the galaxy to exhaust its existing cold gas supply (see Fitts et al. 2017); this behaviour is the same for all of the m09 runs considered here.

2.3.2 Phase structure

Fig. 2.2 and Fig. 2.3 quantify the density distribution of gas particles in temperature bins of cold (< 8000 K), warm (8000-10^5K) and hot ($> 10^5$K) gas at various epochs. In the m10v case, since the "IMF-SMP+HNe" run is restarted from the "IMF-SMP" run at $z = 0.31$ upon exploding a HNe and most of the star formation happens after that, only the low redshift ($z = 0 - 0.31$) results are shown. On the other hand, star formation in m09 ceases by $z \sim 2$ and therefore only $z = 2 - 4$ results are shown. The phase structure is broadly consistent with dwarf galaxy simulations from other groups (see e.g., Hu et al. 2016, 2017, Richings & Schaye 2016.)

Again, the "Continuous" runs differ from the other runs most dramatically in all

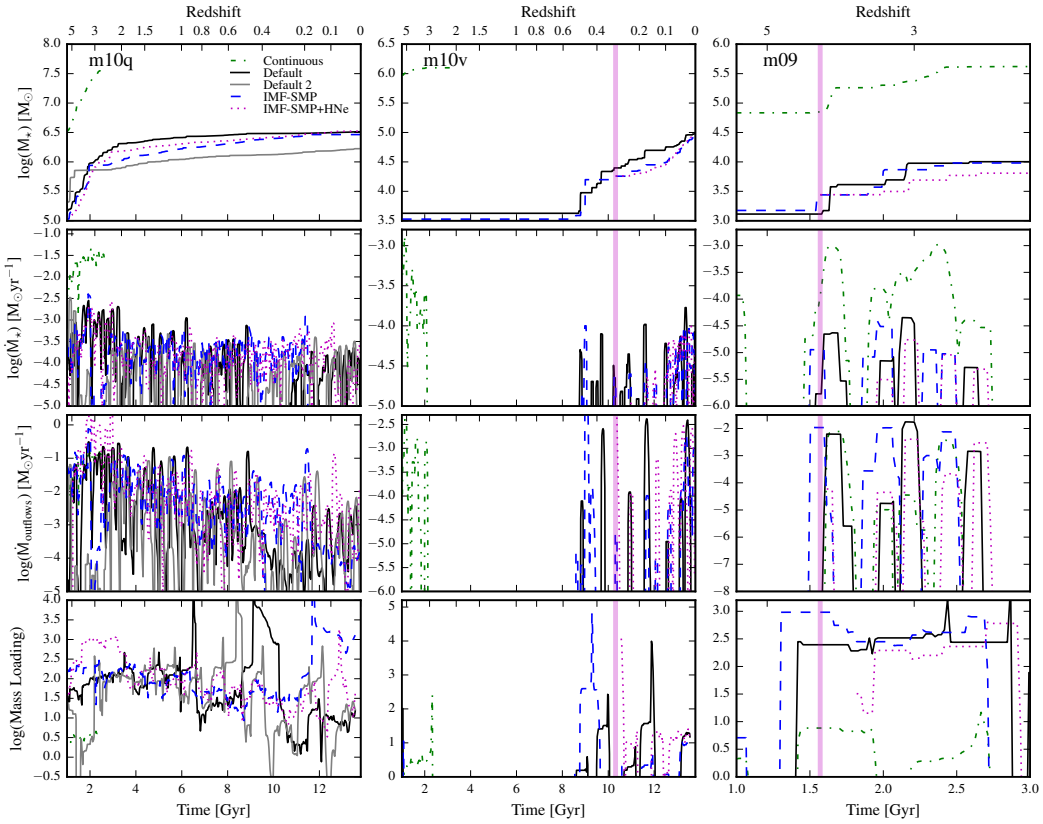

Figure 2.1: **Top row:** Stellar mass as a function of cosmic time in our simulations. The vertical magenta lines label the times when HNe are manually exploded in the m10v and m09 runs (m10q, being more massive, has $\sim$ 30 HNe randomly distributed among the SNe over its history). **Second row:** SFR averaged over the preceding 100 Myr as a function of time. **Third row:** The mass outflow rate as a function of time smoothed over 100 Myr. To estimate the mass outflow rate, we consider all gas particles between 0.08 and 0.1 r_{vir} that have radial velocities greater than 30 km s^{-1}. **Bottom row:** Outflow mass-loading factor, $\eta \equiv \dot{M}_{\rm outflow}/\dot{M}_{\rm SFR}$, smoothed over 500 Myr. Treating SN feedback as continuous results in higher SFRs – and thus stellar masses – and lower outflow mass loading factors. The final stellar mass of m10q "Default" and "Default 2" runs differ by a factor of $\sim$ 2. Given such range of stochastic effect, the effect of IMF sampling or HNe is not obvious. In the m09 run in which an HN was included, the final stellar mass is reduced by $\sim$ 0.2 dex. All panels are plotted after the 1st Gyr of the simulation when the haloes are slightly more settled and the outflows are more well-defined.

cases. All the runs with continuous SNe have higher total gas mass, especially in the cold and warm temperature bins. The total stellar mass is also orders of magnitude higher, which indicates that, without discretizing SNe, feedback is much less efficient and more gas can accrete onto the galaxy.

The lack of cold gas in m10q "Default 2" run during the $z = 2 - 4$ interval is consistent with its lower SFR in the same period. The lower SFR also results in less hot, intermediate density gas. Given the difference between m10q "Default" and "Default 2" runs, the effect of IMF sampling on phase structure is not obvious. IMF sampling does not appear to systematically alter the phase structure of the gas in m10v and m09 as well. Since FIRE dwarf galaxies at this mass scale have relatively bursty star formation histories (El-Badry et al., 2016, Faucher-Giguere, 2017, Fitts et al., 2017, Sparre et al., 2017), IMF sampling is likely subdominant to bursts in establishing the phase structure of gas in these simulations.

In all cases, HNe do not alter the phase structure significantly. Whenever a HNe occurs, its effects only last for a few million years.

2.3.3 Outflows

The third row of Fig. 2.1 shows the outflow rate as a function of time in the simulations. The value shown is averaged over a 100 Myr period. To isolate "outflows", we simply take all gas within a thin layer from 0.08 to 0.1 r_{vir} that has an outward radial velocity greater than 30km s^{-1} (comparable to the circular velocity in these dwarfs). The bottom row of Fig. 2.1 is the outflow mass-loading, defined as $\dot{M}_{\rm outflow}/\dot{M}_{\rm SFR}$, indicating the efficiency of stellar feedback at driving outflows. The plotted mass-loading is averaged over 500 Myr, to suppress stochastic effects. The density distributions of the outflows are shown in the fourth columns of Fig. 2.2 and Fig. 2.3.

The "Continuous" runs again demonstrate fundamental differences: despite having similar outflow masses to the other runs, the star formation rate in the "Continuous" runs is an order of magnitude higher and the mass-loading is therefore much lower. This indicates that without discretizing SNe, the "smeared" SNe energy injection is much less efficient at accelerating gas into outflows.

The difference in outflows among the other m10q runs is consistent with the variation in star formation rates as the difference in outflow mass-loading is not significant during most of the time. This suggests that feedback efficiency in each run is similar on the average. Given the stochastic variance we see from the "Default" and "Default

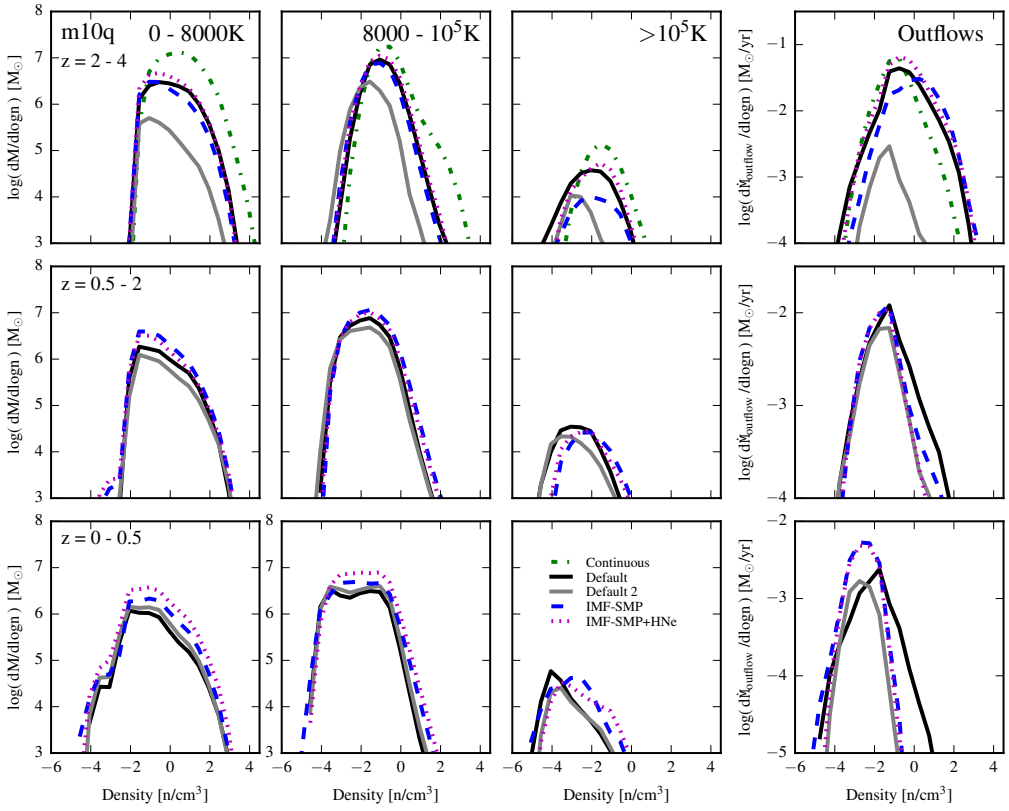

Figure 2.2: Gas density distributions for m10q. Rows show the properties at different redshifts; columns show phases including cold-neutral (*left*), warm-ionized (*middle left*), hot (*middle right*), and in outflows (*right*). The "Continuous" run has more gas in all temperature bins, owing to less efficient feedback. Owing to the orders of magnitude higher stellar mass, it produces a significant outflow despite the feedback being effectively weaker. Given the stochastic difference between "Default" and "Default 2" runs, the effect of IMF sampling is not obvious.

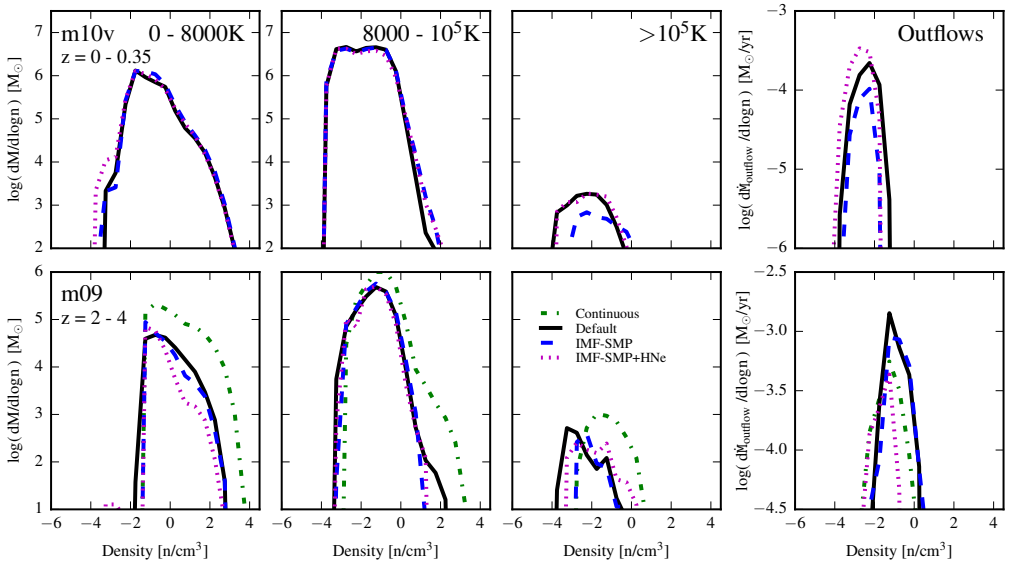

Figure 2.3: Density distributions of outflows and gas in different phases as in Fig. 2.2, but for m10v and m09. **Top Row:** "IMF-SMP+HNe" run of m10v, from the time of the HNe ($z = 0.31$) to $z = 0$. **Bottom Row:** m09 from $z = 4$ to $z = 2$. The accretion rate of the "Continuous" run is higher, and therefore generates more cold and warm gas. HNe and IMF Sampling do not have large effects in these cases.

2" runs, the effect of IMF sampling is again not obvious.

A peak of outflow can be seen just right after the manually-exploded HNe in the m10v and m09 cases. However, the long-term effects of HNe in these runs are, again, not obvious.

2.3.4 Ionizing photon escape fractions

To investigate the ionizing photon escape fractions, we follow the method in Ma et al. (2015b, 2016b). All the snapshots are processed by the 3 dimensional Monte Carlo radiative transfer (MCRT) code, basing on SEDONA base (Kasen et al., 2006). For each snapshot, the intrinsic photon budget Q_{int} is calculated as the sum of the photon budget of each star particle estimated through the BPASSv2 (Stanway et al., 2016) model, which includes detailed binary evolution effects. Because the model stellar evolution tracks exist only for certain metallicities, the input metallicity is assumed to be 0.001 (0.05 $Z_\odot$) [7], which is roughly the averaged value in the simulations. We also assume 40% of the metals are in dust phase with opacity $10^4 \mathrm{cm}^2\mathrm{g}^{-1}$ (Dwek, 1998, Fumagalli et al., 2011). In the runs considering the effects of sampling the

[7] We use $Z_\odot = 0.02$ (Anders & Grevesse, 1989).

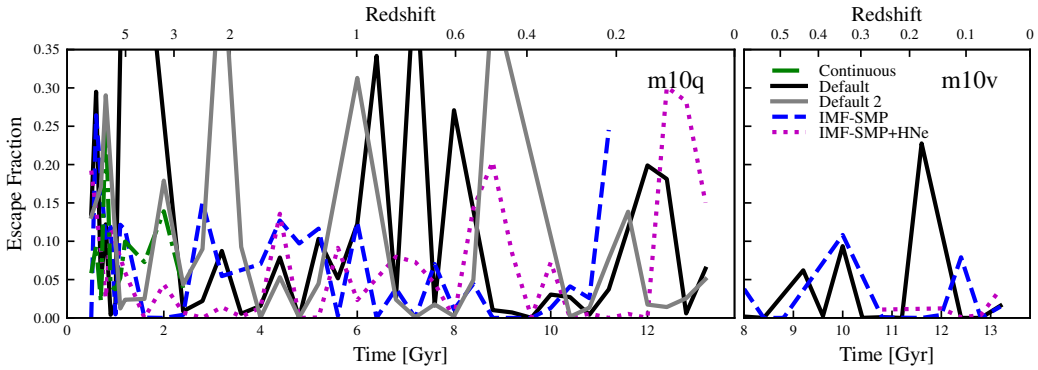

Figure 2.4: Photon escape fractions (Q_{esc}/Q_{int}) for the m10q and m10v cases. No systematic effect from IMF Sampling, SNe discretization, or HNe is observed.

IMF, the photon budget from each star is scaled properly with its O-star number.

The MCRT code includes photoionization (Verner et al., 1996), collisional ionization (Jefferies, 1968), and recombination (Verner & Ferland, 1996). We run the calculation iteratively to reach converged results by assuming the gas in ionization equilibrium. The escape fraction is defined as the Q_{esc}/Q_{int}, where Q_{esc} is the calculated number of escaped photons at approximately R_{vir}. Some examples of convergence test can be found in Ma et al. (2015b).

Fig. 2.4 shows the 400 Myr-averaged escape fraction for m10q and m10v runs. There are very few snapshots with young star particles (< 5 Mry old, when most ionizing photons are emitted) in m09 and in m10v before $z = 0.6$, so the results in those periods are poorly sampled and are therefore not shown. The photon escape fractions are highly variable during the simulated period, ranging from $\lesssim 0.001$ to 0.25, but no systematic effect from different models is observed.

The effects of IMF sampling on photon escape fractions are small. IMF sampling mainly affects the photon budget when there are O stars in the star particles. However, those stars are mostly deeply buried in dense GMCs from which the photons rarely escape in any case.

2.4 Discussion

2.4.1 IMF Sampling effects

We see no obvious effects from our IMF sampling model (in the properties we have analyzed). Our implementation of IMF sampling is based on a simple scaling of the local magnitude of feedback according to the number of massive O stars. Those GMCs with higher O-star number can be destroyed more easily by feedback (both from SNe and "pre-processing" radiative feedback and OB-winds) and form fewer stars in their lifetime. On the other hand, in the regions (periods) where (when) there are fewer O stars, the effects of feedback are weaker and therefore the gas accretion rate increases.

In larger haloes (e.g., SMC-mass and larger), which form orders of magnitude more stars and have much deeper potential wells, phenomena such as galactic winds result from the collective effects of many stars. Hence, the local variation of O-star number will be less significant.

On the other hand, in the haloes where many fewer stars are formed (e.g., dwarfs like m09, m10v or m10q), the amount of gas in the close neighborhood of young stars is reduced and a single SNe (which is already discretized in these simulations) has a large feedback effect regardless of whether or not other SNe explode nearby. As a result, the spatial and time variation of the local magnitude of feedback is already large, and IMF sampling may be a secondary effect compared to strong stellar clustering.

It is also worth noting that IMF sampling does not statistically change the spatial and time distribution of SNe events (primarily determined by the distribution of star formation events, which trace the dense, self-gravitating ISM gas), other than linking the strength in each feedback channel to the local O-star number. In other words, it does not on average increase SNe rate, and nor does it make SNe more or less clustered.

In the runs with IMF sampling, the number of O stars is drawn from a Poisson distribution with mean and variance equal to the average number of O stars. Regardless of the random numbers drawn, most O stars will explode as SNe within 30 Myr. As a result, the statistical properties of SNe are roughly the same as with the default physics. An important difference in runs with IMF sampling is that star particles with higher O-star numbers will not only have more SNe but also generate more powerful stellar wind and radiative feedback (instead of IMF-averaged). In other words, the modified SNe feedback is synchronized with the other feedback

channels. Although this may further boost the total feedback strength in different regions beyond merely the variation in SNe, such boost is probably modest if SNe are the dominant feedback mechanism, which is often the case in dwarfs like m10q, m10v and m09.

We note that our simulations marginally resolve the Sedov-Taylor phase of individual supernova remnants. A single SN remnant cools when it has swept out a mass $\sim 2500\, f(Z)^3\, M_\odot\, (n/\mathrm{cm}^{-3})^{-2/7} (E_{\rm SN}/10^{51}\,\mathrm{erg})^{6/7}$ of gas (where $f(Z) \sim 2$ at $Z \sim 0.01\, Z_\odot$, owing to less efficient cooling at low metallicities; see discussion in Hopkins et al. 2018a). So, at $n \sim 1$ cm^{-3} and our fiducial mass resolution of $250\, M_\odot$, this equates to ~ 80 resolution elements. "Pre-processing" from other (included) stellar feedback channels (e.g., stellar winds and photo-ionized gas pressure) also lead to SNe preferentially exploding in lower-density environments, which are marginally better-resolved given the $n^{-2/7}$ dependence above (Hopkins et al., 2014, Muratov et al., 2015). Although many authors have shown that under-resolving SNe can make them less effective at driving outflows (Forbes et al., 2016, Hu et al., 2016, Naab & Ostriker, 2017, Walch & Naab, 2015)k, our numerical SNe coupling scheme (which explicitly accounts for unresolved Sedov-Taylor phases before coupling) is designed specifically to handle this intermediate-resolution case and give results as close to converged as possible. This is studied and demonstrated in detail in Hopkins et al. (2018a), for both individual SNe remnant simulations and cosmological simulations (including our m10q model here), with resolution reaching $< 1\, M_\odot$. We explicitly show there that our $250\, M_\odot$ runs are well-converged with these much-high resolution runs in terms of bulk galaxy properties (stellar and gas masses, star formation histories, sizes). We find consistent results in our own resolution study in Appendix A.1.

2.4.2 Ineffective HNe feedback

By construction, in m10q and m10v, the *total* injected HNe energy in the simulation period is subdominant at $\sim 10\%$ of the integrated SNe energy. In the m09 run, the energy injected by the HN is comparable to total energy injected by SNe throughout the simulation, because the galaxy has so few stars.

However, just one HN is equivalent to 100 overlapping regular SNe. As such, we see a single HN can eject a large fraction of the core ISM in these low-mass dwarfs, and successfully suppress star formation for ~ 1 Gyr. Eventually, the gas recycles and begins the next cycle of star formation - it is worth noting that even $\sim 10^{53}$ erg

can only accelerate $\lesssim 10^6 M_\odot$ of gas to speeds of order the escape velocity in these systems. However, in our simulations, the star formation in such low-mass dwarfs is highly bursty, and highly concentrated in some time intervals. In m10q or m10v, $\gtrsim 10^4 M_\odot$ stars can form in certain 100-million-year periods. In m09, although only $\sim 10^4 M_\odot$ form in the simulation, roughly half of that forms in the largest star burst. As a result, although HNe are very extreme versions of SNe, ~ 100 overlapping SNe do happen in the simulations occasionally, and have similar effects. Therefore, including HNe in the simulations does not appreciably alter galaxy evolution, in a statistical sense, compared to "normal" clustered and bursty star formation.

2.5 Conclusions

In this study, we have investigated the effects of various discrete processes in stellar feedback, including SNe, HNe and IMF sampling on the formation and evolution of dwarf galaxies with stellar masses in the range of $\sim 10^4 - 3\times10^6 M_\odot$. We summarize our conclusions below.

- Discretizing SNe injection is crucial. Treating SNe as continuous energy/momentum sources with time-averaged rates (instead of individual events) smears the energy in time and space, which allows it to radiate away far too efficiently. This severely the exacerbates the so-called "overcooling problem". As a result, feedback is effectively weaker, making galaxies accrete more gas and form orders of magnitude more stars.

- Given the purely stochastic simulation variations between m10q"Default" and "Default 2" runs, the effects of IMF sampling are not obvious. IMF sampling also has no obvious effect on the smaller and burstier galaxies (m10v or m09).

- HNe and IMF sampling effects as approximated here do not systematically affect the photon escape fraction at an appreciable level in our analysis.

- The effects of HNe are not obvious in the investigated cases. While dramatic as individual events when they occur, and capable of ejecting gas and shutting down SF temporarily (for up to ~ 1 Gyr) in ultra-faint dwarfs, they resemble overlapping SNe from star clusters, so do not qualitatively change galaxy evolution in an aggregate, statistical sense. Since the ISM gas ejected by HNe is mostly recycled after ~ 1 Gyr, it should be possible to observe HNe yields in next-generation stars in faint dwarfs.

We caution that the toy model here for IMF sampling only scales feedback strength with some "O-star number". More accurately, one should draw a mass spectrum from the IMF, and some properties (e.g., photoionization) will be more strongly sensitive to the most massive stars Hu et al. (2017). Of course, these will also produce distinct yields when they explode Hu et al. (2017). Moreover, HNe should have different enrichment properties. HNe rate is also connected with the IMF, which could be redshift dependent. At high redshift, the HNe event rate can be 10 times higher than in low redshift (Cooke et al., 2012), which can possibly further change the halo mass at reionisation, and therefore also the post-reionisation accretion. Modjaz et al. (2008) and Modjaz et al. (2011) also showed that HNe are more likely to happen in low metallicity environment. These aspects are left for future work. Besides the discreteness in feedback processes investigated in the current study, there are other processes that could be interesting and can be crucial in galaxy evolution. For instance, SNe injection should also affect the cosmic-ray (CR) energy budget, which is not included in the current feedback model but can have a large effect on ISM properties and outflows (Girichidis et al., 2016b, Ruszkowski et al., 2017a,b, Simpson et al., 2016). Detailed examination of these processes will also be left for future work.

Chapter 3

FEEDBACK FIRST: THE SURPRISINGLY WEAK EFFECTS OF MAGNETIC FIELDS, VISCOSITY, CONDUCTION AND METAL DIFFUSION ON SUB-L* GALAXY FORMATION

K.-Y. Su, P. F. Hopkins, C. C. Hayward, C.-A. Faucher-Giguère, D. Kereš, X. Ma, and V. H. Robles. Feedback first: the surprisingly weak effects of magnetic fields, viscosity, conduction and metal diffusion on sub-L∗galaxy formation. *MNRAS*, 471:144–166, October 2017. doi: 10.1093/mnras/stx1463.

Using high-resolution simulations with explicit treatment of stellar feedback physics based on the FIRE (Feedback in Realistic Environments) project, we study how galaxy formation and the interstellar medium (ISM) are affected by magnetic fields, anisotropic Spitzer-Braginskii conduction and viscosity, and sub-grid metal diffusion from unresolved turbulence. We consider controlled simulations of isolated (non-cosmological) galaxies but also a limited set of cosmological "zoom-in" simulations. Although simulations have shown significant effects from these physics with weak or absent stellar feedback, the effects are much weaker than those of stellar feedback when the latter is modeled explicitly. The additional physics have no systematic effect on galactic star formation rates (SFRs) . In contrast, removing stellar feedback leads to SFRs being over-predicted by factors of $\sim 10-100$. Without feedback, neither galactic winds nor volume filling hot-phase gas exist, and discs tend to runaway collapse to ultra-thin scale-heights with unphysically dense clumps congregating at the galactic center. With stellar feedback, a multi-phase, turbulent medium with galactic fountains and winds is established. At currently achievable resolutions and for the investigated halo mass range $10^{10}-10^{13}\mathrm{M}_{\odot}$, the additional physics investigated here (MHD, conduction, viscosity, metal diffusion) have only weak ($\sim 10\%$-level) effects on regulating SFR and altering the balance of phases, outflows, or the energy in ISM turbulence, consistent with simple equipartition arguments. We conclude that galactic star formation and the ISM are primarily governed by a combination of turbulence, gravitational instabilities, and feedback. We add the caveat that AGN feedback is not included in the present work.

3.1 Introduction

Feedback from stars is essential to galaxy evolution. In isolated galaxy simulations without strong stellar feedback, giant molecular clouds (GMCs) experience runaway collapse, resulting in star formation rates (SFRs) orders-of-magnitude higher than observed (Bournaud et al., 2010, Dobbs et al., 2011, Harper-Clark & Murray, 2011, Hopkins et al., 2011, Krumholz et al., 2011, Tasker, 2011). This is in direct contradiction with the observed Kennicutt-Schmidt (KS) relation, which shows that the gas consumption time of a galaxy is roughly $\sim 50-100$ dynamical times (Evans, 1999, Evans et al., 2009, Kennicutt, 1998, Williams & McKee, 1997, Zuckerman & Evans, 1974). Cosmological simulations without strong feedback face a similar challenge. The efficiency of cooling causes runaway collapse of gas to high densities within a dynamical time, ultimately forming far too many stars compared to observations (Cole et al. 2000, Katz et al. 1996, Kereš et al. 2009, Somerville & Primack 1999, Springel & Hernquist 2003, and references therein).

Recent years have seen great progress in modeling feedback on galaxy scales (Agertz & Kravtsov, 2016, Ceverino & Klypin, 2009, Governato et al., 2007, Hopkins et al., 2011, 2012a,b, Hu et al., 2016, Thacker & Couchman, 2000, Uhlig et al., 2012). In Hopkins et al. (2011, 2012a), a detailed feedback model including radiation pressure, stellar winds, supernovae and photo-heating was developed and applied to simulations of isolated galaxies. They showed that stellar feedback is sufficient to maintain a self-regulated multi-phase interstellar medium (ISM), with global structure in good agreement with the observations. GMCs survive several dynamical times and only turn a few per cent of their mass into stars, and the galaxy-averaged SFR agrees well with the observed Kennicutt-Schmidt (KS) law. These models were extended with numerical improvements and additional cooling physics, and then applied to cosmological "zoom in" simulations in the FIRE (Feedback In Realistic Environments) project[1]. A series of papers, using the identical code and simulation set have demonstrated that these feedback physics successfully reproduce a wide range of observations, including star formation histories of galaxies (Hopkins et al., 2014), time variability of star formation (Sparre et al., 2017), galactic winds (Muratov et al., 2015), HI content of galaxy haloes (Faucher-Giguère et al. 2015, 2016; Hafen et al., in prep.), and galaxy metallicities (Ma et al., 2015a). Other groups (e.g., Stinson et al. 2013, who implemented energy injection from SNe and an approximate treatment of UV radiation pressure, and Agertz & Kravtsov e.g.,

[1] Project web site: http://fire.northwestern.edu.

2016, who included momentum injection from SNe, radiation pressure and stellar winds) have also found that stellar feedback can regulate galaxy SFRs and lead to realistic disc morphologies.

However, several potentially important physical processes have not been included in most previous galaxy formation simulations. Magnetic fields have long been suspected to play a role in galaxy evolution because the magnetic pressure reaches equipartition with the thermal and turbulent pressures (Beck, 2009, Beck et al., 1996). Isolated galaxy simulations with magnetic fields – but using more simplified models for stellar feedback – have been studied in various contexts and suggest that magnetic fields can provide extra support in dense clouds, thus slowing down star formation (Beck et al., 2012, Pakmor & Springel, 2013, Wang & Abel, 2009). Turbulent box simulations (Piontek & Ostriker, 2005, 2007) also suggest that MRI-driven (magnetorotational instability) turbulence can suppress star formation at large radii in spiral galaxies. In particular, Kim & Ostriker (2015b) explicitly demonstrate such suppression from magnetic fields in a simulation of a turbulent box that includes momentum feedback from SNe. Magnetic fields can also be important because of their effects on fluid mixing instabilities, including the Rayleigh-Taylor (RT) and Kelvin-Helmholtz (KH) instabilities (Armillotta et al., 2017, Jun et al., 1995, McCourt et al., 2015). These instabilities can potentially affect galaxy evolution through processes including the evolution of supernovae (SN) remnants (Jun & Jones, 1999, Jun & Norman, 1996a,b, Kim & Ostriker, 2015b, Thompson, 2000).

Another potentially important effect is viscosity, which has been more extensively studied in simulations of galaxy clusters. It has been suggested that viscosity can affect the turbulent motion of the intracluster medium (ICM) or circum-galactic medium (CGM) and affect the KH stability of various structures in the ICM (Markevitch & Vikhlinin, 2007). It has been shown in particular that viscosity may be important for the dynamics of bubbles in the ICM inflated by active galactic nucleus (AGN) feedback or bursts of SNe activity (Reynolds et al., 2005, Sijacki & Springel, 2006).

Thermal conduction, which in the presence of magnetic fields is highly anisotropic, affects the stability of plasmas at both galactic and cluster scales (Armillotta et al., 2017, Choi & Stone, 2012, Parrish et al., 2012b, Sharma et al., 2009, 2010) and the survival and mixing of multi-phase fluids. Combined with the effect of magnetic fields, conduction may be critical to determine the survival of cool clouds in galactic winds.

Turbulent metal diffusion due to small-scale (un-resolvable) eddies may also have important effects. It has been suggested, for example, that unresolved turbulence in galaxy simulations may be important to effectively "diffuse" metals in the ISM and intergalactic medium (IGM; e.g., Shen et al., 2010), leading non-linearly to different cooling physics at halo centers and within the dense ISM.

While most previous studies considered these physics in isolation, their effects and relative importance may be quite different in a realistic multi-phase ISM shaped by strong stellar feedback processes. Another challenge is that conduction and viscosity in magnetized plasmas are inherently anisotropic. Properly treating this anisotropy requires MHD simulations and is numerically non-trivial; consequently, most previous studies on galactic scales have considered only isotropic conduction and viscosity. However, studies which correctly treat the anisotropy have shown that this anisotropy can produce orders-of-magnitude differences and, in some cases, qualitatively different behavior (Choi & Stone, 2012, Dong & Stone, 2009, Sharma et al., 2009, 2010, ZuHone et al., 2015)

In this paper, we study the effects of these different microphysics in the presence of explicit models for stellar feedback. While the simulations analyzed here implement the same stellar feedback physics from the FIRE cosmological simulations, we focus primarily on non-cosmological simulations of isolated galaxies, because this allows us to achieve higher spatial and mass resolution, and to have well-controlled experiments with identical galaxy initial conditions. In cosmological runs, on the other hand, the inherently chaotic nature of the problem makes detailed one-to-one comparison of simulations with varied physics more complicated; we do, however, include a limited subset of these experiments. We also make use of a new, more accurate hydrodynamic solver, needed to properly treat MHD and anisotropic diffusion.

Overall, we find that at the resolutions currently achievable in isolated galaxy and cosmological simulations, MHD, anisotropic conduction and viscosity, and sub-grid turbulent metal diffusion play a relatively minor role in the regulation of star formation and of the phases and energetics of the ISM *when the dominant effects of stellar feedback are simultaneously modeled*. We caution, however, that despite this result, some of these effects likely have some important and observationally interesting consequences on finer scales, such as for the survival of cool clouds in galactic winds (e.g., Armillotta et al., 2017, Brüggen & Scannapieco, 2016, McCourt et al., 2015), and stellar abundance distribution patterns within star clusters

or small galaxies. It is also possible that some important effects would only reveal themselves in simulations of much higher resolution than currently possible for galaxy simulations. Furthermore, the interaction of physical processes not included in our simulations with, e.g., magnetic fields is likely to prove important. This is the case in particular for the transport of cosmic rays, which a number of recent studies indicate may be an important form of feedback for galaxy evolution (e.g., Booth et al., 2013, Pakmor et al., 2016, Pfrommer et al., 2017a, Ruszkowski et al., 2017a, Salem et al., 2014, Uhlig et al., 2012).

The remainder of this paper is organized as follows: in § 3.2, we describe the initial conditions and the baryonic physics model of our default model. In § 3.3, we summarize the additional physics studied in this paper. In § 3.4, we analyze the effects on the star formation histories, morphologies, phase structures, magnetic and turbulent energies, and outflows of our simulated galaxies. We discuss the reason why the fluid microphysics have minor effects in § 3.5 and conclude in § 3.6.

3.2 Methodology

Our simulations use GIZMO (Hopkins, 2015) [2], in its Meshless Finite Mass (MFM) mode. This is a mesh-free, Lagrangian finite-volume Godunov code designed to capture advantages of both grid-based and smoothed-particle hydrodynamics (SPH) methods built on the gravity solver and domain decomposition algorithms of GADGET-3 (Springel, 2005). The numerical details of the hydrodynamic and MHD versions of the method are presented in Hopkins (2015), Hopkins & Raives (2016), and Hopkins (2016). Hopkins (2017) present tests of the anisotropic diffusion operators used in our code. Extensive comparisons of dozens of test problems demonstrate good code behavior and convergence, in good agreement with state-of-the-art moving mesh codes (e.g., AREPO, Springel 2010) and grid codes (e.g., ATHENA, Stone et al. 2008), including on historically difficult problems such as those featuring the magneto-rotational instability (MRI), magnetic jet launching, and the KH and RT fluid-mixing instabilities. Convergence tests for our isolated galaxy simulations can be found in Appendix A.2.

Note that, for the sake of consistency, previously published FIRE simulations (see references in § 1) were run with the identical source code, using GIZMO's "P-SPH" hydrodynamic solver. P-SPH is an SPH method with improvements designed to address some of the known shortcomings of SPH in treating e.g., fluid mixing in-

[2] A public version of this code is available at *http://www.tapir.caltech.edu/~phopkins/Site/GIZMO.html*.

stabilities (see Hopkins, 2013). This was done to facilitate comparison by matching exactly the code used for the first FIRE paper, Hopkins et al. (2014), written before the MFM methods were developed. Unfortunately, as shown in Hopkins & Raives (2016) and Hopkins (2017), P-SPH (while reasonably well-behaved on pure hydrodynamics problems) exhibits serious inaccuracies and may not converge on MHD and anisotropic diffusion problems. As a consequence, P-SPH *cannot* be used for our study here. We are therefore careful to distinguish our isolated galaxy simulations here from the primary "FIRE project" simulations, although they use the same (operator-split) code modules to treat stellar feedback. In fact, the updated code here - the "FIRE - 2" code, will be the subject of an extensive methods paper in preparation (Hopkins et al., in preparation) and was first used in Wetzel et al. (2016) for studying the satellites around a Milky Way-mass galaxy. A detailed study of the effects of the hydrodynamic method and other numerical details on the conclusions from the previous FIRE simulations will be the subject of the methods paper.

3.2.1 Initial conditions (ICs)

In this paper, five isolated (non-cosmological) galaxy models are studied to consider a range of characteristic galaxy types. Two cosmological zoom-in ICs are also included as a check that our conclusions are applicable in a fully cosmological environment. More details regarding the isolated disc galaxies and the cosmological simulations can be found in Hopkins et al. (2011, 2012a) and Hopkins et al. (2014), respectively, and are summarized in Table 3.1 and below. For all runs, a flat ΛCDM cosmology with $h = 0.702$, $\Omega_M = 1 - \Omega_\Lambda = 0.27$, and $\Omega_b = 0.046$ is adopted.

Note that we have tested simulations with most of our ICs re-run at different resolution, with initial gas particle mass differing by a factor ~ 100. Some absolute properties do vary according to the resolution. For example, finer ISM substructure is observed and some higher density regions are resolved as the resolution increases. Nonetheless, the main conclusions of this paper (the *relative* differences in runs with different microphysics) remain robust at all resolutions investigated. A detailed convergence study is presented in Appendix A.2.

The ICs studied here include the following:

HiZ

HiZ is a high-redshift massive starburst disc galaxy designed to match the properties of non-merging, rapidly star-forming sub-millimeter galaxies (Erb et al., 2006,

Table 3.1: Galaxy models

Model	ϵ_g (pc)	m_g ($M_\odot$)	$M_{\rm halo}$ ($M_\odot$)	c	$V_{\rm Max}$ (km/s)	$M_{\rm bar}$ ($M_\odot$)	M_b ($M_\odot$)	Bulge profile	a (kpc)	M_d ($M_\odot$)	r_d (kpc)	M_g ($M_\odot$)	r_g (kpc)
HiZ	1.4	2.5e4	2.1e12	3.5	280	1.53e11	1.0e10	Exp	1.7	4.3e10	2.3	1.0e11	4.6
Sbc	1.4	2.6e3	2.1e11	11	120	1.5e10	1.4e9	Exp	0.5	5.7e9	1.9	7.9e9	3.7
MW	3.6	3.5e3	2.1e12	12	250	1.02e10	2.1e10	Hq	1.4	6.8e10	4.3	1.3e10	8.6
SMC	0.7	3.6e2	2.9e10	15	67	1.3e9	1.4e7	Hq	2.1	1.9e8	1.0	1.1e9	3.0
Ell	4.2	7.1e4	1.4e13	6	240	1.02e12	1.4e11	Hq	3.9	1.4e10	4.0	8.6e11	4.0
CosmoMW	7	5.7e4	1.2e12	8	290	1.3e11	-	-	-	1.2e11	1.2	7.1e9	2.5
CosmoDwarf	3	2.6e2	7.9e9	9.7	20	5.2e6	-	-	-	1.7e6	-	3.5e6	-

Parameters of the galaxy models studied here (§ 3.2.1):
(1) Model name. HiZ: high-redshift, massive starburst. Sbc: local gas-rich dwarf starburst. MW: Milky-Way analogue. SMC: SMC-mass dwarf. Ell: massive elliptical with an extended gaseous halo. HiZ, Sbc, MW, SMC, and Ell are non-cosmological (isolated galaxy) simulations. CosmoMW: cosmological simulation of a MW-mass disc galaxy. CosmoDwarf: cosmological simulation of a dwarf galaxy. (2) ϵ_g: Gravitational force softening for gas (the softening for gas in all simulations is adaptive; here, we quote the minimum Plummer equivalent softening for a kernel containing 32 particles). (3) m_g: Gas particle mass. (4) $M_{\rm halo}$: Halo mass. M_{vir} for CosmoMW and CosmoDwarf. (5) c: NFW-equivalent halo concentration. (6) $V_{\rm max}$: Halo maximum circular velocity. (7) $M_{\rm bar}$: Total baryonic mass. It is the sum of gas, disc, bulge and stellar mass for isolated galaxy runs, and the sum of gas and stellar mass in the cosmological runs within 0.1 virial radius. (8) M_b: Bulge mass. (9) Bulge profile: Hq: Hernquist (1990), or Exp: Exponential. (10) a: Bulge scale-length. (11) M_d : Stellar disc mass. For CosmoMW and CosmoDwarf runs, this is the total stellar mass within 0.1 virial radius. (12) r_d : Stellar disc scale length. (13) M_g: Gas disc mass. For the Ell runs, this includes gas in the extended halo. For CosmoMW and CosmoDwarf runs, this is the total gas mass within 0.1 virial radius. (14) r_g: Gas disc scale length.
The properties quoted for CosmoMW and CosmoDwarf are the $z = 0$ values measured from the "FB" run. The CosmoDwarf does not have a well-defined disc even at $z = 0$, but is a dwarf irregular galaxy.

Genzel et al., 2008, Tacconi et al., 2010), with halo mass $M_{\rm halo} = 2.1 \times 10^{12}$ $M_\odot$ in a Hernquist (1990) profile with an NFW (Navarro et al., 1996)-equivalent concentration of $c = 3.5$. The baryonic component has a total mass of $M_{\rm bar} = 1.53 \times 10^{11}$ $M_\odot$ and consists of an exponential bulge ($\rho(r) \propto \exp(-r/a)/r$) ($M_b = 10^{10}$ $M_\odot$) with scale length $a = 1.7$ kpc and exponential stellar ($M_d = 4.3 \times 10^{10}$ $M_\odot$) and gas ($M_g = 1 \times 10^{11}$ $M_\odot$) discs with scale lengths $r_d = 2.3$ kpc and $r_g = 4.6$ kpc respectively. The gas disc initially has Toomre $Q = 1$ uniformly. Note that the virial radius is scaled for a halo at redshift $z = 2$ instead of $z = 0$. This model uses 1.65×10^7 particles, 4×10^6 of which are gas particles. The initial metallicity is set to $0.5 Z_\odot$[3].

Sbc

Sbc is a $z = 0$ dwarf starburst intended to be representative of local luminous infrared galaxies (LIRGs). The IC is composed of a dark matter halo with $(M_{\rm halo}, c) = (2.1 \times 10^{11} M_\odot, 11)$ and a baryonic component with masses $(M_{\rm bar}, M_b, M_d, M_g) = (15, 1.4, 5.7, 7.9) \times 10^9 M_\odot$ and scale lengths $(r_d, r_g, a) = (1.9, 3.7, 0.5)$ kpc. The bulge has an exponential profile. This model includes 1.7×10^7 particles, 3×10^6 of which are gas particles. The initial metallicity is set to $0.3 Z_\odot$.

MW

MW is a Milky Way-like galaxy composed of a dark matter halo with $(M_{\rm halo}, c) = (2.1 \times 10^{12}\, M_\odot, 12)$ and baryonic components with $(M_{\rm bar}, M_b, M_d, M_g) = (1.02, 2.1, 6.8, 1.3) \times 10^{10} M_\odot$ respectively. The scale lengths are $(r_d, r_g, a) = (4.3, 8.6, 1.4)$kpc. The bulge follows a Hernquist (1990) profile. The model includes 1.03×10^7 particles, 3.6×10^6 of which are gas particles. The initial metallicity is set to $Z_\odot$.

SMC

SMC is an isolated (field) Small Magellanic Cloud-mass dwarf galaxy composed of a halo with $(M_{\rm halo}, c) = (2.9 \times 10^{10}\, M_\odot, 15)$ and baryonic components with masses $(M_{\rm bar}, M_b, M_d, M_g) = (13, 0.14, 1.9, 11) \times 10^8\, M_\odot$ and scale lengths $(r_d, r_g, a) = (1, 3.9, 1.9)$ kpc. The bulge follows a Hernquist (1990) profile. There are 1.33×10^7 particles, 3×10^6 of which are gas particles. The initial metallicity is set to $0.1 Z_\odot$.

[3]The solar metallicity, $Z_\odot$, of each species (Total, He, C, N, O, Ne, Mg, Si, S, Ca, Fe) is tabulated from Asplund et al. (2009)

Ell

Ell is an elliptical galaxy with halo and disc/bulge baryonic properties $(M_{\rm halo}, c) = (1.4\times10^{13}{\rm M}_\odot, 6)$ and $(M_{\rm bar}, M_b, M_d, M_g) = (15, 14, 1.4, 0.1)\times10^{10}{\rm M}_\odot$, respectively. The baryonic components have scale lengths $(r_d, r_g, a) = (4.0, 4.3, 3.9)$ kpc. The bulge obeys a Hernquist (1990) profile. Besides the gas disc, this galaxy contains an extended live hot gas halo[4] of mass $M_{\rm gas} = 8.6\times10^{11}\,M_\odot$, initialized with a spherically-symmetric β profile with core radius equal to the halo scale radius and $\beta = 3/2$, with an initial temperature profile given by hydrostatic equilibrium and a small angular momentum corresponding to a spin parameter $\lambda = 0.033$. We use 3×10^7 particles, 1.2×10^7 of which are gas particles. The initial metallicity is set to $Z_\odot(0.05 + 0.95/(1. + (r/10{\rm kpc})^3))$.

CosmoMW

CosmoMW is a fully cosmological zoom-in simulation from the suite presented in Hopkins et al. (2014), specifically the **m12i** simulation therein, chosen because it produces a galaxy with stellar mass and morphology similar to the Milky Way. The run uses the zoom-in method (Katz & White, 1993, Porter, 1985) to follow the formation history of the galaxy from an initial redshift $z > 100$ to $z = 0$. The main halo has a total mass of $\sim 10^{12}{\rm M}_\odot$ at $z = 0$ and a typical merger and growth history for haloes of its mass. We use 2.07×10^7 total particles (8.82×10^6 gas). For this analysis, we only follow the most-massive main-progenitor halo (i.e. the center of the zoom-in region) and focus on the particles in the central region (defined as < 0.1 virial radius).

CosmoDwarf

CosmoDwarf is a another cosmological zoom-in from Hopkins et al. (2014), specifically the **m10q** simulation, chosen to be a representative dwarf galaxy – specifically one with a $z = 0$ halo mass of $\sim 10^{10}\,{\rm M}_\odot$ and typical merger and growth history. We use 3.87×10^7 total particles (1.57×10^7 gas). Again, we focus only on the main progenitor galaxy.

[4]Ideally, hot haloes should be included in the other simulated massive isolated galaxies (eg. HiZ and MW). However, because we focus on the ISM properties in the disc and evolve these galaxies for only a few 100 Myr, before the ISM gas is depleted, the lack of hot haloes does not significantly affect our results.

3.2.2 Cooling, star formation, and stellar feedback

The baryonic physics of cooling, star formation, and stellar feedback follow the implementation in Hopkins et al. (2014). In what follows, we summarize the key aspects and focus on the new physics added for this study.

Cooling

Cooling is followed from 10^{10} K to 10K, with 11 separately tracked species followed species-by-species (see e.g., Wiersma et al., 2009a). The low-temperature (metal fine-structure and molecular) cooling rates and ionization state are tabulated from a compilation of CLOUDY runs (as in Robertson & Kravtsov, 2008, Wiersma et al., 2009a), including the effects of a redshift-dependent photo-ionizing background (from Faucher-Giguère et al., 2009) and local ionizing sources as described below.

Star formation

Star formation is allowed only from gas that is locally self-gravitating (where we follow Hopkins et al. 2013b to estimate the local virial criterion at each point in the simulation), is self-shielding molecular (where the molecular fraction is estimated following Krumholz & Gnedin 2011), and exceeds a density $n > 100\,\mathrm{cm}^{-3}$.[5] If these criteria are met, stars form with a rate $\dot{\rho}_\star = \rho_{\rm mol}/t_{\rm freefall}$. In previous studies of these star formation models, we have shown that, provided stellar feedback is explicitly included and the largest fragmentation scales in the galaxy are resolved, the galactic star formation rates and histories are regulated by stellar feedback and are insensitive to changes in these criteria (as well as more complicated chemical or temperature-based star formation models); see Faucher-Giguère et al. (2013), Hopkins et al. (2011, 2012a, 2013b). We have confirmed these studies explicitly with our ICs and simulations both including and excluding the additional microphysics we study here.

Stellar feedback

A star particle inherits its metallicity from its parent gas particle, and is treated as a single stellar population. The feedback quantities (including luminosity, SN rates,

[5] Except for the CosmoMW run with MHD, the self-gravitating criterion does not account for magnetic pressure in order to be consistent with the runs without magnetic fields. However, the magnetic field strength has to reach $100\mu\mathrm{G}\times(m_i/10^5 M_\odot)^{1/3}(n/100\mathrm{cm}^{-3})^{2/3}$ to unbind a cloud, and this is rarely the case, so it is reasonable to ignore the magnetic pressure when deciding whether a cloud is self-gravitating, at least on the relatively large scales we resolve (unlike e.g., protostellar cores).

mass and metal loss rates, etc.) are tabulated from STARBURST99 (Leitherer et al., 1999) assuming a Kroupa (2002) IMF. Our stellar feedback model includes the following processes: (1) an approximate treatment of local and long-range momentum deposition from radiation pressure, including both initial single-scattering of optical/UV photons and (potentially) multiple-scattering of IR photons; (2) SNe (Types Ia and II), which occur stochastically according to the tabulated rates and, when they occur, deposit the appropriate ejecta energy, momentum, mass, and metals into the surrounding gas particles; (3) stellar winds from O-stars and AGB stars, which are treated similarly to SNe except that the injection is continuous; (4) photoionization and photoelectric heating, with each star particle acting as a source and the UV flux incident on a gas particle estimated by accounting for self-shielding and absorption from intervening material.

3.3 Additional physics

3.3.1 Magnetic fields (MHD)

We treat magnetic fields in the ideal-MHD limit, using the GIZMO implementation in the MFM mode described in Hopkins & Raives (2016). The tests described in Hopkins & Raives (2016) show that this MHD implementation correctly captures traditionally difficult phenomena such as the growth rates of the magneto-rotational instability (MRI), magnetic jet launching by discs, and magnetized fluid mixing (RT and KH) instabilities. Compared to SPH MHD methods (e.g., the P-SPH MHD mode in GIZMO; Hopkins & Raives 2016), this method is generally significantly more accurate, exhibits better convergence properties, and requires no artificial viscosity or use of an extremely large kernel size to suppress errors. For the tests presented in Hopkins & Raives (2016), state-of-the-art grid codes (e.g., ATHENA; Stone et al. 2008) can converge to the correct solution with a similar level of accuracy. However, the method employed here typically converges to a desired accuracy more quickly, specifically in problems in which advection, angular momentum conservation, self-gravity and/or following highly compressive flows are important (problems where Lagrangian methods have advantages).

When magnetic fields are present, the homogenous Euler equations of hydrodynamics are replaced by their MHD versions. In a reference frame with velocity $\mathbf{v}_{frame}$, they can be written as a set of hyperbolic PDEs of the form

$$\frac{\partial \mathbf{U}}{\partial t} + \nabla \cdot (\mathbf{F} - \mathbf{v}_{frame} \otimes \mathbf{U}) = \mathbf{S}, \tag{3.1}$$

where $\mathbf{U}$ is the state vector of the conserved quantities, $\mathbf{F}$ is the flux vector of the

conserved variables, and $\mathbf{S}$ is the source vector. In the pure MHD case, $\mathbf{U}$ and $\mathbf{F}$ can be written in the form

$$\mathbf{U} = \begin{pmatrix} \rho \\ \rho\mathbf{v} \\ \rho e \\ \mathbf{B} \end{pmatrix}$$

$$\mathbf{F} = \begin{pmatrix} \mathbf{F}_\rho \\ \mathbf{F}_P \\ \mathbf{F}_e \\ \mathbf{F}_B \end{pmatrix} := \begin{pmatrix} \rho\mathbf{v} \\ \rho\mathbf{v}\otimes\mathbf{v} + P_T\mathcal{I} - \mathbf{B}\otimes\mathbf{B} \\ (\rho e + P_T)\mathbf{v} - (\mathbf{v}\cdot\mathbf{B})\mathbf{B} \\ \mathbf{v}\otimes\mathbf{B} - \mathbf{B}\otimes\mathbf{v} \end{pmatrix}, \tag{3.2}$$

where ρ is the density, $e = u_{int} + |\mathbf{B}|^2/2\rho + |\mathbf{v}|^2/2$ is the total specific energy, and $P_T = P + |\mathbf{B}|^2/2$ is the total pressure[6].

To clean the non-zero $\nabla \cdot B$ resulting from numerical errors, a combination of the Dedner et al. (2002) and Powell et al. (1999) cleaning methods are applied in GIZMO, with important modifications for the Lagrangian nature of the code (see Hopkins & Raives (2016) for detail). In all our ICs we seed the simulation volume with a uniform initial magnetic field in the direction of the galaxy angular momentum vector. For our cosmological runs (CosmoMW and CosmoDwarf), this is a trace (sub-nG) initial field that is quickly amplified even before galaxies form. For isolated discs, we initially set $\sim 10^{-2}\,\mu$G fields, but these are quickly amplified and dominated by the field built up through a combination of the MRI, the supersonic turbulent dynamo, and the galactic fountain dynamo. For our "Ell" run, we also initialize the gas in the extended galactic halo with a purely azimuthal field in equipartition with the thermal energy (set to be in hydrostatic equilibrium).

3.3.2 Anisotropic conduction

Thermal conduction is incorporated into the Euler equations as an extra diffusion term in $\mathbf{F}_e$ from equation (3.2), following the standard Spitzer-Braginskii form. This means the conduction term added to $\mathbf{F}_e$ is $\kappa\,(\hat{\mathbf{B}}\otimes\hat{\mathbf{B}})\cdot\nabla T$, where $\hat{\mathbf{B}}$ is the unit vector along the corresponding magnetic field. $\hat{\mathbf{B}}\otimes\hat{\mathbf{B}}$ in the expression serves as a projection operator constraining the conduction energy flux to follow the magnetic field lines and makes the thermal conduction anisotropic.

The anisotropic conduction equation is solved and consistently implemented into the MFM/MFV methods in GIZMO. Hopkins (2017) presents tests confirming that the

[6] In the MHD mode, the HLLD solver is adopted. The HLLC solver is adopted otherwise.

method is numerically stable, converges with second-order accuracy (as the MHD method in GIZMO itself does), and is capable of fully anisotropic configurations (i.e. the conductive flux vanishes identically when $\hat{\mathbf{B}}$ and ∇T are perpendicular).

Instead of setting the conduction coefficient κ by hand, we calculate it self-consistently as the Spitzer conductivity (Kannan et al., 2016, Sarazin, 1988, Spitzer & Härm, 1953, Zakamska & Narayan, 2003, ZuHone et al., 2015) with the form

$$\begin{aligned}\kappa &= \frac{0.96 k_B (k_B T)^{5/2}}{m_e^{1/2} e^4 \ln\Lambda} \frac{F_i}{1 + 4.2\ell_e/\ell_T} \\ &= \frac{4.87\times10^{-7} F_i}{1 + 4.2\ell_e/\ell_T} T^{5/2} \qquad [\mathrm{erg\ s^{-1} K^{-1} cm^{-1}}],\end{aligned} \tag{3.3}$$

where F_i is the ionized fraction (computed self-consistently in our cooling routines), $\ln\Lambda \sim 37$ is the Coulomb logarithm, $\ell_e \equiv 3^{3/2}(k_B T)^2/4 n_e \sqrt{\pi} e^4 \ln\Lambda$ is the electron mean free path, and $\ell_T \equiv T/|\nabla T|$ is the temperature gradient scale length. The denominator accounts for saturation of κ, which occurs when electrons have large mean-free-paths (it limits the gradient scale length to the mean-free-path (Cowie & McKee, 1977, Kannan et al., 2016, Sarazin, 1988)). The steep temperature dependence indicates that conduction is more efficient in hotter gas.

3.3.3 Anisotropic viscosity

Viscosity is incorporated into MHD through the Navier-Stokes equations, which modify the momentum flux and the energy flux in the Euler equations as

$$\begin{aligned}\mathbf{F}_P &= \rho \mathbf{v}\otimes\mathbf{v} + P_T \mathcal{I} - \mathbf{B}\otimes\mathbf{B} + \Pi \\ \mathbf{F}_e &= (\rho e + P_T)\mathbf{v} - (\mathbf{v}\cdot\mathbf{B})\mathbf{B} + \Pi\cdot\mathbf{v}.\end{aligned} \tag{3.4}$$

For MHD, the anisotropic viscosity again follows the Spitzer-Braginskii anisotropic form, in which the viscous flux Π is

$$\Pi = -3\eta \left(\hat{\mathbf{B}}\otimes\hat{\mathbf{B}} - \frac{1}{3}\mathcal{I}\right)\left(\hat{\mathbf{B}}\otimes\hat{\mathbf{B}} - \frac{1}{3}\mathcal{I}\right) : \nabla\mathbf{v}, \tag{3.5}$$

where ":" is defined by $\mathbf{A} : \mathbf{B} \equiv \mathrm{Tr}(\mathbf{A}\cdot\mathbf{B})$. Anisotropic viscosity is also solved and consistently implemented in the MFM/MFV methods of GIZMO, with the same convergence and stability properties as anisotropic conduction.

The viscous coefficients are calculated self-consistently as the leading-order Braginskii viscosity (Braginskii, 1965, Sarazin, 1988, Sijacki & Springel, 2006, ZuHone

et al., 2015), where the shear viscosity coefficient is

$$\eta = 0.406 \frac{m_i^{1/2}(k_B T)^{5/2}}{(Ze)^4 \ln\Lambda} \frac{F_i}{1 + 4.2\ell_e/\ell_T}$$
$$= \frac{4.5\times10^{-17} F_i}{1 + 4.2\ell_i/\ell_{|v|}} T^{5/2} \quad [\mathrm{g\ s^{-1} cm^{-1}}], \tag{3.6}$$

and the bulk viscosity vanishes. Here, m_i is the average ion mass, m_e is the electron mass, ℓ_i is the ion mean free path and $\ell_{|v|}$ is the scale length of velocity.

3.3.4 Smagorinski (unresolved sub-grid eddy) models for metal diffusion

Metal mixing on large scales is resolved in the simulation. However, unlike other numerical methods with mass exchange,[7] since our code is strictly Lagrangian, mass elements (including metals) are conserved on a per-particle basis unless they are injected directly by SNe or stellar winds. This limits spurious numerical diffusion but implies that unresolved small-scale diffusion between particles is ignored.

Sub-grid models have been proposed to model this unresolved transport. Because the systems we are simulating generally have extremely high Reynolds numbers, the unresolved diffusion is usually dominated by small turbulent eddies rather than e.g., Brownian motion. The former is commonly approximated (see e.g., Shen et al. 2010) following Smagorinsky (1963) by treating the metals as a passive scalar which obey the following diffusion equation:

$$\frac{\partial \mathbf{M}_i}{\partial t} + \nabla\cdot(D\nabla\mathbf{M}_i) = 0$$
$$D = C||\mathbf{S}||_f \mathbf{h}^2, \tag{3.7}$$

where $\mathbf{h}$ is the resolution scale (at which the sub-grid model acts; here, it is the mean inter-particle separation within the kernel function, the equivalent of the cell size Δx in Eulerian codes) and C is the Smagorinsky-Lilly constant, calibrated from direct numerical simulations. C usually ranges from 0.1 to 0.2, as calculated from Kolmogorov theory(Colbrook et al., 2016, Lilly, 1967, Smagorinsky, 1963, Wadsley et al., 2008), and is set to 0.15 in our simulations. Note that this coefficient was set to 0.05-0.1 in some previous works (Brook et al., 2014, Shen et al., 2010, 2013, Williamson et al., 2016), and this value was shown to be sufficient to provide a

[7] The numerical diffusivity of MFV or AREPO (Springel, 2010) is roughly of the scale of the velocity dispersion (or sound speed) times the resolution scale, $\sim v_t \Delta x$, as their "partitions of volume" move with the flow. ATHENA (Stone et al., 2008) could have a larger diffusion owing to its use of a fixed grid, in which case the velocity term in the diffusivity can be dominated by the bulk motion.

level of diffusion comparable to that of grid codes (Wadsley et al., 2008). $\mathbf{S}$ is the symmetric traceless shear tensor defined as

$$\mathbf{S} = \frac{1}{2}(\nabla\mathbf{v} + (\nabla\mathbf{v})^{T}) - \frac{1}{3}\mathrm{Tr}(\nabla\mathbf{v}), \tag{3.8}$$

for which the diffusion vanishes in purely compressive or rotating flows. The norm in the expression is the Frobenius norm.

This model for sub-grid metal diffusion is implemented in GIZMO following Shen et al. (2010). However, because our resolution is much higher than many of the simulations in which it has been used before, the sub-grid diffusivity is much smaller. Moreover, we stress the importance of proper calibration of the constant C, which can change the diffusivity by factors of ~ 100. We also caution that, as we will show in detail in a forthcoming work, this estimator can be very noisy in SPH methods (unlike the finite-volume methods used here), owing to zeroth-order errors in the SPH gradient estimator triggering artificial diffusion. Finally, we stress that this model assumes the motion seen in $\mathbf{S}$ is entirely due to turbulent flows. If there is real bulk motion (e.g., shear in a self-gravitating disc), this estimator will be triggered artificially. Therefore, the estimated turbulent diffusivity using this simplistic sub-grid model is almost certainly an over-estimate of the real turbulent diffusivity. In future work, we will present a detailed study attempting to calibrate and rescale this model for situations where the contribution from galactic rotation is important on the resolution scale (Colbrook et al., in prep.). Our preliminary work suggests this estimator may over-estimate the true diffusivity by an order of magnitude in some cases.

3.4 Results

We simulate the ICs detailed in § 3.2.1 with four distinct combinations of physics:

- **Hydro**: Stellar feedback is not included (cooling, star formation, and self-gravity are, however). No additional microphysics (MHD, conduction, viscosity, metal diffusion) are included.
- **Hydro+MHD**: Stellar feedback is not included, but MHD are included. Additional diffusion microphysics (conduction, viscosity, metal diffusion) are not included.
- **FB**: Stellar feedback is included, but the additional microphysics (MHD, conduction, viscosity, metal diffusion) are not.

- **FB+MHD**: Stellar feedback and MHD are included, but additional diffusion microphysics (conduction, viscosity, metal diffusion) are not.
- **FB+MHD+Micro**: Stellar feedback, MHD, and the additional diffusion operators (conduction, viscosity, metal diffusion) are all included.

We analyze these four variants for each of the ICs below, with two exceptions: the two cosmological runs with no feedback (Hydro) are prohibitively expensive. We are able to run the simulation to $z \sim 6$, where the extremely high-density objects formed via the high star formation efficiencies in the absence of feedback force exceedingly small timesteps. However, some weak-feedback variations of the CosmoMW IC and the CosmoDwarf IC are presented in Hopkins et al. (2014); these are consistent with all of our other conclusions in this paper regarding the role of feedback.

The Hydro+MHD mode is only run for the MW and SMC ICs in order to demonstrate that magnetic fields have a relatively small effect regardless of whether strong stellar feedback is included, and almost all of the differences between Hydro runs and FB+MHD runs are a result of feedback.

Cosmological simulations are highly non-linear and evolved for the entire age of the Universe. Because the equations (even of gravity alone) are formally non-linear, a small perturbation can be amplified and result in surprisingly large differences at low redshift, making it non-trivial to distinguish the systemic effects of fluid microphysics from any particular change owing to stochastic effects. In each of the following CosmoMW plots, we estimate the magnitude of stochastic effects from five independent CosmoMW FB runs with small variations in the SNe coupling scheme (effectively we randomly "re-shuffle" the fraction of the SNe energy and momentum each neighbor particle sees to generate random perturbations to the system). These differences have minor systematic effects on the stellar mass formed but serve the intended purpose of introducing small perturbations between the calculations. The shaded regions in the plots indicate the regions of parameter space spanned by these five runs. Owing to computational constraints, we did not perform such an experiment for the CosmoDwarf runs or for the FB+MHD+Micro CosmoMW runs, but we expect that the magnitude of stochastic effects in these simulations should be of similar size to those in the CosmoMW FB simulations.

3.4.1 Star formation histories

Fig. 3.1 shows the star formation histories of the five isolated galaxies, CosmoMW, and CosmoDwarf, evolved under the different combinations of physics described above. The SFRs of HiZ, Sbc, MW, SMC and Ell shown in Fig. 3.1 are the values averaged over 20 million years, and the SFRs of CosmoMW and CosmoDwarf are averaged over roughly 100 million years (to make systematic, as opposed to stochastic, differences clear). To further suppress stochastic effects, the stellar mass as a function of time is also plotted in Fig. 3.2.

Without stellar feedback, the SFRs are generally higher than observed by factors of $\sim 10-100$, regardless of whether magnetic fields are included (i.e. magnetic fields alone are insufficient to globally suppress star formation). On the other hand, the additional physics we consider changes the SFR by $\lesssim 10\%$. We have also confirmed that the predicted Kennicutt-Schmidt (KS) relation is insensitive to the additional microphysics in the simulations (and in agreement with observations, as in our previous simulations with the FIRE feedback physics).

The largest effect caused by fluid microphysics can be observed in the CosmoDwarf FB+MHD+Micro run, in which the stellar mass is systemically higher than that in the FB run by a factor of ~ 1.5. We argue below that this is most likely to be a consequence of conduction, which can increase the efficiency of cooling when multiple SNe remnants overlap (and overrun small cold gas clumps in the galaxy), thereby dissipating the hot gas energy going into galactic winds slightly more efficiently.

Compared with the other galaxies, the differences in SFRs are smallest among the different Ell simulations (the SFR in the no-feedback run is never more than an order-of-magnitude greater than the SFRs in the variants that include explicit stellar feedback). The reason is that in Ell, the gas disc contributes $< 1\%$ of the total gas mass, while the majority is distributed in a hot gas halo. The cooling efficiency of the hot halo gas onto the star-forming disc therefore controls the gas supply available for star formation and becomes an important regulator of the SFR besides stellar feedback.

Although magnetic fields have been suggested in the literature as a mechanism to suppress star formation owing to their additional pressure (Beck et al., 2012, Pakmor & Springel, 2013, Piontek & Ostriker, 2005, 2007, Wang & Abel, 2009), we actually see a small hint of systemically higher stellar mass in the MHD runs when feedback is included. The difference is more obvious in the smaller galaxies

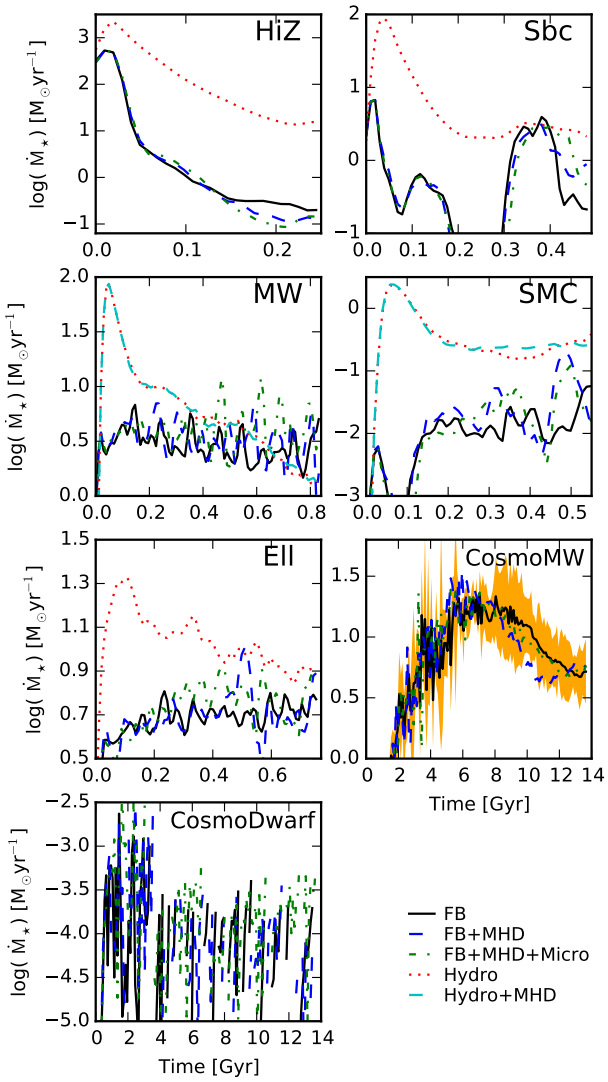

Figure 3.1: Star formation rates (SFRs) as a function of time in each of our simulations (each IC from Table 3.1, as labeled) smoothed over 20 Myr for isolated galaxy simulations and 100 Myr for cosmological simulations so that systematic differences are clearer. HiZ (massive starburst), Sbc (dwarf starburst), MW (Milky-Way analogue), SMC (SMC-mass dwarf), and Ell (massive elliptical with a "cooling flow" halo) are all isolated (non-cosmological) simulations and are thus run for only a few galaxy dynamical times. Because the CosmoMW and CosmoDwarf runs are fully cosmological zoom-in runs of a MW-mass halo and a dwarf halo, the full evolution is shown. In each, we consider four cases: default (stellar feedback, no additional microphysics, "FB"), default+MHD ("FB+MHD"), default+MHD+anisotropic conduction and viscosity+sub-grid turbulent metal diffusion ("FB+MHD+Micro"), a run without stellar feedback ("Hydro"), and a run without stellar feedback but with MHD ("Hydro+MHD", only performed for the MW and SMC ICs). In the CosmoMW case, the orange shaded region indicates the range of stochastic effects (see § 3.4). Once feedback is included, a lower, steady-state SFR emerges; the SFR has relatively small dependence on the different microphysics considered (up to stochastic effects). However, a steadier star formation history can be observed in the CosmoDwarf FB+MHD+Micro run, resulting in a slightly higher SFR on average.

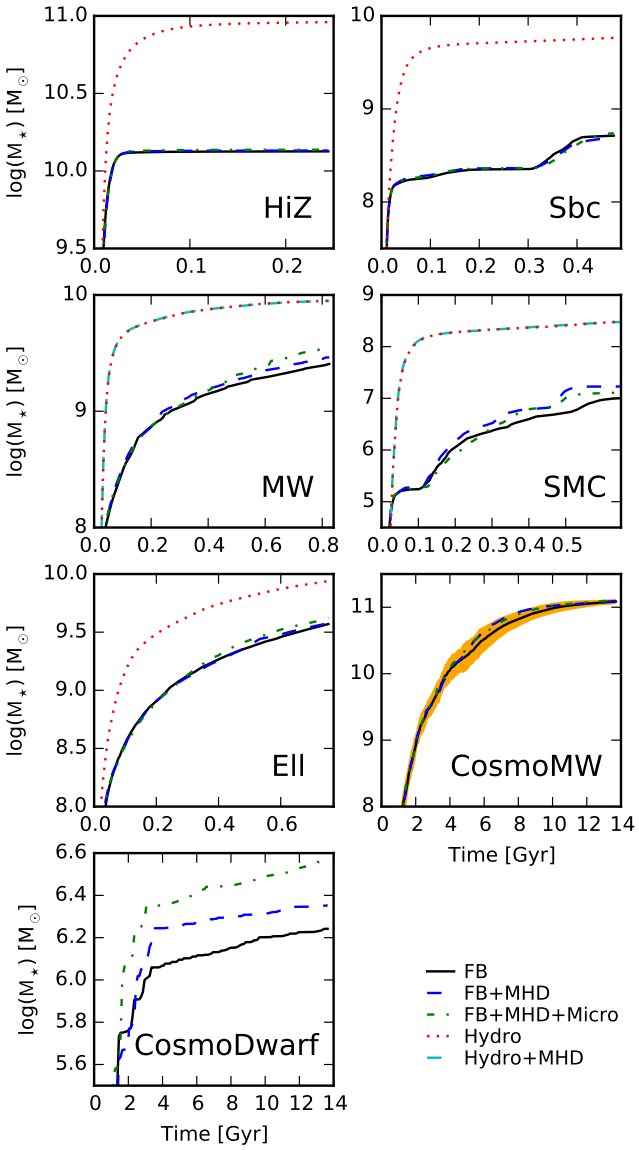

Figure 3.2: Total stellar mass as a function of time in each of our simulations (each IC from Table 3.1, as labeled). The orange shaded region in CosmoMW again indicates the range of stochastic effects. Fluid microphysics has little effect on the stellar mass formed in our simulations, in contrast to stellar feedback, which reduces the stellar mass formed by about an order of magnitude relative to the no-feedback runs. However, a small hint of higher stellar mass can be observed in the runs with magnetic fields, and in the CosmoDwarf simulations, the FB+MHD+Micro run has stellar mass a factor of $\sim$ 1.4 higher than the FB+MHD run. These effects are generally smaller than systematic uncertainties in feedback (e.g., SNe rates).

like CosmoDwarf and SMC. But even in these cases, the difference is less than 0.1 dex, despite the fact that magnetic field strengths consistent with observations are self-consistently obtained. On the other hand, without feedback, the star formation history is not significantly altered when magnetic fields are included. We discuss these points further below in § 3.5. We note, however, that magnetic fields may still play a more important role in regulating the formation of individual stars (which is unresolved in our simulations).

3.4.2 Morphologies

Fig. 3.3, Fig. 3.4 and Fig. 3.5 shows the face-on and edge-on gas morphologies of our simulated galaxies after some dynamical evolution; the colours denote gas in different temperature bins (see caption). The CosmoMW runs and CosmoDwarf runs are shown at $z \sim 0$. The no-feedback runs in Fig. 3.4 (both with and without MHD) again show fundamental differences from the other runs (which incorporate explicit stellar feedback) owing to the runaway collapse of gas, as described in Hopkins et al. (2012a, 2014). The magnetic pressure is unable to stop this process, and therefore the morphologies in the Hydro and Hydro+MHD runs appear essentially identical.

When stellar feedback is included, there is also no significant systematic difference in morphology among runs with different additional physics. Stochastic SNe events can make some parts of some of the variants hotter at the times shown in the figure, but there is little systematic difference in a time-averaged sense. The CosmoMW FB+MHD+Micro run seems to have a slightly more extended disc at $z \sim 0$, suggesting a slightly higher accretion rate owing to turbulent metal diffusion and conduction enhancing cooling from the CGM. Among the different galaxies, Ell stands out as an exception for having little variation even between the runs with and without feedback. This is because cooling from the hot halo gas plays an important role in regulating Ell, as discussed above.

3.4.3 Gas phase structure

Fig. 3.6 and Fig. 3.7 compare the temperature-density phase plots of our isolated and cosmological simulations, respectively. The gas mass in each phase is further quantified in Fig. 3.9 and Fig. 3.10, where the density distributions in the following temperature intervals are plotted: cold neutral ($0 - 8000$ K), warm ionized ($8000 - 10^5$ K) and hot ($> 10^5$ K).

With stellar feedback, a multi-phase ISM is established, with star-forming cold

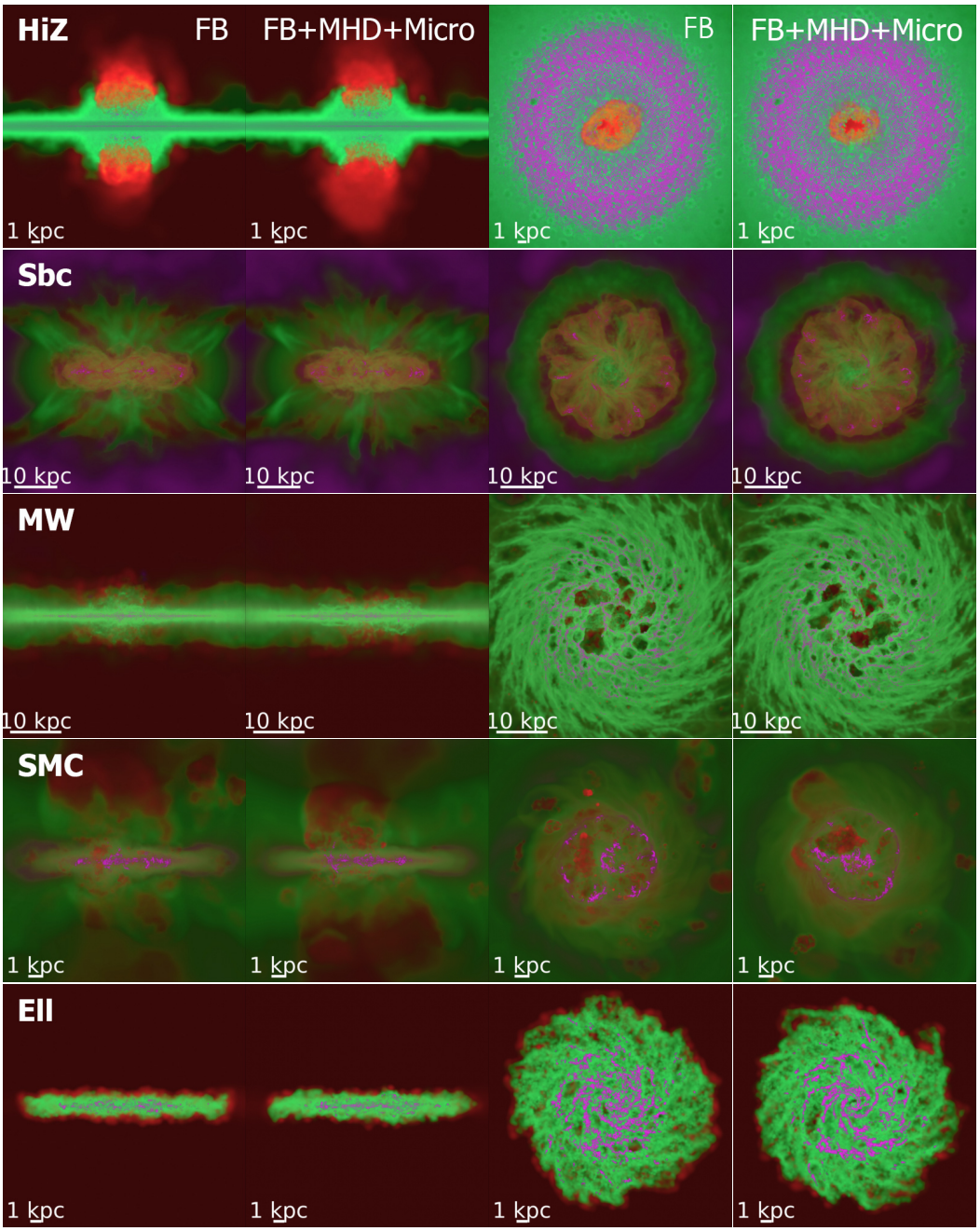

Figure 3.3: Images of the gas morphology of the isolated galaxies with feedback. The intensity encodes the projected density (log-weighted with ~ 4 dex stretch); different temperatures are shown in red ($> 10^5$ K), green ($8000 - 10^5$ K), and magenta (< 8000 K). We show edge-on and face-on projections for our FB and FB+MHD+Micro (FB+MHD is similar). The morphologies of the runs with the same stellar feedback but different additional physics show little difference.

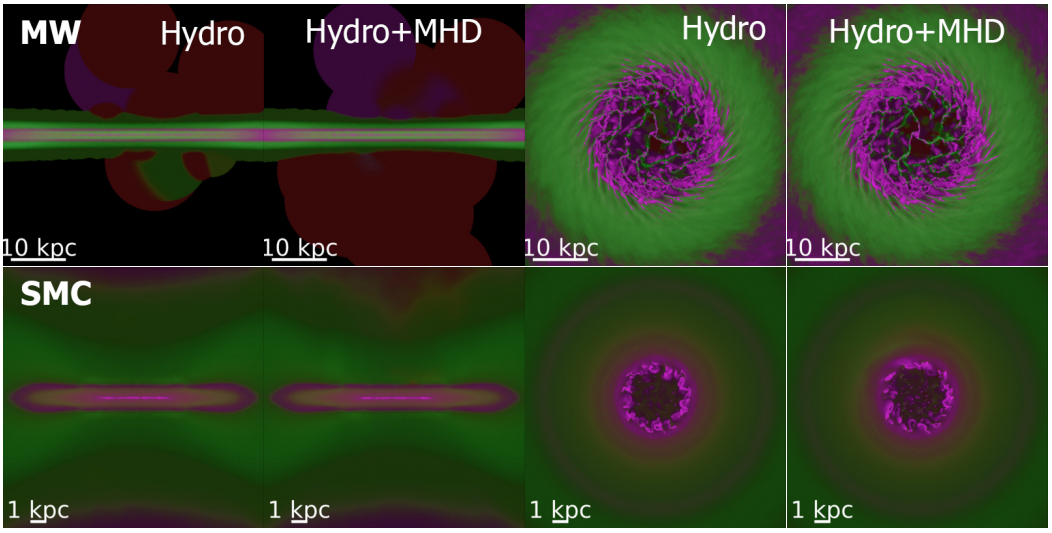

Figure 3.4: The effect of magnetic fields in the absence of feedback on the MW and SMC gas morphology. The Hydro+MHD runs exhibit morphologies that are almost identical to those of the Hydro runs. In both cases, it is clear that the inner gas discs have catastrophically fragmented and been converted into stars, thus indicating that the magnetic pressure alone is insufficient to prevent the gas from undergoing runaway collapse.

atomic/molecular gas, warm ionized gas, and volume-filling hot gas, which is extensively discussed in Hopkins et al. (2011, 2012a,b, 2013c). Turing off stellar feedback, on the other hand, leads to the same results as discussed in § 3.4.2.

Runs with the standard stellar feedback but different additional physics are very similar. Although magnetic fields, viscosity and conduction can in principle alter the cooling efficiency and fluid mixing, these additional physics have less than a $\sim$ 10% effect on the balance of ISM phases in our simulations. In fact, as demonstrated in the MW and SMC case of Fig. 3.9, the effect of magnetic field remains weak without stellar feedback.

The phase structure difference among the Ell runs is again small, as it is dominated by the hot halo phase, and the supply of gas to the other phases relies on and is therefore regulated by the cooling flow.

There is a small difference in our CosmoDwarf runs, where the cold gas mass is larger in our FB+MHD+Micro run by $\sim$ 0.2 dex ($\sim$ 50%) This is consistent with the slightly higher SFR in that run.

Fig. 3.8 presents the radial distributions of temperature, gas density and metallicity of

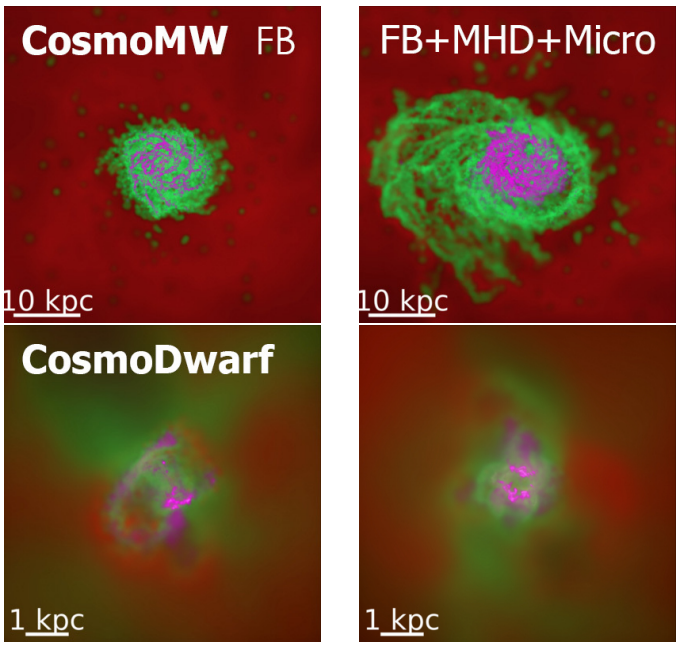

Figure 3.5: Images of the gas morphology of the cosmological simulations at $z = 0$, as Fig. 3.3. The slightly puffier disc in the CosmoMW FB+MHD+Micro run suggests a slightly higher accretion rate in the outer disc of this simulated galaxy. This owes to metal diffusion and conduction enhancing cooling from the "hot" circum-galactic medium (CGM).

the cosmological runs. The results are averaged over the redshift range $z \sim 0 - 0.07$ to suppress stochastic effects. For the CosmoMW runs, the profiles are broadly similar, with the density and metallicity (temperature) slightly higher (lower) in the runs with MHD. These are in consistent with the slightly more extended discs in CosmoMW FB+MHD and FB+MHD+Micro runs at low redshift as discussed in § 3.4.2. For the CosmoDwarf run, there are marked differences in the temperature profiles; this is likely because simulated dwarfs are highly stochastic, with strong starbursts and outflows even at $z \sim 0$ (Hayward & Hopkins, 2017, Muratov et al., 2015). The gas density profiles are similar. In the FB+MHD+Micro run, the metallicity is systematically higher within the central kpc, likely because of the effects of turbulent metal diffusion and the slightly higher stellar mass in this run; this subject will be analyzed in detail in a future work (Escala et al., in preparation).

3.4.4 Magnetic and turbulent energies

Fig. 3.11 compares the turbulent and magnetic energies in these simulations. The "turbulent" energy is difficult to define in practice, since we wish to exclude non-circular bulk motions and galactic winds. For our isolated galaxies, we focus on

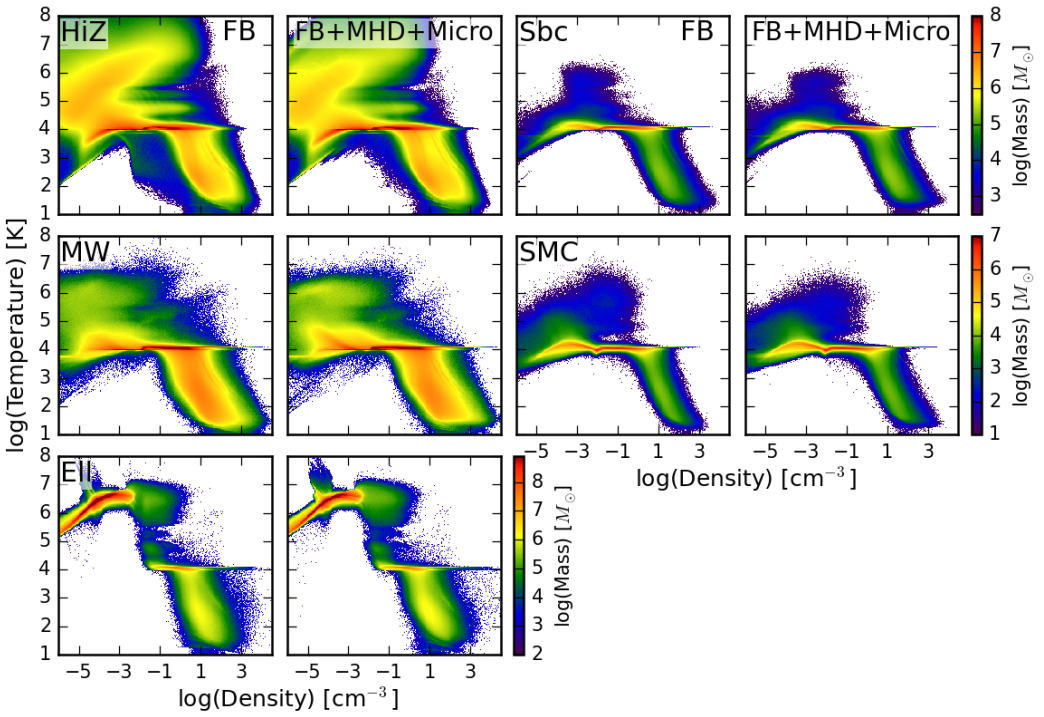

Figure 3.6: Temperature-density phase distribution of our isolated galaxy simulations. Each plot is averaged over the entire simulation duration. With feedback, cold neutral, warm ionized, and hot (feedback-driven) volume-filling phases are present. The additional MHD and diffusion microphysics have little effect on the phase structure in the presence of feedback. Note that the "spike" in the upper-left corners (hot halo phase) of the Ell runs correspond to an artificial shock arising from the IC being out of equilibrium.

the galactic disc by taking a cylinder with radius 10 kpc and height 2 kpc centered on the disc. The cylinder is divided into annuli with thicknesses set so that the number of particles in each layer is proportional to the order of layer counted from inside out. Within each annulus, the average rotational velocity is subtracted, and the particles outside with the highest 32% $|v_z - \bar{v}_z|^2$ are excluded (to approximate an $\pm 1\sigma$ interval) to eliminate outflows in the z direction. Each annulus is then further divided into cells with volumes set so each of them contains roughly 15 gas particles. The dimensions of the cells are chosen so that if all gas particles were distributed uniformly within the cylinder, each cell would be a cube ($\ell_r = \ell_z = \ell_\theta$) with an identical volume. Within each cell, the average velocity in $\hat{r}$, $\hat{z}$ and $\hat{\phi}$ directions are subtracted, and particles with the highest 20% $|\mathbf{v} - \bar{\mathbf{v}}|^2$ are excluded to reduce the contamination from the remaining high-velocity tail resulting from outflows in

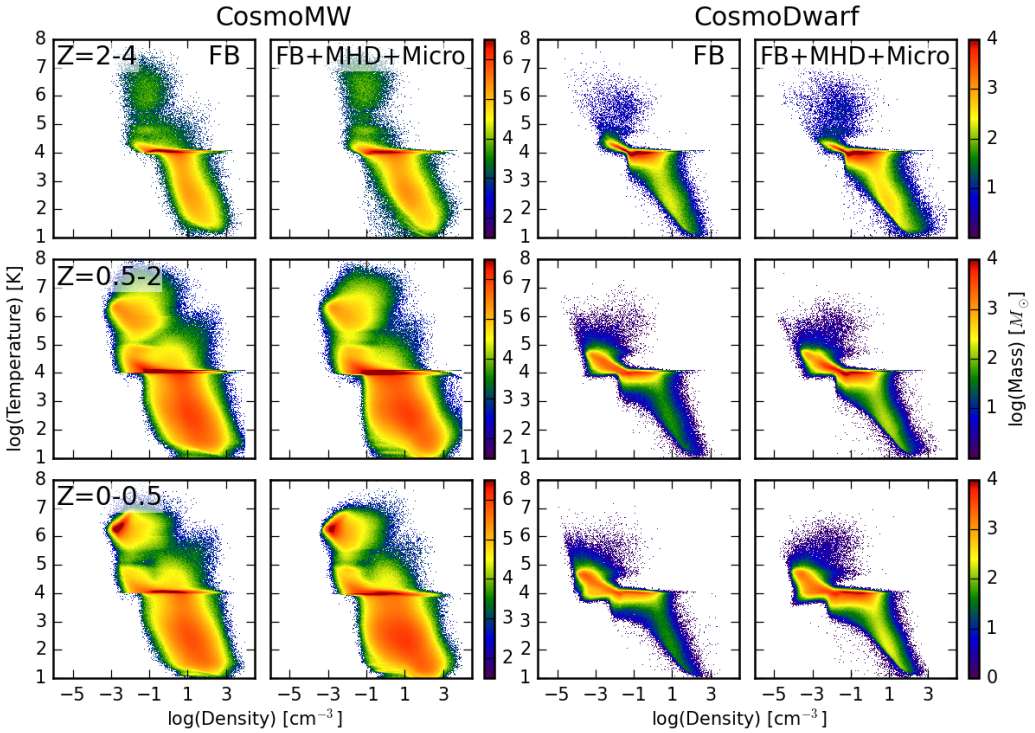

Figure 3.7: Temperature-density phase distribution of the CosmoMW and CosmoDwarf cosmological simulation. Each plot is averaged in three separate redshift intervals (labeled). Recall, only particles within $\lesssim 0.1 R_{\rm vir}$ of the central galaxy are plotted, to focus on ISM properties as in Fig. 3.6. The additional MHD and diffusion microphysics have relatively weaker effects in the presence of feedback, although some changes in the warm, inner CGM gas ($T \sim 10^5 - 10^7$K, $n > 10^{-2}$ cm^{-3}) are evident.

all directions. The kinetic energy that remains defines our estimated "turbulent" energy. [8]

For CosmoMW, which has no well-defined disc structure until $z \lesssim 0.6$, and and CosmoDwarf, which has no disc structure at all, we take all particles within 0.1 virial radius into account. The 0.1 $R_{\rm vir}$ sphere is divided into shells with thicknesses set such that the number of particles within each shell is proportional to the square of the layer number counted from inside out. The total angular momentum of each shell is calculated and used to define the z direction of the corresponding shell. Each shell is then further divided into several annuli at different θ, with heights set such that the

[8] For the HiZ runs, a cylinder with radius 35 kpc and height 10 kpc is used instead because its star-forming regions are spread over a significantly larger volume than in the other runs.

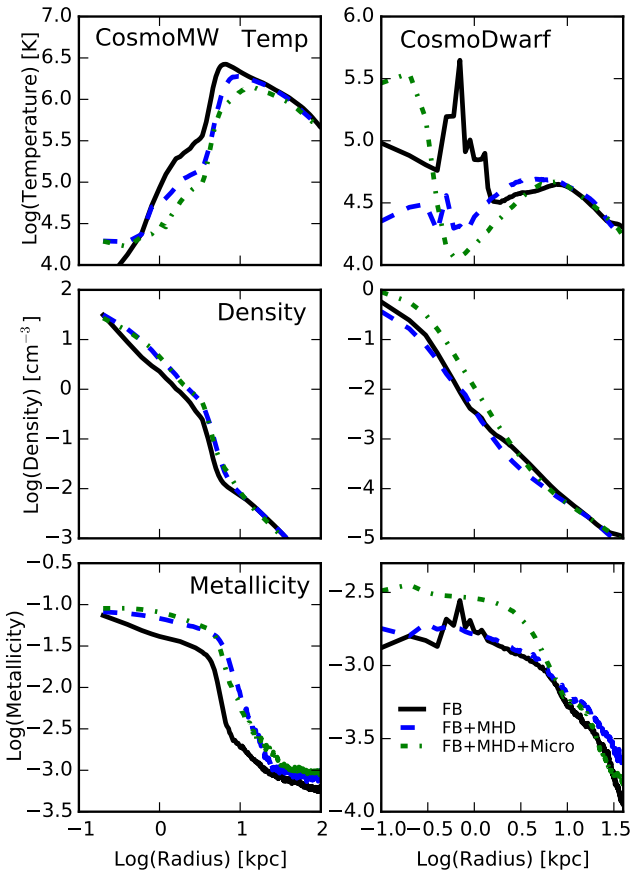

Figure 3.8: Radial distributions of temperature, gas density and metallicity for the cosmological runs averaged over the redshift range $z \sim 0 - 0.07$. The profiles of the CosmoMW runs are broadly similar, with the density and metallicity (temperature) slightly higher (lower) in the runs with MHD. The temperature profiles of the CosmoDwarf runs differ significantly, likely because this galaxy is still highly stochastic, with strong starbursts and outflows, even at $z \sim 0$. The gas density profiles are similar. The metallicity of the FB+MHD+Micro run is higher within the central kpc, likely because of turbulent metal diffusion and the slightly higher stellar mass in this run.

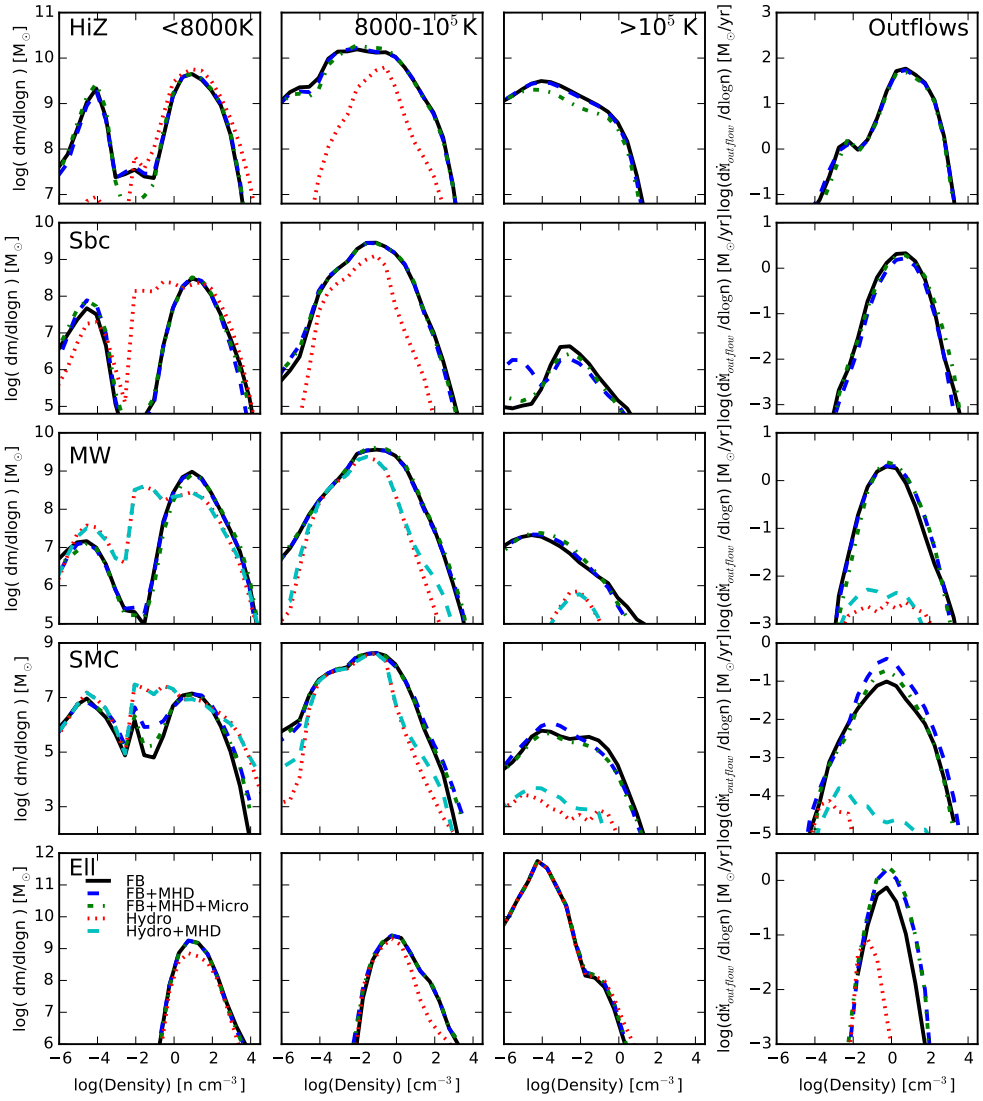

Figure 3.9: Density distribution of gas in different phases. Rows show our isolated galaxy simulations; columns show phases including cold neutral (*left*), warm ionized (*middle left*), hot (*middle right*), and outflow (*right*). To estimate the outflow, we simply take all gas that is within 0.5 kpc of the boundary of the disc (taken as a cylinder with radius 10 kpc and height 2 kpc) and moving with a radial velocity greater than some $v_{\rm min}$ chosen to be an appreciable fraction of the escape velocity in each galaxy ($v_{\rm min}$ = (200, 100, 100, 30, 100) km s^{-1} for HiZ, Sbc, MW, SMC, and Ell runs, respectively). The no-feedback runs produce far less hot gas and more cold gas, as expected (the difference is again less visible in the Ell run since the hot phase is dominated by the initial hot halo gas) with or without magnetic fields. Varying the additional microphysics has relatively weak effects. An increase in the outflow rate is visible in the run that includes magnetic fields but no feedback (Hydro+MHD), but the difference is orders of magnitude less than what is caused by feedback.

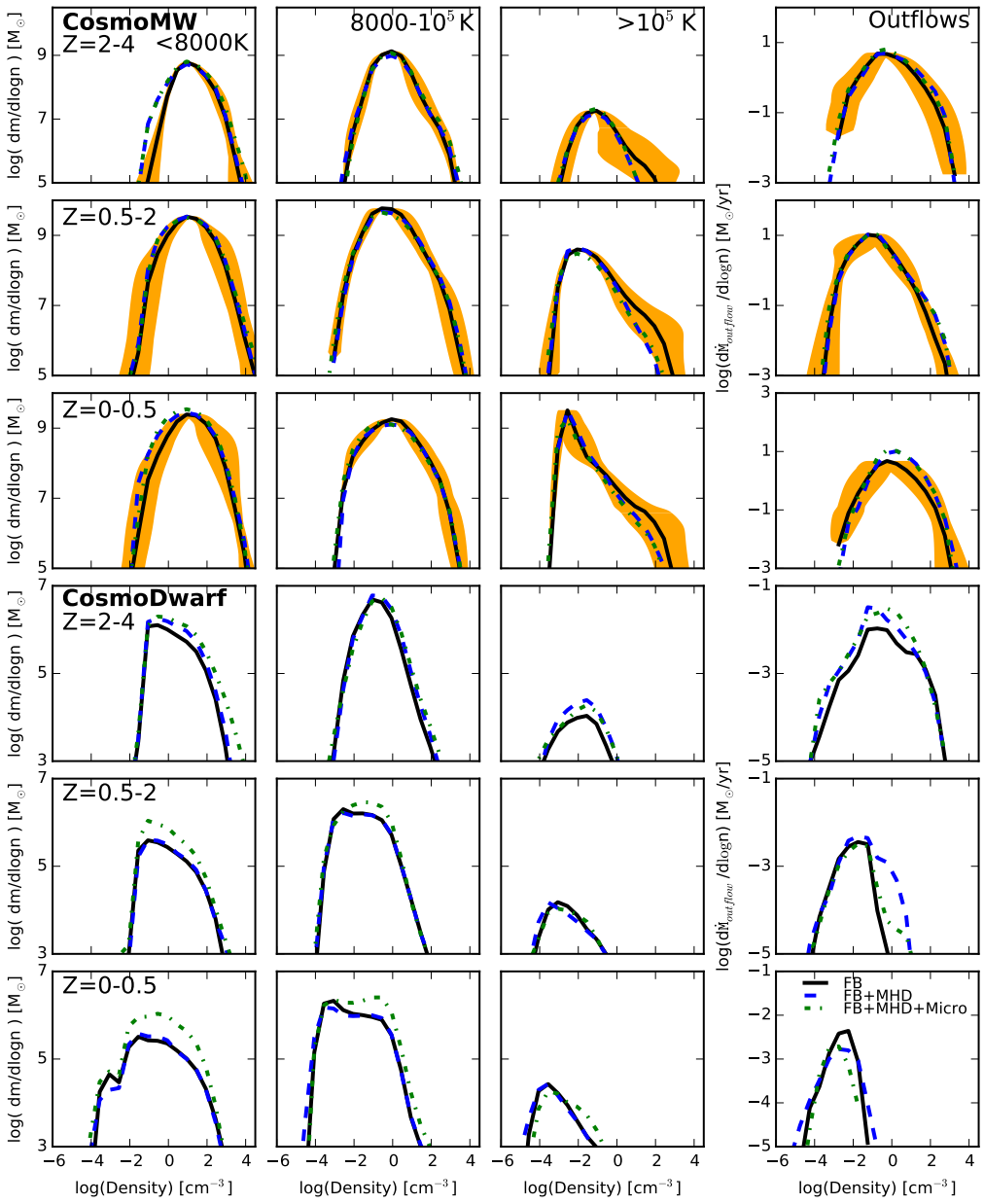

Figure 3.10: Gas density distribution in different phases, as in Fig. 3.9, but for our CosmoMW and CosmoDwarf runs, averaged in different redshift intervals. In the non-outflow panels, we consider only gas within $\lesssim 0.1 R_{\rm vir}$ of the central galaxy as Fig. 3.7. To quantify the outflows at $z = 0.5 - 4$ for CosmoMW and at all redshifts for CosmoDwarf, instead of using a disc, we select all gas located between 0.08 and 0.1 virial radii of the halo center that is moving with a radial velocity greater than $100\,{\rm km\,s^{-1}}$. The orange shaded regions in each panel of CosmoMW indicate the magnitude of stochastic effects (see text for details). At each redshift in both galaxies, the properties are similar in all runs with stellar feedback.

number of particles in each annulus is proportional to the corresponding $\sin\theta$ value. The average rotational velocity of each annulus is then subtracted. After this, each annulus is separated into cells containing roughly 15 particles. The dimensions of the cells are consistently set so that if all gas particles were distributed uniformly within the 0.1 $R_{\rm vir}$ sphere, each cell would be a cube with an identical volume. Within each cell, the average velocities in the $\hat{r}$, $\hat{\theta}$ and $\hat{\phi}$ directions are subtracted, and the particles with the highest 20% $|\mathbf{v} - \bar{\mathbf{v}}|^2$ are excluded. The turbulent kinetic energy is then calculated as the remaining kinetic energy.

To avoid biasing our comparison, we calculate the volume-integrated magnetic energy only for the gas particles kept in the turbulent energy calculation. The comparisons of the resulting turbulent energy and magnetic energy per unit mass are shown in Fig. 3.11. The turbulent kinetic energy grows almost immediately in these runs and quickly reaches a quasi-steady-state saturation level. With standard feedback, the turbulent energies per unit mass of Sbc, Mw and Ell all saturate to roughly $1\times10^{12}-3\times10^{12}$ erg/g, corresponding to an rms turbulent velocity of $7-13$ km/s. HiZ on the other hand has slightly higher turbulent energy, $3\times10^{12}-6\times10^{12}$ erg/g, corresponding to an rms turbulent velocity of $15-20$ km/s. Among all the runs, the SMC and CosmoDwarf runs have the lowest turbulent energy ($1\times10^{11}-3\times10^{11}$ erg/g) and rms turbulent velocity (2-4 km/s), owing to this galaxy having a significantly lower mass and thus requiring less turbulent energy to self-regulate (Faucher-Giguère et al., 2013, Hayward & Hopkins, 2017). The turbulent energy of CosmoMW at low redshift is calculated to be roughly the same as the values of HiZ, which is higher than the results from the isolated MW simulations. However, the turbulent energy at low redshift may be slightly over-predicted since all the particles within 0.1 virial radius are included for consistency even though a disc is already formed. If we include only the gas particles in the disc at low redshift, the turbulent energy drops to roughly $1\times10^{11}-3\times10^{11}$ erg/g, similar to the results from the isolated MW simulations. The values we get are in good agreement with observations (Levine et al., 2006, Merrifield, 1992) and the theoretical prediction that turbulent velocity for a marginally stable (turbulent $Q\sim1$) disc is $\sigma_T \sim f_{\rm gas} v_c$, where v_c is the circular velocity, and $f_{\rm gas}$ is the ratio of the thin-disc gas mass to total enclosed mass in the galaxy (Faucher-Giguère et al., 2013, Hayward & Hopkins, 2017).

In the HiZ, Sbc, and SMC simulations, the turbulent energy is considerably (a factor of $3-10$, corresponding to a factor of $2-3$ in the rms turbulent velocity) higher in

the presence of stellar feedback than when stellar feedback is absent, regardless of whether microphysical processes are included. In the Ell and MW simulations, the differences are much weaker - this is merely because these are our only two gas-poor galaxies ($f_{\rm gas} \lesssim 0.1$). In this case, pure gravitational effects (accretion, spiral arms, etc.) can easily drive sufficient turbulent velocities to reach $Q \sim 1$ where we see the velocities saturate.

As expected, we see that the magnetic energy grows from being negligible relative to the turbulent energy (because of the small initial seed fields used) until it saturates at $3 \times 10^{10} - 5 \times 10^{11}$ erg/g in the HiZ, Sbc, MW and Ell runs and $\sim 3 \times 10^{9} - 10^{10}$ erg/g in the SMC and CosmoDwarf runs; these values are roughly 10% of the turbulent energy similar to values measured in idealized simulations of the supersonic turbulent dynamics (Dubois & Teyssier, 2010, Kotarba et al., 2010, Wang & Abel, 2009). However, since (by construction) the initial field value is close to the equipartition value in the Ell run, the amplification is relatively mild in this case. Conduction, viscosity, and turbulent metal diffusion have little effect on the saturated field strengths. The corresponding volume-weighted rms magnetic fields are shown in Fig. 3.12, where the thick lines show the rms magnetic fields of all gas particles and the thin lines show the values of only the cold (< 8000K) gas[9]. Although the total rms magnetic fields vary among different galaxy types because we use the same sampling volume for galaxies with different size, the rms magnetic fields of cold particles saturates to roughly 10 μG in all cases except CosmoDwarf, in good agreement with both observations (Beck et al., 1996, Bernet et al., 2008, Jansson & Farrar, 2012a,b, Kronberg et al., 2008, Kulsrud & Zweibel, 2008, Widrow, 2002) and other simulations (Beck et al., 2012, Dubois & Teyssier, 2010, Kotarba et al., 2010, 2011, Pakmor & Springel, 2013, Wang & Abel, 2009). In CosmoDwarf, the saturation value of the magnetic field in the cold gas is smaller, 0.1-1μG, perhaps because essentially the entire ISM is blown out multiple times over the course of the simulation; consequently, the time for which a given parcel of cold gas remains in the disc and has its field amplified via differential rotation and the small-scale turbulent dynamo is shorter than in e.g., the MW case. In the MW Hydro+MHD case, although the magnetic energy per mass is higher than in rest of the runs, the volume-weighted rms magnetic field strength is lower because the dense gas fraction is lower than in e.g., HiZ.

The direct comparison of magnetic and turbulent energy clearly illustrates that the

[9]To suppress noise in the mean cold gas magnetic field, we exclude gas with density less than 10^{-6} cm^{-3} for CosmoMW and 10^{-2} cm^{-3} for HiZ.

turbulence is both super-Alfvénic and supersonic. In this limit, we expect magnetic fields to have a negligible effect on the turbulent kinetic energy and only a weak effect on the density fluctuations driven by turbulence (Federrath et al., 2008, 2011b, Kainulainen & Tan, 2013, Molina et al., 2012). In contrast, as shown explicitly in the MW and SMC Hydro+MHD runs, the turbulent energy and magnetic energy of the runs without feedback reach approximate equipartition because both the turbulent and magnetic energy are concentrated in dense clumps and driven by gravitational collapse. In this case, magnetic fields have a stronger back-reaction on the turbulent flow, and the turbulence is therefore no longer isotropic (Molina et al., 2012). This partially explains why magnetic fields have been observed to have strong effects in other studies where stellar feedback is absent or weak but not in ours. However, we also want to add the caveat that the balance of energy in runs without feedback could be affected by the ICs, as mentioned above.

3.4.5 Galactic outflows

In simulations that explicitly include multiple stellar feedback channels, such as those presented in this work, strong outflows are generated self-consistently. We quantify the outflow phase structure in Fig. 3.9- 3.10 and gas velocity distribution in Fig. 3.13. Detailed analyses of these properties using similar simulations with the same physics as our "FB" case are presented in Hopkins et al. (2012b, 2013d) (for isolated galaxies) and in Muratov et al. (2015) (for cosmological simulations); here, our focus is only on how the outflow properties depend on the included microphysics.

Fig. 3.13 and Fig. 3.14 plot the distribution of the radial velocities (defined relative to the baryonic center-of-mass of the galaxy) of gas particles within the same volume as stated in § 3.4.4[10] averaged over the entire simulation duration (or appropriate redshift ranges for the cosmological runs). To isolate "outflows" in Fig. 3.9 and Fig. 3.10, we simply take all gas particles within a thin layer at the boundary of the galaxy region defined above that have a radial velocity greater than some $v_{\rm min}$ chosen to be an appreciable fraction of the escape velocity of each galaxy ($v_{\rm min}$ = 200, 100, 100, 30, 100, 100, and 30 km s^{-1} for the HiZ, Sbc, MW, SMC, Ell, CosmoMW and CosmoDwarf runs, respectively).

Galactic outflows driven by magnetic field via Blandford-Payne-type acceleration (Blandford & Payne, 1982) are visible in the absence of feedback, as shown in the

[10]For CosmoMW, unlike in § 3.4.4, in which the same sampling volume is used for all redshifts, we switch to a cylinder with radius 10 kpc and height 2 kpc at low redshift because it better captures the wind properties at the time when a disc has already formed.

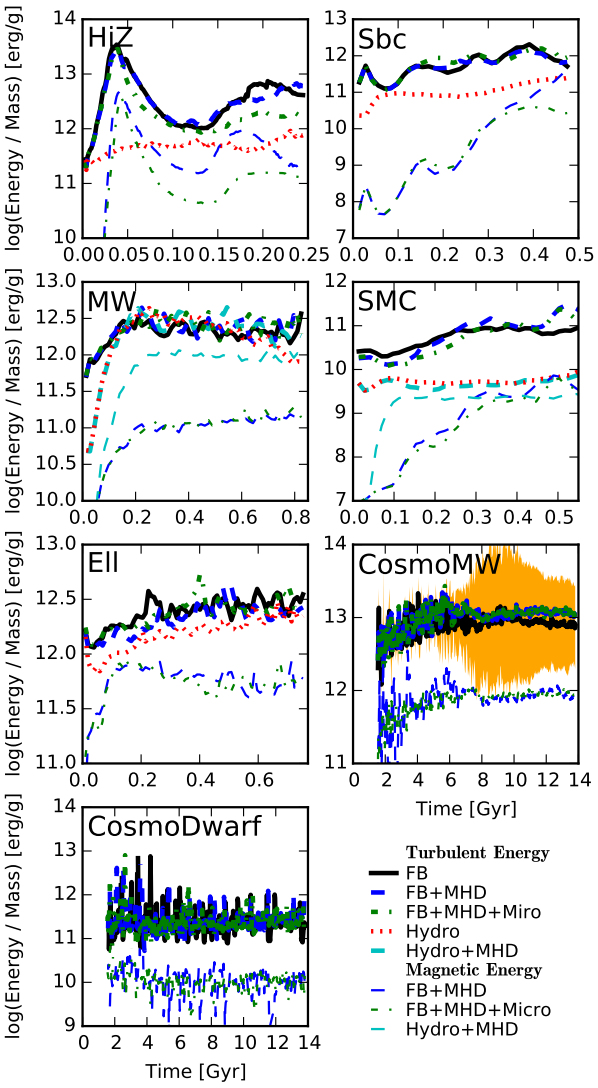

Figure 3.11: The total turbulent kinetic energy (*thick lines*; defined in § 3.4.4) and magnetic energy (*thin lines*) per unit mass of the non-outflowing disc gas in our simulations is shown as a function of time. In the CosmoMW case, the orange shaded region shows the magnitude of stochastic effects on the turbulent energy. In all cases with feedback, the turbulent energy saturates at a steady-state value over many dynamical times, corresponding to supersonic and super-Alfvénic velocity dispersions. The steady-state value is only very weakly altered by MHD and microphysical diffusion, consistent with expectations for super-Alfvénic turbulence on large (galactic) scales. The magnetic energy grows from the seed value to $\sim$ 10% of the turbulent kinetic energy, consistent with idealized simulations of the supersonic turbulent dynamo. Runs without feedback produce noticeably weaker turbulence (although *local* bulk motions from collapsing structures can be large, they are excluded by our estimator) and equipartition magnetic energy, thus suggesting that stellar feedback participates in driving turbulence. Note that MHD+hydro runs were done only for MW and SMC.

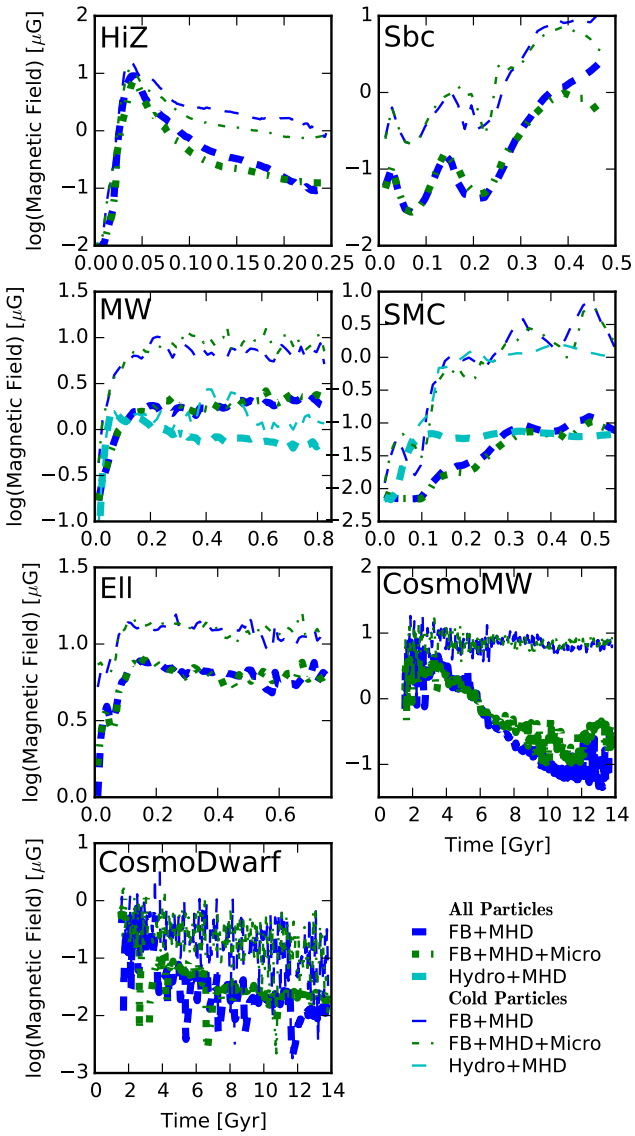

Figure 3.12: The rms magnetic field strength of all (*thick lines*) and the $T < 8000$ K component (*thin lines*) of the non-outflowing disc gas in our simulations is shown as a function of time. Although the average value over all particles varies among different galaxies, the rms magnetic field strength of cold gas saturates at several to 10 μG except CosmoDwarf, consistent with observations and other simulations. In the CosmoDwarf case, the saturation value of the cold-gas magnetic field strength is only 0.1-1 μG, owing to the frequent violent blowouts of the galaxy's ISM.

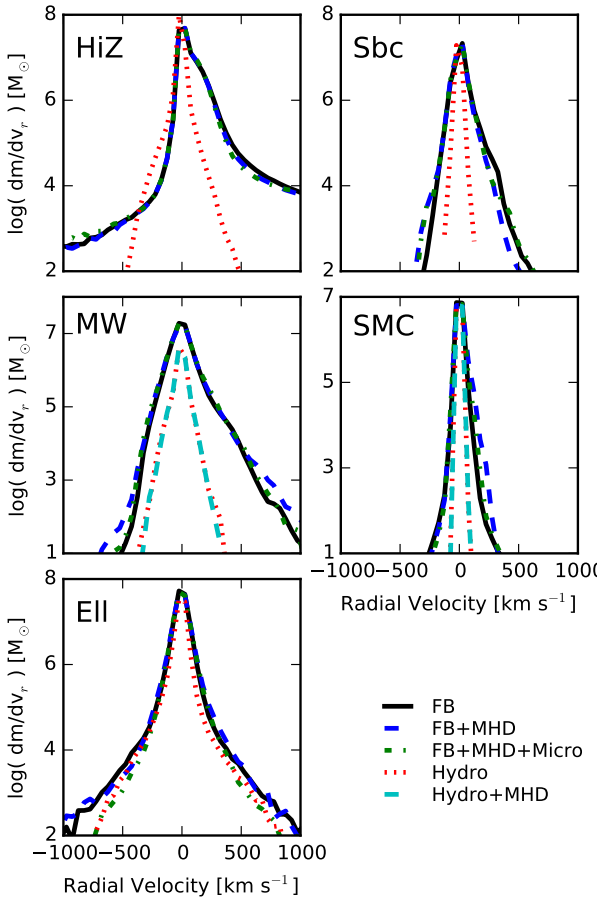

Figure 3.13: Distributions of the radial velocities of the gas particles in the isolated galaxy simulations. For each, we plot the time-averaged distribution of mass as a function of the radial velocity v_r with respect to the galaxy center of mass. Without feedback, there are little outflows, despite the slight boost from magnetic field in the MW and SMC Hydro+MHD runs. Once stellar feedback is included, outflows are self-consistently driven (i.e. there are substantially more particles with large radial velocities) and are insensitive to the microphysics investigated here.

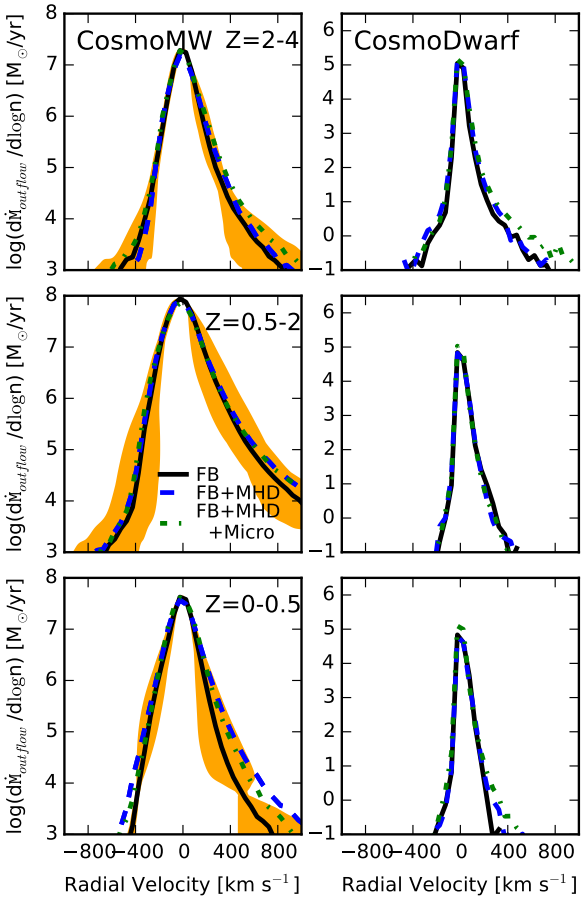

Figure 3.14: Distributions of the radial velocities of the gas particles in the cosmological simulations. For each, we plot the time-averaged distribution of mass as a function of the radial velocity v_r with respect to the galaxy center of mass. The orange shaded regions in the CosmoMW panels represent the magnitude of stochastic effects. The velocity distribution function is insensitive to the microphysics investigated here.

Hydro+MHD runs in both the MW and SMC cases. However, it turns out that the wind mass loading owing to Blandford-Payne acceleration is orders of magnitude smaller than what is caused by feedback and therefore not evident in FB+MHD runs. In sum, MHD and the additional physics that we study appear to have little effect on the velocity or density of the outflows compared with the effects of feedback.

3.5 Discussion: why are the effects of the additional microphysics weak?

We have seen systematically that for the large-scale properties of star formation, ISM structure, and galactic outflows, magnetic fields and microphysical diffusion processes make little difference once explicit stellar feedback is included. Here we

discuss why this is the case.

3.5.1 Sub-grid metal diffusion from unresolved turbulence

The microscopic (Brownian) diffusivity of metals is negligibly small for the systems we simulate. Instead, Smagorinski-type (mixing length theory) models assume that unresolved turbulent eddies can be treated as a scale-dependent diffusion process with diffusivity $\sim v_t(\lambda)\,\lambda$ (where $v_t(\lambda)$ is the rms turbulent velocity measured on length scale λ). The "sub-grid" part of the model applies an explicit extra diffusion term using $\lambda \rightarrow \Delta x$ (where Δx is the spatial resolution) to account for unresolved eddies, with the assumption that all larger eddies are resolved and that the $v_t(\Delta x)$ measured around each point is indeed turbulent motion. But for a supersonic cascade, or any system obeying the observed line width-size relation (which we have demonstrated is satisfied by our simulations with stellar feedback in Hopkins et al., 2012a), $v_t(\lambda)\,\lambda \sim (G\Sigma\pi)^{1/2}\lambda^{3/2}$, where Σ is the surface density. Thus, the power and diffusivity are concentrated in the largest-scale eddies. In the disc, these have scales of order the disc scale height; in the halo, the relevant scales are a large fraction of the halo core radius. In either case, the largest-scale eddies are well-resolved. In fact, taking the resolved line width-size relations found in our previous work (Hopkins et al., 2012a) and integrating (assuming an infinite inertial range), we expect that most of the global diffusivity is resolved. Thus, the only effect of the sub-grid diffusivity is to smooth particle-to-particle variations in metallicity after bulk mixing of the metals (by particle motion) is resolved. In principle, this can alter the cooling rates, but the effect is weak because the resolution is high enough that we account for individual SNe explosions (so that the Poisson noise in the number of enrichment events that each particle sees is small; Ma et al. 2015a, van de Voort et al. 2015). Although subtle effects, e.g., the predicted dispersion in abundances within star clusters, may not be well captured by our simulations, these have little effect on the global properties that we focus on herein.

To the extent that much larger effects are found using similar mixing models (Shen et al., 2010, Wiersma et al., 2009b), one of three effects is likely to be occurring in those works. (1) The turbulent driving scales are not resolved (so there is little or no resolved mixing). This is certainly the case in simulations with force softening $\gtrsim 100\,$pc. However, in this case, it is not correct to apply the Smagorinski model in its typical form, since (as discussed above) it explicitly assumes that all shear motion in the simulation around a particle is resolved turbulent motion (from which it extrapolates the inertial range). (2) Additional motions (e.g., orbital motions

in a disc or outflow motions in winds) are accidentally triggering the numerical "turbulent velocity" estimator. This effect is also likely to be more severe in lower-resolution simulations but is a serious concern when sub-grid diffusion models are applied to galaxy simulations at any resolution. (3) The coefficient of the diffusivity is too large (or the numerical gradient estimator is inaccurate), so the diffusivity assigned to unresolved eddies can be larger than that of larger, resolved eddies. This can easily occur if $C \gtrsim 1$ is used, or if the gradient estimator is noisy (which is commonly the case in SPH).

We note that the mean metallicity and the vertical metallicity gradient are not affected by sub-grid turbulent metal diffusion (Ma et al., 2016a). This and the fact that the initial metallicity of some ICs is already high also help suppress the effect of turbulent metal diffusion on the properties investigated. However, when sub-grid turbulent metal diffusion is included, the metallicity PDF become much narrower because most of the gas particles eventually reach the mean metallicity value in some local annulus of the disc and therefore so do the star particles spawned from gas particles. A detailed study of the stellar metallicity distribution with and without sub-grid turbulent metal diffusion and comparisons with observational constraints will be included in Escala et al. (2016, in preparation).

In this study, we only apply the sub-grid model for unresolved turbulence to metal diffusion. In principle, unresolved turbulence can also cause diffusion of the other quantities, such as energy or momentum. However, unlike metallicity (which is not advected across particles in the MFM approach or in e.g., SPH), these quantities are readily exchanged between particles through the hydrodynamic equations and therefore have the inherent numerical diffusion from our Godunov-type solver that scales (crudely) as $\sim c_s \Delta x$ (where Δx is the spatial resolution). As a result, the corresponding small-scale diffusion is not as significantly underestimated as metal diffusion when sub-grid turbulent diffusion is omitted. Moreover, in the sub-grid model here, the magnitude of unresolved turbulence is estimated through the sheer tensor, whereas the SGS model (Schmidt et al., 2006a,b) may possibly be a more rigorous approach, especially when the motion is highly shearing Colbrook et al. (2016).

3.5.2 Conduction & viscosity

We can also understand why physical conduction and viscosity have weak effects in the simulations presented in this work. Like all numerical methods, our Godunov-

type solver has inherent numerical diffusion, with a numerical diffusivity $\sim c_s\,\Delta x$. Comparing this to Spitzer-Braginskii conduction (diffusivity $\sim (\kappa\, m_p)/(k_B\,\rho)$), and using the fact that our code is Lagrangian (so $\rho \sim m_i/\Delta x^3$, where m_i is the particle mass), we estimate that physical conductivity dominates our numerical when $T \gtrsim 0.3\times10^7\,\mathrm{K}\,(m_i/10^4\,M_\odot)^{1/6}\,(n/0.01\,\mathrm{cm}^{-3})^{1/3}$. Moreover, as mentioned in § 3.5.1, large-scale turbulent eddies have diffusivity $\sim v_t(\lambda)\,\lambda \sim (G\Sigma\pi)^{1/2}\lambda^{3/2}$. We estimate the micro-physical conductivity to surpass this turbulent value at an even higher temperature $T \gtrsim 3\times10^7\mathrm{K}(\Sigma/(100M_\odot pc^{-2}))^{3/5}(\lambda/100pc)^{1/5}$. Thus, only in the hot, tenuous gas phase can physical conductivity be significant relative to the turbulent (and numerical) diffusivity. The field length, i.e. the characteristic scale below which conduction is faster than cooling, under these conditions is $\sim [(\kappa\, m_p\, t_{\rm cool})/(k_B\,\rho)]^{1/2} \sim 10\mathrm{kpc}\,(T/10^7\,\mathrm{K})^{7/4}\,(n/0.01\,\mathrm{cm}^{-3})^{-1}$. In hot gas, this scale is resolved. However, for typical ISM temperatures ($\sim 10^4K$), which is the relevant regime for clump formation and star formation, the field length is sub-pc. In our simulations, this is typically much smaller than the resolved scales of structures (including coherent filaments and dense gas blobs). This indicates that while conduction and viscosity may have interesting effects on small scales, explicitly including them in galaxy simulations at present is not expected to have a large impact. This does not, of course, guarantee that conduction and viscosity cannot have effects that feed back to large scales in fully resolved simulations. More work will be needed to answer this latter question.

The only exception, where conduction and viscosity generate a small, but visible systematic effect is the CosmoDwarf case, in which the FB+MHD+Micro run has ~ 0.2 dex higher stellar mass and cold gas mass and more stable SFR and cold clumps. These are most likely caused by conduction. In a dwarf galaxy of this mass, an overlap of SNe can easily wipe out all the cold gas in the galaxy, which happens several times throughout the simulations. However, conduction could dissipate part of the SNe energy, making it more difficult for them to completely destroy the cold clumps in the ISM. From the star formation histories, we infer that a typical event capable of "wiping out" all the cold gas requires an overlap of ~ 100 SNe. To show that conduction can actually be effective in this limit, we can compare the time scale of energy dissipation by conduction, $\tau_c \equiv E/\dot{E}_{\rm conduction}$, to the free expansion time of SNe in the energy conserving phase, $\tau_{\rm exp} \equiv R/v$, where $E = N_{\rm SNe}10^{51}$ erg is the energy sum of the $N_{\rm SNe}$ overlapping SNe, R is the radius of the expanding hot bubble and v is the speed of expansion. $\tau_c/\tau_{\rm exp}$ turns out to be $\sim 6\times10^{-6}(R/10pc)^7(N_{\rm SNe}/100)^{-2}(n/cm^{-3})^3 < 1$, which means conduction cannot

be neglected, (see also Keller et al. (2014, 2015)). As the expansion continues, the radius grows, $\tau_c/\tau_{\rm exp}$ increases and the importance of conduction gradually decays. However, before conduction ceases to be important ($\tau_c/\tau_{\rm exp} = 1$), the hot bubble can entrain a total mass of $\sim 10^4 (N_{\rm SNe}/100)^{6/7} (n/cm^{-3})^{-2/7} M_\odot$, which is well resolved in our CosmoDwarf simulations. The effects of conduction are therefore expected to be visible in our CosmoDwarf simulations, where the resolution is high enough and the size small enough for the cold gas to be mixed in overlapping SNe remnants.

3.5.3 Magnetic fields

We can also understand in simple terms why magnetic fields have little effect on the galaxy SFRs and, consequently, their position in the Schmidt-Kennicutt diagram and other SF scaling laws. In a series of previous studies (Faucher-Giguère et al., 2013, Hopkins et al., 2011, 2012a, 2013a,b,c, 2014), we have repeatedly shown that galaxy SFRs are set by a balance between stellar feedback injecting momentum ("resisting" collapse and the"stirring" of supersonic turbulence) and dissipation of that motion via gravitational collapse. Other groups have reached consistent conclusions in calculations that include self-gravity, resolve fragmentation and turbulence, and explicitly model stellar feedback (Agertz et al., 2013, Kim et al., 2013, 2014, Shetty & Ostriker, 2008). In such simulations, galactic SFRs are independent of the sub-grid model for how dense gas turns into stars (Hopkins et al., 2011, 2013c), the shape and orders-of-magnitude variations in the cooling function and modeled dense gas chemistry (Hopkins et al., 2012a), and the temperature and detailed kinematics of the star-forming gas (Hopkins et al., 2013b). Even equipartition magnetic fields would change the equilibrium SFR in this scenario by only tens of percent, and the effect should be even weaker in the super-Alfvénic case when feedback in present.

Comparing our results with those of galaxy simulations with weaker/non-explicit stellar feedback presented in the previous literature (Beck et al., 2012, Pakmor & Springel, 2013, Wang & Abel, 2009), the SFR difference caused by inclusion of magnetic fields is small even in our runs without feedback. In Beck et al. (2012), Pakmor & Springel (2013), the Springel and Hernquist feedback model (Springel & Hernquist, 2003) is adopted, resulting in a smooth, pressure-supported ISM with a stiff "effective equation of state". In this case, the extra pressure support from magnetic fields could be more effective. In Wang & Abel (2009), instead of explicit star formation, the star formation rate is calculated from the amount of dense gas assuming a specific star formation efficiency. In this case, gas could possibly stay in high-density clumps for a longer time, thus allowing more time for magnetic

pressure to build up and become effective.

Similar arguments apply to galactic outflows: the mass outflow rate is set by the momentum injected by feedback, which is divided into stirring turbulence in the disc and ejecting low-density material (Hayward & Hopkins, 2017, Martizzi et al., 2016a, Murray et al., 2011, Thompson & Krumholz, 2016), and ultimately limited by the depth of the potential (Muratov et al., 2015). We thus do not expect the mass outflow rate to vary by large factors when magnetic fields are present.

Perhaps the most surprising result of this study is how weak the effects of magnetic fields are on the ISM phase structure. Using the same code in idealized tests, we have shown that sufficiently strong magnetic fields do produce qualitatively different behavior in fluid mixing instabilities, cloud entrainment or "crushing" by ambient winds, and anisotropic supersonic turbulence (Hopkins & Raives, 2016), in agreement with a vast literature. Moreover, the rms fields we predict in both ambient gas and dense clouds are in reasonable agreement with those observed, as discussed in § 3.4.4. However, it appears that two main effects lead to relatively weak effects of magnetic fields on the large-scale phase structures we consider. (1) The turbulence in most of the disc is super-Alfvénic, at least on large scales that contain most of the power (of order the disc scale height, which also corresponds to the size of the largest GMCs, which contain most of the dense gas mass and star formation). Thus, the turbulent velocity dispersions, isotropy, and density fluctuations generated are not strongly altered (Federrath et al., 2008, 2011b, Kainulainen & Tan, 2013, Molina et al., 2012). (2) GMCs are not steady-state, pressure-confined, equilibrium objects in the simulations. We have previously shown (Hopkins et al., 2012a) that in similar simulations, GMCs form rapidly (in a single dynamical time) from gravitational instability (and are self-gravitating) and live just a few dynamical times, forming stars via turbulent fragmentation until feedback disrupts the cloud.

McCourt et al. (2015) recently showed that magnetized gas clouds can survive much longer than unmagnetized ones when accelerated by supersonic hot wind. Moreover, Armillotta et al. (2017), Brüggen & Scannapieco (2016) showed that thermal conduction can also help cold clouds survive by suppressing the Kelvin-Helmholtz instability at the interface. Although such effects are confirmed to exist in high-resolution wind-tunnel-type simulations run with the code used here (Hopkins et al. in preparation), the simulations presented in the current study suggest that magnetic fields play a less important role in the formation and survival of dense cold clouds in the ISM of galaxies, such as molecular clouds. One important

difference is that massive molecular clouds are typically self-gravitating rather than in pressure equilibrium with the surrounding ISM. Moreover, as explained above, in our simulations, massive molecular clouds are disrupted by stellar feedback rather than by hydrodynamic instabilities. Consequently, the aforementioned idealized tests may not represent the physical conditions relevant for simulated (or real) GMCs. As for the cold clouds in outflows, although our simulations also suggest weak effects from magnetic fields, we caution that only two galaxies in our study contain "hot haloes" (Ell and CosmoMW). In our other simulations, such cloud "shredding" or mixing effect will be much weaker since there is little or no hot gas halo for the cold outflow gas to mix into. In the Ell and CosmoMW cases where there are hot haloes, the achievable resolutions are inevitably lower, meaning the phase structure in the outflows may not fully resolved. Besides, most of the outflow mass which reaches large radii ($\gtrsim R_{vir}$) is hot gas in the first place - cold outflows tend to be recycled in small-scale fountains (see Muratov et al. 2015).

Despite the weak role that magnetic fields play, we see a hint of a small (< 0.1 dex) increase of stellar mass in those runs with magnetic fields. Interestingly, magnetic fields may, if anything, enhance star formation on large scales. The fact that the difference is more obvious in the smallest galaxy suggests that this may result from the magnetic field helping stabilizing colds clumps in the ISM, especially in small galaxies with a less stable cold phase.

3.6 Conclusions

We use simulations with parsec-scale resolution, explicit treatments of stellar feedback identical to those used in the FIRE project, magnetic fields, anisotropic Spitzer-Braginskii conduction and viscosity, and sub-grid turbulent metal diffusion to study how these affect galaxy-scale star formation, the phase structure of the ISM, and the generation of galactic outflows. We consider both isolated (non-cosmological) simulations of a range of galaxy types and fully cosmological zoom-in simulations of a Milky Way-mass halo and a dwarf halo.

In all cases, we find the following:

- Stellar feedback plays the dominant role in regulating the SFR. We find that magnetic fields and additional microphysical diffusion processes change the SFR (and therefore the KS law) by small amount comparing to the effect from stellar feedback in the investigated ma. This is consistent with the models advocated in the aforementioned papers (see the references in § 3.5.3), in

which the SFR and star formation scaling relations are set by self-regulation via feedback, which drives supersonic turbulence and balances the disc against gravity.

- The ISM phase structure and galactic winds is also primarily established by stellar feedback. Stellar feedback also serves as an extra source of turbulent energy, boosting the rms turbulent velocity by a factor of 2-3. Perhaps surprisingly, however, neither MHD nor the additional diffusion microphysics appear to produce larger than $\sim$ 10%-level systematic effects on these quantities. In fact, in some earlier experiments where we artificially increased the viscosity coefficient η by a factor of 100, there were still weak systematic effects. It appears that because the turbulence is super-Alfvénic on the scales most important for fragmentation, ISM phase structure and outflow generation (of order the disc scale height), these effects are subdominant. A more detailed discussion of why such small effects are seen is provided in § 3.5.

- The magnetic field energies saturate at $\sim$ 10% of the turbulent kinetic energies on of order the galactic scale height (Fig. 3.11). The ratio is smaller still if we include the kinetic energy of small-scale galactic fountains in the "turbulence" budget. This is consistent with both observations (Beck et al., 1996, Bernet et al., 2008, Jansson & Farrar, 2012a,b, Kronberg et al., 2008, Kulsrud & Zweibel, 2008, Widrow, 2002) and other simulations (Beck et al., 2012, Dubois & Teyssier, 2010, Kotarba et al., 2010, 2011, Pakmor & Springel, 2013, Wang & Abel, 2009). This result partially explains why the magnetic field's effects are subdominant on the large scales of order the disc scale height (the scales containing most of the turbulent energy).

- A systemic increase of stellar mass and cold gas is observed in CosmoDwarf run with all fluid microphysics included. This may result from conduction dissipating part of the SNe energy making it more difficult to wipe out cold clumps. Our cosmoMW run shows a similar enhancement in late-time cooling from the CGM with all microphysics present. A more detailed discussion of this is provided in § 3.5.

It appears that, at least on galactic scales, in the presence of explicit models for multi-mechanism stellar feedback as well as self-gravity, magnetic fields and additional diffusion microphysics (such as conduction, viscosity, and sub-grid turbulent metal diffusion) are subdominant in the star formation and galaxy formation process at

currently achievable resolutions. This general result appears to contradict some earlier claims in the literature. However, to our knowledge, these prior studies have not focused on the combination of large galactic scales (yet with high enough resolution to resolve vertical disc scale heights and the phase structure in discs) and fully explicit models for stellar feedback. For example, it is relatively "easy" for magnetic fields to have a large fractional effect in simulations with either no or weak stellar feedback or stellar feedback modeled only in a "sub-grid" fashion (so it e.g., does not locally alter the gas dynamics but only ejects gas in outflows or adds an effective pressure term). However, the claimed effects in these cases are typically order-unity (Beck et al., 2012, Pakmor & Springel, 2013, Piontek & Ostriker, 2005, 2007, Wang & Abel, 2009) and thus still orders of magnitude less than the factor $\sim 100-1000$ changes in the properties we study here that occur when the full model for stellar feedback is introduced.

Altogether, our results support the emerging picture wherein galaxy-scale ($\gtrsim 10-100\,$pc) star formation, ISM structure, and outflows are determined primarily by a competition among supersonic (and super-Alfvénic) turbulence, stellar feedback, and self-gravity. The microphysics we study here may certainly be important on smaller scales (e.g., for regulating the structure of turbulent cores as they collapse to form stars) or in the more diffuse CGM and IGM (e.g., the outskirts of galaxy clusters). However, they do not, to leading order, significantly alter the dynamics on the scales we study here. We also caution that certain unresolved processes (e.g., conduction altering mixing and cooling in single SNe blastwaves or cool cloud "shredding" in the circum-galactic medium) may have large non-linear effects on the efficiency of feedback or cooling, and these cannot be captured in our simulations. We see tentative evidence of this in our fully cosmological MW-mass simulation, which shows enhanced late-time cooling and a larger gas disc with conduction, viscosity and sub-grid metal diffusion active.

Although the magnetic field has little effect on the properties analyzed in our current study, it might for instance provide important pressure support in the violent tidal compression that occurs in galaxy mergers, which could possibly affect the properties of the star clusters formed in merger-induced starbursts. Besides stellar feedback and fluid microphysics, AGN feedback may be an important determinant of galaxies' physical properties, especially for massive galaxies. Moreover, cosmic rays may significantly affect galaxy evolution, and properly treating cosmic ray transport requires an accurate determination of the magnetic field. Detailed investigations

of these processes and their interaction with fluid microphysics in the context of simulations with explicit stellar feedback will be presented in future work.

Chapter 4

STELLAR FEEDBACK STRONGLY ALTERS THE AMPLIFICATION AND MORPHOLOGY OF GALACTIC MAGNETIC FIELDS

K.-Y. Su, C. C. Hayward, P. F. Hopkins, E. Quataert, C.-A. Faucher-Giguère, and D. Kereš. Stellar feedback strongly alters the amplification and morphology of galactic magnetic fields. *MNRAS*, 473:L111–L115, January 2018. doi: 10.1093/mnrasl/slx172.

Using high-resolution magnetohydrodynamic simulations of idealized, non-cosmological galaxies, we investigate how cooling, star formation, and stellar feedback affect galactic magnetic fields. We find that the amplification histories, saturation values, and morphologies of the magnetic fields vary considerably depending on the baryonic physics employed, primarily because of differences in the gas density distribution. In particular, adiabatic runs and runs with a sub-grid (effective equation of state) stellar feedback model yield lower saturation values and morphologies that exhibit greater large-scale order compared with runs that adopt explicit stellar feedback and runs with cooling and star formation but no feedback. The discrepancies mostly lie in gas denser than the galactic average, which requires cooling and explicit fragmentation to capture. Independent of the baryonic physics included, the magnetic field strength scales with gas density as $B \propto n^{2/3}$, suggesting isotropic flux freezing or equipartition between the magnetic and gravitational energies during the field amplification. We conclude that accurate treatments of cooling, star formation, and stellar feedback are crucial for obtaining the correct magnetic field strength and morphology in dense gas, which, in turn, is essential for properly modeling other physical processes that depend on the magnetic field, such as cosmic ray feedback.

4.1 Introduction

Magnetic fields may play a role in galaxy evolution because the magnetic pressure can reach approximate equipartition with the turbulent or/and thermal pressure (Beck, 2009, Beck et al., 1996). Idealized simulations of isolated galaxies with magnetic fields suggest that magnetic fields can provide extra support in dense clouds and suppress star formation (Beck et al., 2012, Pakmor & Springel, 2013, Wang &

Abel, 2009), and magnetic acceleration has been suggested as a mechanism to drive outflows (Blandford & Payne, 1982). Moreover, magnetic fields can also suppress fluid mixing instabilities, including the Rayleigh-Taylor and Kelvin-Helmholtz instabilities (Jun et al., 1995), and therefore also largely suppress the 'cloud shredding' process (McCourt et al., 2015).

In Su et al. (2017), we performed high-resolution magnetohydrodynamic (MHD) simulations incorporating multi-channel explicit stellar feedback, including both cosmological 'zooms' and idealized isolated galaxies to investigate the effect of magnetic fields and other 'microphysics' on galaxy formation. We found that the presence of a magnetic field had at most $\sim$ 10-per cent-level effects on global galaxy properties such as the star formation history (SFH) because the turbulence in the simulated galaxies' ISM is super-Alfvénic; thus, the magnetic field is dynamically unimportant compared with turbulence.

However, our previous results do *not* necessarily imply that magnetic fields can be neglected in galaxy formation simulations. In particular, the simulations presented in Su et al. (2017) did not include cosmic rays, which may be an important driver of galactic outflows (Booth et al., 2013, Hanasz et al., 2013, Salem & Bryan, 2014, Uhlig et al., 2012). Because cosmic rays are coupled to magnetic fields, to treat cosmic ray transport correctly, one must first accurately determine the magnetic field (e.g., Pakmor et al., 2016), which requires correctly capturing various potentially important amplification mechanisms, including flux freezing compression and the turbulent and $\alpha-\Omega$ dynamos (e.g., Beck et al., 1996). Moreover, accurate models of galactic magnetic fields are crucial to inform the interpretation of many observables.

In this Letter, we demonstrate that differences in the treatments of cooling, star formation, and stellar feedback can yield very different magnetic field saturation values and morphologies. We note that although a detailed analysis of magnetic amplification mechanism is beyond the scope of this paper, we do argue that the magnetic amplification history and saturation values in our simulations are reasonable. The remainder of this Letter is organized as follows: in § 4.2, we describe the initial conditions and investigated baryonic physics. In § 4.3, we present the results. We summarize in § 4.4.

4.2 Methodology

Our simulations use GIZMO (Hopkins, 2015)[1], a mesh-free, Lagrangian finite-volume Godunov-type code designed to combine the advantages of Eulerian and Lagrangian methods, in its 'meshless finite mass mode' (MFM). GIZMO is built on the gravity solver and domain decomposition algorithms of GADGET-3 (Springel, 2005). Magnetic fields are treated in the ideal-MHD limit. To eliminate spurious numerical divergence errors (i.e. non-zero $\nabla \cdot B$), both the Dedner et al. (2002) and Powell et al. (1999) divergence cleaning methods are applied. The details of the methods and tests are presented in Hopkins & Raives (2016) and Hopkins (2016).

In this paper, two isolated (non-cosmological) galaxy models, MW and SMC, that have been used previously in various other works (Hayward et al., 2014, Hopkins et al., 2011, 2012a, Su et al., 2017) are studied. MW is a Milky Way-like galaxy with $(M_{\rm halo}, M_{\rm bulge}, M_{\rm disc}, M_{\rm gas}) = (210, 2.1, 6.8, 1.3) \times 10^{10} {\rm M}_{\odot}$, whereas SMC is Small Magellanic Cloud-mass dwarf with $(M_{\rm halo}, M_{\rm bulge}, M_{\rm disc}, M_{\rm gas}) = (290, 0.14, 1.9, 11) \times 10^{8}$ M$_{\odot}$. The gas mass resolution is $3500 M_{\odot}$ for MW and $360 M_{\odot}$ for SMC, which correspond to adaptive spatial resolutions of $\sim 50\,(n/{\rm cm}^{-3})^{-1/3}$ and $\sim 20\,(n/{\rm cm}^{-3})^{-1/3}$ pc for the MW and SMC models, respectively. At these resolutions, the fastest-growing mode of amplification via the magnetorotational instability (MRI; ~ 100 pc) is well resolved once $B \sim \mu$G (it is not well-resolved initially). Detailed descriptions of the galaxy models can be found in Su et al. (2017). An initially uniform magnetic field with an amplitude of 0.01 μG pointing in the positive-z direction (i.e. perpendicular to the initial disc galaxies) is assumed. We have confirmed that our results are insensitive to the initial magnetic field amplitude and orientation as long as the amplitude is sufficiently small that the magnetic pressure is initially dynamically unimportant.

We simulate both galaxy models using the four different baryonic physics treatments summarized in Table 4.1. The adiabatic runs include gravity and MHD, but radiative heating and cooling, star formation, and stellar feedback are omitted. The no-feedback ('NoFB') runs include gravity, MHD, radiative heating and cooling, and star formation, but no stellar feedback. The FIRE runs add in explicit multi-channel stellar feedback (from supernovae, stellar winds, photo-heating, and an approximate treatment of radiation pressure) from the Feedback in Realistic Environments (FIRE) project (Hopkins et al., 2014, 2018b). Specifically, the same version of code as the isolated runs in Su et al. (2017) (FIRE-1 feedback with MFM hydrodynamics)

[1] A public version of this code is available at *http://www.tapir.caltech.edu/~phopkins/Site/GIZMO.html*.

Table 4.1: Physics variations in our simulation suite

Model	Star Formation	Cooling	Feedback
Adiabatic	No	None	None
NoFB	Yes	$10 - 10^{10}$ K	None
FIRE	Yes	$10 - 10^{10}$ K	FIRE
S&H	Yes	$10^4 - 10^{10}$ K	Springel & Hernquist

is used to facilitate comparison. In both the NoFB and FIRE runs, stars form only from gas that is self-gravitating at the resolution scale and has a density $n > 100$ cm^{-3}, and the instantaneous SFR density is assumed to be the molecular gas density divided by the local free-fall time (see Hopkins et al. 2014). Except for the differences noted explicitly above, the code used for the runs is otherwise identical (and the NoFB and MHD runs specifically employ the exact same code as the corresponding runs in Su et al. 2017). Finally, the 'S&H' runs employ the Springel & Hernquist (2003, hereafter SH03) model, which implicitly treats the ISM as gas with two phases (cold clouds & ambient gas) in pressure equilibrium, but only has one explicit, single-phase gas with a barytropic equation of state (EOS) in the hydrodynamics. The model includes stochastic star formation via a Kennicutt-Schmidt-type prescription and implicitly treats the effects of supernova feedback by increasingly overpressurising the gas (relative to an ideal gas) with increasing density. To explore potential self-consistent magnetically driven outflows, we do not employ the SH03 kinematically decoupled wind model. We have run the FIRE versions of the SMC and MW models at multiple resolutions spanning two orders of magnitude in mass resolution and confirmed that the global properties of the galaxies (e.g., SFHs and magnetic field strengths) are converged (Su et al., 2017). We have also re-run both of the FIRE runs starting with an initial seed magnetic field strength an order of magnitude less (10^{-3} μG) than our default value. Although the results differed during the initial exponential amplification phase, as expected, quantities such as the saturation values of the magnetic field strength in all and dense gas were similar.

4.3 Results

4.3.1 Magnetic field morphologies

Fig. 4.1 shows edge-on and face-on projected gas density maps of the MW and SMC simulations. The MW runs are shown after 0.83 Gyr of evolution, whereas the SMC runs have been evolved for 0.69 Gyr. The colour encodes the projected

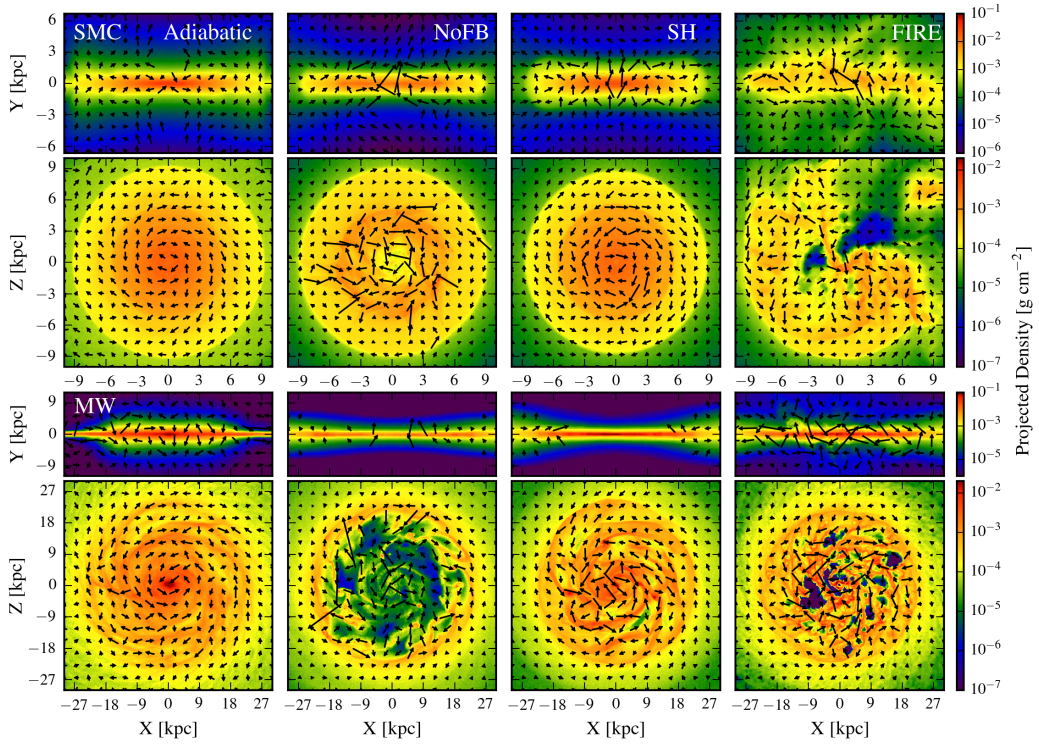

Figure 4.1: Edge-on and face-on projections of the gas density of the simulated galaxies (MW, t = 0.83 Gyr: rows 1-2; SMC, t = 0.69 Gyr: rows 3-4). Arrows indicate the relative magnitudes and directions of the magnetic field. Different columns correspond to different baryonic physics models. In all maps, the magnetic fields in dense clumps are not only stronger but also more randomly distributed. No-feedback runs fragment most dramatically and therefore exhibit magnetic fields highly concentrated in dense clumps with random directions. Runs that employ the FIRE explicit stellar feedback model have irregular magnetic field distributions owing to supernova shocks, turbulence and outflows driven by stellar feedback, in addition to the greater fragmentation present in these runs compared with the Adiabatic and S&H sub-grid stellar feedback runs. The latter two types of runs generally have smooth, highly ordered gas and magnetic field morphologies.

density, as specified by the colour bars on the right of each row (note that the scales in each row differ). The arrows in each subplot indicate the directions and relative magnitudes of the local magnetic field in a central slice with a thickness of 0.8 kpc for the SMC runs and 1.6 kpc for the MW runs. Note that the lengths of the arrows are separately rescaled in each subplot to cover a larger dynamic range. Different columns correspond to the different sets of included physics.

The gas and magnetic field morphologies of runs with different baryonic physics differ significantly. The local strength and orderedness of the magnetic field are strongly related to the local density, with higher gas density corresponding to stronger and more irregularly distributed local magnetic fields. The NoFB runs fragment most dramatically because there is no stellar feedback to prevent catastrophic fragmentation. As a result, the magnetic fields are highly concentrated in the clumps and exhibit random directions. The magnetic fields in the FIRE runs are also highly irregular, not only because of fragmentation but also due to turbulence and outflows driven by strong stellar feedback (Anglés-Alcázar et al., 2017b, Hayward & Hopkins, 2017, Muratov et al., 2015). In contrast, the Adiabatic and S&H runs have very smooth, well-ordered gas morphologies and magnetic fields.

To quantify the spatial coherence of the magnetic field, we calculate $\xi_1 \equiv |\langle \mathbf{B} \rangle| / B_{\rm rms}$ and $\xi_2 \equiv \langle |\mathbf{B}| \rangle / B_{\rm rms}$ in various regions of the disc. Low values of ξ_1 correspond to randomly directed local magnetic fields. Lower values of ξ_2 indicate broader local magnetic field strength distributions. In the top row of Fig. 4.2, we plot ξ_1 and ξ_2 for gas at different densities. We first average (volume-weighted) over the gas particles from snapshots (over the time period 350-850 Myr for MW and 290-700 Myr for SMC) with similar densities within each 1 kpc cell and then plot the average of all cells in the disk region ($\Delta z = 1$ kpc and $3 < r < 10$ kpc).[2]

We generally find high ξ_1 and ξ_2 at densities $n \lesssim 0.1$ cm^{-3}, indicating coherently directed magnetic field lines and narrowly distributed magnetic field strengths. In denser gas ($n \gtrsim 0.1$ cm^{-3}), fragmentation causes the local magnetic field to be amplified and become more randomly oriented, which lowers both ξ values in the cell. The FIRE runs generally have the lowest ξ_2 over $0.1 < n < 100$ cm^{-3}. This indicates a broader distribution of magnetic field strengths owing to disturbances from feedback. On the other hand, the S&H and Adiabatic runs have almost no gas with $n > 0.1$ cm^3, which explains the extremely smooth magnetic field. At

[2]The center is excluded to prevent the average ξ values from being dominated by extreme values.

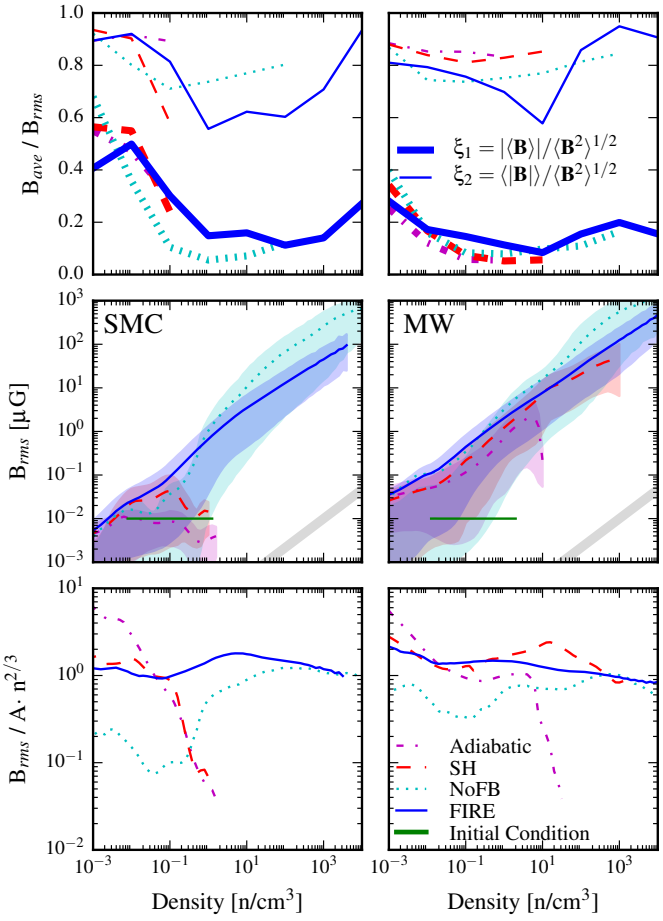

Figure 4.2: *Top*: volume-weighted average values of $\xi_1 \equiv |\langle \mathbf{B} \rangle| / B_{\rm rms}$ and $\xi_2 \equiv \langle |\mathbf{B}| \rangle / B_{\rm rms}$ in 1 kpc cells in the galactic disc. ξ_1 and ξ_2 are both high in gas with density < 0.1 cm^{-3} averaged over 350-850 Myr for MW and 290-700 Myr for SMC. In higher-density, fragmenting gas, the magnetic field is less spatially coherent, as indicated by the lower values of both ξ_1 and ξ_2 relative to the less-dense gas. In the density range $0.1 - 100$ cm^{-3}, the FIRE runs generally have lower ξ_2 values, indicating a broader distribution of local magnetic field strengths. The S&H and Adiabatic runs have much less gas with density > 0.1 cm^{-3} than do the FIRE and NoFB runs. *Middle*: relationship between the magnetic field strength and gas density of each resolution element (time-averaged as in the top panel). The gray lines show a scaling of $n^{2/3}$ with arbitrary normalization. The shaded regions denote the 5th–95th percentile range of the magnetic field strength at each density. *Bottom*: magnetic field strength divided by the best-fitting relation of the form $A \cdot n^{2/3}$ for each run. In most density bins and most runs, $B_{\rm rms}$ scales as $n^{2/3}$, indicating isotropic flux freezing or equipartition between the magnetic and gravitational energies. However, in the Adiabatic and S&H runs, gas that is initially at 'high' density cannot be compressed significantly owing to the high effective pressure; consequently, the field is not strongly amplified.

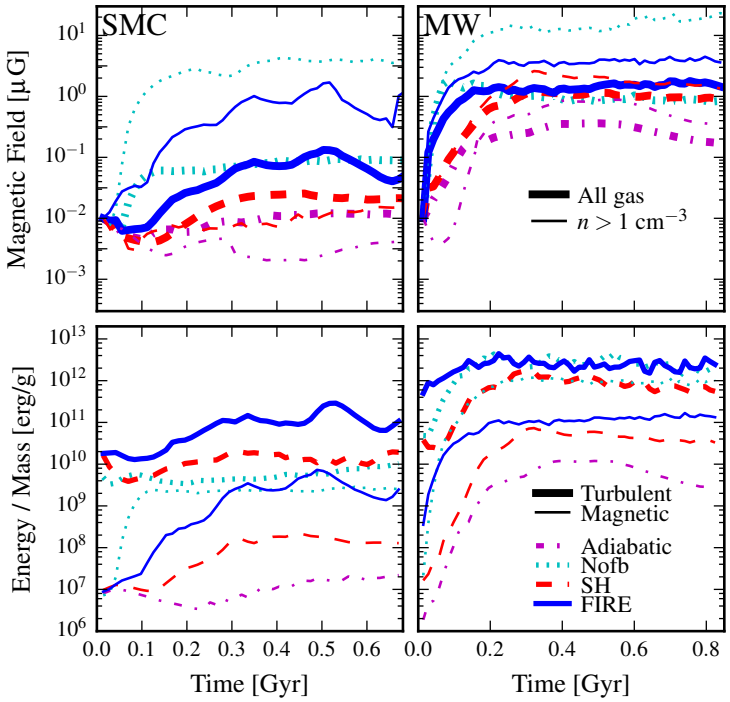

Figure 4.3: *Top*: the rms magnetic field strength of gas in the disc as a function of time. The different treatments of baryonic physics are indicated by the line color. Thick lines represent the rms magnetic field strength computed considering all gas, $B_{\rm rms}^{\rm all}$, whereas thin lines indicate the results for gas with density > 1 cm^{-3}, $B_{\rm rms}^{\rm dense}$. Greater gas fragmentation is associated with a higher magnetic field strength saturation value. The Adiabatic and S&H runs, which do not fragment as much as the no-feedback and FIRE runs, exhibit lower saturation values. *Bottom*: comparison of turbulent and magnetic energy per unit mass as a function of time. In the FIRE and S&H runs, the magnetic energy saturates to $\sim 2-6\%$ of the turbulent energy, consistent with the idealized supersonic turbulent dynamo.

$n \gtrsim 100$ cm^{-3}, ξ_2 increases again, indicating that the magnetic field in most gas within this density range has been amplified to a similar value.

4.3.2 Galactic magnetic field evolution

Fig. 4.3 shows the evolution of the rms magnetic field strength of the gas in the disc (defined as a cylinder of height 2 kpc and radius 10 kpc). We compare the rms B in all gas and just gas with $n \gtrsim 1$ cm^{-3}. In the MW runs, the magnetic field exponentially grows from the initial value (10^{-2} μG throughout the volume) at the start of simulation. Even in the MW Adiabatic run, the magnetic is amplified significantly through gravitational compression. In the SMC runs, on the other hand, the saturation values for all but the very dense particles are approximately

equal to the initial value of magnetic field (10^{-2} μG); hence, the amplification is much weaker for the SMC runs, especially the Adiabatic run. In the FIRE-low runs, the amplification is more obvious. Regardless of the initial magnetic field strength, the saturation value for each IC (using the FIRE baryonic physics model) is robust.

Since the denser gas has much stronger magnetic fields, the time evolution and saturation value of the field is closely tied to the amount of fragmentation in each run. The Adiabatic runs generally fragment the least and therefore have the lowest magnetic field strength. In the S&H runs, the stiff EOS adopted in the model and the temperature floor (10^4 K) prevent gas from being compressed and fragmenting as much as in the NoFB and FIRE runs. As a result, the magnetic fields in the S&H runs are also weaker overall. However, in gas with densities less than or similar to the galactic average, the S&H model yields quite similar field strengths to the NoFB or FIRE runs. Due to the absence of feedback, the NoFB runs fragment most severely, and the densest gas therein has the highest rms magnetic field strengths.

The magnetic field strength in the gas disc in the MW FIRE run saturates at ~ 2 μG, and the field strength of "dense" ($n > 1\,\mathrm{cm}^{-3}$) gas saturates at ~ 5 μG. These values are consistent with observations (Beck, 2007, Beck et al., 1996, Han et al., 2006, Kulsrud & Zweibel, 2008, Rand & Kulkarni, 1989). At higher densities ($n \sim 100\,\mathrm{cm}^{-3}$), comparable to H I clouds in the cold neutral medium or molecular clouds, $|\mathbf{B}|$ is typically a few 10s of μG, again similar to observations.

As shown in the second row of Fig. 4.3, the magnetic energies in the FIRE and S&H runs saturate to $\sim 2-6\%$ of the turbulent energy [3]. This is true regardless of the initial magnetic field strength, consistent with theoretical predictions (Schober et al., 2015) and idealized simulations of the supersonic turbulent dynamo (Federrath et al., 2011a, 2014, Tricco et al., 2016) and other galaxy simulations with feedback (Dubois & Teyssier, 2010, Kotarba et al., 2010, Rieder & Teyssier, 2017, Su et al., 2017). We therefore believe that our magnetic amplification histories and saturation values are reasonable. In contrast, in the NoFB runs, the magnetic energy reaches $\gtrsim 30\%$ of the turbulent energy, indicating equipartition between the turbulent and magnetic energy.

As can be seen from the evolution of the magnetic field strength and energy, the exponential growth happens during the first $\sim 0.2-0.3$ Myr, which is shorter than the time scale for amplification driven by galactic global motion. This indicates that

[3] The turbulent energy calculation is performed using the method described in Su et al. (2017). This is not applicable for Adiabatic runs, so these runs are not included here.

either local turbulent motion or local gravitational motion dominates the magnetic amplification during this time. However, separating these two processes is difficult in galactic simulations, since the local gravitational and turbulent energy can be in equipartition. A detailed study of the dominant amplification mechanism(s) will be presented in a future work.

4.3.3 Relationship between magnetic field strength and density

The second row of Fig. 4.2 shows the relationship between the local magnetic field strength and local gas density. Over most of the density range, $B_{\rm rms} \propto n^{2/3}$. In low-density gas, this is a result of isotropic flux freezing in gas compression dominating the field amplification (or in expansion, for the lowest-density gas). In denser gas, this indicates either isotropic flux freezing or equipartition between the magnetic and gravitational energies in collapsed structures with constant mass. The latter holds because

$$\frac{\mathbf{B}^2}{4\pi}V \sim \frac{GM^2}{r} \rightarrow B \propto \frac{1}{(rV)^{1/2}} \propto \frac{1}{V^{2/3}} \propto n^{2/3}. \tag{4.1}$$

In the MW runs, gas in the initial disc (green line in Fig. 4.2) has a magnetic field strength at least 1 order of magnitude less than the average magnetic field in later snapshots and outside the shaded region spanned by the gas particles therein. In the SMC runs with the fiducial seed field strength, on the other hand, the magnetic field strength is relatively high to begin with, so the initial magnetic field strength is marginally within the shaded region, indicating weaker amplification. However, in the 'FIRE-low' runs for both model galaxies, although the initial magnetic field strength is one order of magnitude lower, the $B_{\rm rms} - n$ curves from the later snapshots are almost identical to the curves in the default-seed-value 'FIRE' runs. If the same plots are made for individual time snapshots, $B_{\rm rms} \propto n^{2/3}$ holds at all times, albeit with systematic shifts in the normalisation. Within the first $\sim 0.2 - 0.3$ Myr, the lines move toward the upper left and approach the lines shown in Fig. 4.2. This indicates that although isotropic flux freezing or equipartition between the magnetic and gravitational energies dominates the field amplification as gas undergoes density changes, other amplification mechanisms (local turbulent or gravitationally driven amplification) occur in these runs, especially within the exponential growth phase of the magnetic fields.

Gas at the high-density ends of both the Adiabatic and S&H runs deviates from the adiabatic curve (i.e. is less amplified than expected). This is an artifact caused

by the fact that gas initially at 'high' density in those runs cannot be significantly compressed further. For the Adiabatic runs, the reason is that the lack of cooling results in high pressure in high-density regions. In the S&H run, the lack of cooling below 10^4 K and the effective EOS have the same effect. In particular, owing to the small depth of the potential well of the SMC model, gas in the Adiabatic and S&H runs is only weakly compressed; thus, the magnetic field is not significantly amplified.

4.4 Summary and discussion

We have demonstrated that the morphology and saturation value of galactic magnetic fields strongly depend on baryonic physics, specifically cooling, star formation and stellar feedback. This is primarily because baryonic physics affect the magnetic field strength through altering the amount of fragmentation and balance amongst different ISM phases. Moreover, strong turbulence and outflows driven by multi-channel stellar feedback (present in our FIRE runs) can further increase the amount of randomness in the magnetic field morphology. The Adiabatic (no cooling, no star formation) and S&H ("effective equation of state", unresolved ISM) runs have significantly lower magnetic field saturation values in dense gas compared with the NoFB (cooling and star formation but no feedback) and FIRE (cooling, star formation, and feedback) runs, and the former tend to have more ordered large-scale magnetic fields. It appears that the S&H model (which is used by many modern galaxy formation simulations, either directly or with modifications, such as IllustrisTNG, Pillepich et al. 2018; EAGLE, Schaye et al. 2015; and MUFASA, Davé et al. 2016) works reasonably well for gas with density lower than or equal to the galactic average but suppresses gas fragmentation in higher-density gas, thus causing discrepancies in the magnetic field amplification.

We find that in the simulated galactic discs, the field strength scales with density as $B \propto n^{2/3}$, similar to the results for galactic cores found by Pakmor et al. (2017). This results from a combination of isotropic flux freezing in compression/expansion without a preferred direction and equipartition between the magnetic and gravitational energies (in dense, self-gravitating gas). We caution that although the aforementioned processes dominate the field amplification as gas undergoes density changes, they are not the only amplification mechanisms at work.

Note that although Zeeman observations (Crutcher et al., 2010) suggest $B \propto n^0$ at low density and $B \propto n^{2/3}$ at high density, the scatter in the data points is quite

large. Moreover, the magnetic field strength inferred is highly correlated with whether the object is an H I cloud/dark cloud or a molecular cloud, and the scaling between the magnetic field strength and density is weak within each category. Since both of these categories of objects have nearly constant surface density (Blitz & Rosolowsky, 2004, Cayatte et al., 1994, Wevers et al., 1986, Wong & Blitz, 2002), the aforementioned observations might actually constrain the scaling between magnetic field strength and surface density (instead of volume density) and are not necessarily inconsistent with our results.

Rieder & Teyssier (2016, 2017) have also argued that stellar feedback is crucial for magnetic field amplification; in simulations of isolated gas cooling haloes, they find that supernova feedback drives a turbulent dynamo that is the dominant source of magnetic field amplification. A detailed comparison of our results is beyond the scope of this work, but it is worth noting that we both agree that the effects of stellar feedback must be captured accurately in order to model the amplification of galactic magnetic fields.

Our results also have important implications for incorporating cosmic rays, which may play an important role in driving galactic outflows (e.g., Booth et al., 2013, Hanasz et al., 2013, Salem & Bryan, 2014, Uhlig et al., 2012), because cosmic rays propagate along magnetic field lines. We have shown that 'effective' treatments of stellar feedback lead to significantly more ordered magnetic fields compared with simulations with explicit stellar feedback; it is thus likely that in the former types of simulations, cosmic rays will propagate over large scales and drive outflows more easily than in simulations with explicit stellar feedback.

Chapter 5

THE FAILURE OF STELLAR FEEDBACK, MAGNETIC FIELDS, CONDUCTION, AND MORPHOLOGICAL QUENCHING IN MAINTAINING RED GALAXIES

K.-Y. Su, P. F. Hopkins, C. C. Hayward, X. Ma, C.-A. Faucher-Giguère, D. Kereš, M. E. Orr, and V. H. Robles. The failure of stellar feedback, magnetic fields, conduction, and morphological quenching in maintaining red galaxies. *MNRAS, in press, arXiv:1809.09120*, September 2018.

The quenching "maintenance" and related "cooling flow" problems are important in galaxies from Milky Way mass through clusters. We investigate this in haloes with masses $\sim 10^{12}$ – $10^{14}\,M_\odot$, using non-cosmological high-resolution hydrodynamic simulations with the FIRE-2 (Feedback In Realistic Environments) stellar feedback model. We specifically focus on physics present *without* AGN, and show that various proposed "non-AGN" solution mechanisms in the literature, including Type Ia supernovae, shocked AGB winds, other forms of stellar feedback (e.g., cosmic rays), magnetic fields, Spitzer-Braginskii conduction, or "morphological quenching" do not halt or substantially reduce cooling flows nor maintain "quenched" galaxies in this mass range. We show that stellar feedback (including cosmic rays from SNe) alters the balance of cold/warm gas and the rate at which the cooled gas *within* the galaxy turns into stars, but not the net baryonic inflow. If anything, outflowing metals and dense gas promote additional cooling. Conduction is important only in the most massive haloes, as expected, but even at $\sim 10^{14}\,M_\odot$ reduces inflow only by a factor ~ 2 (owing to saturation effects and anisotropic suppression). Changing the morphology of the galaxies only slightly alters their Toomre-Q parameter, and has no effect on cooling (as expected), so has essentially no effect on cooling flows or maintaining quenching. This all supports the idea that additional physics, e.g., AGN feedback, must be important in massive galaxies.

5.1 Introduction

Perhaps the biggest unsolved question in galaxy formation is what explains the "quenching"[1] of star formation and maintenance of "red and dead" galaxy popu-

[1]Throughout this paper, when we refer to "quenching" and red galaxies, we exclusively refer to *central* galaxies, as opposed to satellite galaxies which can be quenched by a variety of environmental

lations over a large fraction of cosmic time (Baldry et al., 2004, Bell et al., 2003, Blanton et al., 2005, Dekel & Birnboim, 2006, Kauffmann et al., 2003, Kereš et al., 2009, Madgwick et al., 2003, Pozzetti et al., 2010, Wetzel et al., 2012), at stellar masses $\gtrsim 3-5\times10^{10}\,\mathrm{M}_{\odot}$ (above $\sim L_{*}$ in the galaxy luminosity function at $z\approx0$). This is closely related to the classic "cooling flow problem": X-ray observations show there exists significant radiative cooling of hot gas in massive ellipticals and clusters with cool-core, indicating cooling times much less than a Hubble time (Fabian et al., 1994, Peterson & Fabian, 2006). Comparing with the inferred cooling flows (reaching up to $\sim 1000\,\mathrm{M}_{\odot}\,\mathrm{yr}^{-1}$ in clusters McDonald et al. 2018), there are neither sufficient amounts of cold gas (in observed HI, e.g., McDonald et al. 2011, or CO, Werner et al. 2013), or sufficient star formation rates (SFRs; O'Dea et al., 2008, Rafferty et al., 2008, Tamura et al., 2001), to account for the rapidly-cooling gas (see also Ciotti et al. 1991, Cowie & Binney 1977, Fabian 1994, Mathews & Bregman 1978, Silk 1976 for the "classical" cooling flow case). Simulations and semi-analytic models which do not suppress these cooling flows, and simply allow the material to cool into galaxies, typically over-produce the observed star formation rates of massive galaxies by at least an order of magnitude (for recent examples, see e.g., the weak/no feedback runs in Booth & Schaye, 2009, Choi et al., 2015, Li et al., 2015, Sijacki et al., 2007).

To compensate for the observed cooling, there must be some sort of heat source or pressure support. The presence of the shock heated hot-halo can help feedback mechanisms and quench galaxies (e.g., Kereš et al., 2005). However, the hot halo itself does not prevent later gas cooling from the cooling flows. The most popular, and perhaps promising, solution is "feedback" from an active galactic nucleus (AGN) which can both expel gas from galaxies (shutting down star formation) and inject heat or stirring in the circum-galactic medium (CGM) or intra-cluster medium (ICM), preventing new gas accretion (for recent studies see also e.g Anglés-Alcázar et al. 2017a, Eisenreich et al. 2017, Faucher-Giguère & Quataert 2012, Gaspari & Sądowski 2017, Li et al. 2017, 2018, Martizzi et al. 2018, Pellegrini et al. 2018, Weinberger et al. 2018, Yoon et al. 2018; see e.g., Ciotti & Ostriker 2001, Croton et al. 2006, Fabian 1999, Hopkins et al. 2005, 2006a, McNamara & Nulsen 2007, Silk & Rees 1998 for earlier works). However, despite its plausibility, the detailed physics of AGN feedback (e.g., what determines jet energetics and how they transfer energy into the ICM) remains uncertain, as do the relevant "input parameters" (e.g., kinetic luminosities, duty cycles).

processes (e.g., ram pressure and tidal stripping, starvation, strangulation, etc.).

Perhaps as a result, a variety of "non-AGN" mechanisms to quench galaxies and keep them red have been proposed in the literature. These generally invoked physics are un-ambiguously present, but play an uncertain role in quenching and the cooling flow problem, including: stellar feedback from shock-heated AGB winds, Type Ia supernovae (SNe), or SNe-injected cosmic rays (CRs); magnetic fields and thermal conduction in the CGM/IGM; or "morphological quenching" via altering the galaxy morphology and gravitational stability properties. Our focus in this paper is therefore to attempt a systematic theoretical study of these possibilities, *without* considering AGN.

This is important for several reasons: if one (or more) of these mechanisms can, indeed, quench galaxies, this is critical to understand! Even if they do not quench galaxies, they could, in principle, "help" by suppressing cooling or star formation (lessening "requirements" for AGN). And although many previous studies have claimed AGN feedback is "necessary" to explain quenching (see e.g., Ciotti et al., 1991, Conroy & Ostriker, 2008, Khalatyan et al., 2008, McNamara & Nulsen, 2007, Taylor & Kobayashi, 2015, in addition to the references above), almost all studies of AGN feedback to date have neglected some or all of these additional processes (often treating e.g., stellar feedback in a highly simplified, sub-grid manner). Therefore, it is important to understand whether they alter the "initial conditions" (e.g., typical CGM properties, cooling rates, etc.) for AGN feedback, and "how much more" does AGN feedback need to do. We hope that by studying the "overcooling problem" in global simulations with higher resolution and more detailed physical treatments of the multi-phase ISM and stellar feedback, we can better understand where and how AGN or other feedback, if indeed necessary, must act.

In § 5.2 we summarize the physics considered here, and describe our numerical simulations. Results are presented in § 5.3. We then discuss the effects of each of these physics in turn, in § 5.4.

5.2 Methodology

We used isolated galaxy simulations ranging from $10^{12}-10^{14}M_{\odot}$ to test how various physical processes affect the galactic cooling flows. We set up the initial conditions according to the observed profiles of cool-core clusters at low redshift, as detailed in § 5.2.2. Without proper quenching mechanisms, although the haloes have initial properties agree with the observations, their cooling flow rates and SFRs quickly runaway, surpassing the observational values by orders of magnitude. We ran the

simulations with various proposed quenching mechanisms and tested to what extent (if any) do they suppress the cooling flow and whether they can maintain stably quenched galaxies.

Our simulations use GIZMO (Hopkins, 2015) [2], in its meshless finite mass (MFM) mode, which is a Lagrangian mesh-free Godunov method, capturing advantages of grid-based and smoothed-particle hydrodynamics (SPH) methods. Numerical implementation details and extensive tests are presented in a series of methods papers for e.g., the hydrodynamics and self-gravity (Hopkins, 2015), magnetohydrodynamics (MHD; Hopkins, 2016, Hopkins & Raives, 2016), anisotropic conduction and viscosity (Hopkins, 2017, Su et al., 2017), and cosmic rays (Chan et al., in prep.).

Our default simulations use the FIRE-2 implementation of the Feedback In Realistic Environments (FIRE) physical treatments of the ISM and stellar feedback, details of which are given in Hopkins et al. (2018a,b) along with extensive numerical tests. This follows cooling from $10 - 10^{10}$K, including the effects of photoelectric and photoionization heating by a UV background Faucher-Giguère et al. (2009) and local source, collisional, Compton, fine structure, recombination, atomic, and molecular cooling. Star formation is allowed only in gas that is molecular, self-shielding, locally self-gravitating (Hopkins et al., 2013b), and above a density $n > 100\,\mathrm{cm}^{-3}$. Star particles, once formed, are treated as a single stellar population with metallicity inherited from their parent gas at formation. All feedback rates (SNe and mass-loss rates, spectra, etc.) and strengths are IMF-averaged values calculated from STARBURST99 (Leitherer et al., 1999) with a Kroupa (2002) IMF. The feedback model includes: (1) Radiative feedback including photoionization and photoelectric heating, as well as single and multiple-scattering radiation pressure tracked in five bands (ionizing, FUV, NUV, optical-NIR, IR). (2) Stellar particles continuously lose mass and inject mass, metals, energy, and momentum in the form of OB and AGB winds. (3) Type II and Ia SNe happen stochastically according to the rate mentioned above. Once they occur, the stellar particles lose mass and inject the appropriate mass, metal, momentum and energy to the surrounding gas.

5.2.1 Physics surveyed

Stellar feedback: young/massive stars

Feedback from massive stars is un-ambiguously crucial to galaxy evolution. In the last decade, with progress in modeling stellar feedback, simulations of $\lesssim L*$

[2] A public version of this code is available at *http://www.tapir.caltech.edu/~phopkins/Site/GIZMO.html*.

galaxies (see e.g., Agertz & Kravtsov, 2016, Ceverino & Klypin, 2009, Governato et al., 2007, Hopkins et al., 2011, 2012a,b, Hu et al., 2016, Kim et al., 2014, Muratov et al., 2015, Uhlig et al., 2012) are now able to produce reasonably realistic galaxy populations, without the runaway collapse and star formation that occurs absent feedback. However, in these (mostly star-forming) lower-mass galaxies, feedback is dominated by young, massive stars (e.g., radiation and OB winds from massive stars, Type-II SNe). Given the *observed* low specific star formation rates (sSFRs) in quenched systems (e.g., $\lesssim 10^{-11}\,\mathrm{yr}^{-1}$ for $10^{14}\mathrm{M}_{\odot}$ haloes; Kravtsov et al., 2014, Weinmann et al., 2006, Woo et al., 2013), the number of massive stars is very low, so it seems unlikely this can maintain a quenched galaxy without (paradoxically) a much larger SFR. But these physics must be present whenever star formation does occur, so we include them with the methods described above.

Stellar Feedback: SNe Ia

At the observed low sSFRs of massive (quenched) galaxies, the SNe Ia rate (including both prompt and delayed populations) is much larger than the core-collapse rate, giving a time-averaged energy-injection rate $\sim 10^{41.5}\,erg\,s^{-1}\,(M_*/10^{11}{}_{\odot})$, which can be comparable to the cooling rates in some systems. Since these come from old populations, and are distributed smoothly in space and time, it has been proposed that they could be an important CGM/ICM heating mechanism (e.g., Sharma et al., 2012, Tang & Wang, 2005, Tang et al., 2009, and references therein). We include Ia's following the FIRE-2 method described above, using with the rates from Mannucci et al. (2006) (including both the prompt and delayed components), assuming 10^{51} erg per event. Note that although there has been considerable debate about Ia rates, it has focused on the prompt component, which is unimportant for our conclusions.

Stellar feedback: AGB winds

AGB winds from old stellar populations return a significant fraction of the stellar mass, but have low launch velocities $\sim 10\,\mathrm{km\,s}^{-1}$ and correspondingly negligible kinetic luminosities. However, Conroy et al. (2015) note that if the AGB stars are moving through the ambient gas medium with large velocity dispersions $\gtrsim 300\,\mathrm{km\,s}^{-1}$, the kinetic luminosities and post-shock temperatures are greatly elevated in the wind bow shocks, and this can suppress cooling and inject energy well above the Ia rate. Crucially, our default FIRE-2 models account in detail for the relative star-gas velocity when injecting stellar mass loss of any kind (AGB or OB winds or

SNe), in an exactly conservative manner, as described and tested in Hopkins et al. (2018a).

Magnetic fields, conduction & viscosity

Magnetic fields can, in principle, directly suppress cooling flows via providing additional pressure support (Beck et al., 1996, 2012, Soker & Sarazin, 1990), although they have limited effects on global star formation properties of sub-L_* galaxies (Su et al., 2017). They can also non-linearly influence essentially all the gas dynamics.

Thermal conduction can carry heat from the outer parts of hot haloes into cool inner cores, and so might serve as an important heating mechanism (Binney & Cowie, 1981, Dolag et al., 2004, Fabian et al., 2002, Kim & Narayan, 2003a, Pope et al., 2006, Tucker & Rosner, 1983, Voigt & Fabian, 2004, Voigt et al., 2002, Voit, 2011, Wagh et al., 2014, Zakamska & Narayan, 2003). However, under the conditions in the CGM/ICM, this cannot be considered in the absence of MHD, as the conduction is highly anisotropic. Convective instabilities driven by anisotropic (Spitzer-Braginskii) conduction (Kannan et al., 2016, Sarazin, 1988, Spitzer & Härm, 1953, Zakamska & Narayan, 2003, ZuHone et al., 2015) along magnetic field lines, including the heat-flux-driven buoyancy instability (HBI; Parrish & Quataert, 2008, Quataert, 2008) and the magnetothermal instability (MTI; Balbus, 2000, Parrish et al., 2008), may further change the magnetic configuration and conduction time scale (Parrish et al., 2009) or even drive turbulence and provide extra pressure support or mixing (Parrish et al., 2012a). It is also been argued that conduction can help AGN feedback quench galaxies more effectively (e.g., Kannan et al., 2017).

We therefore consider a set of additional fluid "microphysics" runs, with ideal MHD and physical (temperature-dependent, fully-anisotropic) Spitzer-Braginskii conduction and viscosity (we assume the perpendicular transport coefficients are vanishingly small). The implementation is identical to Su et al. (2017).

Cosmic rays (not from AGN)

Cosmic rays (CRs) can provide additional pressure support to gas, drive galactic outflows, and heat the CGM/ICM directly via hadronic and streaming losses (Enßlin et al., 2011, Fujita & Ohira, 2011, Fujita et al., 2013, Guo & Oh, 2008, Jacob & Pfrommer, 2017a,b, Jacob et al., 2018, Pfrommer, 2013, Pfrommer et al., 2017a, Ruszkowski et al., 2017a,b, Sharma et al., 2010, Wiener et al., 2013). As a result several of the studies above suggest they can help quench star formation; however,

this is usually in the context of CRs from AGN. Here we wish to explore non-AGN mechanisms, so we consider simulations adopting the CR physics and numerical implementation described in (Chan et al., in prep.). This CR treatment includes including streaming (at the local Alfvén speed or sound speed, whichever is larger, $v_{\rm st} \sim \sqrt{v_{\rm Alf}^2 + v_{\rm c}^2}$, with the appropriate streaming loss term, which thermalizes, following Uhlig et al. 2012), diffusion (with a fixed diffusivity $\kappa_{\rm cr}$), adiabatic energy exchange with the gas and cosmic ray pressure in the gas equation of motion, and hadronic and Coulomb losses (following Guo & Oh 2008). We follow a single energy bin (i.e. GeV CRs, which dominate the pressure), treated in the ultra-relativistic limit. Streaming and diffusion are fully-anisotropic along field lines. CRs are injected in SNe (a fixed fraction $\epsilon_{\rm cr} = 0.1$ of each SNe energy goes into CRs; see e.g., Pfrommer et al. 2017a,b). In Chan et al. (in prep.), we show that matching observed γ-ray luminosities, in simulations with the physics above requires $\kappa_{\rm cr} \sim 10^{29}\,{\rm cm^2\,s^{-1}}$ (in good agreement with detailed CR transport models that include an extended gaseous halo around the galaxy, (see e.g., Strong & Moskalenko, 1998, Strong et al., 2010, Trotta et al., 2011), so we adopt this as our fiducial value, but discuss variations below.

We note that in addition to SNe shocks, the other major non-AGN source of CRs of interest here is shocks from cosmological large-scale structure (LSS) formation/accretion. Since our simulations are not fully-cosmological, this is not directly accounted for. [3]

Morphological quenching

Finally, Martig et al. (2009) and Dekel et al. (2009) described a scenario they referred to as "morphological quenching," whereby quenching could be accomplished (SF suppressed) simply by altering a galaxy's morphology. Specifically, they argued that turning a stellar disk into a more gravitationally stable spheroid would raise the Toomre-Q and stabilize the gas against fragmentation/star formation. This involves no new physics beyond those above (our simulations easily resolve Q and the vertical scale-heights and gravitational fragmentation of the cold gaseous disks), but rather different galaxy initial conditions given the same halo properties.

[3] We implicitly effectively model this in the CR energy density in our initial conditions by assuming equipartition with magnetic energy

5.2.2 Initial conditions

It is important to note that the overcooling problem exists over several orders of magnitude in halo mass, not just at $\sim L^*$ where most galaxies first quench, or in massive clusters where the classical "cooling flow problem" is defined. We therefore consider three fiducial initial conditions (ICs), with halo masses of 1.5×10^{12} (m12), 10^{13} (m13) and 8.5×10^{13}M$_\odot$ (m14), respectively. The DM halo, stellar bulge, stellar disc are set following Springel & White (1999). We assume a spherical, isotropic, NFW (Navarro et al., 1996) profile dark matter halo (scale lengths (20.4, 93, 218.5) kpc), and Hernquist (1990) profile stellar bulge (scale lengths (1, 2.8, 3.9) kpc). We also assume exponential, rotation-supported gas and stellar disks (scale lengths (6, 2.8, 3.9) kpc and (3, 2.8, 3.9) kpc, respectively; scale-height (0.3, 1, 1.4) kpc for both, gas temperatures initialized to pressure equilibrium Springel 2000), and an extended spherical, hydrostatic gas halo with a beta profile (scale-radius (20.4, 9.3, 21.85) kpc and $\beta = (0.5, 0.43, 0.5)$). [4] All the initial conditions except the m13 case are run adiabatically (no feedback, no cooling) for at least 50 Myr before putting into use, to ensure stability. [5] The properties are summarized in Table 5.1. In the m12 cases, we explicitly test the effect of different stellar morphology on the cooling, so besides the fiducial (disc-dominated) m12 IC, we also construct bulge-dominated and gas-disk-free ICs (m12 Bulge and m12 Bulge-NoGD).

The initial conditions are set up to be similar to typical cooling-core systems observed, insofar as this is possible. For example, m12 is a Milky Way-mass galaxy, where the hot gas halo, roughly follows the observed Milky Way profile estimated in Miller & Bregman (2013, 2015) and Gupta et al. (2017), except that we assume a universal baryonic fraction (0.16) inside twice the virial radius (we do not allow for missing baryons as suggested in the aforementioned papers). It is possible that the solution to overcooling involves expulsion of a large fraction of the Universal baryonic mass; however our intention here is to see if this does occur, not to put it in "by hand" (moreover, direct observations indicate the full baryon content does exist within similar radii, in external systems, see Greco et al. 2015, Lim et al. 2017, Planck Collaboration et al. 2013). Our m13 is the elliptical galaxy (Ell) in Su et al. (2017)[6] The mass and radial distribution of gas, stars and dark mater are consistent

[4] The hot halo gas rotates at a fix fraction of the circular velocity, which is twice the DM halo streaming velocity in Springel & White (1999). It is then $\sim 10-15\%$ rotation-supported, and $\sim 85-90\%$ thermal-pressure-supported.

[5] This is necessary for the runs with radially-dependent super-Lagrangian refinement scheme (m14), but less relevant for the others.

[6] There is minor typographical error in the tabulated Ell properties in Su et al. (2017). The values

with the observations of similar-mass haloes compiled in Humphrey et al. (2012b) and Anderson et al. (2016) . Our m14 is initialized as as cool core cluster, with a massive central elliptical galaxy, by design. The halo properties and profiles are consistent with typical observed systems of the same mass (Humphrey & Buote, 2013, Humphrey et al., 2012a, Su et al., 2013, 2015)

The comparison of the X-ray luminosity of our halo to the observations is plotted in the X-ray luminosity - halo mass plane in Fig. 5.1.[7] The luminosity is calculated using the same method in Ressler et al. (2018), in which the cooling curve is calculated for the photospheric solar abundances (Lodders, 2003), using the spectral analysis code SPEX (Kaastra et al., 1996) in the same way of Schure et al. (2009) and scaled according to the local hydrogen, helium, and metal mass fractions. All our initial conditions have cooling luminosity within the scatter of the observed X-ray luminosity - halo mass relation (Anderson et al., 2015, Balogh et al., 2006, Kim & Fabbiano, 2013, Reiprich & Böhringer, 2002, Stanek et al., 2006).

In all runs, unless otherwise noted, the initial metallicity is set to solar ($Z = 0.02$) at the core, and drops to $Z = 0.001$ at larger radii. [8] The m14 'Low Metal' run is set to $Z = 0.001$ uniformly. For runs with magnetic fields, the initial magnetic field strength of the gas in the core is set to 0.03 μG, 0.1 μG and 0.3 μG for m12, m13 and m14, respectively (roughly according to $m_{\rm vir}^{1/2}$). The initial field configuration is azimuthal, and decays as a function of radius.[9] For runs with cosmic rays, the initial CR energy density is set to be in local equipartition with the initial magnetic energy density, at all positions.

Given that m14 is very massive (with much of the gas mass in the extended, non-cooling halo at radii ~Mpc), resolving it with a uniform gas mass resolution is computationally formidable and not necessary for the convergence of FIRE stellar feedback. We therefore adopt a radially-dependent super-Lagrangian refinement scheme in this case: the target gas mass resolution is set to 8000 $M_\odot$ inside $r <$

in Table 5.1 are correct.

[7] The X-ray luminosity in our simulation is measured over 0.5 – 7 keV. That from Reiprich & Böhringer (2002) and Reiprich & Böhringer (2002) is from 0.5 – 2.4 keV, while that from Kim & Fabbiano (2013) is measured from 0.3 – 8 keV, but these are corrected given their median estimated spectral slope to the same range we measure. Given that most of the X-ray emission halo in this mass range in below 2 keV, and we are not trying to reproduce a specific halo, the comparison here is not particularly sensitive to this.

[8] The metallicity scales as $Z_\odot(0.05 + 0.95/(1 + (r/R_c)^{1.5}))$, where R_c is set to (20,10,20) kpc for (m12, m13, m14).

[9] Magnetic field strength scales as $(1/(1 + (r/R_c)^2))^\beta$, where $R_c = (20, 10, 20)$ kpc, and $\beta = (0.375, 1, 0.375)$ for (m12, m13, m14)

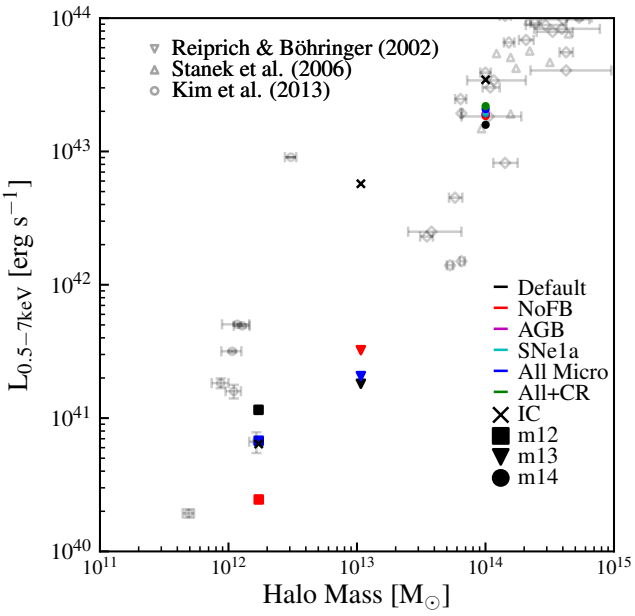

Figure 5.1: The X-ray luminosity (0.5-7 keV) of our initial conditions and the average luminosity of the last 100 Myr of each run are plotted on the X-ray luminosity - halo mass plane in comparison to the observations. All our runs lie reasonably within the scatter of the observed X-ray luminosity - halo mass relation. In m12, the low halo temperature means the X-ray luminosity is significantly influenced by SNe heating; in m13 & m14, the effects of stellar FB on the X-ray luminosity are small (most comes from the initial hot halo). Magnetic fields and CR feedback have little effect on the X-ray luminosity.

10 kpc, and increases smoothly $\propto r$ outside this radius up to a maximum 2×10^6 $M_\odot$ at $\sim$ 300 kpc. Gas resolution elements are automatically merged or split appropriately if they move inward/outward, to maintain this mass resolution (to within a factor = 2 tolerance) at all times.

Most simulations have been re-run with different resolutions, with the initial mass resolution differing by at least two orders of magnitude. The conclusions are robust in this resolution range, with resolution studies provided in Appendix A.3. The list of runs ua summarized in Table 5.2. We note that the m14 runs with the "extended fluid microphysics" set or cosmic rays are more expensive, and are therefore run with lower resolution, but within the range where our results appear robust (see Appendix A.3).

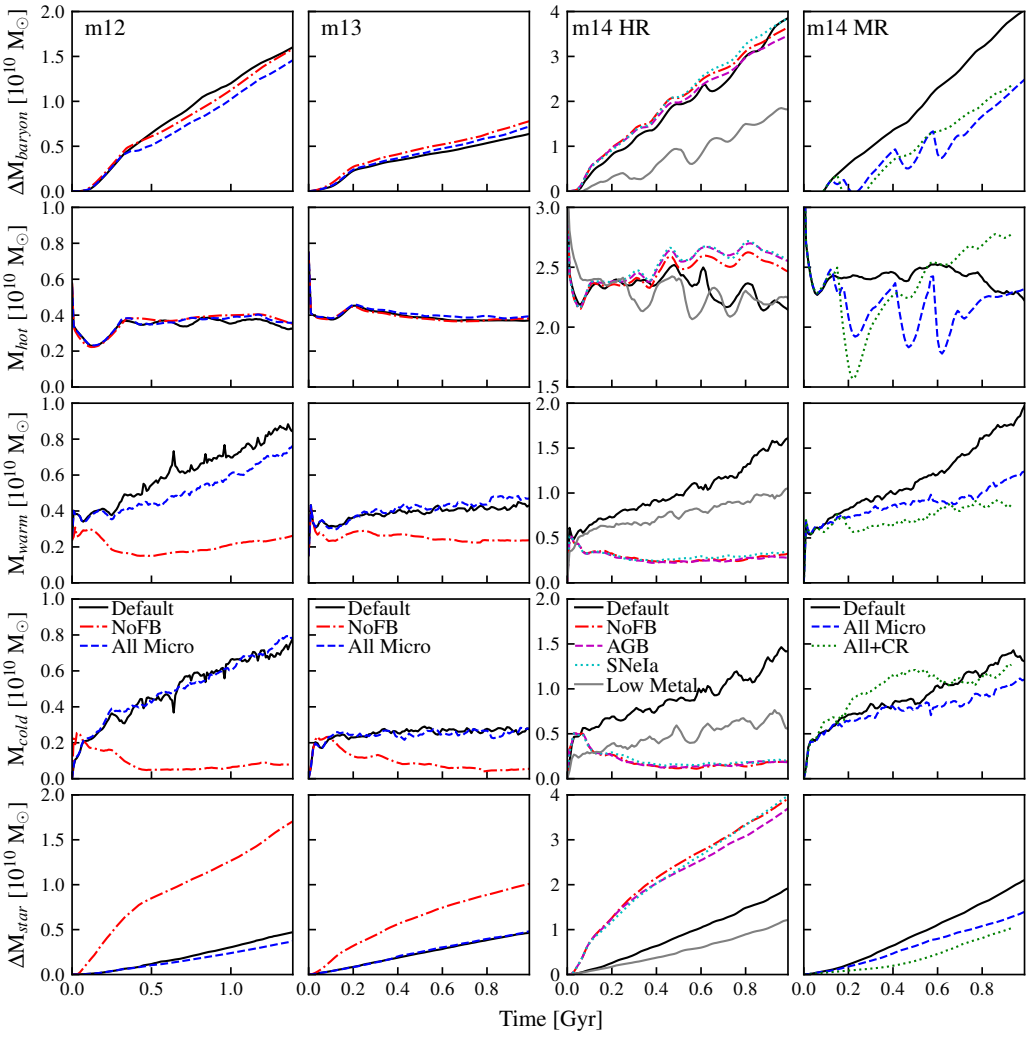

Figure 5.2: Cooling flows in different phases as a function of time: **Top row:** The baryonic mass variation within 30 kpc ($\Delta M_{\rm baryon}$). **2nd row:** The total hot gas ($> 10^6$ K) mass within 30 kpc ($M_{\rm hot}$). **3rd row:** The total warm gas (8000 – 10^6 K) mass within 30 kpc ($M_{\rm warm}$). **4th row:** The total cold gas (< 8000 K) mass within 30 kpc ($M_{\rm cold}$). **Bottom row:** The variation of stellar mass within 30 kpc ($\Delta M_{\rm star}$). In the 'Default' run, the cold and warm gas mass within 30kpc grows rapidly as gas cools, but in the 'NoFB' runs, any cooled gas almost immediately forms star, so only stellar mass increases. Both the'AGB' and 'SNeIa' runs behave roughly similarly to the 'NoFB' runs, indicating most of the FB comes from massive stars in these runaway-cooling simulations. Without metal-line cooling ('Low Metal' m14 run), the built-up cold and warm gas are all suppressed by a factor of 1.5-2. Both the 'All Micro' and 'All+CR' runs are similar to the 'Default' run in lower mass cases, but have a modest difference in the m14 halo, where conduction suppresses cooling flow by a factor of 2, and CR feedback suppresses SF and allows the build-up of additional cold gas.

Table 5.1: Simulation properties

Model	Resolution		DM halo				Stellar Bulge		Stellar Disc		Gas Disc		Gas Halo	
	ϵ_g (pc)	m_g ($M_\odot$)	$M_{\rm halo}$ ($M_\odot$)	c	$V_{\rm Max}$ (km/s)	$M_{\rm bar}$ ($M_\odot$)	M_b ($M_\odot$)	a (kpc)	M_d ($M_\odot$)	r_d (kpc)	M_{gd} ($M_\odot$)	r_{gd} (kpc)	M_{gh} ($M_\odot$)	r_{gh}/r_{dh}
m12	1	8e3	1.5e12	12	174	2.2e11	1.5e10	1	5e10	3	5e9	6	1.5e11	1
m12 Bulge	1	8e3	1.5e12	12	174	2.2e11	6e10	1.6	5e9	1.4	5e9	6	1.5e11	1
m12 Bulge-NoGD	1	8e3	1.5e12	12	174	2.2e11	6e10	1.6	5e9	1.4	5e8	2.8	1.6e11	1
m13	3	5e4	1.0e13	6	240	7.2e11	1e11	2.8	1.4e10	2.8	5e9	2.8	6e11	0.1
m14 MR	1	3e4*	8.5e13	5.5	600	1.52e13	2e11	3.9	2e10	3.9	1e10	3.9	1.5e13	0.1
m14 HR	1	8e3*	8.5e13	5.5	600	1.52e13	2e11	3.9	2e10	3.9	1e10	3.9	1.5e13	0.1

Parameters of the galaxy models studied here (§ 5.2.2):
(1) Model name. The number following 'm' labels the approximate logarithmic halo mass. m12 is a disc dominant halo, while m12 Bulge, m13 and m14 are bulge-dominant. The run labeled NoGD have an order of magnitude smaller gas disc. (2) ϵ_g: Gravitational force softening for gas (the softening for gas in all simulations is adaptive, and matched to the hydrodynamic resolution; here, we quote the minimum Plummer equivalent softening). (3) m_g: Gas mass (resolution element). There is a resolution gradient for m14, so its m_g (with *) is the mass of the highest resolution elements. (4) $M_{\rm halo}$: Halo mass. (5) c: NFW halo concentration. (6) $V_{\rm max}$: Halo maximum circular velocity. (7) $M_{\rm bar}$: Total baryonic mass. It is the sum of gas, disc, bulge and stellar mass for isolated galaxy runs, and the sum of gas and stellar mass in the cosmological runs within 0.1 virial radius. (8) M_b: Bulge mass. (9) a: Bulge scale-length (Hernquist profile). (10) M_d : Stellar disc mass. For CosmoMW and CosmoDwarf runs, this is the total stellar mass within 0.1 virial radius. (11) r_d : Stellar disc scale length (exponential disc). (12) M_{gd}: Gas disc mass. (13) r_{gd}: Gas disc scale length (exponential disc). (14) M_{gh}: Gas halo mass. (15) r_{gh}/r_{dh}: Gas halo scale length (beta profile) over dark matter scale length.

5.3 Results

5.3.1 Gas masses & phases in cores

Fig. 5.2 plots the baryonic mass within $< 30\,$kpc ($M_{\rm baryon}^{30\,\rm kpc}$). As gas cools, this increases, with rate $\dot{M}_{\rm baryon}^{30\,\rm kpc}/M_\odot\,{\rm yr}^{-1} \sim$ (12, 6, 40) in (m12,m13,m14): there is a competition at increasing mass between higher temperatures (lower cooling rates per particle) and simply larger gas masses available to cool (so this decreases slightly from m12 to m13, then rises rapidly to m14). This is also partially because the viral temperature of 'm13' is roughly at the minimum of the cooling curve (a few times 10^6 K). Gas with $T > 10^6\,$K is mostly hot halo gas from the ICs and is replenished (from larger radius) at small radii as it cools (only a small fraction comes from stellar feedback) so the "hot" gas mass evolves only weakly. In our default runs the cold and warm gas mass inside $< 30\,$kpc grows rapidly as gas cools. In the "NoFB"

Table 5.2: List of runs

Model	Feedback	Microphysics	CR
m12			
NoFB	None	Hydro	no
Default	FIRE 2	Hydro	no
All Micro	FIRE 2	MHD+Viscosity+Conduction	no
Default-Bulge	FIRE 2	Hydro	no
NoFB-Bulge -NoGD	FIRE 2	Hydro	no
m13			
NoFB	None	Hydro	no
Default	FIRE 2	Hydro	no
All Micro	FIRE 2	MHD+Viscosity+Conduction	no
m14 HR			
NoFB	None	Hydro	no
Default	FIRE 2	Hydro	no
AGB	AGB winds only	Hydro	no
SNeIa	Type Ia SNe only	Hydro	no
Low Metal	FIRE 2	Hydro	no
m14 MR			
Default	FIRE 2	Hydro	no
All Micro	FIRE 2	MHD+Viscosity+Conduction	no
All+CR	FIRE 2	MHD+Viscosity+Conduction	yes

runs this does not appear only because that cold/warm gas turns into stars almost immediately (in ~ 1 local free-fall time); stellar FB slows the cold gas consumption time to $\sim 1-2$ Gyr.

The "All Micro" and "All+CR" runs are similar to our Default at lower masses, and produce modest effects at m14-mass, with conduction lowering cool inflow rates by a factor ~ 2, and CRs suppressing SF in cool gas (and building up additional cold gas) by a similar factor at early times. "AGB" and "SNeIa" (runs using *only* these stellar FB mechanisms) are similar to NoFB, indicating most of the FB comes from massive stars in these runaway-cooling simulations. Our "Low Metal" run suppresses the build-up of cold+warm gas by a factor $\sim 1.5-2$, owing to the lack of metal-line cooling from the hot gas.

5.3.2 Star formation rates

Fig. 5.3 shows SFRs and sSFRs (averaged in rolling 10 Myr bins): typical $\dot{M}_* \sim 2-5\,M_\odot\,\mathrm{yr}^{-1}$ in m12 and m13, and $\sim 20-40\,M_\odot\,\mathrm{yr}^{-1}$ in m14. In sSFR m12 & m14 have $\dot{M}_*/M_* \sim 10^{-10}\,\mathrm{yr}^{-1}$, m13 $\sim 3-5\times10^{-11}\,\mathrm{yr}^{-1}$: none of is "quenched." In fact, in m14, the SFRs and cooling flows are accelerating, indicating development of a stronger cooling flow with time. The "NoFB" runs have an early, rapid burst, where gas in the initial core undergoes runaway collapse and SF, until ~ 100 Myr when

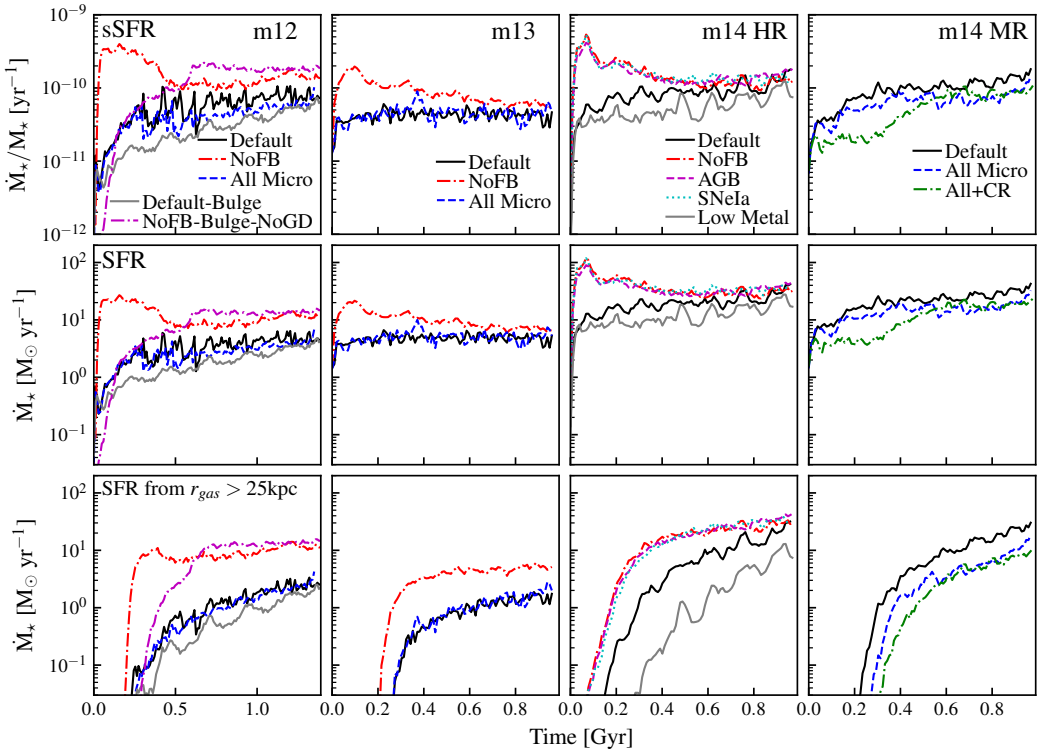

Figure 5.3: **Top row:** Specific star formation rate (sSFR) as a function of time. **Second row:** Star formation rate (SFR) as a function of time, averaged over 100 Myr. **Third row:** Star formation rates from gas initially at radii larger than 25 kpc (fueled by cooling flow). None of the galaxies are quenched. The 'NoFB' runs (similarly also the 'AGB' and 'SNe1a' runs) have an initial rapid star burst, where the initial core gas cools rapidly and forms stars. After $\sim$ 100 Myr, gas depletion in the core lowers the initial core SF, and then the subsequent SF tracks the cooling flow gas. The other runs ('Default', 'All Micro', 'All+CR') which initially form fewer stars, and preserve larger gas reservoirs as gas cools, but they all eventually have cooling-regulated SFRs resembling the SFR of the 'NoFB' runs. Suppressing metal-line cooling ('Low Metal' run) lowers the SFR by a factor of 2. With or without feedback, the saturated SFRs of the disc-dominant m12 runs ('Default' and 'NoFB') are very similar to the corresponding bulge-dominant runs ('Default-Bulge' and 'NoFB-Bulge-NoGD'), indicating that the morphology of the stellar distribution has little effect on star formation.

gas depletion in the core lowers the SFR and subsequent SF comes from gas initially at larger radii, tracking the cooling rate (again, the only-"AGB" and only-"SNeIa" runs resemble NoFB). The Default, "All Micro," and "All+CR" runs initially turn less gas into stars, but this leads to their preserving a larger gas reservoir as cooling continues, until eventually the SFRs are similar to "NoFB" (cooling-regulated). Again, effectively removing metal-line cooling in the "Low Metal" run reduces cooling and late SFRs by a factor ~ 2.

Note m13 & m14 are entirely bulge-dominated, but still feature high sSFRs. In m12 we explicitly test different initial stellar morphologies: the "Default-Bulge" (bulge-dominated) and "Default" (disk-dominated) runs give similar SFRs (with or without stellar FB). We also compare "NoFB-Bulge-NoGD," a run with no feedback and no *gas* disk initially, so the only SF can come from gas cooling from large radius. Even in this case, while the initial SFR is lower owing to the lack of initial gas supply, the SFR saturates to the same value as the "NoFB" (disk-dominated, with gas disk) run.

5.3.3 Cooling rimes & thermal stability

Fig. 5.4 shows the cooling time (τ_c) of gas hotter than 10^5 K as a function of radius averaged over the 80-90th Myr since the beginning of the simulations. Within $\sim$ (200, 40, 100) kpc in (m12,m13,m14) cooling times are short compared to the Hubble time (at large radii temperatures are higher, metallicities and densities lower, so τ_c rise rapidly). The ratio of cooling time to dynamical time (τ_c/τ_d) is also shown[10]. In m12, the halo is not fully in the "hot mode" given its relatively low virial temperature, so τ_c/τ_d is steady at ~ 10 at large radii (actually highest in the core, where τ_d becomes very short). Here m13 is the "most stable" case (consistent with its lower sSFR), with $\tau_c/\tau_d \sim 100$ from $\sim 5-100$ kpc. The higher density of halo gas in m14's core gives $\tau_c/\tau_d \sim 20$ within ~ 50 kpc. Note these all exhibit rapid cooling, despite $\tau_c/\tau_d \sim 20-100$ being the lowest values in m13 & m14, compared to the often-quoted critical value of ~ 10 in the literature (Sharma et al., 2012, Voit et al., 2017). This partly owes to the structure being much more strongly multi-phase here – the cooling gas has already cooled out of the thermally-unstable temperature range (to $T < 10^5$ K; not included in Fig. 5.4), which makes the cooling rate of the remaining gas here appear longer.

Differences between physics variations are consistent with the SFR and cool gas mass plots above. Note the "NoFB" runs actually feature the longest cooling times

[10] $\tau_c = E_{\rm thermal}/\dot{E}_{\rm cool}$, and $\tau_d = (r^3/GM_{\rm enc})^{1/2}$.

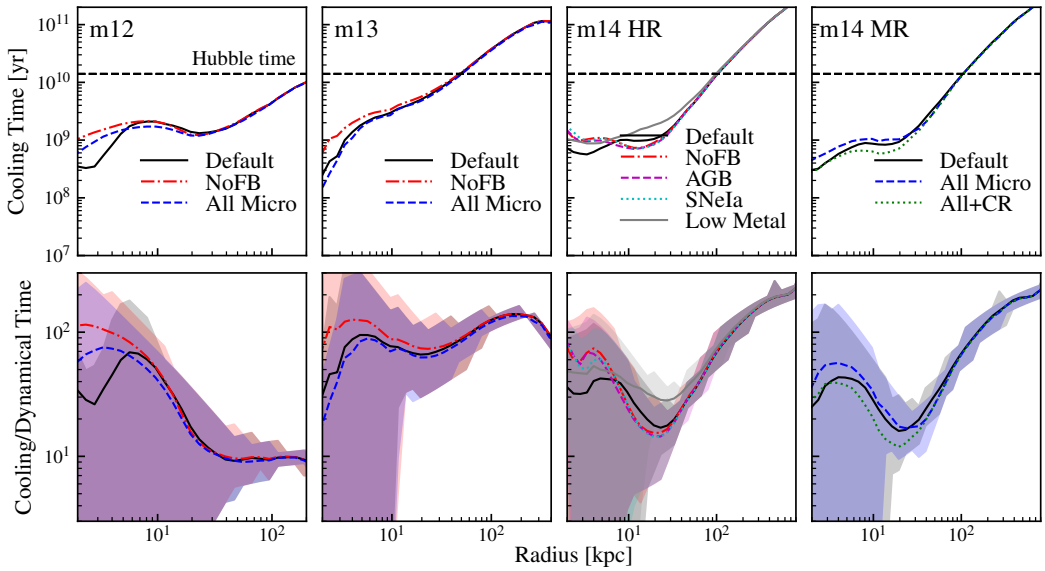

Figure 5.4: **Top row:** Cooling time of gas hotter than 10^5K, as a function of radius. Black dashed lines indicate the Hubble time. **Bottom row:** Ratio of cooling time to dynamical time, as a function of radius. The lines are mass-weighted averages and the shaded region covers 10-90% of the distribution. All the quantities are averaged over the 80-90th Myr since the beginning of the simulations. The 'Default' runs have lower τ_c/τ_d than the 'NoFB' runs within $\sim$ 10kpc since FB enriches the gas with metals. Both the 'AGB-only' and 'SNe1a-only' runs resemble the 'NoFB' run. Conduction and CR feedback do not have a significant effect. Suppressing metal-line cooling ('Low Metal' run) increases τ_c by a factor of 2.

in the center, as FB injects metals and dense gas into the hot phase, lowering its cooling time.

5.3.4 Cooling vs. energy input

Fig. 5.5 compares cooling rates (all cooling channels added) and energy input rates (adding photoionization, photoelectric, cosmic ray, and the energy input from SNe and winds) within < 30 kpc. Cooling always exceeds heating. As expected, energy input in our "Default" run exceeds "NoFB" owing to higher energy input from e.g., SNe, but "Default" also maintains an even higher cooling rate. "Low Metal" has a factor $\sim$ 2 lower cooling rate without metal-line cooling. Magnetic fields and viscosity produce negligible effects on their own. Conduction has weak effects here. We quantify the energy injection from each stellar feedback mechanism:[11]

[11]The plotted SNe energy input rate includes 10^{51}erg per event. The plotted stellar wind energy input rate is actually an upper bound, since a relative velocity between gas and stars is assumed to be 300 km s^{-1} for purposes of this post-processing estimate (it is calculated self-consistently in the

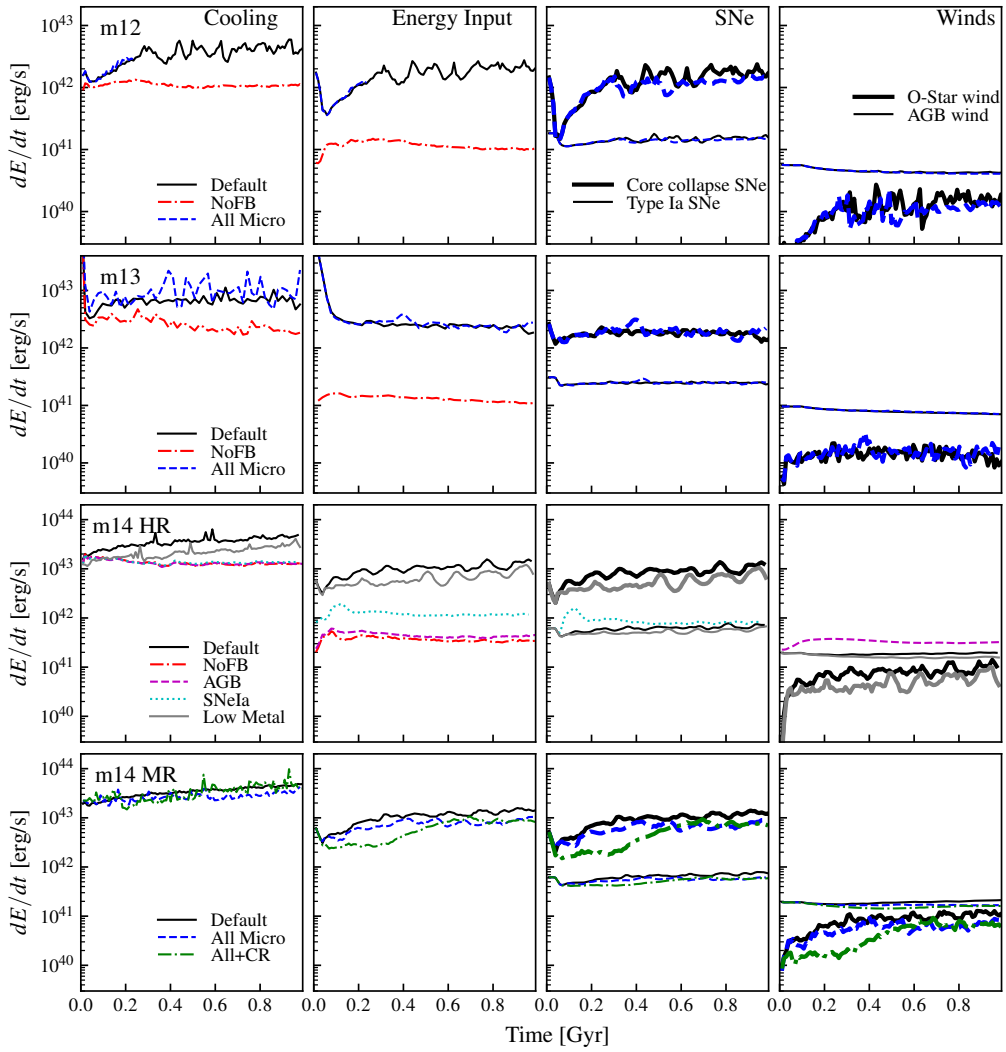

Figure 5.5: Energy input, cooling, and feedback, as a function of time in m12 (top row), m13 (2nd row), m14 HR (3rd row), and m14 MR (bottom row) runs. **Left column:** Total cooling rate within 30 kpc as a function of time. **Middle left column:** Energy input rate, including UV background, cosmic ray heating, dust collisional heating, photoelectric heating, and the energy input from SNe and winds, within 30 kpc. **Middle right column:** The energy input of core collapse SNe (thick lines) and Type Ia SNe (thin lines) colored by simulation . **Right column:** The energy input of O-star winds (thick lines) and AGB winds (thin lines), colored by simulation. The plotted energy input from SNe assumes 10^{51}erg per event, while winds energy input is calculated assuming the relative velocity between stars and gas is 300 km s^{-1} (upper bound). Cooling rates are always higher than heating rates. Core collapse SNe input energy at $\sim 1/3 - 1/4$ the cooling rate. Type 1a SNe input 20x lower energy (time-averaged) compared to core-collapse in these runs, and AGB winds produce 2-3x lower energy injection compared to Ia's. With suppressed metal-line cooling ("Low Metal"), the cooling rate is lowered by a factor of 2.

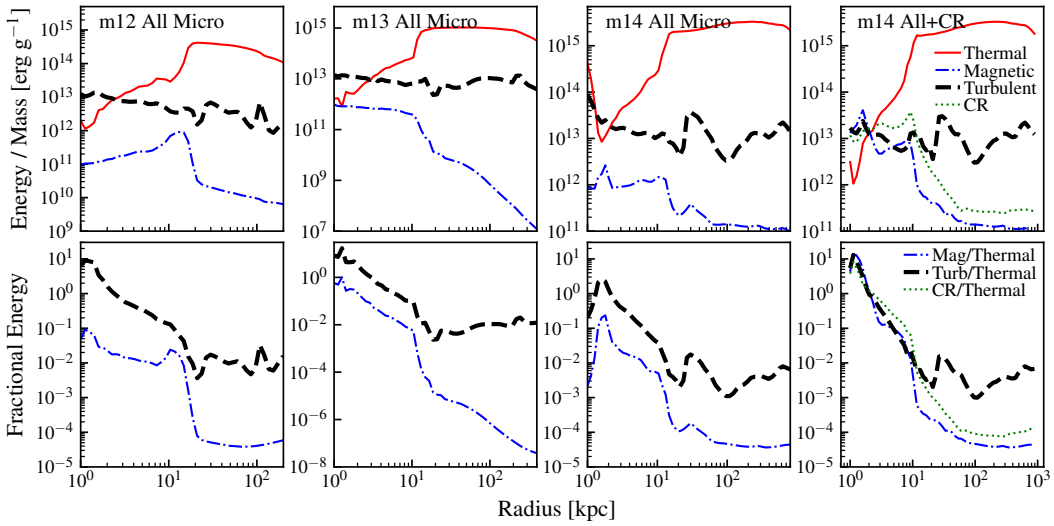

Figure 5.6: **Top row:** The comparisons of thermal, magnetic, CR and turbulent energy per unit mass, averaged over the 90-100th Myr. **Bottom row:** The comparison of the ratio of magnetic, CR, and turbulent energy to thermal energy. For $r \lesssim 3$ kpc, magnetic energy is subdominant to turbulent energy, except in the 'All+CR' run, where CR and magnetic energy reach equipartition with turbulent energy, showing that the turbulence is mostly super-Alfvénic and supersonic. At larger radius, $E_{\rm thermal} > E_{\rm turb} > E_{\rm CR} \gtrsim E_{\rm mag}$, so magnetic and CR energy have little effect on cooling flow.

SNe Ia, O/B or AGB winds, and CRs contribute relatively little to total heating, with core-collapse SNe present (given that our galaxies are not quenched and have high SFRs). However, even the core-collapse input is only $\sim 1/4 - 1/3$ of the cooling rate. SNe Ia input $\sim$ 20x lower energy compared to core-collapse, and AGB winds produce a factor $\sim 2 - 3$x lower energy injection rate compared to Ia's.

The total X-ray luminosity of each run (in Fig. 5.1) scales with the cooling rates, as expected. In m12, the low halo temperature means the X-ray luminosity is significantly influenced by SNe heating; in m13 & m14, the effects of stellar FB on the X-ray luminosity are small (most comes from the initial hot halo) (van de Voort et al., 2016).

5.3.5 Energetic balance

Fig. 5.6 compares the specific energy in thermal, magnetic, CR and turbulent forms averaged over 90-100th Myr.[12] Within a few kpc, turbulent energy dominates (the

code).

[12]Turbulent energies are measured using the method from Su et al. (2017) which attempts to separate turbulent motion from outflows and non-circular but bulk orbital motion.

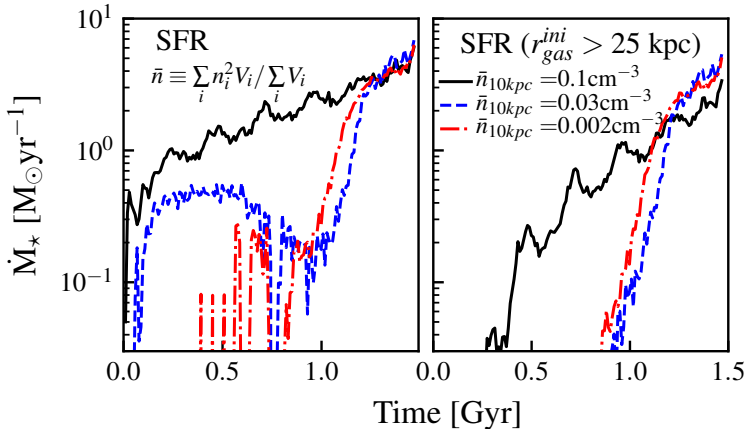

Figure 5.7: The star formation rate of m12 runs with different core gas density within 10 kpc. $\bar{n}$ is defined as $\sum_i n_i^2 V_i / \sum_i V_i$. The SFRs are significantly suppressed if the core gas density is low. However, in all the cases, the SFR eventually catches up as the gas supplied by cooling flows builds up.

turbulence is supersonic and super-Alfvénic), consistent with studies of the ISM inside galaxies (Su et al., 2017, 2018c). At larger radii, thermal energy dominates (by at least ~ 1 dex). Note at very large radii ($\gg 10$ kpc), the magnetic energies are simply dominated by the ICs, since the flow is approximately laminar so the classical global dynamo amplification time is many orbital times ($\gg$ Gyr). The same is true for the CR, as it does not have a chance to diffuse or stream to $\gg 10$ kpc within the simulation time.

5.4 Discussion: Why don't we quench?

Here we briefly discuss why none of the mechanisms in § 5.2.1 produces quenching, at any mass we survey.

5.4.1 Stellar feedback

Young/massive stars

Feedback from massive stars clearly reduces the rate at which gas *within the galaxy* turns into stars, self-regulating to a gas consumption time $\sim 1-2$ dex longer than a case without feedback (bringing it into agreement with the observed Schmidt-Kennicutt relation Kennicutt 1998, Schmidt 1959), and drives local outflows from the disk (e.g., Faucher-Giguère et al., 2013, Hayward & Hopkins, 2017, Orr et al., 2018). However, cooling from the hot halo onto the galaxy eventually builds up the core gas mass and the SFR runs away.

Stellar feedback fails to suppress cooling in massive haloes on long timescales for three reasons. **(1)** Even with the elevated (much higher-than-observed) runaway SFRs, the total energy input from SNe is $\sim 1/4 - 1/3$ of the cooling rate (Fig. 5.5). **(2)** The energy is injected locally in the galaxy core, either as slow-moving (sub-$V_{\rm esc}$) cool gas or fast-but-tenuous hot gas, so is rapidly decelerated and does not couple outside the cooling radius (e.g., we verify that outflows in m14 rarely reach past $\sim 20 - 30\,$kpc; see also Anglés-Alcázar et al. 2017b, Muratov et al. 2015 for more detail of the wind properties and the baryonic cycles in FIRE simulations). **(3)** As is commonly seen in galactic fountains (e.g., Fraternali et al., 2013, Silk, 2009, Silk, 2010, Silk, 2011), the outflows carry relatively dense, metal-rich gas into the halo, which *increases* the net cooling rate (Fig. 5.3 & Fig. 5.5) as it mixes with a larger mass of less-dense and lower-metallicity gas. The effect of metal enrichment on the cooling flows will be even clearer if the metal in the simulations were solely from the stellar feedback, instead of partially from the initial conditions. In fact, we do see a factor of 2 lower SFR and core baryonic mass in the run with negligible initial metallicity ('Low Metal' run).

Fig. 5.7 explicitly compares three variations of m12 that have initial central ($<$ 10 kpc) gas fractions $f_{\rm gas} = \bar{n}_{\rm gas}/n_{\rm star} \approx 0.05$, 0.01, 0.004 (mean central densities $\bar{n}/{\rm cm}^{-3} = 0.1$, 0.03, 0.002). If there is little or no initial gas inside $< 10\,$kpc, then (as expected) the initial SFR is suppressed strongly. More interestingly, we *also* see the SFR from gas with initial $r > 25\,$kpc is suppressed for $\approx 1\,$Gyr: this partially demonstrates how winds from SF in the disk (now absent) *enhance* cooling/inflow through enriching the halo gas. After $\approx 1\,$Gyr, however, cooling runs away and SF is dominated by the newly-cooled gas.

SNe Ia & AGB winds

Considering just Ia's or shock-heated AGB winds, we show in Fig. 5.5 that the feedback energy injection rate is even lower compared to cooling (by more than an order of magnitude), exacerbating problem **(1)** above, and problems **(2)** and **(3)** remain. The explosions decelerate rapidly, and mixing the highly metal-rich gas[13] promotes cooling.

[13] It is important to note that while AGB ejecta are much less metal-rich than pure Ia ejecta, it is still approximately solar (the mass-weighted mean stellar metallicity in massive galaxies) or somewhat more enriched in C and O (the primary coolants), and carries much larger mass, so it is less rapidly diluted. In fact, for a $\sim 10\,$Gyr old stellar population, the *total* metal return rate is *higher* by a factor of ~ 4 in AGB winds, compared to Ia SNe.

Some previous studies (see § 5.2.1) appeared to reach different conclusions. However, these were largely based on simple analytic energetics arguments, so could not follow the non-linear effects of **(2)** and **(3)** above. Moreover, even for **(1)**, although we find energy injection rates "per star" from SNe Ia and shocked AGB ejecta similar to these previous estimates, we find that clumping in the gas, mixing of winds, and cooling from larger radii enhances the central densities (and corresponding cooling rates) beyond the relatively low values assumed in those papers, rendering the heating insufficient.[14] Even if the initial gas density within 10 kpc is lowered to $0.002\,\mathrm{cm}^{-2}$ (as shown in Fig. 5.7) , the stellar feedback (mostly SNe Ia given the SFR ~ 0 within 1Gyr) can at most suppress the SFR for ~ 1 Gyr, after which the core gas density builds up and the cooling runs away.

We note that the supernovae implementation deal with the unresolved Sedov-Taylor phases following Hopkins et al. (2018a), which assumes negligible surrounding pressure (Cioffi et al., 1988). However, if a SN happens in CGM where the surrounding pressure is potentially high, it has to do extra pdV work as the blast wave expands, which lowers the coupling momentum. Therefore, assuming negligible surrounding pressure only means overestimating the effect from SNe, but, even so, the effect of SNe is still limited.

5.4.2 Magnetic fields, conduction, & viscosity

It is expected that magnetic fields alone cannot quench or suppress cooling flows: since they do not (directly) alter cooling, magnetic pressure would have to "hold up" the cooling gas in the halo, requiring un-physically strong fields (plasma $\beta \ll 1$, while $\beta \gg 1$ is observed and expected).[15] Moreover even in that case, in 3D all field orientations are Rayleigh-Taylor unstable (see e.g., Stone & Gardiner, 2007). And extensive previous work has shown the fields have a small effect on galaxy-scale SF (Su et al., 2017, and references therein). Viscosity has equally small effect: it is weak and, if anything, slows and mixes outflows, slightly enhancing cooling.

[14] Consider m12: Type Ia SNe and shocked AGB winds input energy at $\sim 1.5\times10^{41}\,\mathrm{erg\,s^{-1}}$ and $\sim 5\times10^{40}\,\mathrm{erg\,s^{-1}}$, respectively, roughly consistent with the value quoted in Conroy et al. (2015) for a similar-mass galaxy. However, in m12, the average effective gas density within $< 10\,\mathrm{kpc}$ can be ~ 1 dex higher than the $0.01\,\mathrm{cm}^{-3}$ assumed in Conroy et al. (2015). Note that clumping matters here: cooling rates scale $\propto n^2$, so the density that matters is $\bar{n} \equiv \langle n^2\rangle^{1/2}$, which is a factor of several higher in our runs than $\langle n\rangle$ inside $R_{\rm cool}$. Even assuming primordial gas (ignoring metal-cooling, **(3)** above), and ignoring whether heating can reach large radii **(2)**, the analytic scaling from Conroy et al. (2015) then predicts $\dot{e}_{\rm cool}/\dot{e}_{\rm heat} \sim 40\,(f_{\rm gas}/0.01)\,(\bar{n}/0.1\,\mathrm{cm}^{-3})$ within the galaxy.

[15] We confirm that we can, in principle, "quench" if we initialize enormously strong fields, but this requires magnetic field strengths exceeding self-gravity which simply "explode" the halo gas in a dynamical time.

Because of its strong temperature dependence (diffusivity $\propto T^{5/2}/\rho$), Spitzer-Braginskii conduction is expected to play a role only in the most massive haloes, and we confirm this. The diffusion time for bulk heat transport across a distance $\sim R$ is $\sim 0.3\,\mathrm{Gyr}\,(R/10\,\mathrm{kpc})^2\,(n/0.01\,\mathrm{cm^{-3}})\,(T/10^7\,\mathrm{K})^{-5/2}$ – only comparable to cooling times (inside the cooling radius $R_{\rm cool}$) in our most massive halo (m14). Moreover, in a turbulent medium, eddies mix with approximate diffusivity $\sim v_{\rm eddy}(\lambda_{\rm eddy})\,\lambda_{\rm eddy}$; if we assume transsonic, Kolmogorov turbulence then micro-physical conduction dominates over turbulent only at scales $\lesssim 50\,\mathrm{pc}\,(\lambda_{\rm driving}/10\,\mathrm{kpc})^{1/4}\,(T/10^6\,\mathrm{K})^{3/2}\,(n/0.01\,\mathrm{cm^{-3}})^{-3/4}$. This is only larger than our resolution (and correspondingly, microphysical conduction dominates over both turbulent and numerical conduction with $\kappa \sim c_s\,\Delta x$ only) if $T \gtrsim 10^7\,\mathrm{K}\,(m_g/10^4\,\mathrm{M_\odot})^{0.2}\,(n/0.01\,\mathrm{cm^{-3}})^{0.3}$. So except in the outer regions of our most massive halo, the dominant heat transport/mixing is not Braginskii conduction.

In m14, conduction is not negligible, but it only lowers the inflow rates and SFR from halo gas by a factor ~ 2. The effect is modest because **(1)** Lower temperatures and higher densities inside the core make conduction globally less efficient. **(2)** Once something (e.g., dense outflows, turbulence) triggers thermal instability, cool "clouds" radiate efficiently and develop sharp density contrasts with the ambient medium so the conduction becomes saturated and can only out-compete cooling in the very smallest clouds (McKee & Cowie, 1977) – in fact, recent work (Armillotta et al. 2017, Brüggen & Scannapieco 2016; Hopkins et al., 2018, in prep) has shown that conduction often actually *increases* cold cloud lifetimes via cloud compression suppressing surface-mixing instabilities, in this limit. **(3)** Magnetic fields modestly suppress perpendicular transport (quantified in Fig. 5.8, where in cores the conductivity is suppressed by a factor ~ 2, and in outskirts a factor $\sim 3-10$, levels (Voit 2011 and Wagh et al. 2014 argue will suppress many effects of conduction).

Conduction may still be important to unresolved small-scale thermal instabilities in hot haloes (as noted above), but we note first that at finite resolution our numerical diffusion dominates (so if anything we over-estimate true conductivities), and second, most of the discussion in the literature on this question has focused on the regime where there is some *global* heat source injecting energy sufficient to offset cooling losses (where conduction plays the role of *local* heat transport into unresolved clouds). When there is no heat input from feedback (or the heat input is less than the cooling rate, as in our default case here), then conduction does *not* significantly modify the consequences of the small-scale thermal instability (cold clouds "absorb" the conducted heat, condense and rain out efficiently; see Voit &

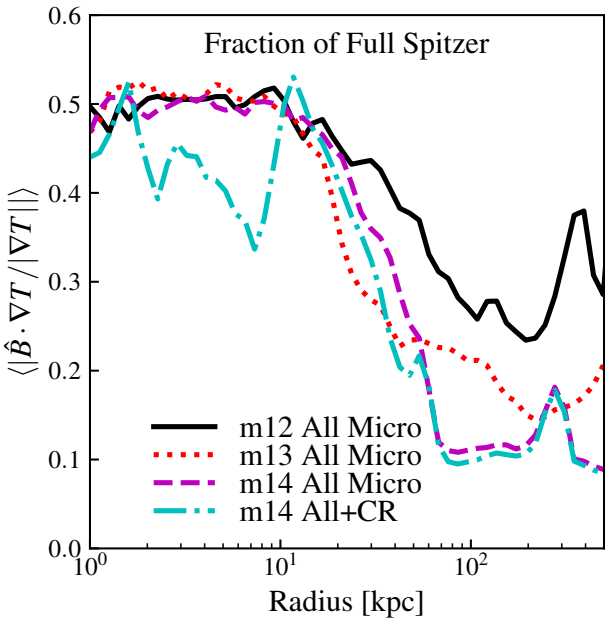

Figure 5.8: The effective fraction of Spitzer conductivity, as a function of radius, estimated as the mass weighted average of $|\hat{B}\cdot\nabla T/|\nabla T||$. This fraction drops as a function of radius. In the core region, the conductivity is effectively half of the full Spitzer value, while it drops to 0.1-0.3 of it at large radii.

Donahue 2015).

5.4.3 Cosmic rays from stars & LSS (not AGN)

CRs from SNe have limited effect here: **(1)** Direct heating (from e.g., streaming/hadronic interactions) cannot compete with cooling; the total CR energy injection rate is $\sim$ 10% of SNe, so order-of-magnitude less than cooling rates (Fig. 5.2, 5.5). **(2)** CR pressure is approximately in equipartition with magnetic energy (Fig. 5.6), so does not have a dramatic dynamical effect "holding up" the halo (though it can help accelerate some winds from massive stellar feedback at the disk). **(3)** Like other feedback from massive stars, CRs do help suppress the collapse/SFR from cold gas locally (see Fig. 5.3, 'All+CR' m14), but this leads to a pile-up of that gas (Fig. 5.2) from large-scale cooling, which runs away. **(4)** It requires some fine-tuning to make CRs do all their "work" around cooling-flow radii, rather than diffusing out.[16]

[16]While not shown here, we have experimented with e.g., variations in the CR diffusivity. If it is much lower ($\kappa_{\rm cr} \lesssim 10^{28}\,{\rm cm^2\,s^{-1}}$), CRs are trapped in the inner regions ($<10\,$kpc) and suppress SF from cold gas in the short-term more efficiently. But precisely because of this trapping and build-up of cold gas the CR energy is then mostly lost to catastrophic hadronic interactions, so the CRs

Although we do not directly model it, CRs from structure formation will have all these limitations as well. We find, for example, that we can "quench" via initializing an enormous CR density, but only if this is so large it overcomes gravity and blows out most of the halo gas. But this (a) does not resemble observed haloes, and (b) is not possible from structure formation, since (by definition) only a fraction of the gravitational energy (in e.g., shocks) goes into CRs.

5.4.4 Morphological quenching

Although galaxy colors and morphologies are correlated, that does not mean morphology *causes* quenching; we find that changing the stellar morphology of the galaxies here has very weak effects on their cooling/SF properties. **(1)** Changing the morphology of stars has no direct effect on cooling rates, so even if it somehow quenched SF within the galaxy, cool gas would still pile up. For m14, this would give $> 3\times10^{11}\,M_\odot$ of molecular gas by the end of our simulation (Fig. 5.2), orders-of-magnitude higher than usually observed (e.g., Popping et al., 2015, Salomé et al., 2006) (reference added). **(2)** Moreover, if gas is self-shielding (i.e. reaches surface densities $\gtrsim 10\,M_\odot\,pc^{-2}$, requiring just $\sim 3\times10^9\,M_\odot$ of gas within $< 10\,kpc$, vastly less than that produced by the cooling flow), then it can cool to $T \ll 10^4$K, at which point Toomre $Q \ll 1$ will *always* be true in the cold gas for *any* mass distribution with a physically-plausible rotational velocity. Indeed, the few known BCGs with large gas reservoirs $> 10^{10}\,M_\odot$, as predicted by our simulations here, all have observed SFRS $\sim 10-100\,M_\odot\,yr^{-1}$, like our m14, and obviously not quenched (see O'Dea et al. 2008). **(3)** The effect of the stellar morphology on Q is quite weak: somehow converting the *entire* MW stellar disk *and* all DM within $< 10\,kpc$ to a compact bulge or point mass would only increase the Q at the solar circle by $\sim 50\%$ (see e.g., Romeo & Wiegert, 2011). In fact the stronger, but still weak, effect of changing an initial stellar disk to a bulge in Fig. 5.3 comes from slightly reducing the impact of stellar feedback on the inner halo (by making the stars older and less extended, so they have weaker feedback that reaches less far into the halo). **(4)** All our m13 and m14 runs, and, of course, observed massive galaxies, are completely bulge-dominated, yet still feature a "cooling flow problem."

---

have weaker long-term effects. For much higher diffusivity ($\kappa_{cr} \gtrsim 10^{30}\,cm^2\,s^{-1}$), CRs free-stream completely out of the haloes with negligible interaction with gas.

5.5 Conclusions

In this paper we used high-resolution, idealized, isolated galaxy simulations including detailed physical treatments of star formation, stellar feedback, and ISM/CGM/ICM microphysics (cooling, magnetic fields, conduction, cosmic rays, etc.) to explore and quantify the quenching and cooling flow problems – *in the absence of AGN feedback* – across a range of halo masses from $\sim 10^{12}$ – $10^{14}\,M_{\odot}$. We started the simulations from the initial conditions resembling the observed cool-core clusters at low redshift and tested whether any of them could maintain a stably quenched galaxy consistent with the observations. We specifically explored several "non-AGN" quenching or cooling-flow "solution" mechanisms, which have been previously proposed in the literature (e.g., feedback from old stellar populations in Type Ia SNe or shocked AGB ejecta, heat transport from the outer halo via conduction, cosmic rays from Ia's or structure formation, or "morphological quenching"). None of these mechanisms resolve the fundamental problem of overcooling and excessive star formation in massive galaxies, at any mass scale, that we simulate. The main effects of these physics are as follow:

- Stellar feedback alters the balance of cold/warm gas and suppresses SFRs *for a given cold gas mass* (i.e. controls the location of galaxies on the Kennicutt-Schmidt relation). However, it has only weak effects on cooling from the outer halo, and in fact tends to *enhance* cooling in the inner halo, as denser, more metal-rich ejecta mix and promote cooling in halo gas. This applies to all stellar feedback mechanisms (Ia's, AGB ejecta, feedback from young stars where present).

- Magnetic fields and Braginskii viscosity have minor effects on the global cooling and inflow rates.

- Conduction is, as expected, only important to bulk cooling/inflow in the most massive haloes ($\geq 10^{14}\,M_{\odot}$). Even there, the effects are modest, reducing inflow rates by a factor ~ 2, owing to a combination of saturation effects, suppression by magnetic fields, and inefficient conduction in the cores once runaway cooling begins.

- Cosmic rays from SNe (and shocked stellar winds) alone can, like other stellar feedback mechanisms, modestly reduce the SFR in cool gas already in/near the central galaxy, but their bulk energetics are insufficient to suppress cooling flows. We expect the same for CRs from structure formation.

- Stellar morphology has essentially no effect on cooling rates and only weakly alters star formation either in pre-existing gas disks or in gas disks formed via runaway cooling. Making our galaxies entirely bulge-dominated does not make them quenched.

Precisely because the effects of the above physics are weak, our summary of the quenching "maintenance" and/or "cooling flow" problems is consistent with many previous studies that treated some of the physics above in a more simplified manner:

- At all halo masses $\gtrsim 10^{12}\,M_\odot$, we find efficient cooling of halo gas in cores, with cooling luminosities similar to observations (where available), but excessive cooling/cold gas masses and SFRs in central galaxies (from $\sim 5\,M_\odot\,yr^{-1}$ in $\sim 10^{12-13}\,M_\odot$ haloes, to $\sim 50\,M_\odot\,yr^{-1}$ by $\sim 10^{14}\,M_\odot$).
- The excess gas comes, in an immediate sense, from an overcooling core where higher densities and metallicities (enhanced by earlier generations of recycled galactic winds) produce rapid cooling and multi-phase CGM structure. Although the "median" cooling times in this core can be large compared to dynamical times ($t_{\rm cool}/t_{\rm dyn} \sim 100$), the fastest-cooling (denser, more metal-rich) material reaches $t_{\rm cool}/t_{\rm dyn} \ll 10-30$ – this is what rapidly forms stars.
- The core providing immediate fuel for SF can have a relatively small extent $\lesssim 30\,$kpc, but gas within this radius at later times originates from larger radii (up to $\sim 100\,$kpc) and migrates slowly inwards before "runaway," so it may be possible to "starve" the cooling flow on longer timescales by suppressing just cooling/inflow from $\sim 30-100\,$kpc.
- It is possible, in principle, to *temporarily* quench galaxies in this mass range if one can remove all their dense gas within $\lesssim 10\,$kpc. This will suppress star formation for $\approx 1\,$Gyr (surprisingly independent of halo mass), before runaway cooling from the extended halo restores the excessive SFRs.

Our simulations have several limitations upon which future work could improve. We wished to construct idealized, controlled experiments so did not evolve fully-cosmological simulations – we do not expect this to alter the fundamental conclusions above, but it could introduce additional important effects (e.g., stirring turbulence in haloes via structure formation). We of course have finite resolution,

so micro-physical phase structure in the CGM remains unresolved and could alter the effective large-scale cooling rates. Our treatment of some physics (SNe, cosmic rays) is necessarily approximate ("sub-grid") but it would require truly dramatic qualitative changes to our assumptions reverse our conclusions. We also did not include rare events like hypernovae. However, as we have shown in Su et al. (2018d), their net effects resemble overlapped supernovae, which readily happen in simulations due to the clustered star formation.

Due to computational expense we could only run ~ 20 high-resolution simulations, which means we could not explore the potential diversity of properties of different haloes at the same mass. We also did not explore various initial cosmic ray and magnetic field configurations. For the cosmic rays, We refer the readers to Su et al. (2018b), in which we explored how the cooling flows are affected by the cosmic ray profiles caused by various CR injection rates. The magnetic fields at the core region, are quickly amplified to the saturation values, independent of the seed values. The initial magnetic field strength and configuration at a larger radius could depend more on the seed magnetic fields, but we still do not expect them to alter any of our conclusions.[17]

Most obviously, we neglect AGN feedback, in various forms (jets, bubbles, winds, radiation, etc.). This work furthers the argument that something – perhaps AGN – beyond the "known" physics we include here, must be at work. We emphasize that many or all of the physics explored here (e.g., magnetic fields, cosmic rays, etc.) may indeed play a critical role in AGN feedback, even if they do not dramatically alter cooling flows *absent* an AGN. In future work, we will explore generic classes of AGN feedback models proposed in the literature, in simulations incorporating the additional physics here which must (in reality) be present as well, in order to better understand the non-linear interactions of different feedback and ISM/CGM/ICM physics.

[17] We have an m12 run accidental started with magnetic fields two orders of magnetic higher. With a much higher value, the star formation becomes bursty but is still not quenched.

Chapter 6

COSMIC RAYS OR TURBULENCE CAN SUPPRESS COOLING FLOWS (WHERE THERMAL HEATING OR MOMENTUM INJECTION FAIL)

Kung-Yi Su, Philip F. Hopkins, Christopher C. Hayward, Claude-André Faucher-Giguère, Dušan Kereš, Xiangcheng Ma, Matthew E. Orr, T. K. Chan, and Victor H. Robles. Cosmic Rays or Turbulence can Suppress Cooling Flows (Where Thermal Heating or Momentum Injection Fail). *arXiv e-prints*, art. arXiv:1812.03997, December 2018.

The quenching "maintenance" and "cooling flow" problems are important from the Milky Way through massive cluster elliptical galaxies. Previous work has shown that some source of energy beyond that from stars and pure magnetohydrodynamic processes is required, perhaps from AGN, but even the qualitative form of this energetic input remains uncertain. Different scenarios include thermal "heating," direct wind or momentum injection, cosmic ray heating or pressure support, or turbulent "stirring" of the intra-cluster medium (ICM). We investigate these in 10^{12} – 10^{14} $M_\odot$ haloes using high-resolution non-cosmological simulations with the FIRE-2 (Feedback In Realistic Environments) stellar feedback model, including simplified toy energy-injection models, where we arbitrarily vary the strength, injection scale, and physical form of the energy. We explore which scenarios can quench without violating observational constraints on energetics or ICM gas. We show that turbulent stirring in the central $\sim$ 100 kpc, or cosmic-ray injection, can both maintain a stable low-SFR halo for >Gyr timescales with modest energy input, by providing a non-thermal pressure which stably lowers the core density and cooling rates. In both cases, associated thermal-heating processes are negligible. Turbulent stirring preserves cool-core features while mixing condensed core gas into the hotter halo and is by far the most energy efficient model. Pure thermal heating or nuclear isotropic momentum injection require vastly larger energy, are less efficient in lower-mass haloes, easily over-heat cores, and require fine-tuning to avoid driving unphysical temperature gradients or gas expulsion from the halo center.

6.1 Introduction

How to "quench" the *massive* galaxies and keep them "red and dead" over a large fraction of cosmic time, at stellar masses $\gtrsim 10^{11}\,M_\odot$ (above $\sim L_*$ in the galaxy luminosity function), has been a major outstanding problem in galaxy formation for decades (see e.g., Baldry et al., 2004, Bell et al., 2003, Blanton et al., 2005, Dekel & Birnboim, 2006, Kauffmann et al., 2003, Kereš et al., 2005, 2009, Madgwick et al., 2003, Pozzetti et al., 2010, Wetzel et al., 2012). The major difficulty lies in the classic "cooling flow" problem — X-ray observations have found significant radiative cooling in the hot gas of elliptical galaxies and clusters, indicating cooling times shorter than a Hubble time (Fabian et al., 1994, Peterson & Fabian, 2006). However, comparing the inferred cooling flow (reaching up to $\sim 1000\,M_\odot \mathrm{yr}^{-1}$ in clusters), neither sufficient cold gas from HI and CO observations (McDonald et al., 2011, Werner et al., 2013) nor sufficient star formation (O'Dea et al., 2008, Rafferty et al., 2008, Tamura et al., 2001) have been found in galaxies. Simulations and semi-analytic models, which do not suppress cooling flow and simply allow gas to cool into the galactic core, typically predict over an order of magnitude higher star formation rates (SFRs) than observed (for recent examples, see e.g., the weak/no feedback runs in Booth & Schaye, 2009, Choi et al., 2015, Li et al., 2015, Sijacki et al., 2007).

To compensate for the observed cooling, there must be some sort of heat source or pressure support. Moreover, the heat must still preserve the cool core structure in the majority of galaxies according to the observations (Mittal et al., 2009, Peres et al., 1998). One way to achieve this is to suppress the cooling flow and maintain a very-low-SFR stable cool-core (CC) cluster. Another possibility is that clusters undergo cool-core – non-cool-core (NCC) cycles: a stronger episode of feedback overturns the cooling flows, resulting in a non-cool-core cluster, which gradually recovers to a cool-core cluster and start another episode of feedback.

The various non-AGN solutions to the cooling flow problem proposed in the literature generally belong to the former case, as they are mostly steady heating mechanisms. These generally invoke physics that are un-ambiguously present, but play an uncertain role in quenching and/or the cooling flow problem, including: stellar feedback from shock-heated AGB winds (Conroy et al., 2015), Type Ia supernovae (SNe) (e.g., Sharma et al., 2012, and references therein), or SNe-injected cosmic rays (CRs) (Butsky & Quinn, 2018, Farber et al., 2018, Jacob et al., 2018, Pfrommer et al., 2017a, Ruszkowski et al., 2017a); magnetic fields (Beck et al., 1996, 2012,

Soker & Sarazin, 1990) and thermal conduction (Binney & Cowie, 1981, Fabian et al., 2002, Tucker & Rosner, 1983, Voigt et al., 2002, Zakamska & Narayan, 2003) in the circum-galactic medium (CGM) or intra-cluster medium (ICM); or "morphological quenching" via altering the galaxy morphology and gravitational stability properties (Dekel et al., 2009, Martig et al., 2009). Although these processes can slightly suppress the star formation, and "help" suppress the cooling flows, most previous studies, including our own exhaustive survey studying each of these in simulations similar to those presented here (Su et al., 2018a, hereafter Paper I), have shown that they do not fundamentally alter the classic cooling flow picture. In the end, the star formation is still cooling flow regulated, and the star formation rate is orders of magnitude too high.

Consequently, AGN feedback seem to be the most promising possible solution to the cooling flow problem, and there has been a tremendous amount of theoretical work on the topic (for recent studies see Eisenreich et al. 2017, Gaspari & Sądowski 2017, Jacob & Pfrommer 2017a,b, Li et al. 2017, 2018, Martizzi et al. 2018, Pellegrini et al. 2018, Weinberger et al. 2018, Yoon et al. 2018; and see e.g., Choi et al. 2012, Ciotti & Ostriker 2001, Ciotti et al. 2009, Croton et al. 2006, Fabian 1999, Guo & Oh 2008, Hopkins et al. 2005, 2006a, McNamara & Nulsen 2007, Ostriker et al. 2010, Pfrommer 2013, Silk & Rees 1998, Wiener et al. 2013 for earlier works). Observations show that the available energy budget can easily be comparable to the cooling rate, and un-ambiguous cases of AGN expelling gas from galaxies, injecting thermal energy via shocks or sound waves or photoionization and Compton heating, "stirring" the CGM and ICM, and creating "bubbles" of hot plasma with non-negligible relativistic components, are ubiquitous (see e.g., Hickox & Alexander, 2018, for a detailed review).

However, despite its plausibility and the extensive work above, the detailed physics of AGN feedback remains uncertain, as do the relevant "input parameters." Unlike stellar feedback, where we have strong theoretical and observational constraints on supernovae event rates, energy inputs, metal yields, etc., AGN properties like energetics, kinetic luminosities, duty cycles, geometries, and their dependence on the black hole mass and accretion are much less well-constrained. Besides, even with the same energy input rate, how and where the energy is coupled to the CGM and ICM remain highly uncertain.

Therefore, instead of jumping into a specific (potentially more realistic) AGN feedback model, in this study we "take a step back" and explore various idealized AGN

"toy models" with energy injection in different forms (e.g., direct isotropic momentum injection, turbulent stirring, thermal heating, cosmic-ray injection), acting on different spatial scales, and with different energetics. Our goal is to answer the following simple questions: **(a)** What form[s] of energy input (if any) can possibly quench a cooling flow, *without* generating un-realistic galaxy or halo properties in obvious disagreement with observations? For example, one could easily imagine scenarios which "quench" galaxies by simply expelling all the gas in the halo – but this would violate the wealth of observations indicating massive haloes retain most of the cosmological baryon fraction (e.g., Giodini et al., 2009, Gonzalez et al., 2013, Sanderson et al., 2013) (let alone more detailed constraints on density/temperature/entropy profiles). **(b)** If any form of energy injection is viable, over what (order-of-magnitude) spatial scales must it act? In other words, if the energy is primarily deposited around the galactic nucleus, does this yield behavior that is "too explosive"? Does the injection have to be fine-tuned to occur where the cooling is occurring? **(c)** Likewise, what are the required energetics, and are they reasonable compared to observational constraints and plausible accretion efficiencies of supermassive black holes in these systems? **(d)** If a model quenches, what is the actual mechanism? For example, turbulent stirring could suppress cooling flows via heating through thermalized kinetic energy (viscous or shock-heating), or through providing non-thermal pressure which "holds up" the halo despite its cooling, or through bulk mixing of cold and hot gas. **(e)** Does the model quench by maintaining a low-SFR stable cool-core cluster or turning it into a non-cool-core cluster? If it is the latter case, how long (if ever) does it take to recover a cool-core after the injection is turned off?

All of these questions have been studied to varying extent in the literature already (see references above). And we will argue below that our conclusions are largely consistent with this previous work. But this manuscript expands on these previous studies in at least three important ways. **(a)** We attempt a broader and more comprehensive survey, across a variety of energy injection mechanisms, scales, and energetics, in different halo masses, using an otherwise identical set of physics and numerics, to enable fair comparisons. **(b)** We aim to implement all of these in fully "live," global simulations that self-consistently (and simultaneously) treat the entire halo and star-forming galactic disk. For such global simulations, our survey also reaches higher resolution compared to most previous work, allowing us to resolve more detailed sub-structure in the CGM and galactic disk. **(c)** We include explicit, detailed treatments of radiative cooling, the multi-phase ISM and CGM, star for-

mation, and stellar feedback following the FIRE[1] simulations (Hopkins et al., 2014, 2018b, Muratov et al., 2015), in order to more robustly model both the gas dynamics and the response of galactic star formation rates to cooling flows.

In § 6.2 we summarize the AGN toy models considered here, and describe our numerical simulations. Results are presented in § 6.3. We then discuss the effects of each of these model in turn, in § 6.5.

6.2 Methodology

Our simulations use GIZMO (Hopkins, 2015), [2] in its meshless finite mass (MFM) mode, which is a Lagrangian mesh-free Godunov method, capturing advantages of grid-based and smoothed-particle hydrodynamics (SPH) methods. Numerical implementation details and extensive tests are presented in Hopkins (2015).

Our default simulation uses the FIRE-2 implementation of the Feedback In Realistic Environments (FIRE) physical treatments of the ISM and stellar feedback, the details of which are given in Hopkins et al. (2018a,b) along with extensive numerical tests. Cooling is followed from $10 - 10^{10}$K, including the effects of photoelectric and photoionization heating, collisional, Compton, fine structure, recombination, atomic, and molecular cooling. Star formation is treated via a sink particle method, allowed only in molecular, self-shielding, locally self-gravitating (Hopkins et al., 2013b) gas, above a density $n > 100\,\mathrm{cm}^{-3}$. Star particles, once formed, are treated as a single stellar population with metallicity inherited from their parent gas particle at formation. All feedback rates (SNe and mass-loss rates, spectra, etc.) and strengths are IMF-averaged values calculated from STARBURST99 (Leitherer et al., 1999) with a Kroupa (2002) IMF. The feedback model includes: (1) Radiative feedback including photoionization and photoelectric heating, as well as single and multiple-scattering radiation pressure tracked in five bands (ionizing, FUV, NUV, optical-NIR, IR). (2) Stellar particles continuously lose mass and inject mass, metals, energy, and momentum in the form of OB and AGB winds. (3) Type II and Ia SNe (including both prompt and delayed populations) happen stochastically according to the tabulated rate. Once they occur, the stellar particles lose mass and inject the appropriate mass, metal, momentum and energy to the surrounding gas.

[1] FIRE project website: *http://fire.northwestern.edu*

[2] A public version of this code is available at *http://www.tapir.caltech.edu/~phopkins/Site/GIZMO.html*.

6.2.1 Initial conditions

The initial conditions studied here are presented and described in detail in Paper I. Their properties are summarized in Table 6.1. In this paper, the bulk of our study will initially focus on the **m14** halo, which has the most dramatic (massive) cooling flow (we will then consider the other haloes in turn). The dark matter (DM) halo, bulge, black hole, and gas+stellar disk are initialized following Springel (2000), Springel & White (1999). We assume a spherical, isotropic, Navarro et al. (1996) profile DM halo; a Hernquist (1990) profile stellar bulge; an exponential, rotation-supported disk of gas and stars (10^{10} and $2\times10^{10} M_{\odot}$) initialized with Toomre $Q \approx 1$; a BH with mass $1/300$ of the bulge mass (e.g., Häring & Rix, 2004); and an extended spherical, hydrostatic gas halo with a β-profile ($\beta = 1/2$) and rotation at twice the net DM spin (so $\sim 10-15\%$ of the support against gravity comes from rotation, the rest thermal pressure resulting from the virial shock). The initial metallicity drops from solar ($Z = 0.02$) to $Z = 0.001$ with radius as $Z = 0.02\,(0.05 + 0.95/(1 + (r/20\,\mathrm{kpc})^{1.5}))$. For the runs with CR injection, initial magnetic fields are azimuthal with $|\mathbf{B}| = 0.3\,\mu\mathrm{G}/(1 + (r/20\,\mathrm{kpc})^{0.375})$ (extending throughout the ICM), and initial CR energy density is in equipartition with the local initial magnetic energy density. The ICs are run adiabatically (no cooling or star formation) to relax any initial transients before use.

The ICs are designed to be similar to observed cool-core systems of similar mass wherever possible (see e.g., Humphrey & Buote, 2013, Humphrey et al., 2012a, Su et al., 2013, 2015). Our **m14** halo has initial cooling rate at $\sim 8\times10^{43}\mathrm{erg\,s^{-1}}$, with $\sim 3\times10^{43}\mathrm{erg\,s^{-1}}$ radiated in X-ray (0.5-7 kev).

In **m12** and **m13** the mass resolution is constant; in **m14** (given its much larger total mass but the need to ensure fixed physical mass resolution in e.g., the star-forming disk) the resolution here matches run "MR-MRS" in Paper I, adopting a radially-dependent super-Lagrangian refinement scheme. The target gas mass resolution is set to $= 3\times10^{4}\,\mathrm{M_{\odot}}$ inside $r < 10\,\mathrm{kpc}$, and increases smoothly $\propto r$ outside outside this radius up to a maximum $= 2\times10^{6}\,\mathrm{M_{\odot}}$ at $\sim 300\,\mathrm{kpc}$. Gas resolution elements are automatically merged or split appropriately if they move inward/outward, to maintain this mass resolution (to within a factor = 2 tolerance) at all times. A resolution study is included in the appendix of Paper I.

Table 6.1: Properties of Initial Conditions for the Simulations/haloes Studied Here

	Resolution		DM halo				Stellar Bulge		Stellar Disc		Gas Disc		Gas Halo	
Model	ϵ_g (pc)	m_g ($M_\odot$)	$M_{\rm halo}$ ($M_\odot$)	r_{dh} (kpc)	$V_{\rm Max}$ (km/s)	$M_{\rm bar}$ ($M_\odot$)	M_b ($M_\odot$)	a (kpc)	M_d ($M_\odot$)	r_d (kpc)	M_{gd} ($M_\odot$)	r_{gd} (kpc)	M_{gh} ($M_\odot$)	r_{gh} (kpc)
m12	1	8e3	1.5e12	25	174	2.2e11	1.5e10	1.0	5.0e10	3.0	5.0e9	6.0	1.5e11	25
m13	3	5e4	1.0e13	100	240	7.2e11	1.0e11	2.8	1.4e10	2.8	5.0e9	2.8	6.0e11	10
m14	**1**	**3e4**	**8.5e13**	**220**	**600**	**1.5e13**	**2.0e11**	**3.9**	**2.0e10**	**3.9**	**1e10**	**3.9**	**1.5e13**	**22**

Parameters of the galaxy models studied here (§ 6.2.1): (1) Model name. The number following 'm' labels the approximate logarithmic halo mass. (2) ϵ_g: Minimum gravitational force softening for gas (the softening for gas in all simulations is adaptive, and matched to the hydrodynamic resolution; here, we quote the minimum Plummer equivalent softening). (3) m_g: Gas mass (resolution element). There is a resolution gradient for m14, so its m_g is the mass of the highest resolution elements. (4) $M_{\rm halo}$: Halo mass. (5) r_{dh}: NFW halo scale radius (the corresponding concentration of m12,m13,m14 is $c = 12,\ 6,\ 5.5$). (6) $V_{\rm max}$: Halo maximum circular velocity. (7) $M_{\rm bar}$: Total baryonic mass. (8) M_b: Bulge mass. (9) a: Bulge Hernquist-profile scale-length. (10) M_d : Stellar disc mass. (11) r_d : Stellar disc exponential scale-length. (12) M_{gd}: Gas disc mass. (13) r_{gd}: Gas disc exponential scale-length. (14) M_{gh}: Hydrostatic gas halo mass. (15) r_{gh}: Hydrostatic gas halo $\beta = 1/2$ profile scale-length.

6.2.2 Energy injection models surveyed

The toy models we investigate include momentum injection (simulations prefixed "Momm"), turbulent stirring ("Turb"), thermal input ("Th") and CR input ("CR"). All the simulations are listed in Table 6.2, which also tabulate the energy and momentum input within different ranges. The 'Default' run includes only 'FIRE-2' stellar feedback. The other runs have various AGN toy models implemented on top of 'FIRE-2' stellar feedback. Only the runs with cosmic ray injection have magnetic fields. The runs labeled as "BH" have energy (momentum) injected in the black hole neighborhood, while the "core" runs have a wider-distributed injection with the kernel functions listed in the last column of Table 6.2. The other runs labeled "uni" have uniform input per unit gas mass (so most of the energy is deposited at large radii). The detailed radial dependence of the energy and momentum input is shown in Fig. 6.1. The simulation duration is also listed in Table 6.2. All runs are run to 2 Gyr, unless either the halo is completely "blown out" or completely un-affected.

Although we will treat the energy/momentum injection rates as essentially arbitrary in our survey, for context it is worth noting that for a $\sim 10^9\ M_\odot$ BH (about as massive as we expect in our **m14** halo) the Eddington limit is $\sim 10^{47}\ {\rm erg\ s^{-1}}$. The associated

photon momentum flux is $L/c \sim 4\times10^{36}$ g cm s^{-2}. For more typical low-luminosity AGN observed in massive galaxies, the energies associated with e.g., their jets reach $\sim 10^{44} - 10^{45}$erg s^{-1} (see Fabian 2012).

Thermal input ("pure heating")

Any process that ultimately transfers some energy to gas thermal energy can be said to have a "heating" component. This can occur via radiative (photoionization, Compton), mechanical (shocked winds/jets, compression), viscous (damped sound waves or turbulence), cosmic ray (collisions, streaming instabilities), and other processes. Many models in the literature have invoked the idea that heating from AGN can effectively offset cooling and drive strong pressure-driven outflows, if roughly a few percent of the luminosity associated with near-Eddington phases can couple thermally (Barai et al., 2014, Begelman, 2004, Di Matteo et al., 2005, Dubois et al., 2013, Faucher-Giguère & Quataert, 2012, Hopkins & Elvis, 2010, Hopkins et al., 2006a,b, 2007, 2008, Johansson et al., 2009, Ostriker et al., 2010, Pillepich et al., 2018, Richings & Faucher-Giguère, 2018a,b, Springel et al., 2005, Weinberger et al., 2017).

To mimic this in an intentionally idealized and simplified manner, we directly add (to the usual self-consistent heating and cooling routines) an analytic heating rate per unit mass $\dot{e}_{\rm inj}(r) = \dot{E}_{\rm tot}\,M_0^{-1}\,f(r)$, where $f(r)$ is a dimensionless spherically-symmetric kernel function (centered on the BH at the galaxy center) normalized to $M_0^{-1}\int \rho(\mathbf{x})\,f(|\mathbf{x}|)\,d^3\mathbf{x} = 1$. We vary both $\dot{E}_{\rm tot}$ and $f(r)$ systematically, as shown in Table 6.2. In runs labeled "BH," $f(r)$ is a cubic spline with radius of compact support enclosing the nearest ~ 96 gas elements to the BH. In runs labeled "core," $f(r)$ is a Gaussian ($\propto \exp\,[-(r/r_0)^2]$) with dispersion approximately equal to the β-profile scale-length (which is also approximately the critical cooling radius). And in runs labeled "uni," $f(r)$ is constant out to approximately the virial radius. In the "BH" cases, $f(r)$ is updated at each time step, while in the "core" and "uni" cases, $f(r)$ is set at the beginning of the runs, and kept constant.[3]

Momentum input

Again many processes can transfer momentum/kinetic energy to gas, including radiation pressure, mechanical feedback from AGN winds and jets, and "PdV"

[3] This causes the evolution of energy input, especially in the more explosive runs, since the density profiles also evolve.

work from cosmic ray pressure gradients. Again many models have invoked kinetic feedback to suppress cooling flows and SFRs in massive haloes (Choi et al., 2012, 2015, Gaspari et al., 2011, Li et al., 2015, Martizzi et al., 2018) and many have argued it specifically provides a better match to observational constraints and is more efficient compared to "pure heating" models, especially in the context of "maintenance" or "radio mode" feedback (Barai et al., 2014, Begelman, 2004, Dubois et al., 2013, Fabian, 2012, Martizzi et al., 2018, Meece et al., 2017, Pillepich et al., 2018, Weinberger et al., 2017).

Since we will distinguish "random" or "non-oriented" driving below, we use this term to refer specifically to models with kinetic feedback oriented strictly radially away from the BH. Moreover because the coupling in the models above is primarily local (and we are not interested for this model in e.g., the case of CRs or hot thermally-pressurized gas driving outflows on large scales, since these should be resolved in our "Thermal input" and "Cosmic ray" runs), we will primarily focus on just the "BH" (local-kernel) models in this case. In that case a constant momentum flux $\dot{P}$ (directed radially away from the BH) is injected in a similar kernel-weighted fashion among neighboring gas around the BH (as for thermal energy), but with the kernel weights proportional to the solid angle subtended by each gas element (as seen by the BH).[4]

Turbulent driving or "stirring"

Rather than simply "pushing outwards," a variety of processes can instead transfer energy to kinetic energy of bulk quasi-random motion, what we call "turbulent stirring." AGN bubbles may generate turbulence through Rayleigh-Taylor (RT) and Richtmyer-Meshkov (RM) instabilities (Brüggen & Scannapieco, 2009, Dimonte & Tipton, 2006, Scannapieco & Brüggen, 2008); jets (precessing or not) can drive turbulence through changing bulk motion or secondary instabilities (e.g., Bourne & Sijacki, 2017, Li & Bryan, 2014, Martizzi et al., 2018, Yang & Reynolds, 2016) with driving scale $\sim 100\,\mathrm{kpc}$ (Hitomi Collaboration et al., 2018, ZuHone et al., 2016); and non-AGN processes like halo mergers (e.g., Mitchell et al., 2009, Norman & Bryan, 1999, Paul et al., 2011, Ricker & Sarazin, 2001, Roettiger et al., 1993, 1997, Vazza et al., 2011), sloshing of cold fronts (e.g., Fujita et al., 2004, ZuHone et al., 2013, 2018), and winds from satellites can do likewise (Anglés-Alcázar et al., 2017b). Studies have argued turbulence could suppress cooling flows by providing

[4] We emphasize that while this is launched at the BH, it is not a jet model. The scaling with solid angle simply ensures that momentum is launched uniformly in all directions.

direct pressure support to gas (Parrish et al., 2012a), or heating the gas "directly" via viscous dissipation (Banerjee & Sharma, 2014, Zhuravleva et al., 2014), or mixing cold structures back into hot gas in a thermally-unstable medium and so efficiently re-distributing heat (e.g., Banerjee & Sharma, 2014, Kim & Narayan, 2003b, Parrish et al., 2010, Ruszkowski & Oh, 2010, Vernaleo & Reynolds, 2006).

We represent "turbulent stirring" by driving turbulence directly following the "turbulent box" simulations in Bauer & Springel (2012). Turbulence is driven in Fourier space as an Ornstein-Uhlenbeck process (see Federrath et al., 2010, Price & Federrath, 2010, Schmidt et al., 2009) with characteristic driving wavelength ($\lambda = 2\pi/k$) set to $1/2$ of the halo scale radius (experimenting with this, compared to the kernel or total energy, makes little difference to our conclusions). The compressive part of the acceleration is projected out via a Helmholtz decomposition in Fourier space so that the driving is purely incompressible (solenoidal). After Fourier-transforming back to real space, the stirring is applied as a continuous acceleration $\mathbf{a}(\mathbf{x})$ to each element; at this stage, we apply the desired kernel function $\mathbf{a}(\mathbf{x}) \rightarrow \mathbf{a}(\mathbf{x})\, f(r)\, V_0^{-1}$ (with $V_0^{-1} \int f(|\mathbf{x}|)\, d^3\mathbf{x} = 1$). In runs labeled "uni," $f(r)$ is constant out to approximately the virial radius. In the runs labeled "core," $f(r)$ is either a Gaussian function or an exponential function as shown in Table 6.2. The energy and momentum input rates labeled in Table 6.2 are calculated through $\dot{E} \sim \int dm\ \max(|\mathbf{a}(\mathbf{x})|)|\mathbf{v}|$ and $\dot{P} \sim \int dm\ \max(|\mathbf{a}(\mathbf{x})|)$, which estimate the upper bounds. [5]

Cosmic ray injection

CRs arise generically from processes that result in fast shocks, so could come from shocked winds or outflows, but are particularly associated with relativistic jets from AGN (where they can make up the bulk of the jet energy; Berezinsky et al. 2006, Ruszkowski et al. 2017b) and hot, relativistic plasma-filled "bubbles" or "cavities" (perhaps inflated by jets in the first place) around AGN. Different authors have argued that they could help suppress cooling flows via providing additional pressure support to gas, driving pressure-driven outflows in the galaxy or CGM, or via heating the CGM/ICM directly via collisional (hadronic & Coulomb) and streaming-instability losses (Enßlin et al., 2011, Fujita & Ohira, 2011, Fujita et al., 2013, Guo & Oh, 2008, Jacob & Pfrommer, 2017a,b, Jacob et al., 2018, Pfrommer, 2013, Pfrommer et al., 2017a, Ruszkowski et al., 2017a,b, Sharma et al., 2010, Wiener et al., 2013).

[5] Although the acceleration of the gas (as a function of space) is constant in time, the density profiles change. Therefore, the total energy input rates also vary as a function of time.

We treat this analogous to our "thermal heating" runs – simply injecting cosmic ray energy at some fixed rate within a kernel. The CR physics and numerical implementation are described in detail in Chan et al. (2018). Briefly, this treats CRs including streaming (at the local Alfvén speed, with the appropriate streaming loss term, which thermalizes, following Uhlig et al. 2012, but with $v_{\rm st} = v_A$), diffusion (with a fixed diffusivity $\kappa_{\rm cr}$), adiabatic energy exchange with the gas and cosmic ray pressure in the gas equation of motion, and hadronic and Coulomb losses (following Guo & Oh 2008). We follow a single energy bin (i.e. GeV CRs, which dominate the pressure), treated in the ultra-relativistic limit. Streaming and diffusion are fully anisotropic along magnetic field lines. In Chan et al. (2018), we show that matching observed γ-ray luminosities, in simulations with the physics above requires $\kappa_{\rm cr} \sim 10^{29}\,{\rm cm^2\,s^{-1}}$, in good agreement with detailed CR transport models that include an extended gaseous halo around the galaxy (see e.g., Strong & Moskalenko, 1998, Strong et al., 2010, Trotta et al., 2011), so we adopt this as our fiducial value.[6] In practice, because of the large diffusivity, the CR energy density rapidly converges to the same quasi-equilibrium profile regardless of the shape of the injection kernel, so long as the injection scale is not extremely large ($\lesssim 100\,$kpc), so we simplify by focusing on the "BH" kernel choice and keeping the injection isotropic.[7]

6.3 Results in our massive halo (m14) survey

As will be shown in the following subsections, 'Th-core-44' ($\dot{E}_{\rm th} \sim \dot{E}_{\rm cool}$), 'Turb-core-4' ($\dot{E}_{\rm turb} < 1\%\dot{E}_{\rm cool}$), and 'CR-BH-43' ($\dot{E}_{\rm CR} \sim 10\%\dot{E}_{\rm cool}$) are the more successful runs in the corresponding toy model scenario. We, therefore, highlight these runs in the subsequent plots, while tuning down the contrast of the "explosive" runs.

6.3.1 Star formation history

The first row of Fig. 6.2 plots the baryonic mass (as a function of time) within 30 kpc ($M_{\rm baryon}^{30\,{\rm kpc}}$) excluding the pre-existing stars, which characterizes the cooling flow rates. The second, third and bottom rows show SFRs, SFRs from gas initially sitting outside 25 kpc (SFRs supplied by the cooling flows) and specific star formation rates (sSFRs), averaged in rolling 10 Myr bins. Momentum injection below $\sim$

[6] We caveat that we do not account for the possibility of different diffusion coefficient in different environments.

[7] We also note that, in the runs including CR heating, CRs from SNe are not included, so we have a clean test on the black hole CR injection. We showed in Paper I that CRs from SNe contribute negligibly to quenching, and we note below that the total energy injection from SNe is a factor $\sim 10^2 - 10^4$ below the analytically-input CR energy injection rate.

Table 6.2: Physics variations (run at highest resolution) in our halo-**m14** survey

Model	Summary	ΔT (Gyr)	$\dot{E}_{tot}$	$\dot{E}_{r<30}$ (erg s^{-1})	$\dot{E}_{r<100}$	$\dot{E}_{r>100}$	$\dot{P}_{tot}$	$\dot{P}_{r<30}$ (g cm s^{-2})	$\dot{P}_{r<100}$	$\dot{P}_{r>100}$	kernel (r in kpc)
Default	-	2.0	-	-	-	-	-	-	-	-	-
Momm-BH-34	minor	0.4	4.7-7.6 e40	-	-	-	1.2e34	-	-	-	BH neighbour
Momm-BH-35	minor	2.0	1.8-3.6 e42	-	-	-	1.2e35	-	-	-	BH neighbour
Momm-BH-36	explosive	0.3	2.0-0.07 e44	-	-	-	3.6e36	-	-	-	BH neighbour
Turb-uni-1	minor	2.0	3.6-7.7 e42	5.2-17 e39	4.6-5.7 e40	3.5-7.6 e42	1.6-1.6 e35	3.3-5.1 e32	3.0-1.7 e33	1.6-1.6 e35	Uniform
Turb-uni-2	$L_X \downarrow$	2.0	6.5-20 e42	9.5-11 e39	8.4-5.8 e40	6.4-20 e42	2.9-2.9 e35	6.0-3.4 e32	5.5-1.5 e33	2.9-2.9 e35	Uniform
Turb-core-1	moderate	2.0	5.0-5.6 e41	8.6-15 e39	6.2-8.5 e40	4.4-4.8 e41	2.5-2.0 e34	5.5-4.5 e32	4.1-2.3 e33	2.1-1.8 e34	$a \sim \exp(-r/200)$
Turb-core-2	moderate	2.0	1.6-2.4 e41	9.1-18 e39	6.7-11 e40	9.8-14 e40	9.8-7.8 e33	5.9-5.4 e32	4.5-2.9 e33	5.3-5.0 e33	$a \sim \exp(-(r/140)^2)$
Turb-core-3	moderate	2.0	2.1-2.9 e41	1.6-2.1 e40	8.1-12 e40	1.3-1.6 e41	1.2-0.9 e34	9.8-6.1e32	5.4-3.1e33	6.6-6.2 e33	$a \sim 2\exp(-r/80)$
Turb-core-4	**quenched**	**2.0**	**5.7-5.9 e41**	**2.7-0.5 e40**	**1.4-1.1 e41**	**4.4-4.8 e41**	**3.1-2.0 e34**	**1.7-0.2 e33**	**9.2-2.4 e33**	**2.1-1.8 e34**	$\mathbf{a_{r<100} \sim 3\exp(-(r/79)^2)}$ $\mathbf{a_{r>100} \sim \exp(-r/200)}$
Turb-core-5	quenched (NCC)	2.0	6.6-6.6 e41	5.2-1.7 e40	2.2-1.8 e41	4.4-4.8 e41	3.6-2.1 e34	3.3-0.3 e33	1.5-0.3 e34	2.1-1.7 e34	$a_{r<100} \sim 6\exp(-(r/66)^2)$ $a_{r>100} \sim \exp(-r/200)$
Turb-core-6	Mach$\uparrow$	0.7	9.9-11 e41	1.7-0.7 e41	5.5-0.5 e41	4.4-5.7 e41	5.9-2.6 e34	1.1-0.06 e34	3.7-0.6 e34	2.1-2.0 e34	$a_{r<100} \sim 20\exp(-(r/54)^2)$ $a_{r>100} \sim \exp(-r/200)$
Th-uni-43	minor	1.4	2.1e43	4.2-8.1 e40	3.9-4.0e41	2.0e43	-	-	-	-	Uniform
Th-uni-44	minor	2.0	2.1e44	4.2-7.3 e41	3.9-3.4 e42	2.0e44	-	-	-	-	Uniform
Th-core-43	minor	2.0	2.0-1.8 e43	1.2-1.2e43	2.0-1.8e43	6.8-7.2 e38	-	-	-	-	$\dot{E} \propto \exp(-(r/30)^2)$
Th-core-44	**quenched**	**2.0**	**2.0-0.5 e44**	**1.2-0.3 e44**	**2.0-0.5 e44**	**6.8-6.4 e39**	-	-	-	-	$\mathbf{E \propto \exp(-(r/30)^2)}$
Th-core-45	explosive	1.0	1.9-0.1 e45	1.2-0.02 e45	1.9-0.1 e45	6.8-5.2 e40	-	-	-	-	$\dot{E} \propto \exp(-(r/30)^2)$
Th-BH-43	minor	2.0	2.1e43	-	-	-	-	-	-	-	BH neighbour
Th-BH-44	explosive	1.2	2.1e44	-	-	-	-	-	-	-	BH neighbour
Th-BH-45	explosive	0.4	2.1e45	-	-	-	-	-	-	-	BH neighbour
CR-BH-42	minor	2.0	2.1e42	-	-	-	-	-	-	-	BH neighbour
CR-BH-43	**quenched**	**2.0**	**2.1e43**	-	-	-	-	-	-	-	**BH neighbour**
CR-BH-44	explosive	0.3	2.1e44	-	-	-	-	-	-	-	BH neighbour

This is a partial list of simulations studied here: each was run using halo **m14**, systematically varying the energy injection mechanism, scale, and energetics, at our highest resolution (a broader low-resolution parameter survey, and our survey of haloes **m12** and **m13**, are not included here). Columns list: (1) Model name. Models labeled "Momm," "Turb," "Th," and "CR" correspond to (radial) momentum injection, turbulent injection or "stirring," thermal energy injection ("heating"), and cosmic ray (CR) injection, respectively. Models labeled "uni," "core," "BH" adopt different kernels (see Fig. 6.1). (2) Summary of the results. Minor, moderate, and quenched correspond, respectively, to a SFR of $\gtrsim 10$, $\sim 1-10$, and $\lesssim 1 M_\odot\,\mathrm{yr}^{-1}$. The runs labeled otherwise are quenched while having a major drawback (as labeled). (3) ΔT: Simulation duration. All runs are run to 2 Gyr, unless either the halo is completely "blown out" or completely un-affected. (4) $\dot{E}_{tot}$, $\dot{E}_{r<30}$, $\dot{E}_{r<100}$, and $\dot{E}_{r>100}$ tabulate the total energy input of the corresponding spherical region (with the two values corresponding to the beginning and end of the run). The energy input of "Momm" and "Turb" runs is the energy used to accelerate gas (e.g., difference in kinetic energy) in each timestep. (5) $\dot{P}_{tot}$, $\dot{P}_{r<30}$, $\dot{P}_{r<100}$, and $\dot{P}_{r>100}$ tabulate the momentum input in the corresponding region. (6) kernel: the form of the injection kernel.

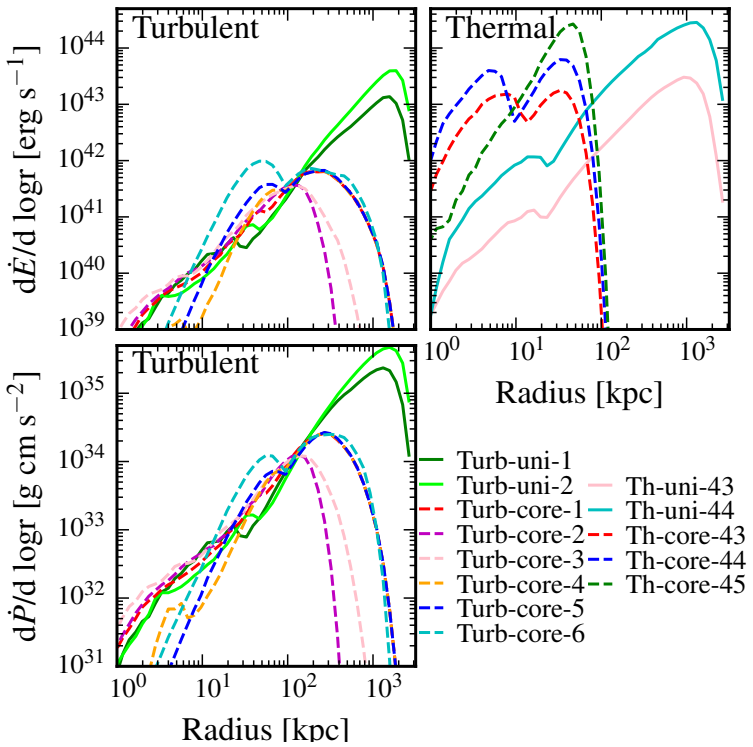

Figure 6.1: Energy (*top*) or momentum (*bottom*) input rate per unit logarithmic galacto-centric radius $\log r$ (time-averaged over the last 100 Myr of each run), in a subset of our halo **m14** runs. Runs labeled "uni" inject these quantities uniformly per unit mass over the whole halo, so large radii (containing most mass/volume) receive most of the injection. Runs labeled "core" have injection in a Gaussian-like kernel, so most of the energy/momentum ends up around the kernel scale radius. Runs labeled "BH" inject everything in a kernel centered in the resolution elements immediately surrounding the BH ($\ll$ kpc, hence not shown).

$10^{35}\,\mathrm{g\,cm\,s^{-2}} \sim 0.03\,L_{\rm Edd}/c$ does not suppress the cooling flow or star formation by much, while an injection above $3\times10^{36}\,\mathrm{g\,cm\,s^{-2}} \sim L_{\rm Edd}/c$ blows everything away within 50 Myr leaving almost no gas within 70 kpc.

With a lower momentum flux ($1-2\times10^{34}\,\mathrm{g\,cm\,s^{-2}}$; non-radial), turbulent stirring can significantly suppress the cooling flows and star formation. When the turbulent energy input within 100 kpc reaches $1.1-1.4\times10^{41}\,\mathrm{erg\,s^{-1}}$ ('Turb-core-4'), the core baryonic mass is suppressed by a factor of 3-10. For turbulent energy input rates above $\sim 2\times10^{41}\,\mathrm{erg\,s^{-1}}$ ('Turb-core-5,6'), the SF is eventually completely quenched.

Uniform thermal heating has little effect on the SFRs and cooling flows even if input rate reaches $\sim 10^{44}\,\mathrm{erg\,s^{-1}}$. Black hole thermal injection, on the other hand, undergoes a sharp transition from having little effect to completely quenching the

galaxy by blowing everything away (through a Sedov-Taylor explosion), between injection rates 10^{43} to 10^{44}erg s^{-1} ($10^{-4} - 10^{-3} L_{\rm Edd}$). The transition is milder if the energy is smoothly injected within a Gaussian kernel of 30 kpc, in which case a stable core baryonic mass and low star formation rate can be maintain by a heating rate of $\sim 10^{44}$erg s^{-1} ('Th-Core-44'). However, with a similar cooling flow rate (e.g., 'Turb-core-1' and 'Th-core-43'), turbulent stirring suppresses SFR more efficiently (with a lower energy input rate) than core thermal heating.

Unlike thermal heating, CR energy input can maintain a semi-stable core baryonic mass and suppressed SFR even if all the energy is deposited in the vicinity of the black hole. The SFR and cooling flows are significantly suppressed by an energy input of 10^{43}erg s^{-1}, less than the rate required for a thermal heating run with Gaussian kernel to quench. However, when the CR input reaches 10^{44}erg s^{-1}, the resulting dramatic suppression of core baryonic mass becomes similar to what is caused by the "explosive" BH-kernel thermal heating.

6.3.2 The resulting halo properties

Temperature, density, and entropy

Fig. 6.3 shows the average density, and luminosity-weighted density, temperature, and entropy as a function of radius averaged over the last 100 Myr of the runs. The shaded regions in the second row indicate the observational density profiles (scaled) for cool-core (blue) and non-core-core (red) clusters (McDonald et al., 2013).[8] The lightened curves in the bottom row indicate the observational entropy profiles for cool-core (blue) and non-core-core (red) clusters (McDonald et al., 2013).[9]

Momentum injection does not affect the resulting halo profiles with an input rate less than $\sim 10^{35}$g cm s^{-2}, while it blows everything away when the input rate reaches $L_{\rm Edd}/c \sim 3 \times 10^{36}$g cm s^{-2}.

With a lower momentum input at $\sim 10^{34}$g cm s^{-2}, turbulent stirring can much more efficiently suppress the core density. When the core ($r < 100$ kpc) energy input reaches $1.1 - 1.4 \times 10^{43}$erg s^{-1} ('Turb-core-4'), the density suppression becomes more significant. When it reaches 2×10^{43}erg s^{-1} ('Turb-core-5,6'), the core gas is eventually completely heated up, and the entropy profile is flattened. If turbulent

[8] We use the panel for $z < 0.1$ in Fig.9 of McDonald et al. (2013) and assume $\rho_{\rm crit} \sim 9.2 \times 10^{30}$g cm^{-3} and $r_{500} = 650$ kpc (our m14 initial condition).

[9] The haloes in McDonald et al. (2013) have a mass range of $\sim 2 \times 10^{14} < M_{500} < 20 \times 10^{14} M_\odot/h_{70}$. We use their Fig.2 and scale the average entropy at $r = 700$ kpc to 500 kev cm^2 given our halo is smaller (cooler).

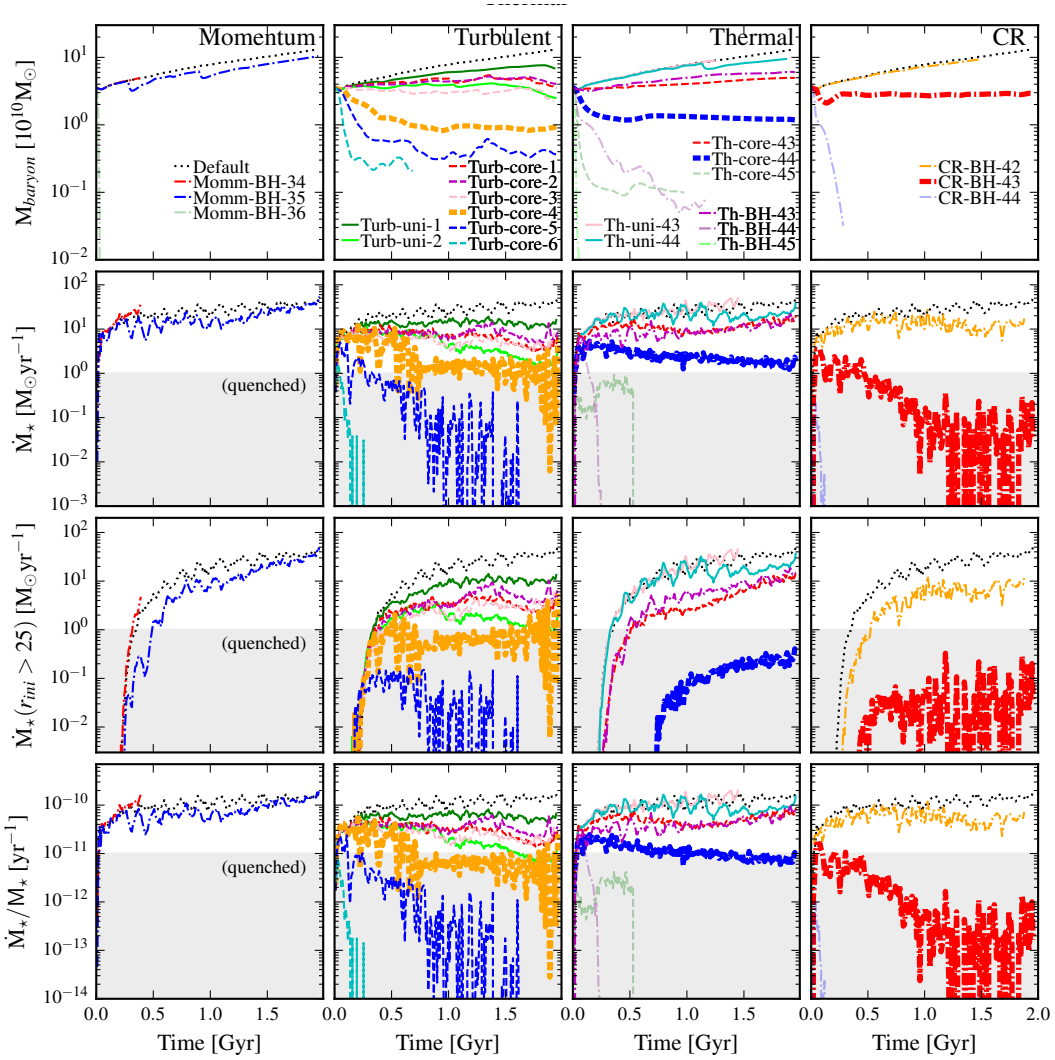

Figure 6.2: *Top:* Baryonic mass within 30 kpc (excluding pre-existing stars from the ICs), as a function of time, in the halo-**m14** runs from Table 6.2. This is a proxy for the net amount of cooling-flow inflow. *Second:* SFRs averaged in 10 Myr intervals. *Third:* SFRs specifically from gas which was at $r > 25$ kpc in the ICs (gas which comes in with the cooling flow). *Bottom:* Specific SFRs. The shaded regions indicate the SFR or specific SFR that we define as quenched. For each, we compare runs with momentum injection, turbulent stirring, thermal heating, and cosmic ray injection (columns, as labeled). Momentum injection below $\dot{P} \lesssim 10^{35}\,\mathrm{g\,cm\,s^{-2}}$ does not suppress cooling flows, while $\dot{P} \gtrsim 3\times10^{36}\,\mathrm{g\,cm\,s^{-2}}$ almost immediately ejects all the gas in the halo. Uniform thermal heating has little effect on SF (most of the energy is "wasted" at large-r), while nuclear ("BH") injection transitions sharply between doing nothing (the heat is radiated away) and driving a Sedov-Taylor explosion that evacuates the halo around $\dot{E} \sim 3\times10^{43}\,\mathrm{erg\,s^{-1}}$. Heating with a semi-extended ~ 30 kpc kernel can suppress SF without explosive ejection for $\dot{E}$ carefully chosen around $\dot{E} \sim 10^{44}\mathrm{erg\,s^{-1}}$. Turbulent stirring more efficiently suppresses SF: when the driving $\dot{E}$ within < 100 kpc reaches $\gtrsim 10^{41}\mathrm{erg\,s^{-1}}$, the core baryonic mass begins to fall, and by 2× this SF is eventually completely quenched. CR energy input at $10^{43}\mathrm{erg\,s^{-1}}$ can maintain a low SFR and semi-stable core baryonic mass even if the energy is deposited in the nucleus.

stirring is not suppressed at large radii, the density beyond 100 kpc is also suppressed by almost a factor of 10, i.e. the halo begins to expel/lose a significant amount of gas. Among the runs with significantly suppressed SFRs, the density and entropy profiles of 'Turb-core-5' and 'Turb-core-6' end up resembling those observed in non-cool-core clusters (compare Hudson et al., 2010, McDonald et al., 2013, Sanderson et al., 2006, 2009), while 'Turb-core-4' lives between cool-core and non-core. The other turbulent stirring runs with moderately suppressed SFRs preserve the cool-core features, although their densities in the core regions are slightly higher than observational values.

The effects of thermal heating on the halo properties strongly correlate with the kernel size of the injection. When concentrated in the black hole neighborhood, $\sim 10^{43}\mathrm{erg\,s^{-1}}$ is sufficient to significantly suppress the density within 5 kpc and heat up the gas up to 10^8 K. Thermal injection rates in the BH neighborhood $\gtrsim 10^{44}\mathrm{erg\,s^{-1}}$ blow out everything within 10 kpc, heat gas to $\gtrsim 10^{10}$K, and produce a negative temperature slope out to > 100 kpc. If the injection is smoothed over a Gaussian kernel of 30 kpc, then the core density is not suppressed until the total energy input reaches $\gtrsim 10^{44}\mathrm{erg\,s^{-1}}$ (when the energy input is comparable to the cooling). Although milder, a negative temperature gradient extending from 10 to 100 kpc is still hard to avoid in that case.

CR injection can significantly suppress the core density with $\dot{E} \gtrsim 10^{43}\mathrm{erg\,s^{-1}}$, and produces an extended region with significant hot gas. If the input exceeds $10^{44}\mathrm{erg\,s^{-1}}$, the injection becomes explosive on large scales (similar to high-$\dot{E}$ BH-kernel thermal injection). Except for the explosive one, runs with CR injection have density and entropy profiles resembling those observed in cool-core clusters. The gas of the most successful CR injection run ('CR-BH-43') within ~ 7 kpc is dominated by the hot gas from stellar mass loss (and/or gas heated by CR) and is less constrained by the observations.

The face-on projected density and average temperature (between $\Delta Z = \pm 1$ kpc) of the more successful runs ('Th-core-44', 'Turb-core-4' and 'CR-BH-43') are shown in Fig. 6.4. Consistent with the aforementioned density and temperature profiles, 'Th-core-44' and 'Turb-core-4' have suppressed density up to a few 10 kpc, while 'CR-BH-43' has suppressed density only within 10 kpc. Thermal heating and CR injection both lead to a heated region, but the heated region in the former case extends to a larger radius.

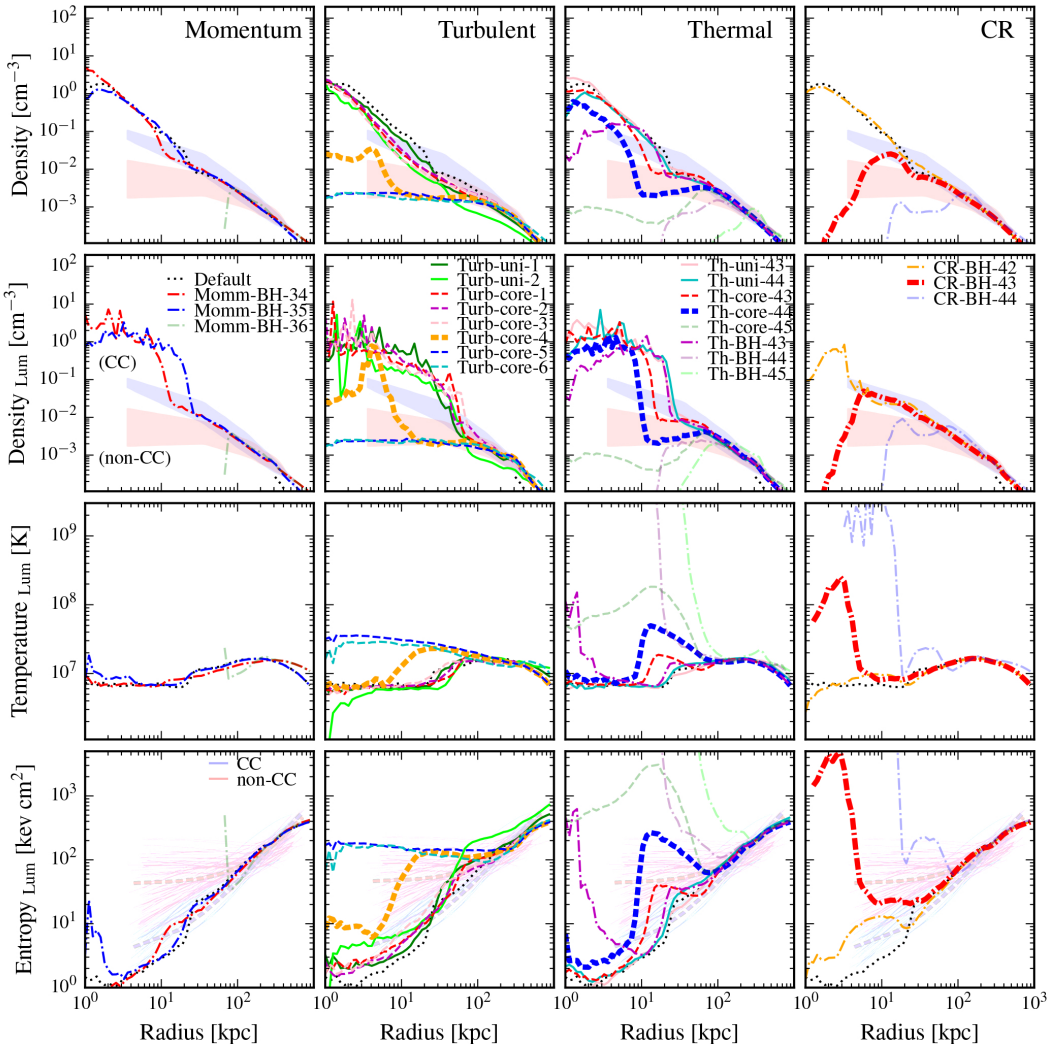

Figure 6.3: Density (*top*), X-ray cooling luminosity-weighted density (*second*), luminosity-weighted temperature (*third*), and luminosity-weighted entropy (*bottom*) versus radius averaged over the last ~ 100 Myr in the **m14** runs from Fig. 6.2. The shaded regions in the second row and the lightened curves in the bottom row indicate the observational density and entropy profiles (scaled) for cool-core (blue) and non-core-core (red) clusters (McDonald et al., 2013). At sufficiently low injection rates, all models do little (as expected). In "Momentum," "Thermal," and "CR" injection, we see that when the injection is nuclear ("BH") and large enough, explosive behavior results (expelling nearly all gas within $\sim 30-100$ kpc, and leaving what remains very hot), in stark contrast with observations. Quasi-stable intermediate cases do exist, for turbulent stirring and CR injection in particular. Among the turbulent runs with suppressed SF, most preserve the initial cool-core features (though they do suppress the density, heat up, and flatten the entropy profile in the core), though "core-5/6" resemble non-cool-core clusters (but do not "explode"); uniform turbulent driving suppresses densities even at $\gg 100$ kpc as well. The 'Th-core-44' run, which has non-explosively suppressed SFR, broadly resembles non-cool-core clusters, but its negative temperature gradient is in tension with observations. The 'CR-core-43' run, which also has non-explosively suppressed SFR, resembles cool-core clusters.

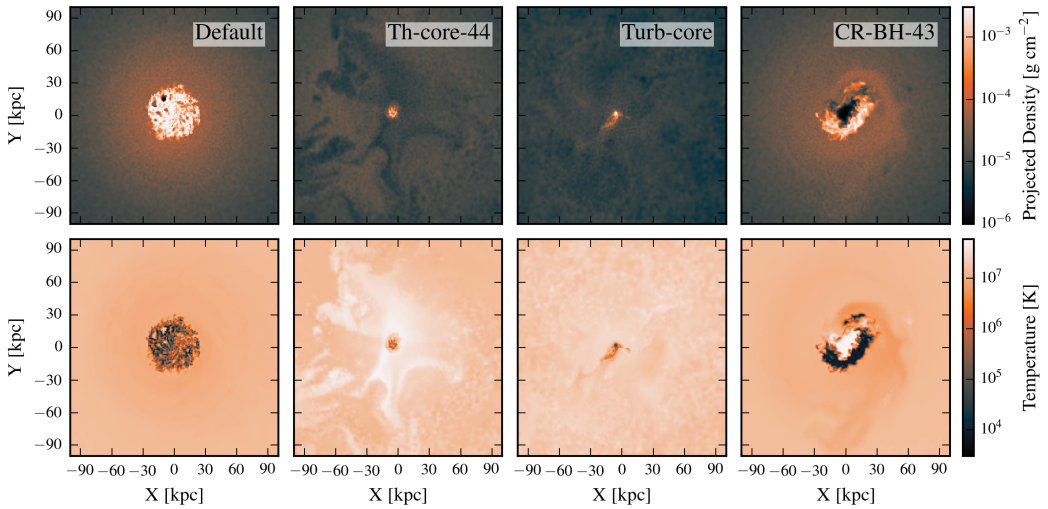

Figure 6.4: The face-on projected density and average temperature (between $\Delta Z = \pm 1$ kpc) of the more successful runs ('Th-core-44', 'Turb-core-4' and 'CR-BH-43'). Consistent with the density and temperature profiles in Fig. 6.3,'Th-core-44' and 'Turb-core-4' have suppressed density up to a few 10 kpc, while 'CR-BH-43' has suppressed density only within 10 kpc. Thermal heating and CR injection both lead to a heated region, but the heated region in the former case extends to a larger radius.

X-ray luminosities

The resultant X-ray luminosity of the gas halo is an important constraint for an AGN feedback model (e.g., Choi et al., 2015, McCarthy et al., 2010). Fig. 6.5 shows the predicted X-ray cooling luminosity, integrated over all gas in the halo, from 0.5 – 7 keV. The luminosity is calculated using the same methods in Ressler et al. (2018), Schure et al. (2009), in which the cooling curve is calculated for the photospheric solar abundances (Lodders, 2003), using the spectral analysis code SPEX (Kaastra et al., 1996) and scaled according to the local hydrogen, helium, and metal mass fractions. The shaded regions indicate the observed X-ray luminosities in Reiprich & Böhringer (2002) and Stanek et al. (2006) for haloes with $m_{\rm halo} \sim 0.7 - 1.5 \times 10^{14} M_{\odot}$. Runs which quench by violently ejecting gas strongly suppress their X-ray luminosities, as does the "uniform" turbulent stirring run (owing to its suppression of gas densities everywhere in the halo). But interestingly, other runs with suppressed SF/cooling flows maintain X-ray luminosities just a factor $\sim 1.5 - 3$ lower, well within the observed range (Anderson et al., 2015, Balogh et al., 2006, Kim & Fabbiano, 2013, Reiprich & Böhringer, 2002, Stanek et al., 2006). This is because a large portion of the total X-ray luminosity is from larger radii, although the surface brightness decays as a function of radius.

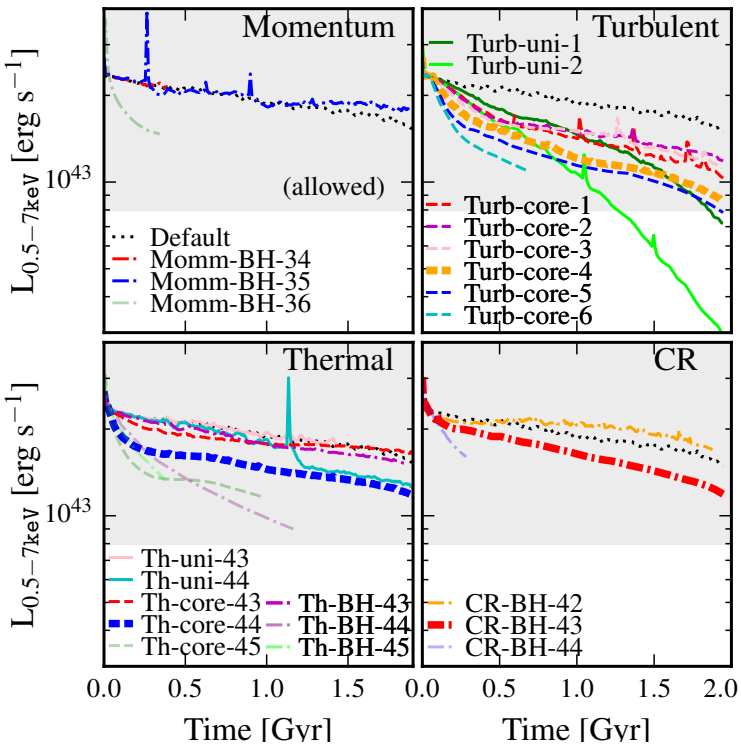

Figure 6.5: X-ray cooling luminosity L_X, integrated from 0.5 – 7 keV, in the runs in Fig. 6.3. The shaded regions indicate the observed X-ray luminosities in Reiprich & Böhringer (2002) and Stanek et al. (2006) for haloes with $m_{\rm halo} \sim 0.7 - 1.5 \times 10^{14} M_\odot$. Runs which explosively eject core gas (e.g., 'Momm-BH-36', 'Th-BH-44,45' and 'CR-BH-44') strongly suppress L_X. Uniform turbulent stirring ('Turb-uni') also suppresses L_X strongly by ejecting gas (at larger radii). But other runs with suppressed SF ('Turb-core-X','Th-Core-44', 'CR-BH-43') have only factor $\sim 1.5 - 3$ lower L_X. This is because a large portion of the total X-ray luminosity is from larger radii, although the surface brightness decays as a function of radius.

Turbulent Mach number

Fig. 6.6 shows the rms 1D turbulent velocity, defined as $v_{\rm turb}/\sqrt{3}$, and the 1D Mach number for gas hotter than 10^7K as a function of radius, averaged over the last 100 Myr of the runs. Radial momentum injection does not alter turbulence much, as it primarily drives coherent motion; likewise for thermal injection when it is weak or spread over large radii. In the "explosive" regime of momentum/thermal/CR input, all drive strong outflows at up to $\sim 1000\,{\rm km\,s^{-1}}$, though the higher shocked-gas temperatures mean this corresponds to Mach~ 0.4. At intermediate CR injection rates, appreciable but modest bulk motions are driven at $\gtrsim 10\,{\rm kpc}$.

By construction, turbulent stirring boosts turbulent velocities where injected. The

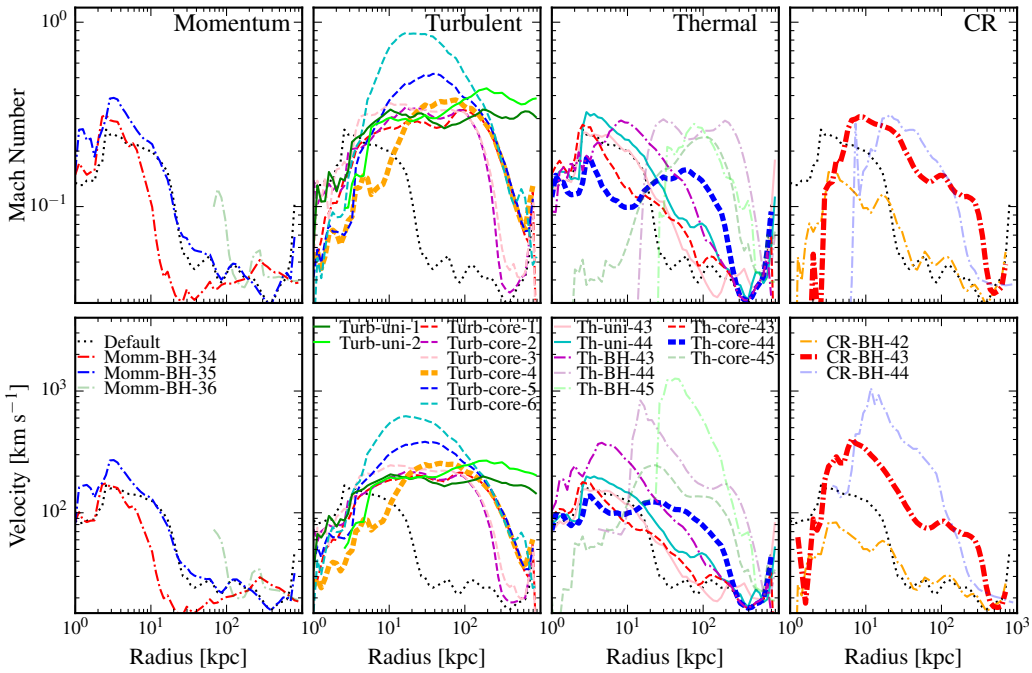

Figure 6.6: *Top:* 1D rms Mach number ($v_{\rm turb}/\sqrt{3}v_{\rm thermal}$, in gas with $T > 10^7$ K, averaged over the last 100 Myr of the runs) as a function of radius for the runs in Fig. 6.3. *Bottom:* 1D rms velocity dispersion $v_{\rm turb}/\sqrt{3}$. The 'Default' run has turbulence driven by a combination of thermal instability and stellar feedback. Weaker momentum/thermal/CR input does not alter this much; when those inputs become "explosive" (see Fig. 6.3), strong shocks appear as jumps in $v_{\rm turb}$ up to $\gtrsim 1000\,{\rm km\,s^{-1}}$. Modest CR injection or distributed thermal injection contribute $\sim 200\,{\rm km\,s^{-1}}$ bulk motions at $r \gtrsim 10$ kpc. Turbulent stirring runs (by construction) produce Mach $\sim 0.2-0.4$ turbulence over the radii of the chosen kernel, although the strongest runs (e.g., 'Turb-core-6') exceed Mach $\gtrsim 1$.

maximal turbulent velocities reach $\sim 200-400\,{\rm km\,s^{-1}}$ (Mach $\lesssim 0.5$) in the 'Turb-uni' and 'Turb-core-1-5' runs, broadly consistent with observations (Hitomi Collaboration et al., 2016, 2018), but towards the higher end of the allowed range, while 'Turb-core-6' exceeds Mach > 1.

6.3.3 Cooling time and gas stability

Fig. 6.7 shows the cooling time ($\tau_c \equiv E_{\rm thermal}/\dot{E}_{\rm cooling}$) versus radius for gas hotter than 10^5 K. Momentum injection does not affect the cooling time strongly. Even in our highest momentum flux run ($\sim 10^{36}\,{\rm g\,cm\,s^{-2}}$), where everything within 70 kpc is blown away, the cooling time at even larger radii still remains very similar to the 'Default' run.

On the other hand, turbulent stirring, which effectively suppresses the gas density, can also suppress the cooling rate (through turbulent mixing and pressure support). The regions with boosted cooling time roughly coincide with the regions with strong stirring. When the stirring injects $\sim \times 10^{41}$erg s^{-1} ('Turb-core-4') within 100 kpc, the average cooling time of gas with $T > 10^5$ K beyond 10 kpc is boosted to $\gtrsim 10$ Gyr. In 'Turb-core-5 and 6', almost all the gas becomes stably non-cooling, consistent with their resulting non-cool-core halo properties.

Thermal heating can significantly boost the cooling time as long as the kernel of injection is small enough (only the 'Th-BH' runs and 'Th-core' runs). The increase of the cooling time basically follows the increase in temperature discussed in § 6.3.2.

CR injection boosts the cooling time significantly within $r \sim 10$ kpc, owing to lower densities and higher temperatures inside these radii, when the injection rate is $\gtrsim 10^{43}$erg s^{-1}.

The ratio of cooling time to dynamical time (τ_c/τ_d, with $\tau_d \equiv (r^3/GM_{enc})^{1/2}$) is also plotted as an indication of gas stability. The runs suffering from the most severe cooling flows in our suite ('Default', 'Momm-BH-34,35', 'Th-uni-43,44', 'Th-core-43', 'Th-BH-43' and 'CR-BH-42') have an extended region within 100 kpc at $\tau_c/\tau_d \lesssim 20$. In the runs with SFRs suppressed to $\lesssim 1 M_\odot$yr^{-1} ('Turb-core-4', 'Th-core-44' and 'CR-BH-43'), most of the gas within this radius has $\tau_c/\tau_d > 10$. In the runs which end up resembling non-cool-core clusters ('Turb-core-4 & 5'), $\tau_c/\tau_d \gtrsim 100$ uniformly. Consistent with previous studies (e.g., Gaspari et al., 2015, Sharma et al., 2012, Voit et al., 2017), we find that our simulations that avoid the cooling catastrophe and also produce "realistic" cool-core profiles have $\tau_c/\tau_d \gtrsim 10$.

6.3.4 Energy input vs. cooling

In Fig. 6.8, we compare cooling rates, energy input rates, and net energy gain/loss of each run, integrated within a radius r. Here "energy input" sums stellar feedback (adding SNe and stellar mass-loss kinetic luminosities) plus the input from our analytic injection models. We also show where gas (above 10^5 K) has cooling times exceeding the Hubble time.

Direct thermal heating, as expected, suppresses cooling in the core region only if the injected heating rate is larger than cooling: this is why uniform or large-kernel heating is inefficient (energy is "wasted" at large radii). When highly-concentrated, this tends to result in explosive behavior, which reduces the cooling rate further out not by direct heating but by ejecting the halo baryons. The only thermal heating

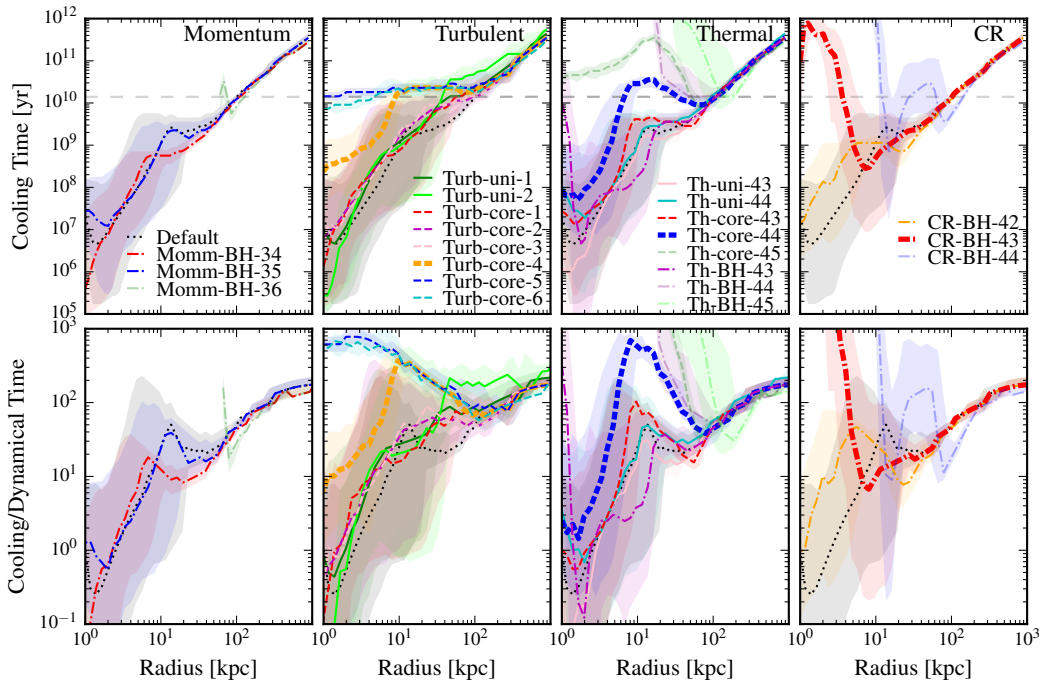

Figure 6.7: *Top:* Gas cooling time ($\tau_c \equiv E_{\rm thermal}/\dot{E}_{\rm cooling}$) versus radius (averaged in the last 100 Myr of the runs in Fig. 6.3). Gray dashed line labels the Hubble time. *Bottom:* Cooling time over dynamical time ($\tau_d \equiv (r^3/GM_{enc})^{1/2}$). With weak injection these are not strongly modified. In explosive cases the cooling time interior to the explosive shock is enormous (the "cutoff" to zero reflects cases where there is no gas in the relevant temperature range inside some radius). CRs and turbulent stirring suppresses cooling primarily by suppressing core gas densities; regions with boosted τ_c correspond to regions with strong stirring. If the stirring exceeds $\gtrsim 2\times10^{41}\,{\rm erg\,s^{-1}}$ within 100 kpc ('Turb-core-5 & 6'), or CR injection exceeds $\gg 10^{43}\,{\rm erg\,s^{-1}}$, the gas has $\tau_c > t_{\rm Hubble}$ and $\tau_c/\tau_d \gtrsim 100$ – this is an excellent predictor of when the system will resemble a non-cool-core-cluster.

run with heating roughly matched to cooling over the extended cooling region is the (intentionally fine-tuned) 'Th-core-44' run.

Akin to the thermal runs, 'CR-BH-42' does little, 'CR-BH-44' is explosive, while 'CR-BH-43' is able to maintain quasi-stable equilibrium. A key difference is (as we show below) this comes primarily from pressure support, where the CR pressure profile (if diffusion is fast and the injection rate is constant, and losses are negligible) is essentially a steady-state $p_{\rm cr} \sim \dot{E}_{\rm cr}/12\pi\,\kappa\,r$. This makes the predictions less sensitive to small variations in the cooling rates or gas densities.

Turbulent stirring can suppress cooling rates significantly without becoming "explosive" and with significantly lower energetic "cost." We discuss the mechanisms

for this in § 6.5.3.

6.3.5 The rejuvenation of non-cool-core clusters, and role of feedback from old stellar populations

Given that 'Turb-core-5' and 'Turb-core-6' evolve from cool-core to non-cool-core in a relatively "gentle" manner, a natural question to ask is whether the halo will become cool-core again if the turbulent stirring is turned off. It turns out that rejuvenation does not necessarily occur, at least in these idealized simulations (remember, our simulations are non-cosmological, so do not include *new* gas accreting into the halo).

We test this by restarting the 'Turb-core-5' run from the 1.4 Gyr point and the 2.0 Gyr point, removing our injection (keeping e.g., stellar feedback and all other physics, however). As shown in Fig. 6.9, the '1.4 Gyr' run rejuvenates (core baryonic mass slowly grows and star formation reoccurs) while the '2.0 Gyr' one does not. The reason is that once the density is lowered to a (very low) point where the residual steady-state energy input from type 1a SNe and AGB winds surpasses cooling, the halo remains quenched for a Hubble time. Fig. 6.10 shows the same comparison of Fig. 6.8 for 'Turb-core-5' at 1.4 Gyr and 2.0 Gyr, but includes only the stellar feedback contribution in "energy input." It is clear that at 1.4 Gyr there is still an extended region ($r \lesssim 30$ kpc) with sufficiently dense gas that stellar feedback from old stars alone (SNe Ia & AGB mass-loss) can only marginally balance cooling, while by 2.0 Gyr, the density has been depleted to the point where the old-star stellar feedback (which is basically identical) now totally surpasses cooling.

If we restart this 2.0 Gyr run without stellar feedback from old stars (disabling Ia's and AGB mass-loss), then it does rapidly resume SF and "rejuvenate." We have confirmed it is the Ia population which dominates the energy injection and results here. But in either case, it appears that stellar feedback can aid in *maintaining* quenched systems, but only once they are well into the non-cool-core stage with especially depleted central gas densities.

We focused on this case because it was only marginally a non-cool-core cluster. In every simulation that produces "explosive" quenching, the central gas densities are extremely low (much lower than our 2.0 Gyr run here) and so, unsurprisingly, rejuvenation never occurs.

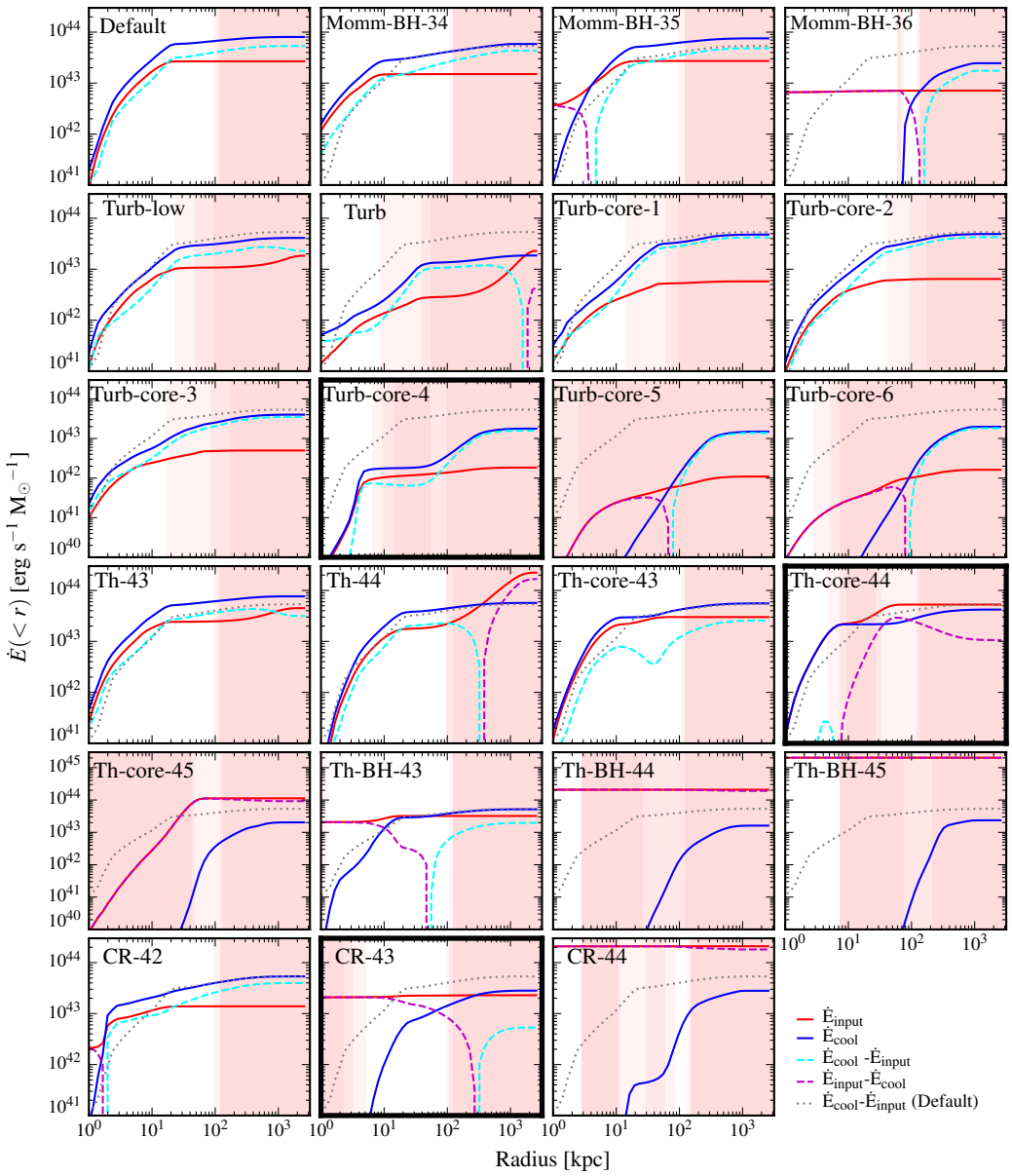

Figure 6.8: Cumulative (integrated inside $< r$) cooling rate ($\dot{E}_{\rm cool}$), total feedback energy input rate ($\dot{E}_{\rm input}$), and difference (net loss/gain), in the runs from Fig. 6.3 averaged over their last 100 Myr. Progressively darker red shading indicates regions where 20/50/80% of gas (above $T > 10^5$ K) has cooling times greater than the Hubble time. Weak input produces little change; "explosive" runs quench by dramatically lowering heating and core gas densities. Several of the turbulent runs suppress cooling significantly, ensuring $\tau_c > t_{\rm Hubble}$, without "exploding." This is also seen in intermediate CR runs ('CR-BH-43'), more or less independent of the injection kernel. In thermal runs this requires an injection kernel and energy fairly carefully matched to the cooling radius/energy.

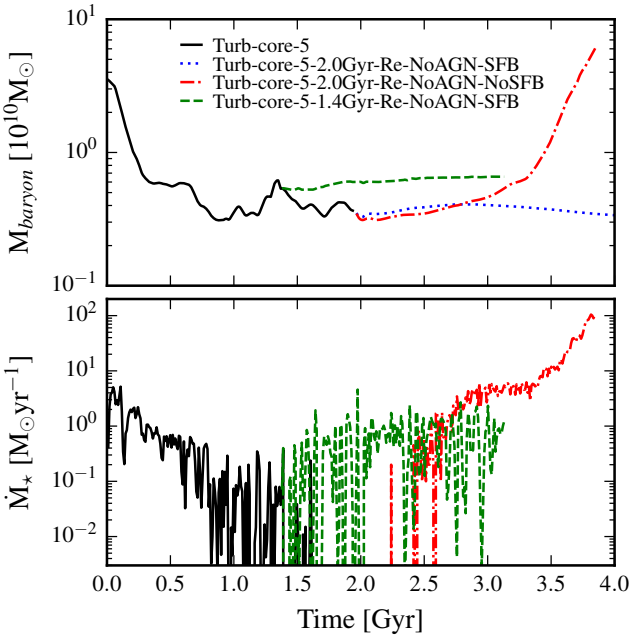

Figure 6.9: Testing "rejuvenation." We restart run 'Turb-core-5' which transitions from cool-core to non-cool-core cluster, at either 1.4 Gyr ('Re-1.4Gyr-SFB') or 2.0 Gyr ('Re-2.0Gyr-SFB'), keeping all physics identical but turning off the turbulent "stirring" at the time of restart. We compare the baryonic mass within $r < 30\,$kpc (excluding pre-existing stars; *top*) and SFR (*bottom*) as Fig. 6.2. The earlier restart "rejuvenates" after additional energy injection is disabled, and $\dot{M}_{ast}$ slowly re-grows over $\sim$ Gyr timescales. The later restart fails to rejuvenate, as in the intervening time, continued driving has lowered the core gas density to the point where stellar feedback from old stars (Ia & AGB) can keep it hot. We confirm the latter by re-running the 2.0 Gyr restart without this feedback ('Turb-core-5-2.0Gyr-Re-NoAGN-NoSFB'), which now rejuvenates.

6.4 Results as a function of halo mass

We now explore models in lower-mass haloes **m12** and **m13** at $M_{\rm halo} \sim 10^{12}$ and $10^{13}\,M_\odot$, respectively (see Table 6.1). We focus our attention on models motivated by those that at least seem plausibly "successful" (able to have some effect, but also not obviously in gross violation of observational constraints) – this includes variations of the turbulent stirring "core-kernel" runs, cosmic ray injection with appropriate energetics, and thermal heating with an appropriate-scaled spatial kernel and energy scale. The survey at high resolution is listed in Table 6.3, though we have run additional low-resolution tests of broader parameter space to confirm our intuition from the **m14** survey continues to hold.

For the thermal and CR injection cases, we scale the input energy from the m14 'Th-

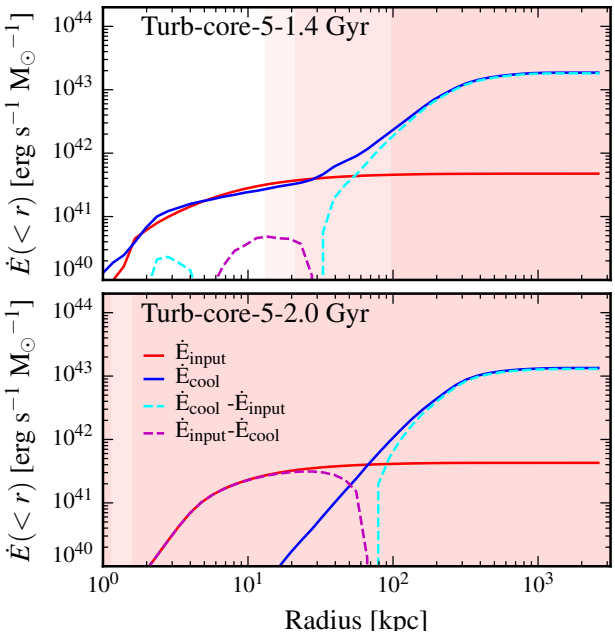

Figure 6.10: Cumulative cooling rate versus energy input (as Fig. 6.8, but including *only* stellar feedback from old stellar populations in the $\dot{E}_{\rm input}$ budget), of the "restarted" runs in Fig. 6.9. In the earlier restart, the higher core densities allow cooling and rejuvenation after the turbulent injection is de-activated. In the later restart, the stellar injection is identical (it comes from the same old stars) but the gas density has been further lowered by the injection to the point where old stars can maintain quenching for a Hubble time.

core-44' and 'CR-BH-43' runs according to the total cooling rate of the halo. For turbulent stirring, we scale the characteristic wavelength of the stirring in Fourier space (λ) and kernel size (r_k) from the m14 'Turb-core-4' run according to the viral radius, and the amplitude of particle acceleration according to the circular velocity at the kernel size: $a r_k \sim v_c^2 \sim G M_{\rm enc}/r$. For the **m12** case, the above scaling makes the kernel very narrow and confines the stirring or energy injection to the disk, so we also included **m12** runs with a wider kernel.

The resulting SFRs are plotted in Fig. 6.11. Turbulent stirring and CR injection quench all haloes, while thermal heating is less efficient in **m12**. Fig. 6.12 shows the density, temperature, and entropy profiles, while Fig. 6.13 compares the energy injection to cooling luminosities as a function of radius.

Thermal heating has similar effects in **m13** and **m14**: the galaxies are quenched but inevitably have a mild negative temperature gradient. The energy input of both matches the cooling in an extended region (by construction). However, in the **m12**

Table 6.3: Physics variations (run at highest resolution) in our survey of lower-mass (**m12** & **m13**) haloes

Model	λ (kpc)	$\dot{E}_{tot}$ (erg s^{-1})	$\dot{P}_{tot}$ (g cm s^{-2})	kernel (r in kpc)
m12-Turb-core	25	5.5-8.4 e39	4.0-4.2 e32	$a_{r<20} \sim 3\exp(-(r/15.8)^2)$ $a_{r>20} \sim \exp(-r/39.6)$
m12-Turb-core-wide	25	4.7-9.3 e39	4.6-4.9 e32	$a_{r<50} \sim 3\exp(-(r/39.6)^2)$ $a_{r>50} \sim \exp(-r/100)$
m13-Turb-core	57	13-7.5 e39	10-3.8 e32	$a_{r<50} \sim 3\exp(-(r/40)^2)$ $a_{r>50} \sim \exp(-r/100)$
m14-Turb-core-4	120	5.7-5.9 e41	3.1-2.0 e34	$a_{r<100} \sim 3\exp(-(r/79)^2)$ $a_{r>100} \sim \exp(-r/200)$
m12-Th-core-43	-	1.3-1.4 e43	-	$\dot{E} \propto \exp(-(r/6)^2)$
m12-Th-core-43-wide	-	1.3-2.5 e43	-	$\dot{E} \propto \exp(-(r/14)^2)$
m13-Th-core-43	-	17 -7.8 e42	-	$\dot{E} \propto \exp(-(r/14)^2)$
m14-Th-core-44	-	2.0-0.5 e44	-	$\dot{E} \propto \exp(-(r/30)^2)$
m12-CR-BH-42	-	1.3e42	-	BH neighbour
m13-CR-BH-42	-	1.8e42	-	BH neighbour
m14-CR-BH-43	-	2.1e43	-	BH neighbour

Partial list (including just simulations at "production" resolution) of runs in haloes **m12** and **m13**. Style is identical to Table 6.2, but we add one column λ, denoting the wavelength of the turbulent driving modes. We focus only on models which were successful without being "explosive" in the **m14** suite, and scale the energetics and kernel sizes with the cooling luminosities and virial radii, respectively. We have run additional low-resolution tests akin to the suite in Table 6.2 to confirm much larger/smaller injection produces similar results to what is seen there.

case, the cooling rate is actually *boosted* by the additional thermal heating (because the virial temperature is low and amount of gas at $\sim 10^4 - 10^5$ K is large, this pushes gas higher on the cooling curve), so the effect is much weaker. In lower-resolution tests, this is not remedied by increasing the thermal energy injection rate: because of the more violent thermal instability, all our thermal-heating runs in **m12** either produce no effect, or violent explosion of the entire halo.

Naively scaling the turbulent "stirring scale" with the viral radius (and strength with the circular velocity) quenches **m13**, but the stirring at large radii > 50 kpc is too strong and a substantial gas mass is thrown out of the halo completely, lowering the density and X-ray luminosity, while the stirring at small radius makes the halo

non-cool-core (akin to stronger stirring cases in **m14**). This can be moderated, as expected, with a somewhat weaker stirring. In **m12** these naive scalings lead to stirring confined to ~ 16 kpc, which effectively stirs the galactic disk and ballistically "launches" the whole disk into fountains, which produce a violently bursty star formation history. Obviously, this is not realistic: increasing the "stirring kernel" size to ~ 40 kpc ('m12-turb-core-wide') produces a much smoother low SFR and stable cool-core structure with slightly-lower core densities and cooling rates.

CR injection successfully and "smoothly" quenches **m12** and **m13**. In **m13** the overall cooling rate is eventually also suppressed significantly as the gas within the central few kpc is ejected.

6.5 Discussion: How do different physics quench (or not)?

The only injection models that result in a semi-stable quenched galaxy are thermal heating with a Gaussian kernel chosen in the correct energy and size range, turbulent stirring confined to radii below the halo scale radius, and cosmic ray heating in the correct energy range. We briefly discuss how each surveyed model in § 6.2.2 operates.

6.5.1 Radial momentum injection

The actual kinetic energy (even if it all thermalized) of the momentum-injection runs is less than the cooling luminosity.[10] At low injection rates this just stirs small-scale turbulence/fountains (e.g., in "Momm-BH-35," 40% of the momentum and 20% of the energy input is used to decelerate in-falling gas, and $\sim 1/2$ of the gas acted directly upon by the nuclear stirring still forms stars). At higher injection rates it acts by dynamically altering halo structure, ejecting material from the core. Without truly enormous energy input this is eventually decelerated in the outer halo, but in e.g., "Momm-BH-36" almost all the gas within $\lesssim 70$ kpc is ejected.

Previous studies have similarly noted that pure isotropic kinetic input tends to fall into burst-quench cycles where either it fails to alter the cooling flow, or explosively ejects all the gas in the cooling radius (Ciotti et al., 2009, Shin et al., 2010). One alternative is to inject energy in a completely different form (discussed below). A second is to inject momentum at larger radii (distributing it away from the center), in a spatially-localized-but-time-dependent manner (i.e. not in a simple radially-outward-moving shell, which simply repeats this problem on larger scales; see

[10] The total kinetic energy input roughly matches the total cooling rate at the begin of the most explosive "Momm-BH-36" case, but soon become subdominant.

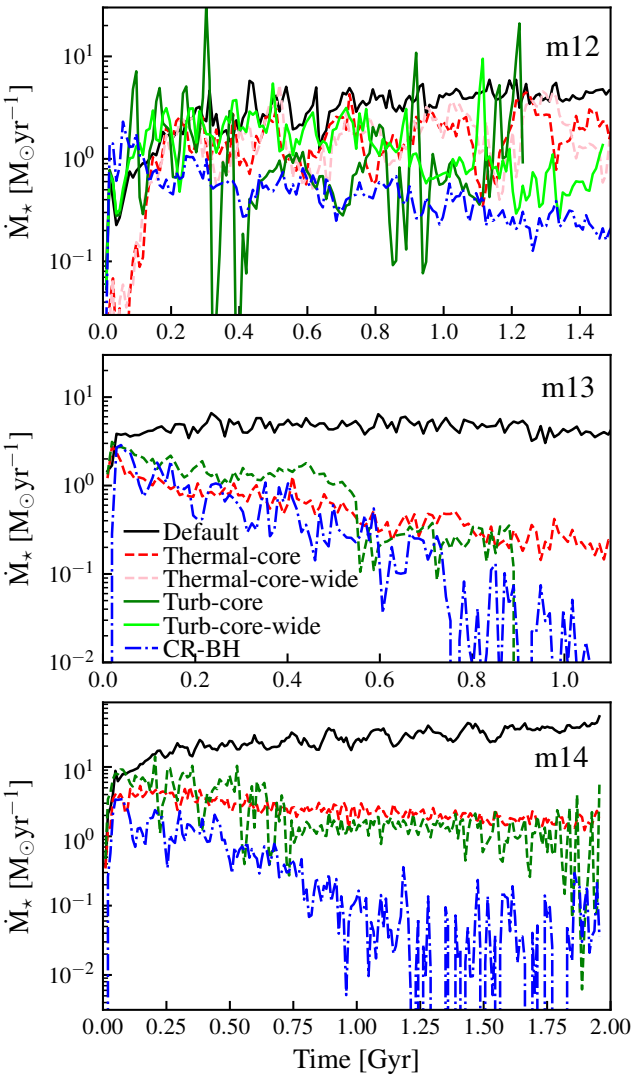

Figure 6.11: Galaxy SFRs (as Fig. 6.2) in our suite of simulations of different mass haloes (Table 6.3). The "wide" runs are only for m12. In **m13** and **m14**, turbulent stirring within the halo scale radius, or CR injection with appropriate energies, can quench, as can somewhat fine-tuned thermal energy injection. **m12** is more unstable and we find no thermal-heating solutions that quench without explosive ejection of halo baryons. Also, in **m12** the 'Turb-core' run confines stirring to $\sim 16\,$kpc, effectively "churning" the galactic disk and producing the bursty star formation; this disappears with a more extended stirring ('Turb-core-wide').

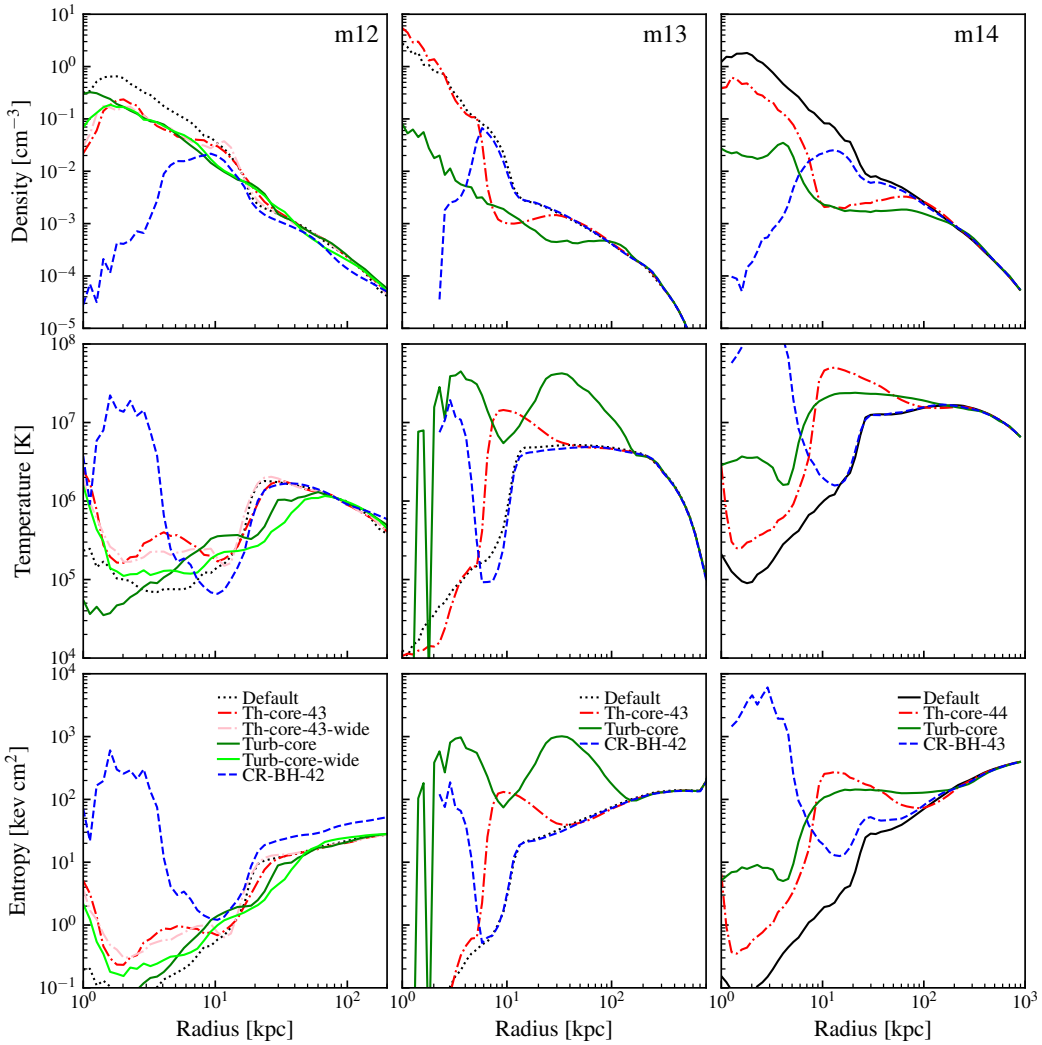

Figure 6.12: Density, temperature, & entropy profiles (as Fig. 6.3) averaged over the last $\sim$ 100 Myr of each run for the runs in Fig. 6.11. Even fine-tuned thermal heating produces negative temperature gradients in **m13** & **m14** and has little effect in **m12**. Turbulent stirring significantly depresses the density of **m13** (and raises its temperature), resembling the stronger-stirred **m14** cases, but a weaker stirring amplitude alleviates this. CR injection suppresses the core density inside the central few kpc (leading to mostly hot gas inside this radius), but leaves a positive temperature profile and intact density profile outside $r > 5 - 10$ kpc.

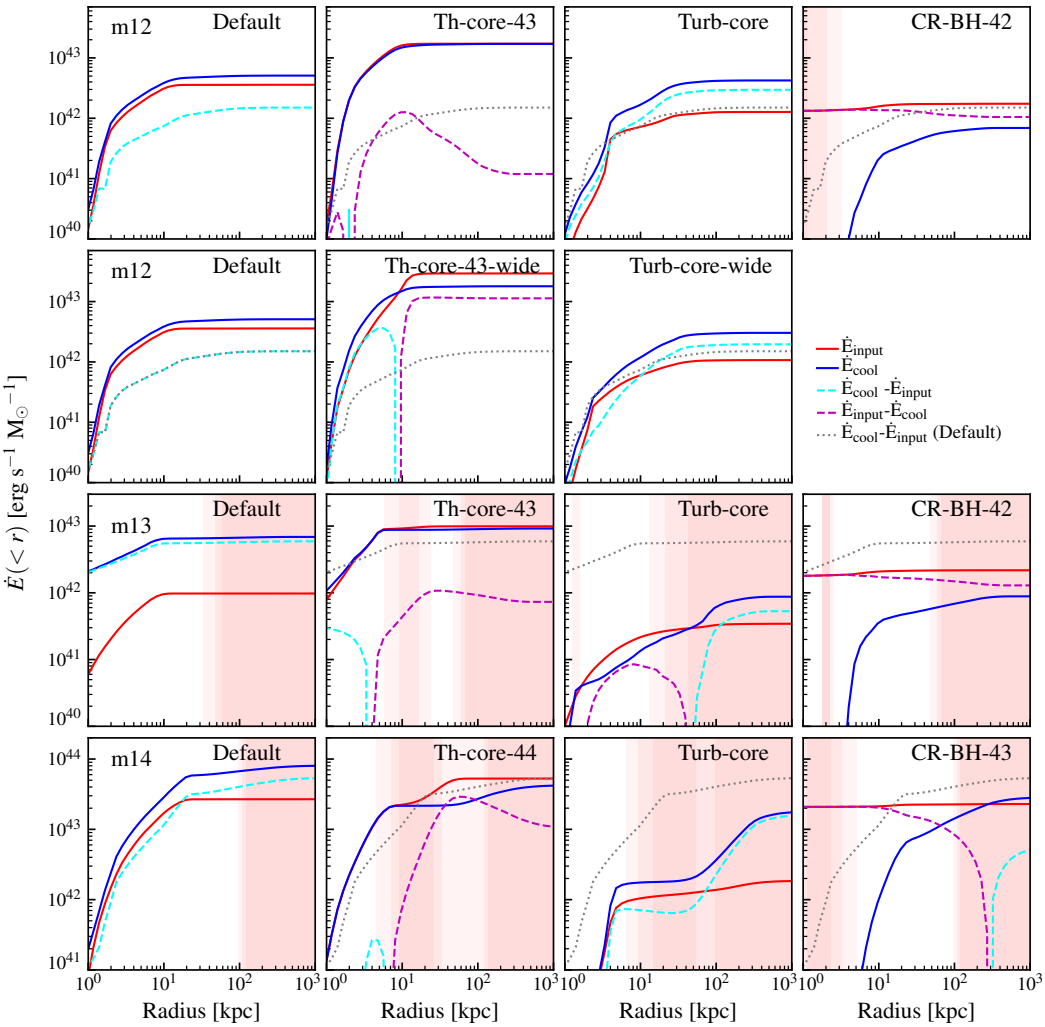

Figure 6.13: Cumulative energy input vs. cooling (as Fig. 6.8) for the simulations in Fig. 6.11. Turbulent stirring significantly decreases cooling in **m13** (owing to lower densities in Fig. 6.12; this is sensitive to the injection rate), but only suppresses cooling in the core in **m12**. Thermal heating can marginally balance cooling in **m13** and **m14** which have hotter, more stable gaseous haloes, but in **m12** heating puts more dense+enriched gas at $\sim 10^4 - 10^{5.5}$ K, increasing its cooling rate. CR injection substantially suppresses cooling rates in all cases.

Bourne & Sijacki 2017, Gaspari et al. 2011, Li & Bryan 2014, Yang & Reynolds 2016 for kinetic jets) – this is much closer in practice to our "turbulent stirring" runs below. A third alternative is to invoke a mix of isotropic kinetic feedback and thermal feedback (as in Ciotti et al., 2010, Dubois et al., 2013, Pillepich et al., 2018, Weinberger et al., 2017), a possibility we discuss below.

6.5.2 Thermal heating

In pure thermal heating models, nothing changes unless the overall heating rate is larger than the cooling rate. However, unless these are carefully balanced, this tends to produce a negative temperature gradient in direct contradiction with observed systems (Brighenti & Mathews, 2002, Mathews et al., 2006), and can drive explosive behavior which removes most of the gas in the halo. As a result, we must tune the energy input to match the cooling rate. We must also tune the injection radius to match the cooling radius, or else the energy is either "wasted" on gas at large radii (not cooling efficiently), or it excessively heats gas in the center driving Sedov-Taylor blastwaves that heat gas to very high temperature, eject gas in the central halo, produce negative temperature gradients, and strong shocks.

This is also consistent with previous studies that have repeatedly found nuclear energy injection alone tends to either fail to quench, or violently eject far too much gas from haloes (Genel et al., 2014). The alternatives are typically to invoke either (1) fine-tuning, or (2) some mix of other feedback mechanisms.

6.5.3 Turbulent stirring

In almost all of our turbulent stirring runs which produce suppressed cooling flows, the turbulent energy injection rate is much lower than the total cooling rate (especially pre-turbulence) – in other words, thermalized turbulent energy "heating" gas is not the dominant channel. We have also directly confirmed this by measuring the turbulent damping rate and comparing it to cooling. More important, turbulence mixes gas to larger radius, which (a) lowers the central density, (b) lowers the density of "up-welling" parcels (lowering their cooling rates), and (c) mixes them with hot gas (providing a form of "bulk conduction"). Together this lowers the effective cooling rate by an order of magnitude in the region with cooling times shorter than the Hubble time.

Taking 'Turb-core-4' for instance, Fig. 6.14 tracks the evolution of gas which is cold and dense at one initial time. After ~ 0.5 Gyr, less than half remains cold and dense or forms stars: most is shifted to larger radius and mixed into with hot gas (e.g.,

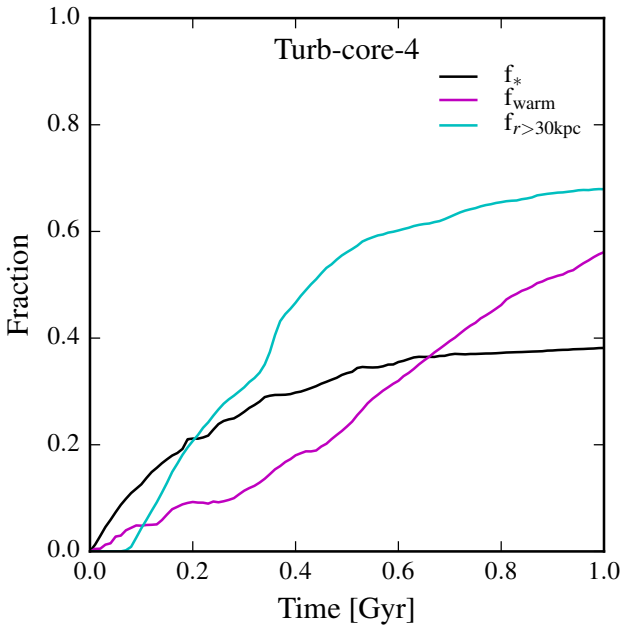

Figure 6.14: An example of what happens to rapidly cooling gas in the turbulent stirring runs which suppress cooling flows. Here in 'Turb-core-4' from Fig. 6.3, we track gas which is cold ($T < 8000$K) and dense ($n > 1\mathrm{cm}^{-3}$) at an early time (20 Myr) and follow its evolution. We first follow how much of the gas forms stars – this stabilizes as $\sim 40\%$ at late times. The majority of the gas is mixed to larger radii (here > 30 kpc), and becomes warm ($T > 10^5$ K).

Banerjee & Sharma, 2014, Kim & Narayan, 2003b, Parrish et al., 2010, Ruszkowski & Oh, 2010, 2011, Vernaleo & Reynolds, 2006).

6.5.4 Cosmic ray injection

Like turbulent stirring, CR injection provides another source of non-thermal pressure support, so the gas density and the cooling rate can be suppressed without directly heating up the gas. As shown in Fig. 6.15, CR energy does contribute as an important pressure source, reaching at least equipartition to the thermal energy. Moreover, CR diffusion spreads out the energy input and forms a quasi-steady-state isotropic pressure gradient even if all the CR energy is injected in the vicinity of the black hole.

Fig. 6.15 shows that only a small fraction of the CR energy is thermalized as the CRs propagate in the 'CR-BH-43/44' models,[11] and in all cases the heating from CRs is well below total cooling rates. This is expected: the timescale for CRs to lose

[11] The total thermalized CR energy as indicated by the green and magenta lines in the second row of Fig. 6.15 is less than 10% of the total CR input.

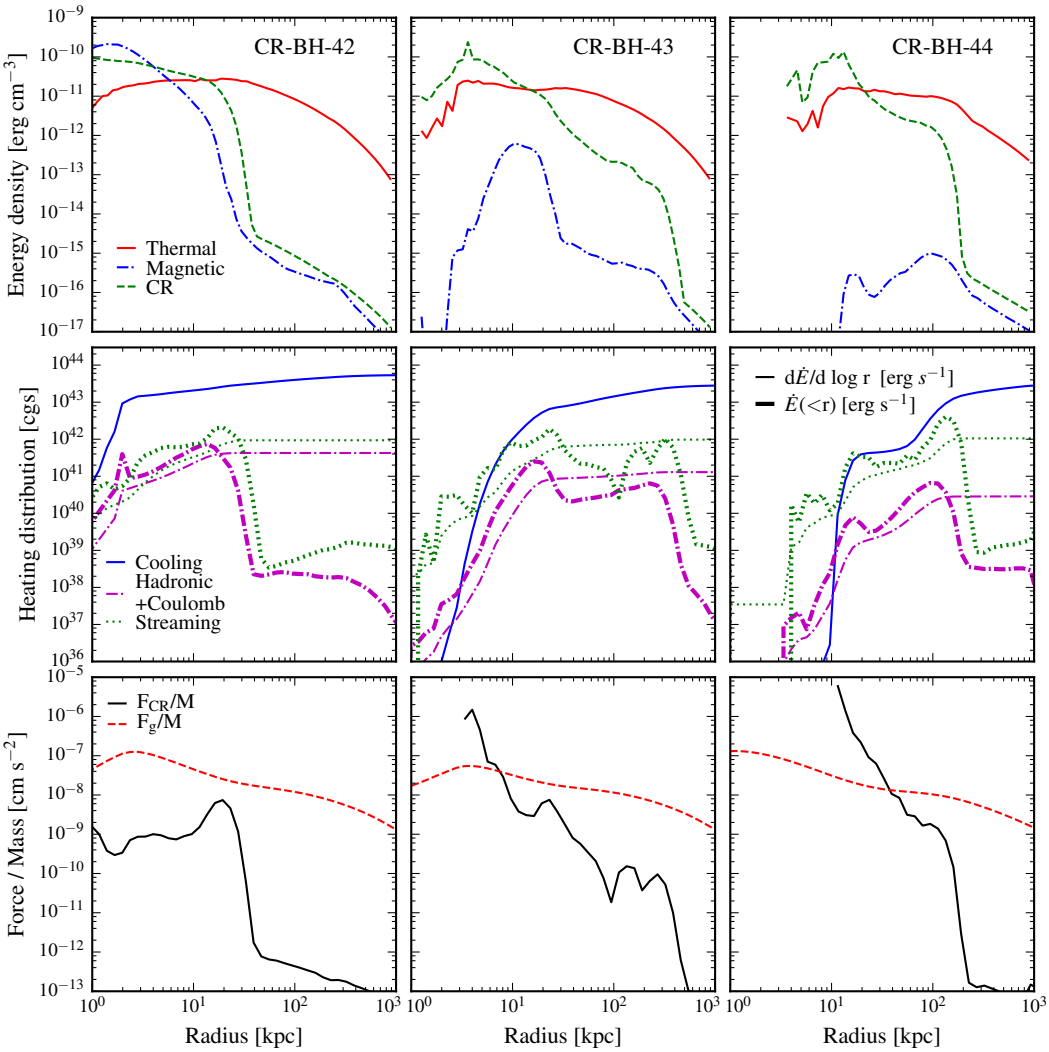

Figure 6.15: Comparison of energetics in our **m14** cosmic ray runs. *Top:* CR, magnetic, and thermal energy densities (averaged in spherical shells in the last 100 Myr of each run), for the three **m14** CR runs (Table 6.2). CR energy is non-negligible within < 30 kpc in each. *Middle:* Comparison of differential per-unit-radius ($d\dot{E}/d\log r$) and cumulative ($\dot{E}(<r)$) gas cooling rates versus CR "heating" rates. The latter includes collisional (hadronic+Coulomb) and streaming losses which transfer energy from CRs to thermal gas energy. CR heating is always much smaller than gas cooling except where the gas is almost completely evacuated in the central few kpc (and $\dot{E}_{\rm cool}$ is extremely small). In CR-BH-42, which retains dense central gas where CR losses are large, $\sim 60\%$ of the injected CR energy is thermalized, but in the CR-BH-43/44 runs where the central few kpc are lower-density, only $\sim 1-5\%$ of the CR energy is ever thermalized. *Bottom:* Gravitational acceleration $F_g/M \approx \partial\Phi/\partial r$ vs. acceleration from the CR pressure gradient ($\rho^{-1}\,\partial P_{\rm cr}/\partial r$). CR pressure dominates and pushes material out from the central cooling-core, to larger-r at larger $\dot{E}_{\rm cr}$.

energy to hadronic+Coulomb processes is $\sim 30\,\mathrm{Myr}\,(n/\mathrm{cm}^{-3})^{-1}$ while the diffusion timescale is $\sim r^2/\kappa_{\rm cr}$, so for our parameters losses in the core are only significant if its mean density exceeds $n \gtrsim 0.1\,\mathrm{cm}^{-3}\,(r_{\rm core}/10\,\mathrm{kpc})^{-2}$.[12] However, in 'CR-BH-43/44,' the temperature in the very center ($\lesssim 5-10\,\mathrm{kpc}$) does become large: this owes to CR pressure gradients suppressing the nuclear gas density sufficiently so that the low-density gas is heated efficiently by stellar feedback from the bulge and CR streaming heating.

On the other hand, the CR pressure gradient in Fig. 6.15 is able to offset gravity. If losses are negligible and diffusion dominates transport, around a point source with constant $\dot{E}_{\rm cr}$, the equilibrium pressure profile (assuming CRs are a $\gamma = 4/3$ ultra-relativistic fluid) is $P_{\rm cr} = \dot{E}_{\rm cr}/12\pi\,\kappa\,r$, which agrees well with the inner parts of our CR runs (outside the "holes" in 'CR-BH-43/44' within the central few kpc, where stellar feedback dominates).[13] Comparing this to the gravitational force we have:

$$\begin{aligned}\frac{F_{\rm CR}}{F_{\rm G}} =& \frac{1}{3\rho}\frac{\partial e_{\rm CR}/\partial r}{GM_{\rm enc}/r^2} \\ \sim& 2\left(\frac{\dot{E}}{10^{43}\mathrm{erg\,s^{-1}}}\right)\left(\frac{\kappa}{10^{29}\mathrm{cm^2\,s^{-1}}}\right)^{-1}\left(\frac{r}{10\,\mathrm{kpc}}\right)^{-1} \\ & \left(\frac{v_c}{500\mathrm{km\,s^{-}1}}\right)^{-2}\left(\frac{n}{0.01\mathrm{cm^{-3}}}\right)^{-1}. \end{aligned} \tag{6.1}$$

This is consistent with our result that when the CR energy input reaches $\sim 10^{43}\mathrm{erg\,s^{-1}}$, the CR pressure gradient starts to surpass the gravitational force in the core region and the core density and cooling rate start to be suppressed.

We emphasize that, as shown in Fig. 6.15, the heating from streaming loss does exceed the cooling rate in the core region in 'CR-BH-43' (the most stably quenched CR injection case), which is consistent with the previous studies (e.g., Ruszkowski et al., 2017b). However, we argue that the quenching is majorly caused by CR pressure lowering the gas density and therefore also the cooling rate instead of CR

[12] This explains why the run 'CR-BH-42', which does not quench and maintains dense gas in the center, does lose a non-negligible fraction $\sim 1/2$ of its CR energy to collisional+streaming losses. For 'CR-BH-43' and 'CR-BH-44', the collisional loss is more significant initially, but it drops to a lower value after the core density is suppressed. The competition between CR energy and gas densities being larger at small r, and diffusion times longer at large r, also explains why the collisional+streaming losses have the broad radial structure seen in Fig. 6.15.

[13] At large radii, if the streaming is at a quasi-constant Alfvén speed, streaming will dominate over diffusion at $r \gtrsim \kappa_{\rm cr}/v_{\rm stream} \sim 30\,\mathrm{kpc}\,(\kappa_{\rm cr}/10^{29}\,\mathrm{cm^2\,s^{-1}})\,(30\,\mathrm{km\,s^{-1}}/v_{\rm stream})$, which also defines the radius where streaming losses $\propto v_{\rm stream}\,\partial P_{\rm cr}/\partial r$ will be largest. Note in the simulations here the "cutoffs" in the CR profiles at $r \sim 100-1000\,\mathrm{kpc}$ owe to the simulations only having finite time for CRs to propagate from the nucleus to large radii.

heating overcoming cooling because a) the cooling rate of 'CR-BH-43' is much lower than the 'Default' run; b) the heating from stellar feedback can be at least comparable to the CR heating in the core region; and c) the black hole thermal heating run with exactly the same energy input does not quench the galaxy.

Given that we are not directly balancing the cooling rate by CR heating, the total CR energy in the halo does not need to be excessively high. The estimated > GeV gamma-ray luminosity of 'CR-BH-43' (from hadronic loss) is $L_\gamma \sim 10^{41}\,\mathrm{erg\,s^{-1}}$, which is lower than the observational upper bounds (Ackermann et al., 2016, Wiener & Zweibel, 2018). Besides, the estimated ~ GHz radio luminosity of 'CR-BH-43' from the secondary CR electrons (from CR protons), which contributes as part of the overall radio luminosity, is $L_{\rm radio} \sim 10^{39}\,\mathrm{erg\,s^{-1}}$, again within the observational constraint from the radio flux (e.g., Bravi et al., 2016, Giacintucci et al., 2014).[14]

6.6 Conclusions

In this paper, we have attempted a systematic exploration of different qualitative physical mechanisms by which energy can be injected into massive haloes to quench galaxies and suppress cooling flows. We specifically considered models with radial momentum injection (e.g., "wind" or "radiation pressure" or "isotropic kinetic" models), thermal heating (e.g., "shocked wind" or "isotropic sound wave" or "photo/Compton-heating" or "blastwave" models), turbulent "stirring" (e.g., "convective/buoyant bubble" or "precessing jet" or "jet/bubble instability-driven" or "subhalo/merger/satellite wind-driven" models), and cosmic ray injection (e.g., CRs from compact or extended radio jets/lobes, shocked disk winds, or inflated bubbles). We vary the associated energetics and/or momentum fluxes, spatial coupling/driving scales, and halo mass scale from $\sim 10^{12} - 10^{14}\,M_\odot$. These were studied in fully global but non-cosmological simulations including radiative heating and cooling, self-gravity, star formation, and stellar feedback from supernovae, stellar mass-loss, and radiation, enabling a truly "live" response of star formation and the multi-phase ISM to cooling flows; we used a hierarchical super-Lagrangian refinement scheme to reach $\sim 10^4\,\mathrm{M_\odot}$ mass resolution, much higher than many previous global studies.

Of the cases surveyed, only turbulent stirring within a radius of order the halo scale radius, or cosmic ray injection (with appropriate energetics) were able to maintain a stable, cool-core, low-SFR halo for extended periods of time, across all halo masses surveyed, without obviously violating observational constraints on halo

[14] We assume that all the secondary CR electrons decay via synchrotron emission.

gas properties or exceeding plausible energy budgets for low-luminosity AGN in massive galaxies.

- Isotropic momentum injection with momentum flux lower than $\sim 10^{36} \mathrm{g\,cm\,s^{-2}}\,(M_{\rm halo}/10^{14}\,M_{\odot})^{1/3}$ has little effect on cooling flows or star formation, while larger momentum fluxes simply generate an "explosion" that evacuates gas from the halo core, drives strong shocks in the outer halo, generates steep negative temperature gradients out to $> 100\,$kpc, and heats gas to enormous temperatures (all in conflict with observations).

- Thermal heating, if concentrated in the halo core, similarly transitions sharply from doing nothing when the input is below cooling rates, to generating an explosive Sedov-Taylor blastwave when the input exceeds cooling rates (again, in conflict with observations). Thermal heating extended over too large a radius "wastes" all its energy at very large radii and does little in the core. It is possible to fine-tune thermal heating (by setting energy input equal to cooling rates, and the coupling scale equal to the cooling radius), but this (a) requires thermal heating rates $\gtrsim 10^{44}\,\mathrm{erg\,s^{-1}}$ in $\gtrsim 10^{14}\,M_{\odot}$ haloes (corresponding to bright quasars if the heating efficiency is $\sim 1\%$), (b) still generates mild negative temperature gradients to $\sim 100\,$kpc, and (c) fails in less massive haloes $\lesssim 10^{12.5}\,M_{\odot}$ where virial temperatures are lower.

- Cosmic rays can suppress cooling and SFRs by supporting non-thermal pressure gradients which are comparable to or exceed gravity in the core, with modest energetics in an order-of-magnitude range around $\dot{E}_{\rm cr} \sim 10^{43}\,\mathrm{erg\,s^{-1}}\,(M_{\rm halo}/10^{14}\,M_{\odot})$. CR "heating" (via streaming or collisional terms) is negligible as modeled here in the interesting regime. For reasonable diffusivities, the injection scale/kernel also does not matter sensitively since CRs form an equilibrium diffusion profile, unless the injection scale is very large $\gtrsim 30-100\,$kpc. The central few kpc tend to be "hot" because they are eventually depleted of all dense gas, but the larger-scale density/temperature/entropy structure of the cool-core halo can be stably maintained for extended periods of time, despite suppressed SFRs and actual cooling flow rates onto the galaxy.

- Turbulent stirring can also suppress star formation, through a combination of suppressing the core gas density (by providing non-thermal pressure and "lofting" parcels up the potential where they buoyantly expand), and mixing

cold and dense gas into the hot halo (providing "bulk conduction"), with even lower energetics in $\dot{E}_{\rm turb} \sim 10^{41-42}\,{\rm erg\,s^{-1}}\,(M_{\rm halo}/10^{14}\,M_{\odot})$ or (equivalently) momentum flux $\dot{P}_{\rm turb} \sim 10^{34}\,{\rm g\,cm\,s^{-2}}\,(M_{\rm halo}/10^{14}\,M_{\odot})$ within a radius of order the halo scale radius ($\lesssim 100\,{\rm kpc}$). Towards the low end of this range, haloes maintain cool-core features, while towards the high end, they evolve from cool-core to non-cool-core. Strong stirring at $r \gtrsim 100\,{\rm kpc}$ tends to remove significant gas from the halo and suppresses the X-ray luminosity below observations; stirring confined only to $\lesssim 10-20\,{\rm kpc}$ acts more like galactic fountains and fails to efficiently suppress cooling. Turbulent "heating" (via compression or shocks or viscosity) is never dominant.

- If injection transforms a halo into a non-cool-core, then if the core density is suppressed to an extent that the energy input from old stellar populations (SNe Ia and AGB mass-loss) exceeds cooling rates, the halo never "rejuvenates" even if the feedback injection shuts off.

In summary, our study supports the idea that quenching – at least of observed $z \sim 0$ massive haloes – is not dominated by single violent or "explosive" events, but by lowering densities and suppressing cooling via mechanisms that involve relatively mild energetics and non-thermal pressure. Turbulence and cosmic rays represent promising avenues to this, either of which has the potential to quench the models surveyed here without obviously contradicting basic observational constraints. Both operate very efficiently, with required energetics comparable to those expected in jets of low-luminosity AGN.

We emphasize that we are not saying it is impossible to devise models of feedback using a combination of thermal and radial mechanical energy input which produce quenching and plausible massive halo properties (in fact, we explore a couple such models here). However, consistent with most previous studies, we find that these classes of models (a) require fine-tuning, in energetics and coupling scale as a function of halo mass, (b) generally require optimistically high energetics (at least order-of-magnitude larger than the CR models, and two orders of magnitude higher than the turbulent models favored here), and (c) may still have difficulty reproducing more subtle observational properties (e.g., distributions of temperature profile slopes).

We should also emphasize that we are not implying that AGN feedback is represented by any one of these mechanisms (especially as we model them). Real feedback is

a mix of many different processes operating at once, often simultaneously on very different scales (e.g., radiation and accretion-disk winds and jets may be coupling to the gas all on different spatial scales). Our goal was simply to focus on an (intentionally) highly-idealized model of each form of injection, to understand the constraints and different qualitative behaviors of different types of energy injection. This paper was a follow-up to Paper I, where we also surveyed a large number of simulations to emphasize that *something* beyond the "default" physics of cooling, self-gravity and gravitational stability, magnetic fields, conduction, viscosity, star formation, and feedback from stars (radiative and supernovae and stellar mass-loss), was required to resolve the cooling flow problem. Here we identify plausible *classes* of physical candidates for that "something" (e.g., enhanced turbulence and CR from AGN). In our next study, we intend to model these classes more realistically: for example, explicitly modeling a narrow jet which simultaneously carries kinetic luminosity and cosmic rays. This raises a host of questions we have (again, intentionally) not tried to address here: for example, what happens if the injection is highly anisotropic? And can turbulence actually be driven by *physical* processes originating from an AGN? And what is the ratio of energy in radial momentum flux, thermal heating, cosmic ray injection, and turbulent stirring which comes from e.g., nuclear winds vs. compact jets vs. "bubbles"? These and many more questions remain open and critical for progress in this field.

Chapter 7

SUMMARY AND FUTURE DIRECTIONS

In this thesis, I investigated the effects of stellar feedback (especially the discrete processes), AGN feedback, and fluid microphysics (including magnetic fields, conduction, and viscosity), on the properties and the evolution of a wide variety of galaxies. These physics are built and explored on top of the state-of-the-art high-resolution cosmological hydrodynamic zoom-in simulations from the FIRE-2 suite, and isolated galaxy simulations that utilize the FIRE-2 stellar feedback. The FIRE stellar feedback naturally generates a multi-phase ISM and CGM, a realistic environment to test these uncertainties in baryonic physics.

In the first part of the thesis, I discussed the discrete effects of stellar feedback including the discretized individual SNe, IMF sampling and extreme events like hypernovae. I concluded that discretizing SNe injection is crucial (which is included in standard FIRE physics) is absolutely crucial. Treating SNe as continuous energy/momentum sources with time-averaged rates (instead of individual events) smears the energy in time and space, which allows it to radiate away far too efficiently – the "overcooling problem". Partially because of strong clustering of star formation, the IMF sampling has a relatively small effect on galaxy properties, within the stochastic uncertainties of galaxy simulations. Hypernovae with a total energy of 100 supernovae are powerful enough to temporarily shut down the star formation, but the effects have no fundamental difference from those of overlapping SNe, which naturally happen. Even in the small ultra-faint galaxy that we explored, a hypernova only quenches the galaxy for $\sim Gyr$, and will not permanently shut down the star formation. Therefore, it should be possible to observe HNe yields in next-generation stars in faint dwarfs.

In the second part of the thesis, I explored the effect of fluid microphysics in galaxies of $10^{10}-10^{13} M_{\odot}$ (majorly sub-L* galaxies). Stellar feedback is shown to be the dominant factor in predicting galactic properties. Once the stellar feedback is explicitly implemented with FIRE stellar feedback model, magnetic fields, conduction, and viscosity only have minor effects on the galaxy properties like SFR, phase structure, or outflows. It also strongly alters the amplifications and morphology of magnetic fields. FIRE stellar feedback results in much more randomly oriented magnetic

fields, while sub-grid feedback models generally predict more coherent large schedule magnetic structure. However, despite the stellar feedback, the amplification of magnetic fields in ISM gas is largely dominated by flux-freezing compression.

In the final part of my thesis, I focus on the massive galaxies of $10^{12} - 10^{14}\mathrm{M}_{\odot}$, where the physical mechanisms that regulate the observation inferred cooling flows are highly uncertain – the classic "cooling flow problem". I showed that non-AGN feedback type solutions in the literature, including stellar feedback, the cosmic ray from stellar feedback, magnetic fields, conduction, and morphological quenching cannot possibly quench the galaxies. Owing to the insufficient energy, stellar feedback (including cosmic rays from SNe) only alters the balance of cold/warm gas and the rate at which the cooled gas within the galaxy turns into stars, but not the net baryonic inflows. Conduction is most effective in the hot gas and is therefore important only in the most massive halo. However, even in a $10^{14} M_{\odot}$ halo, conduction only suppresses the cooling flows by at most a factor of ~ 2. Magnetic pressure and stellar morphology also do not affect the cooling flows because the former never reach equipartition with the thermal or turbulent energy in CGM, and the latter has a negligible effect to the gas stability as cooling flows continuously enhance the gas surface density in the star forming regions.

After ruling out the non-AGN solution to the cooling flow problem, I explored the most popular, and perhaps promising solution – "AGN feedback". Since the qualitative form of this energetic input still remains uncertain, I explore generic classes of AGN feedback models proposed in the literature. I showed that enhancing turbulence and injecting cosmic ray are probably the most important aspects of AGN feedback in quenching of galaxies. Since they provide non-thermal pressure support that stably suppresses the core density, they can stably suppressed the cooling flows without overheating the galactic core. The enhanced turbulence also effectively mixes the cold gas into the hot halo, which also reduces the overall cooling flows.

Although we have explored these baryonic physics in galaxy evolution to great detail, there is still many questions left unanswered. The largest uncertainty probably lies in AGN feedback. We explored a various form of energy injection trying to understand the effect from each possible aspect of AGN feedback, but how AGN feedback should be modeled realistically is unknown. Furthermore, to model AGN feedback self-consistently, the accretion of black holes, which is the physical original of AGN feedback, is also highly relevant. Finally, how does AGN feedback interacts with the magnetic fields and other fluid microphysics to affect the CGM should also be

Table 7.1: Parameters for the preliminary suite of jet simulations.

model	$\dot{M}$ $M_\odot$ s^{-1}	$v_{\rm initial}$ km s^{-1}	$T_{\rm initial}$ K	$\dot{E}_{\rm kinetic}$ erg s^{-1}	$\dot{E}_{\rm thermal}$ erg s^{-1}
Kin-6e42+Th-1.6e41	2.0	3000	1e7	6e42	1.6e41
Kin-6e42+Th-1.6e42	2.0	3000	1e8	6e42	1.6e42
Kin-6e42+Th-1.6e43	2.0	3000	1e9	6e42	1.6e43
Kin-6e44+Th-1.6e41	2.0	30000	1e7	6e42	1.6e41

(1) Model name. (2) Mass flux. (3) Initial velocity. (4) Initial temperature. (5) Initial kinetic energy input rate. (6) Initial thermal energy input rate.

explored. In the following, I will briefly review these possible directions for future study and planned projects aligned with my thesis work.

7.1 The physics of AGN jets

One possible realistic form of AGN feedback that can naturally stir up turbulence and carry cosmic ray energy is jets, frequently observed in massive ellipticals and clusters. I will perform a set of isolated simulations from L* galaxies to massive cluster ellipticals ($M_{\rm halo} \sim 10^{12} - 10^{14} M_\odot$), with different jet models (on top of stellar feedback) of constant energy flux, by systematically varying the opening angle, the level of precession, the strength, and the energy composition of each form (thermal, kinetic, and cosmic ray). By incorporating the "Feedback in Realistic Environment" (FIRE;Hopkins et al. 2018b) stellar feedback model, jets are ensured to be simulated in a realistic environment. Additionally, fluid microphysics (magnetic fields, conduction, and viscosity) will be included to realistically capture its non-linear interactions with jet models. Although some aspects of jets have been explored individually to some extent in the current state-of-the-art simulations (e.g., Bourne & Sijacki, 2017, Gaspari et al., 2012a,b, Li & Bryan, 2014, Li et al., 2017, Martizzi et al., 2018, Ruszkowski et al., 2017b, Yang & Reynolds, 2016), this set simulations will be the first to test all the variations of jet models on top of stellar feedback and fluid microphysics over a wide range of halo mass. They will provide a complete and unbiased picture for how jets interact with gas in the ISM/CGM. Fig. 7.1 shows the edge-on temperature and projected density of a subset of the preliminary suite of jet simulations with different kinetic and thermal input rate (as described in Table 7.1).

This new, state-of-the-art simulations could help us investigate the following ques-

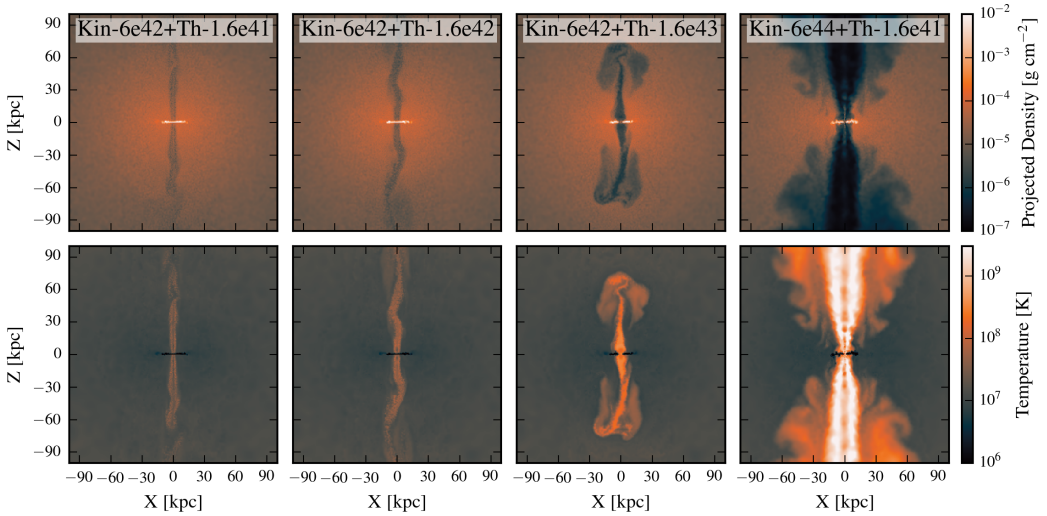

Figure 7.1: The edge-on average temperature and projected density of the central 2kpc slice ($|y| < 1$ kpc) of simulation with different jet models. The plots are all made at 200 Myr after the start of thr simulations. The parameters of the jet modeld are shown in Table 7.1. The hotter the jet is, the more thermal pressure widen the chimney. Despite the same launching speed, the wider the jet is, the slower it propagate given the larger volume of gas above to lift up. The expansion of the shock fronts, especially in the hotter or faster jet cases, have a huge effect in heating up the CGM.

tions:

- **Turbulent structure:** As discussed above in § 6, turbulence can effectively regulate the cooling flow in massive galaxies, but the source of the turbulence is left undefined in that work. Many authors have suggested that jets can drive turbulence in the CGM (e.g., Bourne & Sijacki, 2017, Li & Bryan, 2014, Martizzi et al., 2018, Yang & Reynolds, 2016), but it unclear exactly how the turbulence is generated, whether the amount is sufficient to prevent a cooling flow, and how the detailed structure of that turbulence depends on the properties of the jets. Fortunately, it may be possible to constrain the latter by observations taken with X-ray telescopes such as Hitomi (Hitomi Collaboration et al., 2016, 2018), which provide tight restrictions on the turbulent velocity in the clusters. The relationships between the jet properties discussed above and the resultant turbulent structure in the CGM can be predicted.

- **Energy balance in different phases and regions:** Besides turbulent energy, the distribution of CR energy and thermal energy in different regions of a halo,

and in the gas of different phases is also important. The distributions will be affected not only by the jet models, but also largely by the fluid microphysics and the detailed CR modeling (CR streaming, diffusion, and cooling loss). With a better understanding of the energy distribution, I can tell whether jets quench the galaxy through heating (whether directly or thermalizing the other form of energy) or through generating pressure support, which lowers the gas density and cooling rate.

7.2 Interplay of AGN model and fluid microphysics

Both AGN feedback and fluid microphysics affect the local thermal instability, and hence the rate at which gas precipitates out of the CGM, which contributes to the cooling flow (e.g., Gaspari et al., 2017, Voit et al., 2015, 2017). In addition, magnetic fields, conduction, viscosity, can interact non-linearly with the AGN feedback by altering how energy propagates in the CGM. Specifically, the following two topics can be explored.

- **The impact of AGN over magnetic amplification:** In Chapter 4, I showed that stellar feedback strongly alters magnetic field strength and morphology; particularly the adiabatic compression (with the magnetic flux frozen) dominates the amplification of field strength in stellar-feedback-only simulations. However, that work primarily focused on the ISM where the gas density and magnetic field strength are high. The aforementioned set of simulations can generalize these explorations from ISM to the CGM, where gas densities and field strengths are much lower, and to do so in the presence of jets. Specifically, the magnetic field amplification mechanism can be better understood by analyzing turbulent/magnetic power spectrum, and the relationship between magnetic curvature and field strength.
- **The interplay among conduction, viscosity, and AGN:** In Chapter 3 and Chapter 5, I showed that conduction and viscosity independently have minor effects on ISM properties and cooling flows. However, they may still exert indirect influences. Some literature suggests that the impact of the AGN on the galaxy and halo can be affected by conduction, which alters the AGN energy transport in the CGM (e.g., Kannan et al., 2016, Yang & Reynolds, 2016). Furthermore, viscosity may have an impact on the effective turbulent injection scale of the jet, the turbulent power spectrum, and the organization and evolution of the associated Fermi bubbles (e.g., Guo et al., 2012). Besides the galaxy-scale simulations, small-scale simulations of a patch of the

circum-galactic/intracluster medium also show that magnetic field and fluid microphysics have an impact on local thermal (and other) instabilities (e.g., Ji et al., 2018, Kunz et al., 2012, McCourt et al., 2012, Sharma et al., 2010). The insights from smaller scale simulations could be utilized to conduct a thorough investigation of the interplay between conduction, viscosity, and various jet models in galaxy-scale simulation.

7.3 Black hole accretion

Tradition accretion models (e.g., Bondi-Hoyle (Bondi, 1952, Springel et al., 2005) and the gravitational torque accretion models (Anglés-Alcázar et al., 2017a, Hopkins & Quataert, 2011)) make simplifying assumptions about the $\sim$ kpc environment around the black hole, leading to predicted accretion rates that differ by orders of magnitude. The assumptions can be tested in the aforementioned simulations. The inferred accretion rate can also be compared to the required AGN energy for maintaining a stable quenched simulation in the simulations.

Moreover, with the super-Lagrangian refinement scheme, which enforces higher resolution through particle splitting at the designated region, resolving the gravitational capture of gas by a black hole in galaxy simulations become possible. This can potentially lead to a more realistic implementation of black hole accretion than the traditionally sub-grid accretion models.

A combination of my thesis work and the planned future direction and projects can lead to a more physically motivated self-consistent AGN feedback model.

BIBLIOGRAPHY

Ackermann M., et al., 2016, ApJ, 819, 149

Agertz O., Kravtsov A. V., 2016, ApJ, 824, 79

Agertz O., Kravtsov A. V., Leitner S. N., Gnedin N. Y., 2013, ApJ, 770, 25

Amorisco N. C., Zavala J., de Boer T. J. L., 2014, ApJ, 782, L39

Anders E., Grevesse N., 1989, Geochimica et Cosmochimica Acta, 53, 197

Anderson M. E., Gaspari M., White S. D. M., Wang W., Dai X., 2015, MNRAS, 449, 3806

Anderson M. E., Churazov E., Bregman J. N., 2016, MNRAS, 455, 227

Anglés-Alcázar D., Davé R., Faucher-Giguère C.-A., Özel F., Hopkins P. F., 2017a, MNRAS, 464, 2840

Anglés-Alcázar D., Faucher-Giguère C.-A., Kereš D., Hopkins P. F., Quataert E., Murray N., 2017b, MNRAS, 470, 4698

Armillotta L., Fraternali F., Werk J. K., Prochaska J. X., Marinacci F., 2017, MNRAS, 470, 114

Asplund M., Grevesse N., Sauval A. J., Scott P., 2009, ARA&A, 47, 481

Balbus S. A., 2000, ApJ, 534, 420

Baldry I. K., Glazebrook K., Brinkmann J., Ivezić Ž., Lupton R. H., Nichol R. C., Szalay A. S., 2004, ApJ, 600, 681

Balogh M. L., Babul A., Voit G. M., McCarthy I. G., Jones L. R., Lewis G. F., Ebeling H., 2006, MNRAS, 366, 624

Banerjee N., Sharma P., 2014, MNRAS, 443, 687

Barai P., Viel M., Murante G., Gaspari M., Borgani S., 2014, MNRAS, 437, 1456

Bauer A., Springel V., 2012, MNRAS, 423, 2558

Beck R., 2007, in Miville-Deschênes M.-A., Boulanger F., eds, EAS Publications Series Vol. 23, EAS Publications Series. pp 19–36 (arXiv:astro-ph/0603531), doi:10.1051/eas:2007003

Beck R., 2009, Astrophysics and Space Sciences Transactions, 5, 43

Beck R., Brandenburg A., Moss D., Shukurov A., Sokoloff D., 1996, ARA&A, 34, 155

Beck A. M., Lesch H., Dolag K., Kotarba H., Geng A., Stasyszyn F. A., 2012, MNRAS, 422, 2152

Begelman M. C., 2004, Coevolution of Black Holes and Galaxies, p. 374

Bell E. F., McIntosh D. H., Katz N., Weinberg M. D., 2003, ApJS, 149, 289

Berezinsky V., Gazizov A., Grigorieva S., 2006, PhRvD, 74, 43005

Bernet M. L., Miniati F., Lilly S. J., Kronberg P. P., Dessauges-Zavadsky M., 2008, Nature, 454, 302

Binney J., Cowie L. L., 1981, ApJ, 247, 464

Blandford R. D., Payne D. G., 1982, MNRAS, 199, 883

Blanton M. R., Eisenstein D., Hogg D. W., Schlegel D. J., Brinkmann J., 2005, ApJ, 629, 143

Blitz L., Rosolowsky E., 2004, ApJ, 612, L29

Bondi H., 1952, MNRAS, 112, 195

Booth C. M., Schaye J., 2009, MNRAS, 398, 53

Booth C. M., Agertz O., Kravtsov A. V., Gnedin N. Y., 2013, ApJ, 777, L16

Bournaud F., Elmegreen B. G., Teyssier R., Block D. L., Puerari I., 2010, MNRAS, 409, 1088

Bourne M. A., Sijacki D., 2017, MNRAS, 472, 4707

Braginskii S. I., 1965, Reviews of Plasma Physics, 1, 205

Bravi L., Gitti M., Brunetti G., 2016, arXiv e-prints, p. arXiv:1603.00368

Brighenti F., Mathews W. G., 2002, ApJ, 567, 130

Brook C. B., Stinson G., Gibson B. K., Shen S., Macciò A. V., Obreja A., Wadsley J., Quinn T., 2014, MNRAS, 443, 3809

Brüggen M., Scannapieco E., 2009, MNRAS, 398, 548

Brüggen M., Scannapieco E., 2016, ApJ, 822, 31

Bryan G. L., Norman M. L., 1998, ApJ, 495, 80

Bullock J. S., Kravtsov A. V., Weinberg D. H., 2000, ApJ, 539, 517

Butsky I. S., Quinn T. R., 2018, ApJ, 868, 108

Cayatte V., Kotanyi C., Balkowski C., van Gorkom J. H., 1994, AJ, 107, 1003

Ceverino D., Klypin A., 2009, ApJ, 695, 292

Chan T. K., Keres D., Hopkins P. F., Quataert E., Su K. Y., Hayward C. C., Faucher-Giguere C. A., 2018, arXiv e-prints, p. arXiv:1812.10496

Choi E., Stone J. M., 2012, ApJ, 747, 86

Choi E., Ostriker J. P., Naab T., Johansson P. H., 2012, ApJ, 754, 125

Choi E., Ostriker J. P., Naab T., Oser L., Moster B. P., 2015, MNRAS, 449, 4105

Cioffi D. F., McKee C. F., Bertschinger E., 1988, ApJ, 334, 252

Ciotti L., Ostriker J. P., 2001, ApJ, 551, 131

Ciotti L., D'Ercole A., Pellegrini S., Renzini A., 1991, ApJ, 376, 380

Ciotti L., Ostriker J. P., Proga D., 2009, ApJ, 699, 89

Ciotti L., Ostriker J. P., Proga D., 2010, ApJ, 717, 708

Colbrook M. J., Ma X., Hopkins P. F., Squire J., 2016, ArXiv e-prints, arXiv:1610.06590,

Cole S., Lacey C. G., Baugh C. M., Frenk C. S., 2000, MNRAS, 319, 168

Conroy C., Ostriker J. P., 2008, ApJ, 681, 151

Conroy C., van Dokkum P. G., Kravtsov A., 2015, ApJ, 803, 77

Cooke J., et al., 2012, Nature, 491, 228

Cowie L. L., Binney J., 1977, ApJ, 215, 723

Cowie L. L., McKee C. F., 1977, ApJ, 211, 135

Croton D. J., et al., 2006, MNRAS, 365, 11

Crutcher R. M., Wandelt B., Heiles C., Falgarone E., Troland T. H., 2010, ApJ, 725, 466

Davé R., Thompson R., Hopkins P. F., 2016, MNRAS, 462, 3265

Dedner A., Kemm F., Kröner D., Munz C.-D., Schnitzer T., Wesenberg M., 2002, Journal of Computational Physics, 175, 645

Dekel A., Birnboim Y., 2006, MNRAS, 368, 2

Dekel A., Sari R., Ceverino D., 2009, ApJ, 703, 785

Di Matteo T., Springel V., Hernquist L., 2005, Nature, 433, 604

Dimonte G., Tipton R., 2006, Physics of Fluids, 18, 085101

Dobbs C. L., Burkert A., Pringle J. E., 2011, MNRAS, 413, 2935

Dolag K., Jubelgas M., Springel V., Borgani S., Rasia E., 2004, ApJ, 606, L97

Dong R., Stone J. M., 2009, ApJ, 704, 1309

Dubois Y., Teyssier R., 2010, A&A, 523, A72

Dubois Y., Pichon C., Devriendt J., Silk J., Haehnelt M., Kimm T., Slyz A., 2013, MNRAS, 428, 2885

Dwek E., 1998, ApJ, 501, 643

Eisenreich M., Naab T., Choi E., Ostriker J. P., Emsellem E., 2017, MNRAS, 468, 751

El-Badry K., Wetzel A., Geha M., Hopkins P. F., Kereš D., Chan T. K., Faucher-Giguère C.-A., 2016, ApJ, 820, 131

Enßlin T., Pfrommer C., Miniati F., Subramanian K., 2011, A&A, 527, A99

Erb D. K., Steidel C. C., Shapley A. E., Pettini M., Reddy N. A., Adelberger K. L., 2006, ApJ, 646, 107

Escala I., Kirby E. N., Wetzel A. R., Hopkins P. F., 2016, in American Astronomical Society Meeting Abstracts. p. 209.01

Evans II N. J., 1999, ARA&A, 37, 311

Evans II N. J., et al., 2009, ApJS, 181, 321

Fabian A. C., 1994, ARA&A, 32, 277

Fabian A. C., 1999, MNRAS, 308, L39

Fabian A. C., 2012, ARA&A, 50, 455

Fabian A. C., Arnaud K. A., Bautz M. W., Tawara Y., 1994, ApJ, 436, L63

Fabian A. C., Voigt L. M., Morris R. G., 2002, MNRAS, 335, L71

Farber R., Ruszkowski M., Yang H.-Y. K., Zweibel E. G., 2018, ApJ, 856, 112

Faucher-Giguere C.-A., 2017, preprint, (arXiv:1701.04824)

Faucher-Giguère C.-A., Quataert E., 2012, MNRAS, 425, 605

Faucher-Giguère C.-A., Lidz A., Zaldarriaga M., Hernquist L., 2009, ApJ, 703, 1416

Faucher-Giguère C.-A., Quataert E., Hopkins P. F., 2013, MNRAS, 433, 1970

Faucher-Giguère C.-A., Hopkins P. F., Kereš D., Muratov A. L., Quataert E., Murray N., 2015, MNRAS, 449, 987

Faucher-Giguère C.-A., Feldmann R., Quataert E., Kereš D., Hopkins P. F., Murray N., 2016, MNRAS, 461, L32

Federrath C., Klessen R. S., Schmidt W., 2008, ApJ, 688, L79

Federrath C., Roman-Duval J., Klessen R. S., Schmidt W., Mac Low M.-M., 2010, A&A, 512, A81

Federrath C., Chabrier G., Schober J., Banerjee R., Klessen R. S., Schleicher D. R. G., 2011a, Physical Review Letters, 107, 114504

Federrath C., Sur S., Schleicher D. R. G., Banerjee R., Klessen R. S., 2011b, ApJ, 731, 62

Federrath C., Schober J., Bovino S., Schleicher D. R. G., 2014, ApJ, 797, L19

Fielding D., Quataert E., Martizzi D., Faucher-Giguère C.-A., 2017, MNRAS, 470, L39

Fitts A., et al., 2017, MNRAS, 471, 3547

Flores R. A., Primack J. R., 1994, ApJ, 427, L1

Forbes J. C., Krumholz M. R., Goldbaum N. J., Dekel A., 2016, Nature, 535, 523

Fraternali F., Marasco A., Marinacci F., Binney J., 2013, ApJ, 764, L21

Fujita Y., Ohira Y., 2011, ApJ, 738, 182

Fujita Y., Matsumoto T., Wada K., 2004, ApJ, 612, L9

Fujita Y., Kimura S., Ohira Y., 2013, MNRAS, 432, 1434

Fumagalli M., Prochaska J. X., Kasen D., Dekel A., Ceverino D., Primack J. R., 2011, MNRAS, 418, 1796

Gal-Yam A., 2012, Science, 337, 927

Gaspari M., Sądowski A., 2017, ApJ, 837, 149

Gaspari M., Melioli C., Brighenti F., D'Ercole A., 2011, MNRAS, 411, 349

Gaspari M., Brighenti F., Temi P., 2012a, MNRAS, 424, 190

Gaspari M., Ruszkowski M., Sharma P., 2012b, ApJ, 746, 94

Gaspari M., Brighenti F., Temi P., 2015, A&A, 579, A62

Gaspari M., Temi P., Brighenti F., 2017, MNRAS, 466, 677

Genel S., et al., 2014, MNRAS, 445, 175

Genzel R., et al., 2008, ApJ, 687, 59

Giacintucci S., Markevitch M., Venturi T., Clarke T. E., Cassano R., Mazzotta P., 2014, ApJ, 781, 9

Giodini S., et al., 2009, ApJ, 703, 982

Girichidis P., et al., 2016a, MNRAS, 456, 3432

Girichidis P., et al., 2016b, ApJ, 816, L19

Gonzalez A. H., Sivanandam S., Zabludoff A. I., Zaritsky D., 2013, ApJ, 778, 14

Governato F., Willman B., Mayer L., Brooks A., Stinson G., Valenzuela O., Wadsley J., Quinn T., 2007, MNRAS, 374, 1479

Greco J. P., Hill J. C., Spergel D. N., Battaglia N., 2015, ApJ, 808, 151

Guetta D., Della Valle M., 2007, ApJ, 657, L73

Guo F., Oh S. P., 2008, MNRAS, 384, 251

Guo F., Mathews W. G., Dobler G., Oh S. P., 2012, ApJ, 756, 182

Gupta A., Mathur S., Krongold Y., 2017, ApJ, 836, 243

Hafen Z., et al., 2017, MNRAS, 469, 2292

Han J. L., Manchester R. N., Lyne A. G., Qiao G. J., van Straten W., 2006, ApJ, 642, 868

Hanasz M., Lesch H., Naab T., Gawryszczak A., Kowalik K., Wóltański D., 2013, ApJ, 777, L38

Hansen B. M. S., 1999, ApJ, 512, L117

Häring N., Rix H.-W., 2004, ApJ, 604, L89

Harper-Clark E., Murray N., 2011, in Alves J., Elmegreen B. G., Girart J. M., Trimble V., eds, IAU Symposium Vol. 270, Computational Star Formation. pp 235–238, doi:10.1017/S1743921311000445

Hayward C. C., Hopkins P. F., 2017, MNRAS, 465, 1682

Hayward C. C., Torrey P., Springel V., Hernquist L., Vogelsberger M., 2014, MNRAS, 442, 1992

Hensler G., Steyrleithner P., Recchi S., 2016, Proceedings of the International Astronomical Union, 11, 99–101

Hernquist L., 1990, ApJ, 356, 359

Hickox R. C., Alexander D. M., 2018, preprint, (arXiv:1806.04680)

Hitomi Collaboration et al., 2016, Nature, 535, 117

Hitomi Collaboration et al., 2018, PASJ, 70, 9

Hopkins P. F., 2013, MNRAS, 428, 2840

Hopkins P. F., 2015, MNRAS, 450, 53

Hopkins P. F., 2016, MNRAS, 462, 576

Hopkins P. F., 2017, MNRAS, 466, 3387

Hopkins P. F., Elvis M., 2010, MNRAS, 401, 7

Hopkins P. F., Quataert E., 2011, MNRAS, 415, 1027

Hopkins P. F., Raives M. J., 2016, MNRAS, 455, 51

Hopkins P. F., Hernquist L., Cox T. J., Di Matteo T., Martini P., Robertson B., Springel V., 2005, ApJ, 630, 705

Hopkins P. F., Hernquist L., Cox T. J., Di Matteo T., Robertson B., Springel V., 2006a, ApJS, 163, 1

Hopkins P. F., Hernquist L., Cox T. J., Robertson B., Springel V., 2006b, ApJS, 163, 50

Hopkins P. F., Hernquist L., Cox T. J., Robertson B., Krause E., 2007, ApJ, 669, 45

Hopkins P. F., Hernquist L., Cox T. J., Kereš D., 2008, ApJS, 175, 356

Hopkins P. F., Quataert E., Murray N., 2011, MNRAS, 417, 950

Hopkins P. F., Quataert E., Murray N., 2012a, MNRAS, 421, 3488

Hopkins P. F., Quataert E., Murray N., 2012b, MNRAS, 421, 3522

Hopkins P. F., Cox T. J., Hernquist L., Narayanan D., Hayward C. C., Murray N., 2013a, MNRAS, 430, 1901

Hopkins P. F., Narayanan D., Murray N., 2013b, MNRAS, 432, 2647

Hopkins P. F., Narayanan D., Murray N., Quataert E., 2013c, MNRAS, 433, 69

Hopkins P. F., Kereš D., Murray N., Hernquist L., Narayanan D., Hayward C. C., 2013d, MNRAS, 433, 78

Hopkins P. F., Kereš D., Oñorbe J., Faucher-Giguère C.-A., Quataert E., Murray N., Bullock J. S., 2014, MNRAS, 445, 581

Hopkins P. F., et al., 2017, preprint, (arXiv:1707.07010)

Hopkins P. F., et al., 2018a, MNRAS, 477, 1578

Hopkins P. F., et al., 2018b, MNRAS, 480, 800

Hu C.-Y., Naab T., Walch S., Glover S. C. O., Clark P. C., 2016, MNRAS, 458, 3528

Hu C.-Y., Naab T., Glover S. C. O., Walch S., Clark P. C., 2017, MNRAS, 471, 2151

Hudson D. S., Mittal R., Reiprich T. H., Nulsen P. E. J., Andernach H., Sarazin C. L., 2010, A&A, 513, A37

Humphrey P. J., Buote D. A., 2013, MNRAS, 436, 2879

Humphrey P. J., Buote D. A., Brighenti F., Flohic H. M. L. G., Gastaldello F., Mathews W. G., 2012a, ApJ, 748, 11

Humphrey P. J., Buote D. A., O'Sullivan E., Ponman T. J., 2012b, ApJ, 755, 166

Jacob S., Pfrommer C., 2017a, MNRAS, 467, 1449

Jacob S., Pfrommer C., 2017b, MNRAS, 467, 1478

Jacob S., Pakmor R., Simpson C. M., Springel V., Pfrommer C., 2018, MNRAS, 475, 570

Jansson R., Farrar G. R., 2012a, ApJ, 757, 14

Jansson R., Farrar G. R., 2012b, ApJ, 761, L11

Jarosik N., et al., 2011, ApJS, 192, 14

Jefferies J. T., 1968, Spectral line formation

Ji S., Oh S. P., McCourt M., 2018, MNRAS, 476, 852

Johansson P. H., Naab T., Burkert A., 2009, ApJ, 690, 802

Jun B.-I., Jones T. W., 1999, ApJ, 511, 774

Jun B.-I., Norman M. L., 1996a, ApJ, 465, 800

Jun B.-I., Norman M. L., 1996b, ApJ, 472, 245

Jun B.-I., Norman M. L., Stone J. M., 1995, ApJ, 453, 332

Kaastra J. S., Mewe R., Nieuwenhuijzen H., 1996, in Yamashita K., Watanabe T., eds, UV and X-ray Spectroscopy of Astrophysical and Laboratory Plasmas. pp 411–414

Kainulainen J., Tan J. C., 2013, A&A, 549, A53

Kannan R., Springel V., Pakmor R., Marinacci F., Vogelsberger M., 2016, MNRAS, 458, 410

Kannan R., Vogelsberger M., Pfrommer C., Weinberger R., Springel V., Hernquist L., Puchwein E., Pakmor R., 2017, ApJ, 837, L18

Kasen D., Thomas R. C., Nugent P., 2006, ApJ, 651, 366

Katz N., White S. D. M., 1993, ApJ, 412, 455

Katz N., Weinberg D. H., Hernquist L., 1996, ApJS, 105, 19

Kauffmann G., White S. D. M., Guiderdoni B., 1993, MNRAS, 264, 201

Kauffmann G., et al., 2003, MNRAS, 341, 54

Keller B. W., Wadsley J., Benincasa S. M., Couchman H. M. P., 2014, MNRAS, 442, 3013

Keller B. W., Wadsley J., Couchman H. M. P., 2015, MNRAS, 453, 3499

Kennicutt Jr. R. C., 1998, ApJ, 498, 541

Kereš D., Katz N., Weinberg D. H., Davé R., 2005, MNRAS, 363, 2

Kereš D., Katz N., Davé R., Fardal M., Weinberg D. H., 2009, MNRAS, 396, 2332

Khalatyan A., Cattaneo A., Schramm M., Gottlöber S., Steinmetz M., Wisotzki L., 2008, MNRAS, 387, 13

Kim D.-W., Fabbiano G., 2013, ApJ, 776, 116

Kim W.-T., Narayan R., 2003a, ApJ, 596, 889

Kim W.-T., Narayan R., 2003b, ApJ, 596, L139

Kim C.-G., Ostriker E. C., 2015a, ApJ, 802, 99

Kim C.-G., Ostriker E. C., 2015b, ApJ, 815, 67

Kim C.-G., Ostriker E. C., 2017, ApJ, 846, 133

Kim C.-G., Ostriker E. C., Kim W.-T., 2013, ApJ, 776, 1

Kim C.-G., Ostriker E. C., Kim W.-T., 2014, ApJ, 786, 64

Kim C.-G., Ostriker E. C., Raileanu R., 2017, ApJ, 834, 25

Klypin A., Kravtsov A. V., Valenzuela O., Prada F., 1999, ApJ, 522, 82

Kotarba H., Karl S. J., Naab T., Johansson P. H., Dolag K., Lesch H., Stasyszyn F. A., 2010, ApJ, 716, 1438

Kotarba H., Lesch H., Dolag K., Naab T., Johansson P. H., Donnert J., Stasyszyn F. A., 2011, MNRAS, 415, 3189

Kravtsov A., Vikhlinin A., Meshscheryakov A., 2014, preprint, (arXiv:1401.7329)

Kronberg P. P., Bernet M. L., Miniati F., Lilly S. J., Short M. B., Higdon D. M., 2008, ApJ, 676, 70

Kroupa P., 2002, Science, 295, 82

Krumholz M. R., Gnedin N. Y., 2011, ApJ, 729, 36

Krumholz M. R., Klein R. I., McKee C. F., 2011, ApJ, 740, 74

Krumholz M. R., Fumagalli M., da Silva R. L., Rendahl T., Parra J., 2015, MNRAS, 452, 1447

Kulsrud R. M., Zweibel E. G., 2008, Reports on Progress in Physics, 71, 46901

Kunz M. W., Bogdanović T., Reynolds C. S., Stone J. M., 2012, ApJ, 754, 122

Kuzio de Naray R., McGaugh S. S., de Blok W. J. G., 2008, ApJ, 676, 920

Leitherer C., et al., 1999, ApJS, 123, 3

Levine E. S., Blitz L., Heiles C., 2006, ApJ, 643, 881

Li Y., Bryan G. L., 2014, ApJ, 789, 54

Li Y., Bryan G. L., Ruszkowski M., Voit G. M., O'Shea B. W., Donahue M., 2015, ApJ, 811, 73

Li Y., Ruszkowski M., Bryan G. L., 2017, ApJ, 847, 106

Li Y.-P., et al., 2018, preprint, (arXiv:1803.01444)

Lilly D. K., 1967

Lim S., Mo H., Wang H., Yang X., 2017, preprint, (arXiv:1712.08619)

Lodders K., 2003, ApJ, 591, 1220

Ma X., Hopkins P. F., Faucher-Giguere C.-A., Zolman N., Muratov A. L., Keres D., Quataert E., 2015a, ArXiv e-prints, arXiv:1504.02097,

Ma X., Kasen D., Hopkins P. F., Faucher-Giguère C.-A., Quataert E., Kereš D., Murray N., 2015b, MNRAS, 453, 960

Ma X., Hopkins P. F., Wetzel A. R., Kirby E. N., Angles-Alcazar D., Faucher-Giguere C.-A., Keres D., Quataert E., 2016a, ArXiv e-prints, arXiv:1608.04133,

Ma X., Hopkins P. F., Kasen D., Quataert E., Faucher-Giguère C.-A., Kereš D., Murray N., Strom A., 2016b, MNRAS, 459, 3614

Madgwick D. S., Somerville R., Lahav O., Ellis R., 2003, MNRAS, 343, 871

Mannucci F., Della Valle M., Panagia N., 2006, MNRAS, 370, 773

Markevitch M., Vikhlinin A., 2007, PhysRep, 443, 1

Martig M., Bournaud F., Teyssier R., Dekel A., 2009, ApJ, 707, 250

Martizzi D., Faucher-Giguère C.-A., Quataert E., 2015, MNRAS, 450, 504

Martizzi D., Fielding D., Faucher-Giguère C.-A., Quataert E., 2016a, MNRAS,

Martizzi D., Fielding D., Faucher-Giguère C.-A., Quataert E., 2016b, MNRAS, 459, 2311

Martizzi D., Quataert E., Faucher-Giguere C.-A., Fielding D., 2018, preprint, (arXiv:1805.06461)

Mathews W. G., Bregman J. N., 1978, ApJ, 224, 308

Mathews W. G., Faltenbacher A., Brighenti F., 2006, ApJ, 638, 659

McCarthy I. G., et al., 2010, MNRAS, 406, 822

McCourt M., Sharma P., Quataert E., Parrish I. J., 2012, MNRAS, 419, 3319

McCourt M., O'Leary R. M., Madigan A.-M., Quataert E., 2015, MNRAS, 449, 2

McDonald M., Veilleux S., Mushotzky R., 2011, ApJ, 731, 33

McDonald M., et al., 2013, ApJ, 774, 23

McDonald M., Gaspari M., McNamara B. R., Tremblay G. R., 2018, ApJ, 858, 45

McKee C. F., Cowie L. L., 1977, ApJ, 215, 213

McNamara B. R., Nulsen P. E. J., 2007, ARA&A, 45, 117

Meece G. R., Voit G. M., O'Shea B. W., 2017, ApJ, 841, 133

Merrifield M. R., 1992, AJ, 103, 1552

Miller M. J., Bregman J. N., 2013, ApJ, 770, 118

Miller M. J., Bregman J. N., 2015, ApJ, 800, 14

Mitchell N. L., McCarthy I. G., Bower R. G., Theuns T., Crain R. A., 2009, MNRAS, 395, 180

Mittal R., Hudson D. S., Reiprich T. H., Clarke T., 2009, A&A, 501, 835

Modjaz M., et al., 2008, AJ, 135, 1136

Modjaz M., Kewley L., Bloom J. S., Filippenko A. V., Perley D., Silverman J. M., 2011, ApJ, 731, L4

Molina F. Z., Glover S. C. O., Federrath C., Klessen R. S., 2012, ArXiv e-prints, arXiv:1203.2117,

Moore B., Ghigna S., Governato F., Lake G., Quinn T., Stadel J., Tozzi P., 1999, ApJ, 524, L19

Muratov A. L., Kereš D., Faucher-Giguère C.-A., Hopkins P. F., Quataert E., Murray N., 2015, MNRAS, 454, 2691

Muratov A. L., et al., 2017, MNRAS, 468, 4170

Murray N., Ménard B., Thompson T. A., 2011, ApJ, 735, 66

Naab T., Ostriker J. P., 2017, ARA&A, 55, 59

Navarro J. F., Frenk C. S., White S. D. M., 1996, ApJ, 462, 563

Nomoto K., Maeda K., Mazzali P. A., Umeda H., Deng J., Iwamoto K., 2004, in Fryer C. L., ed., Astrophysics and Space Science Library Vol. 302, Astrophysics and Space Science Library. pp 277–325 (arXiv:astro-ph/0308136), doi:10.1007/978-0-306-48599-2_10

Norman M. L., Bryan G. L., 1999, in Röser H.-J., Meisenheimer K., eds, Lecture Notes in Physics, Berlin Springer Verlag Vol. 530, The Radio Galaxy Messier 87. p. 106 (arXiv:astro-ph/9802335), doi:10.1007/BFb0106425

O'Dea C. P., et al., 2008, ApJ, 681, 1035

Ogiya G., Burkert A., 2015, MNRAS, 446, 2363

Oh S.-H., de Blok W. J. G., Walter F., Brinks E., Kennicutt Robert C. J., 2008, AJ, 136, 2761

Orr M. E., et al., 2018, MNRAS, 478, 3653

Ostriker J. P., Choi E., Ciotti L., Novak G. S., Proga D., 2010, ApJ, 722, 642

Pakmor R., Springel V., 2013, MNRAS, 432, 176

Pakmor R., Pfrommer C., Simpson C. M., Kannan R., Springel V., 2016, MNRAS, 462, 2603

Pakmor R., et al., 2017, preprint, (arXiv:1701.07028)

Parrish I. J., Quataert E., 2008, ApJ, 677, L9

Parrish I. J., Stone J. M., Lemaster N., 2008, ApJ, 688, 905

Parrish I. J., Quataert E., Sharma P., 2009, ApJ, 703, 96

Parrish I. J., Quataert E., Sharma P., 2010, ApJ, 712, L194

Parrish I. J., McCourt M., Quataert E., Sharma P., 2012a, MNRAS, 419, L29

Parrish I. J., McCourt M., Quataert E., Sharma P., 2012b, MNRAS, 422, 704

Paul S., Iapichino L., Miniati F., Bagchi J., Mannheim K., 2011, ApJ, 726, 17

Pellegrini S., Ciotti L., Negri A., Ostriker J. P., 2018, ApJ, 856, 115

Peres C. B., Fabian A. C., Edge A. C., Allen S. W., Johnstone R. M., White D. A., 1998, MNRAS, 298, 416

Peterson J. R., Fabian A. C., 2006, PhysRep, 427, 1

Pfrommer C., 2013, ApJ, 779, 10

Pfrommer C., Pakmor R., Schaal K., Simpson C. M., Springel V., 2017a, MNRAS, 465, 4500

Pfrommer C., Pakmor R., Simpson C. M., Springel V., 2017b, ApJ, 847, L13

Pillepich A., et al., 2018, MNRAS, 473, 4077

Piontek R. A., Ostriker E. C., 2005, ApJ, 629, 849

Piontek R. A., Ostriker E. C., 2007, ApJ, 663, 183

Planck Collaboration et al., 2013, A&A, 557, A52

Podsiadlowski P., Mazzali P. A., Nomoto K., Lazzati D., Cappellaro E., 2004, ApJ, 607, L17

Pope E. C. D., Pavlovski G., Kaiser C. R., Fangohr H., 2006, MNRAS, 367, 1121

Popping G., Behroozi P. S., Peeples M. S., 2015, MNRAS, 449, 477

Porter D. H., 1985, PhD thesis, California Univ., Berkeley

Powell K. G., Roe P. L., Linde T. J., Gombosi T. I., De Zeeuw D. L., 1999, Journal of Computational Physics, 154, 284

Pozzetti L., et al., 2010, A&A, 523, A13

Price D. J., Federrath C., 2010, MNRAS, 406, 1659

Quataert E., 2008, ApJ, 673, 758

Rafferty D. A., McNamara B. R., Nulsen P. E. J., 2008, ApJ, 687, 899

Rand R. J., Kulkarni S. R., 1989, ApJ, 343, 760

Reiprich T. H., Böhringer H., 2002, ApJ, 567, 716

Ressler S. M., Quataert E., Stone J. M., 2018, MNRAS, 478, 3544

Reynolds C. S., McKernan B., Fabian A. C., Stone J. M., Vernaleo J. C., 2005, MNRAS, 357, 242

Richings A. J., Faucher-Giguère C.-A., 2018a, MNRAS, 474, 3673

Richings A. J., Faucher-Giguère C.-A., 2018b, MNRAS, 478, 3100

Richings A. J., Schaye J., 2016, MNRAS, 458, 270

Ricker P. M., Sarazin C. L., 2001, ApJ, 561, 621

Rieder M., Teyssier R., 2016, MNRAS, 457, 1722

Rieder M., Teyssier R., 2017, preprint, (arXiv:1704.05845)

Robertson B. E., Kravtsov A. V., 2008, ApJ, 680, 1083

Roettiger K., Burns J., Loken C., 1993, ApJ, 407, L53

Roettiger K., Loken C., Burns J. O., 1997, ApJS, 109, 307

Romeo A. B., Wiegert J., 2011, MNRAS, 416, 1191

Ruszkowski M., Oh S. P., 2010, ApJ, 713, 1332

Ruszkowski M., Oh S. P., 2011, MNRAS, 414, 1493

Ruszkowski M., Yang H.-Y. K., Zweibel E., 2017a, ApJ, 834, 208

Ruszkowski M., Yang H.-Y. K., Reynolds C. S., 2017b, ApJ, 844, 13

Salem M., Bryan G. L., 2014, MNRAS, 437, 3312

Salem M., Bryan G. L., Hummels C., 2014, ApJ, 797, L18

Salomé P., et al., 2006, A&A, 454, 437

Salucci P., Wilkinson M. I., Walker M. G., Gilmore G. F., Grebel E. K., Koch A., Frigerio Martins C., Wyse R. F. G., 2012, MNRAS, 420, 2034

Sanderson A. J. R., Ponman T. J., O'Sullivan E., 2006, MNRAS, 372, 1496

Sanderson A. J. R., O'Sullivan E., Ponman T. J., 2009, MNRAS, 395, 764

Sanderson A. J. R., O'Sullivan E., Ponman T. J., Gonzalez A. H., Sivanandam S., Zabludoff A. I., Zaritsky D., 2013, MNRAS, 429, 3288

Sarazin C. L., 1988, X-ray emission from clusters of galaxies

Scannapieco E., Brüggen M., 2008, ApJ, 686, 927

Schaye J., et al., 2015, MNRAS, 446, 521

Schmidt M., 1959, ApJ, 129, 243

Schmidt W., Niemeyer J. C., Hillebrandt W., 2006a, A&A, 450, 265

Schmidt W., Niemeyer J. C., Hillebrandt W., Röpke F. K., 2006b, A&A, 450, 283

Schmidt W., Federrath C., Hupp M., Kern S., Niemeyer J. C., 2009, A&A, 494, 127

Schober J., Schleicher D. R. G., Federrath C., Bovino S., Klessen R. S., 2015, PhRvE, 92, 23010

Schure K. M., Kosenko D., Kaastra J. S., Keppens R., Vink J., 2009, A&A, 508, 751

Sharma P., Chandran B. D. G., Quataert E., Parrish I. J., 2009, ApJ, 699, 348

Sharma P., Parrish I. J., Quataert E., 2010, ApJ, 720, 652

Sharma P., McCourt M., Quataert E., Parrish I. J., 2012, MNRAS, 420, 3174

Shen S., Wadsley J., Stinson G., 2010, MNRAS, 407, 1581

Shen S., Madau P., Guedes J., Mayer L., Prochaska J. X., Wadsley J., 2013, ApJ, 765, 89

Shetty R., Ostriker E. C., 2008, ApJ, 684, 978

Shin M.-S., Ostriker J. P., Ciotti L., 2010, ApJ, 711, 268

Sijacki D., Springel V., 2006, MNRAS, 371, 1025

Sijacki D., Springel V., Di Matteo T., Hernquist L., 2007, MNRAS, 380, 877

Silk J., 1976, ApJ, 208, 646

Silk J., 2009, in Andersen J., Nordströara m B., Bland-Hawthorn J., eds, IAU Symposium Vol. 254, The Galaxy Disk in Cosmological Context. pp 401–410 (arXiv:0809.0513), doi:10.1017/S1743921308027889

Silk J., 2010, in Block D. L., Freeman K. C., Puerari I., eds, Galaxies and their Masks. Springer New York, New York, NY, pp 399–408

Silk J., 2011, in Carignan C., Combes F., Freeman K. C., eds, IAU Symposium Vol. 277, Tracing the Ancestry of Galaxies. pp 273–281 (arXiv:1102.0283), doi:10.1017/S1743921311022939

Silk J., Rees M. J., 1998, A&A, 331, L1

Simpson C. M., Pakmor R., Marinacci F., Pfrommer C., Springel V., Glover S. C. O., Clark P. C., Smith R. J., 2016, ApJ, 827, L29

Smagorinsky J., 1963, Monthly Weather Review, 91, 99

Soderberg A. M., et al., 2006, Nature, 442, 1014

Soker N., Sarazin C. L., 1990, ApJ, 348, 73

Somerville R. S., Primack J. R., 1999, MNRAS, 310, 1087

Sparre M., Hayward C. C., Feldmann R., Faucher-Giguère C.-A., Muratov A. L., Kereš D., Hopkins P. F., 2017, MNRAS, 466, 88

Spitzer L., Härm R., 1953, Physical Review, 89, 977

Springel V., 2000, MNRAS, 312, 859

Springel V., 2005, MNRAS, 364, 1105

Springel V., 2010, MNRAS, 401, 791

Springel V., Hernquist L., 2003, MNRAS, 339, 289

Springel V., White S. D. M., 1999, MNRAS, 307, 162

Springel V., Di Matteo T., Hernquist L., 2005, MNRAS, 361, 776

Stanek R., Evrard A. E., Böhringer H., Schuecker P., Nord B., 2006, ApJ, 648, 956

Stanway E. R., Eldridge J. J., Becker G. D., 2016, MNRAS, 456, 485

Stinson G. S., Brook C., Macciò A. V., Wadsley J., Quinn T. R., Couchman H. M. P., 2013, MNRAS, 428, 129

Stone J. M., Gardiner T., 2007, ApJ, 671, 1726

Stone J. M., Gardiner T. A., Teuben P., Hawley J. F., Simon J. B., 2008, ApJS, 178, 137

Strigari L. E., Frenk C. S., White S. D. M., 2014, arXiv e-prints, p. arXiv:1406.6079

Strong A. W., Moskalenko I. V., 1998, ApJ, 509, 212

Strong A. W., Porter T. A., Digel S. W., Jóhannesson G., Martin P., Moskalenko I. V., Murphy E. J., Orlando E., 2010, ApJ, 722, L58

Su Y., White III R. E., Miller E. D., 2013, ApJ, 775, 89

Su Y., Buote D., Gastaldello F., Brighenti F., 2015, ApJ, 805, 104

Su K.-Y., Hopkins P. F., Hayward C. C., Faucher-Giguère C.-A., Kereš D., Ma X., Robles V. H., 2017, MNRAS, 471, 144

Su K.-Y., Hopkins P. F., Hayward C. C., Ma X., Faucher-Giguère C.-A., Kereš D., Orr M. E., Robles V. H., 2018a, MNRAS, in press, arXiv:1809.09120,

Su K.-Y., et al., 2018b, arXiv e-prints, p. arXiv:1812.03997

Su K.-Y., Hayward C. C., Hopkins P. F., Quataert E., Faucher-Giguère C.-A., Kereš D., 2018c, MNRAS, 473, L111

Su K.-Y., et al., 2018d, MNRAS, 480, 1666

Tacconi L. J., et al., 2010, Nature, 463, 781

Tamura T., et al., 2001, A&A, 365, L87

Tang S., Wang Q. D., 2005, ApJ, 628, 205

Tang S., Wang Q. D., Mac Low M.-M., Joung M. R., 2009, MNRAS, 398, 1468

Tasker E. J., 2011, ApJ, 730, 11

Taylor P., Kobayashi C., 2015, MNRAS, 448, 1835

Thacker R. J., Couchman H. M. P., 2000, ApJ, 545, 728

Thompson C., 2000, ApJ, 534, 915

Thompson T. A., Krumholz M. R., 2016, MNRAS, 455, 334

Tricco T. S., Price D. J., Federrath C., 2016, MNRAS, 461, 1260

Trotta R., Jóhannesson G., Moskalenko I. V., Porter T. A., Ruiz de Austri R., Strong A. W., 2011, ApJ, 729, 106

Tucker W. H., Rosner R., 1983, ApJ, 267, 547

Uhlig M., Pfrommer C., Sharma M., Nath B. B., Enßlin T. A., Springel V., 2012, MNRAS, 423, 2374

Vazza F., Brunetti G., Gheller C., Brunino R., Brüggen M., 2011, A&A, 529, A17

Vernaleo J. C., Reynolds C. S., 2006, ApJ, 645, 83

Verner D. A., Ferland G. J., 1996, ApJS, 103, 467

Verner D. A., Ferland G. J., Korista K. T., Yakovlev D. G., 1996, ApJ, 465, 487

Voigt L. M., Fabian A. C., 2004, MNRAS, 347, 1130

Voigt L. M., Schmidt R. W., Fabian A. C., Allen S. W., Johnstone R. M., 2002, MNRAS, 335, L7

Voit G. M., 2011, ApJ, 740, 28

Voit G. M., Donahue M., 2015, ApJ, 799, L1

Voit G. M., Donahue M., Bryan G. L., McDonald M., 2015, Nature, 519, 203

Voit G. M., Meece G., Li Y., O'Shea B. W., Bryan G. L., Donahue M., 2017, ApJ, 845, 80

Wadsley J. W., Veeravalli G., Couchman H. M. P., 2008, MNRAS, 387, 427

Wagh B., Sharma P., McCourt M., 2014, MNRAS, 439, 2822

Walch S., Naab T., 2015, MNRAS, 451, 2757

Walker M. G., Peñarrubia J., 2011, ApJ, 742, 20

Wang P., Abel T., 2009, ApJ, 696, 96

Weinberger R., et al., 2017, MNRAS, 465, 3291

Weinberger R., et al., 2018, MNRAS, 479, 4056

Weinmann S. M., van den Bosch F. C., Yang X., Mo H. J., 2006, MNRAS, 366, 2

Werner N., et al., 2013, ApJ, 767, 153

Wetzel A. R., Tinker J. L., Conroy C., 2012, MNRAS, 424, 232

Wetzel A. R., Hopkins P. F., Kim J.-h., Faucher-Giguère C.-A., Kereš D., Quataert E., 2016, ApJ, 827, L23

Wevers B. M. H. R., van der Kruit P. C., Allen R. J., 1986, A&AS, 66, 505

Widrow L. M., 2002, Reviews of Modern Physics, 74, 775

Wiener J., Zweibel E. G., 2018, arXiv e-prints, p. arXiv:1812.02179

Wiener J., Oh S. P., Guo F., 2013, MNRAS, 434, 2209

Wiersma R. P. C., Schaye J., Smith B. D., 2009a, MNRAS, 393, 99

Wiersma R. P. C., Schaye J., Theuns T., Dalla Vecchia C., Tornatore L., 2009b, MNRAS, 399, 574

Williams J. P., McKee C. F., 1997, ApJ, 476, 166

Williamson D., Martel H., Kawata D., 2016, ApJ, 822, 91

Wong T., Blitz L., 2002, ApJ, 569, 157

Woo J., et al., 2013, MNRAS, 428, 3306

Yang H.-Y. K., Reynolds C. S., 2016, ApJ, 818, 181

Yoon D., Yuan F., Gan Z.-M., Ostriker J. P., Li Y.-P., Ciotti L., 2018, preprint, (arXiv:1803.03675)

Zakamska N. L., Narayan R., 2003, ApJ, 582, 162

Zhuravleva I., et al., 2014, Nature, 515, 85

ZuHone J. A., Markevitch M., Brunetti G., Giacintucci S., 2013, ApJ, 762, 78

ZuHone J. A., Kunz M. W., Markevitch M., Stone J. M., Biffi V., 2015, ApJ, 798, 90

ZuHone J. A., Markevitch M., Zhuravleva I., 2016, ApJ, 817, 110

ZuHone J. A., Miller E. D., Bulbul E., Zhuravleva I., 2018, ApJ, 853, 180

Zuckerman B., Evans II N. J., 1974, ApJ, 192, L149

da Silva R. L., Fumagalli M., Krumholz M., 2012, ApJ, 745, 145

de Blok W. J. G., Walter F., Brinks E., Trachternach C., Oh S. H., Kennicutt R. C. J., 2008, AJ, 136, 2648

van de Voort F., Quataert E., Hopkins P. F., Kereš D., Faucher-Giguère C.-A., 2015, MNRAS, 447, 140

van de Voort F., Quataert E., Hopkins P. F., Faucher-Giguère C.-A., Feldmann R., Kereš D., Chan T. K., Hafen Z., 2016, MNRAS, 463, 4533

Appendix A

RESOLUTION STUDY

A.1 Resolution study for Chapter 2

The resolution-dependence and convergence properties of our simulations (as well as other numerical properties, e.g., sensitivity to the numerical hydrodynamic methods) – including specifically the three dwarf galaxies studied here – have been studied extensively over several orders of magnitude in resolution (involving many additional galaxy properties) in Hopkins et al. (2018b) and Hopkins et al. (2018a). We refer to those papers for much more extensive analysis.

However, we have briefly considered resolution studies of our "new physics" IMF-SMP runs, for each of our haloes. The conclusions are identical so we focus on m10q here, and compare a run with ~ 10 times higher particle mass – i.e. $30\,M_{\odot}$ resolution (we have also varied the resolution by a factor of ~ 10 towards *lower* resolution, and again find consistent results, but these are less interesting).

The run list is included in Table A.1.1. The MR runs match the resolution of the corresponding m10q runs in the main text. The two "Default" runs from the main text are also included, indicating the range of stochastic variations of different physical quantities.

Fig. A.1.1 shows the total stellar mass, star formation rate, outflow rate, and outflow mass loading of the "IMF-SMP" runs with different resolutions. Fig. A.1.2 shows the escape fractions. Fig. A.1.3 shows the masses of gas in different phases, including cold-neutral, warm-ionized, and hot, and in outflows as a function of density at different redshifts. For all plotted quantities, the difference between the "IMF-SMP" HR and MR runs are within the stochastic range characterized by the two "Default" runs. This indicates that our results are reasonably converged at the fiducial resolution.

This higher-resolution run, as well as similar runs at ultra-high resolution (~ 10 – $50\,M_{\odot}$ mass resolution), will be studied systematically in future work (Wheeler et al., in prep).

Table A.1.1: Particle resolutions used in our convergence tests for the default m10q run

Resolution	Physics	$m_{i,1000}$	$m_{d,1000}$
MR	Default	0.25	1.3
MR	Default	0.25	1.3
MR	IMF-SMP	0.25	1.3
HR	IMF-SMP	0.03	0.16

(1) Resolution name. MR: Medium resolution. HR: High resolution. (2) Physics: The variants are described in § 2.2. (3) $m_{i,1000}$: Baryonic (star and gas) mass resolution in units of 1000 $M_\odot$. (4) $m_{d,1000}$: Dark matter mass resolution in units of 1000 $M_\odot$.

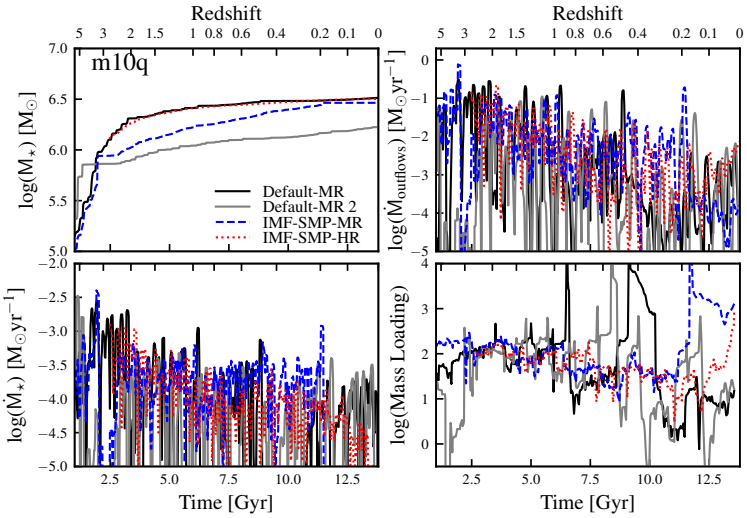

Figure A.1.1: Comparison of the total stellar mass *(upper left)*, SFR *(bottom left)*, outflow rate *(upper right)*, and outflow mass loading *(bottom right)*. The differences between the "IMF-SMP" HR and MR runs are within the stochastic range characterized by the two "Default" runs.

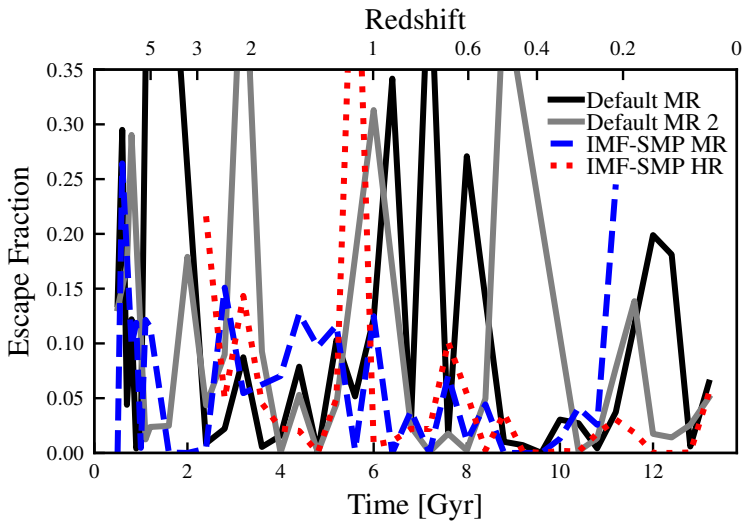

Figure A.1.2: Comparison of the photon escape fractions. The "IMF-SMP" runs with different resolutions have similar photon escape fractions.

A.2 Resolution study for Chapter 3

We performed convergence tests using our isolated SMC model, varying the particle mass by two orders of magnitude (see Table A.2.1). The HR run in Table A.2.1 matches the resolution of the standard SMC runs in the main text.

The resulting SFRs are shown in Fig. A.2.1, the phase structure and radial velocity distribution are shown in Fig. A.2.2 and Fig. A.2.3, respectively, and the turbulent and magnetic energies are shown in Fig. A.2.4. The star formation rate inFig. A.2.1 converges most rapidly with resolution. Among the inspected resolutions, there is little difference. As for the phase structure Fig. A.2.2, the cold neutral and warm ionized gas have very similar density distributions at all the resolutions tested. The hot gas and outflow density distributions converge more slowly but appear to be converged when at the MR resolution (i.e. resolution elements of a few thousand solar masses), as does the radial velocity distribution of gas particles Fig. A.2.3. Above this resolution, individual SN remnants begin to have their Sedov-Taylor phases resolved, and therefore generation of hot gas and outflows can be captured more robustly. The turbulent and magnetic energies similarly appear converged at the MR resolution. As the resolution increases, minor increases in the magnetic energy and minor decreases in the turbulent energy are found. This is because the small-scale shear field, which can dissipate turbulent kinetic energy and enhance the magnetic energy through field-line stretching, is suppressed at low resolution (Jun et al., 1995).

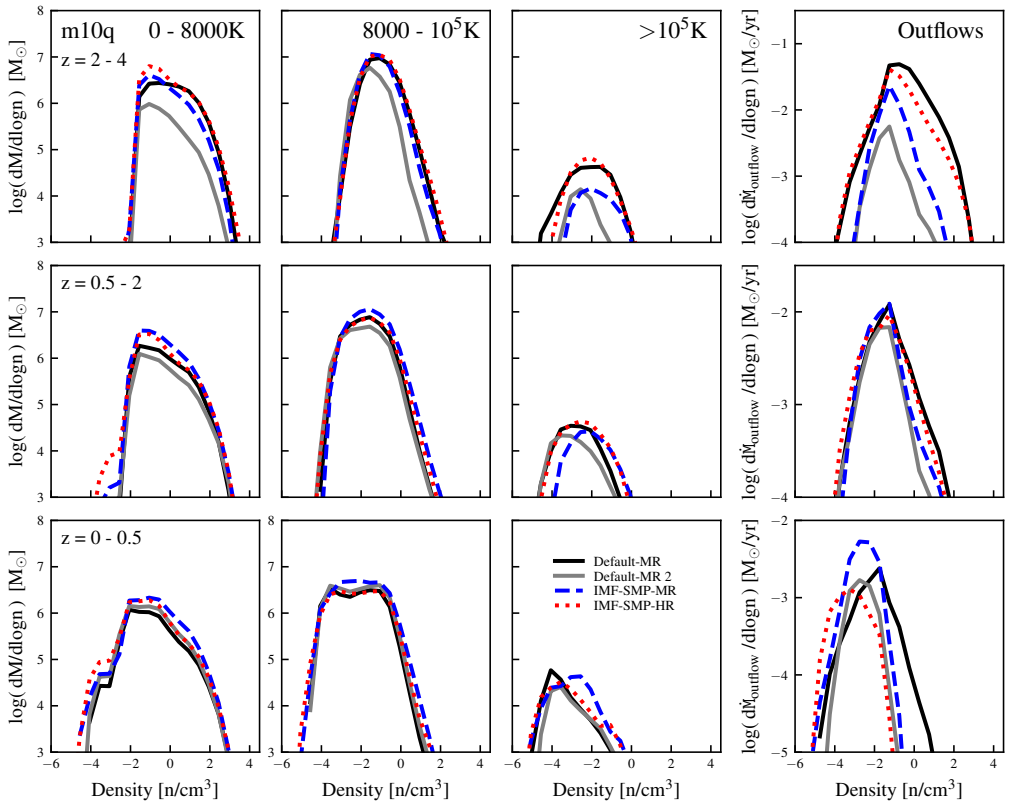

Figure A.1.3: Gas density distributions for m10q. Rows show the properties at different redshifts; columns show different phases, including cold-neutral (*left*), warm-ionized (*middle left*), hot (*middle right*), and outflows (*right*). The differences between the "IMF-SMP" HR and MR runs are within the stochastic range characterized by the two "Default" runs.

The convergence tests imply that our simulations of the more-massive galaxies, such as HiZ, Ell and CosmoMW, might not have sufficient resolution for all of their properties to be fully converged, especially their hot gas and outflow properties. Moreover, it is worth noting that, although we do not expect this to be the case, we cannot exclude the possibility of false convergence. The best resolution that we can achieve for galaxy simulations is inevitably many orders of magnitude coarser than the natural viscosity scale (the Kolmogorov length scale). Thus, it is possible that some important effects of fluid microphysics will appear only at much higher resolutions than these that will be achievable for galaxy simulations in the foreseeable future.

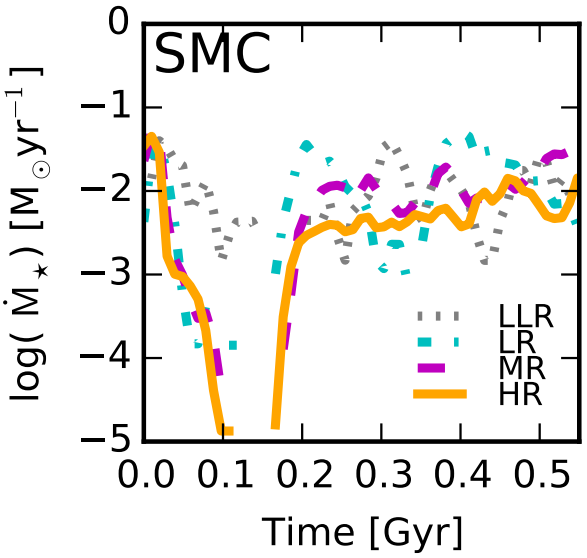

Figure A.2.1: Convergence of the star formation rate of the SMC model. The star formation rate converges quickly. Even at a resolution two orders of magnitude lower than the standard resolution, the SFR has a similar quasi-equilibrium value, $\sim 0.01 M_\odot/yr$.

Table A.2.1: Galaxy models used in our convergence tests

Initial Condition	Physics	Resolution	m_g	m_h	m_d	m_b
SMC	FB+MHD+Micro	LLR	3.6e4	2.9e5	6.2e4	4.8e4
SMC	FB+MHD+Micro	LR	3.6e3	2.9e4	6.2e3	4.8e3
SMC	FB+MHD+Micro	MR	1.1e3	8.6e3	1.9e3	1.4e3
SMC	FB+MHD+Micro	HR	3.6e2	2.9e3	6.2e2	4.8e2

(1) Initial Condition: Galaxy model used. These all adopt our SMC IC. (2) Physics: These all consider FB+MHD+Micro, the most demanding case. (3) Resolution name. LLR: The lowest resolution. LR: Low resolution. MR: Medium resolution. HR: High resolution. (4) m_g: Gas particle mass. (5) m_h: Halo particle mass. (6) m_d: Stellar disc particle mass. (7) m_b: Bulge particle mass.

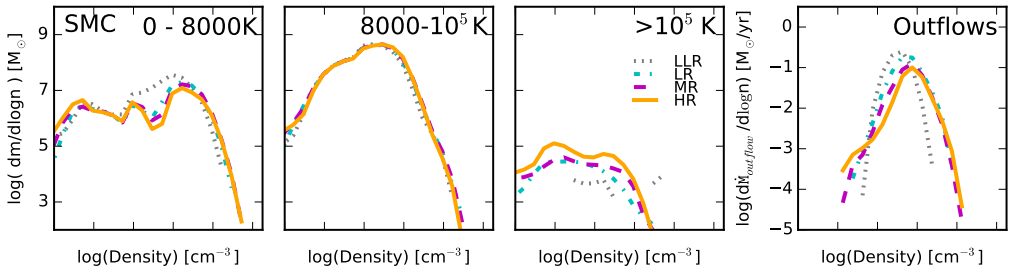

Figure A.2.2: Convergence of the density distribution of gas in different phases in the SMC model. The cold neutral and warm ionized gas have very similar density distributions at all of the resolutions inspected. The properties of the hot gas and outflows, on the other hand, appear to require resolution elements of $\sim$ 1000 $M_\odot$ per gas particle, which roughly separates whether SNe are individually resolved. Nevertheless, the density distributions of the hot gas and outflows in the lower-resolution runs do not differ drastically from the converged values.

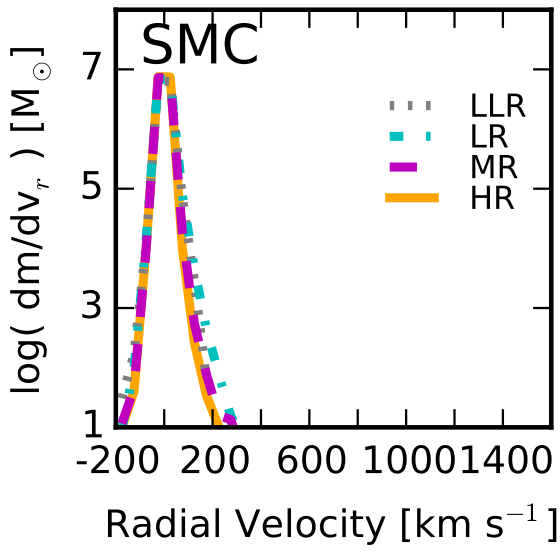

Figure A.2.3: Convergence of the radial velocity distribution of the gas particles in the SMC model. For all of the tested resolutions, the gas particles have almost identical radial velocity distributions.

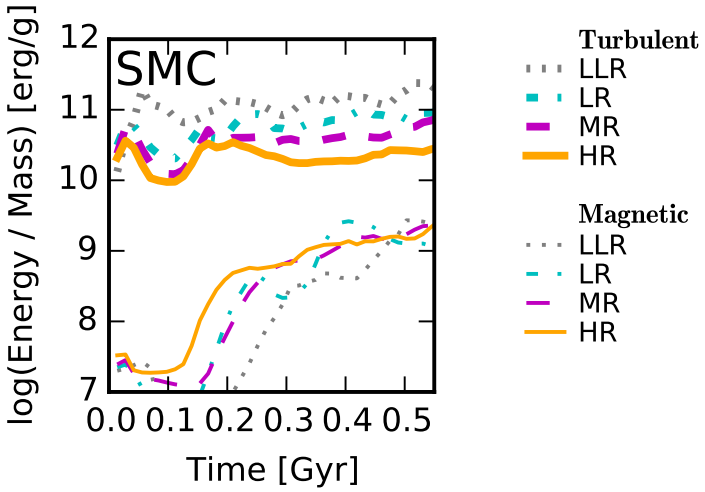

Figure A.2.4: The total turbulent kinetic energy (*thick lines*; defined in § 3.4.4) and magnetic energy (*thin lines*) per unit mass of the non-outflowing disc gas in the SMC model. Both the magnetic and turbulent energies appear converged once the gas mass resolution is $\sim 1000\ M_\odot$.

Table A.3.1: Mass resolutions used in our studies for the default m14 Run

Resolution	m_g	m_h	m_d	m_b
HR-HRS	8e3-2e6	4e7	8e3	8e3
HR	8e3-2e6	4e7	2.5e6	2.5e6
MR-MRS	3e4-2e6	4e7	3e4	3e4
MR	3e4-2e6	4e7	2.5e6	2.5e6
LR	2e6	4e7	1e7	1e7

(1) Resolution name. LR: Low resolution. MR: Medium resolution. HR: High resolution. MRS(HRS):Medium (High) resolution initial stellar particles. (2) m_g: Gas particle mass. (3) m_h: Dark matter halo particle mass. (4) m_d: Pre-existing stellar disc particle mass. (5) m_b: Pre-existing bulge particle mass. Note: All runs use the m14 halo with 'Default' FIRE physics.

A.3 Resolution study for Chapter 5

Extensive resolution studies of the FIRE-2 feedback and physics models used in this paper are presented in Hopkins et al. (2018b). However, since these did not address all of the specific questions in this paper, we performed a series resolution studies using our "Default" m14 halo, varying the mass resolution by a factor ~ 300 (Table A.3.1). The "HR" ("MR") run in Table A.3.1 matches the m14-HR (m14-MR) resolution in the text.

Fig. A.3.1 shows the evolution of the total core ($r < 30$ kpc) baryonic, hot gas

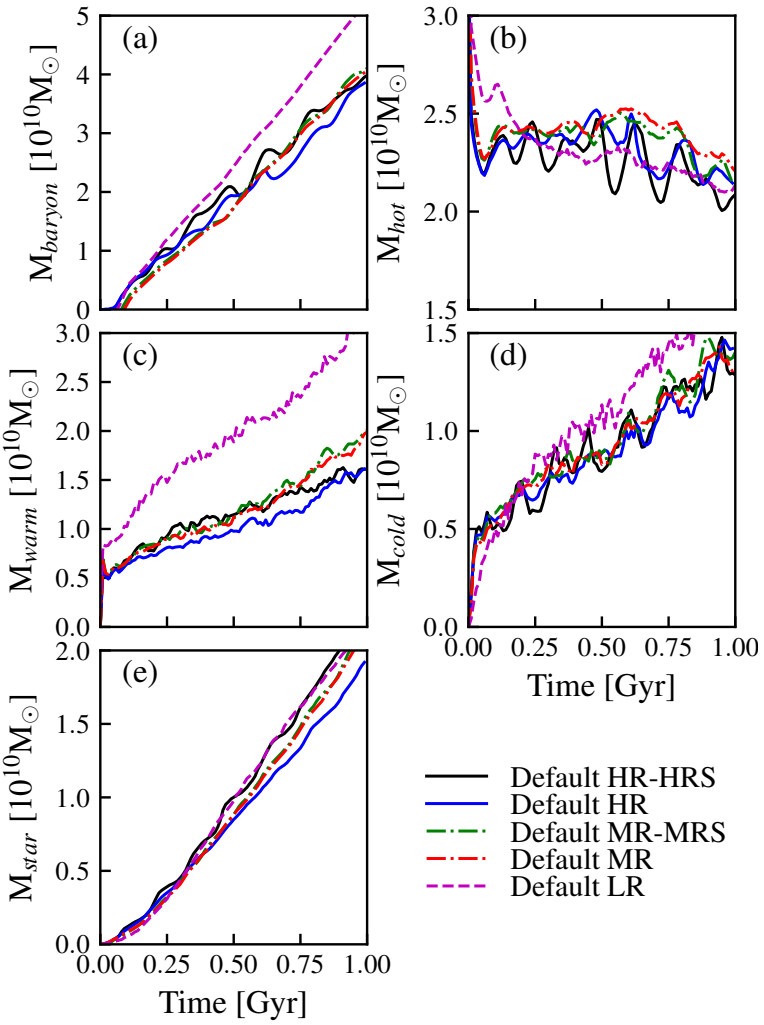

Figure A.3.1: The comparison of (a) core (< 30kpc) baryonic mass, (b) hot gas (> 10^6K) mass, (c) warm gas (8000 – 10^6K) mass, (d) cold gas (< 8000K) mass, and (e) stellar mass, for 'Default' m14 runs at different resolutions. 'MR' and 'HR' runs behave very similarly. 'LR' run, on the other hand has more gas accumulated in the warm phase.

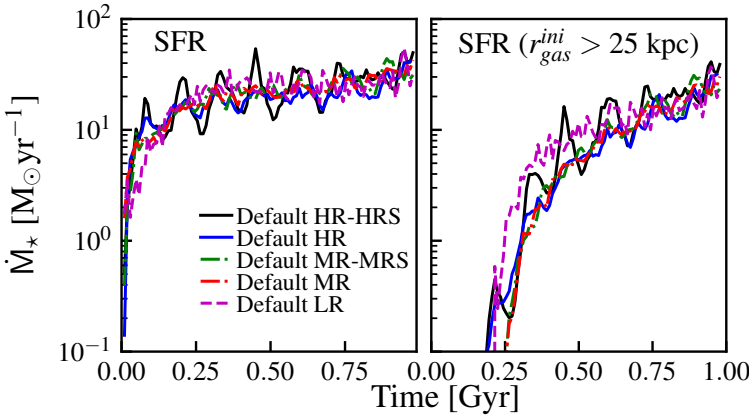

Figure A.3.2: Comparison of total SFR, and SFR from gas initially outside 25kpc, for 'Default' m14 runs with different resolutions. Runs at different resolutions have very similar SFRs.

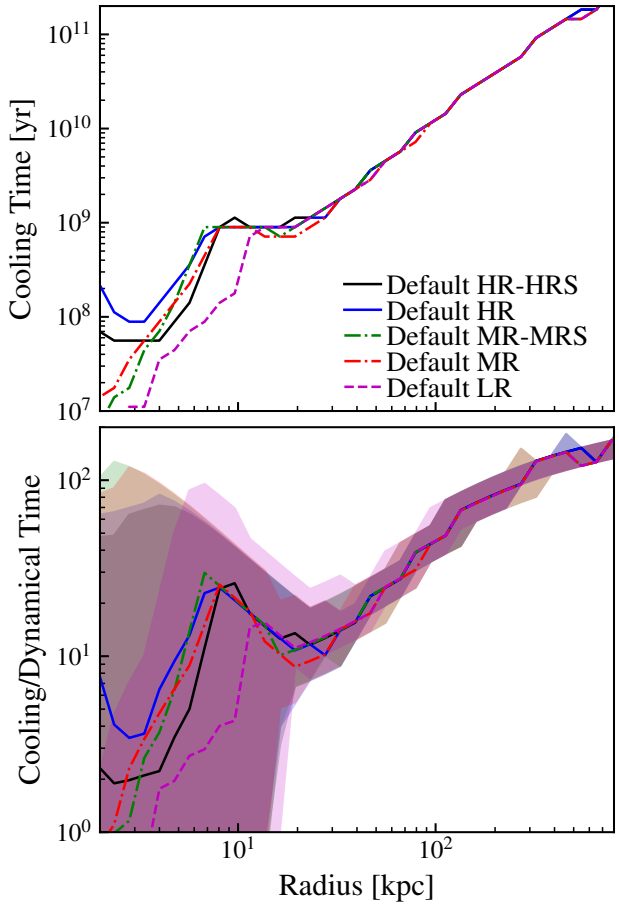

Figure A.3.3: Cooling time, and cooling time over dynamical time, as a function of radius for gas hotter than 10^5K. 'MR' and 'HR' runs have very similar cooling properties. 'LR' run, has slightly shorter cooling time at small radius.

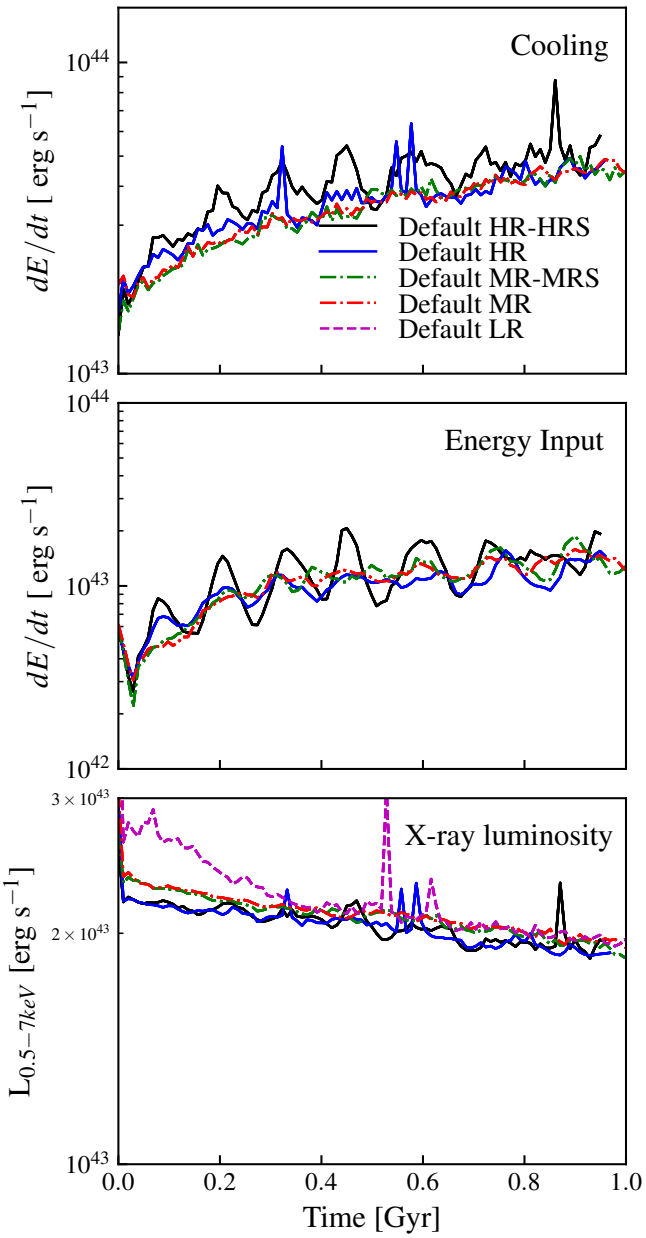

Figure A.3.4: The upper row plots the cooling and energy input rates within 30 kpc, as a function of time. The bottom row shows the X-ray luminosity in the 0.5 – 7 kev band. Runs with different resolutions have very similar cooling and energy input rates.

($> 10^6$K), warm gas ($8000 - 10^6$K), cold gas (< 8000K), and stellar masses at different resolutions. Fig. A.3.2 shows the comparison of total SFR, and SFR from gas initially outside 25kpc. Fig. A.3.3 shows the comparison of cooling time and cooling time over dynamical time for gas within 30 kpc. Fig. A.3.4 shows the evolution of cooling and energy input rates within 30 kpc, and the total X-ray luminosity of the whole halo. In these calculated properties, runs with resolution equal to or higher than that of our 'MR' run do not differ significantly. The 'LR' run on the other hand, exhibits more gas buildup in the warm phase at small radius, which leads to the shorter cooling time there. This, and the more detailed resolution studies referenced above, suggest the results are here are robust to resolution, at least over the dynamical range, that we explore here.

Appendix B

EFFECTS OF MAGNETIC FIELDS, CONDUCTION, AND VISCOSITY ON TURBULENT "STIRRING" MODELS

Given that turbulent stirring can (a) amplify magnetic fields, (b) be damped by viscosity from the hot gas, and (c) acts to mix hot and cold gas in a manner similar to physical conductivity, it is reasonable to ask what the impact of including or excluding explicit treatment of magnetic fields and physical (anisotropic) Braginskii conduction and viscosity in the hot gas might be. We explored these physics in Paper I in detail so only briefly note their effects here. Fig. B1 shows the SFRs of the 'Turb-core-1' run with and without explicit inclusion of these fluid microphysics in the simulations. Magnetic fields and conduction mildly suppress the SFR at the beginning of the 'Turb-core-1' run, and suppress the core baryonic mass by a factor of ~ 2, which is roughly consistent with their effect on the 'Default' run, but the systematic effects are small and get *smaller* as time goes on and the systems become more steady-state. Because viscosity and conduction are strongly temperature-dependent, their effects are even weaker in the smaller halo masses. Accordingly, the treatment of these physics does not substantially alter our conclusions.

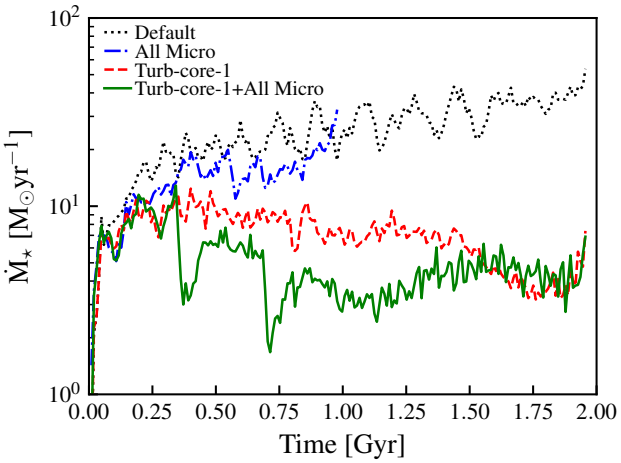

Figure B1: SFR (as Fig. 6.2) in our 'Default' and 'Turb-core-1' **m14** runs, comparing runs which treat the gas as pure-hydrodynamic, to runs which include magnetic fields and fully-anisotropic Spitzer-Braginski conduction and viscosity following Su et al. (2017) ("All Micro"). Consistent with our study in Paper I, these additional microphysics (mostly conduction) suppress the SFRs by a factor ~ 2, but do not qualitatively change any of our conclusions.